A search for Gamma Ray Burst Neutrinos

using the

Radio Ice Cherenkov Experiment

by

Pauline L Harris

A thesis
submitted in partial fulfilment
of the requirements for the Degree of
Doctorate of Philosophy
at the
University of Canterbury
Christchurch, New Zealand

University of Canterbury
2008

Abstract

The Radio Ice Cherenkov Experiment (RICE) located at the South Pole, is designed to detect the coherent broad-band radio Cherenkov radiation emitted when a high energy (10^{15} to 10^{18} eV) neutrino interacts with a nucleon in the ice. Observations have identified that Gamma Ray Bursts (GRBs) are possible sites for high energy neutrino production. We consider here GRBs which occurred in the years 2001 to 2005 inclusive during the operational times of RICE. Using GRB photon spectral data, we calculate the neutrino spectra predicted for these GRBs and the subsequent event number expected in RICE. We re-analyze RICE data in small time windows surrounding the GRB burst start times using a refined method involving by eye analysis of this reduced data set and find no neutrino events in the data set. Using the effective volume of RICE appropriate for each GRB we calculate neutrino flux limits for the GRBs. Although the flux limits are several orders of magnitude weaker than the expected flux, the RICE GRB neutrino limits are the only limits in the PeV to EeV energy range.

Acknowledgments

I would like to especially thank my supervisor, Dr Jenni Adams, for her guidance, support, patience and the multitude of knowledge she has passed onto me. A special thanks to Dr. Surujhdeo Seunarine and Dr. Steven Churchwell for their extensive help and guidance. To Dr. Kevin Hurley (Principle Investigator for the Interplanetary Network) and to Dr. David Besson (Principle Investigator for the Radio Ice Cherenkov Experiment) and the RICE team, many thanks for providing data and invaluable advice which made this research possible. Thank you to Dr. Peter Gilberd, Prof. Linda Smith, Prof. Graham Smith, Dr. Hazel Phillips, Dr. Simon Lambert, Dr. Adreanne Ormond, Asoc. Prof. Peter Cottrell, Prof. John Hearnshaw, Dr. Dennis Sullivan, Mr Mills, Dr. Athel Bins, and the late Dr. Noel Doughty, for their friendship and support. Thank you to my collegues, Dr Sarah Anderson, Dr Ocean Mercier, Dr. Bevan Cresswell, Dr. Hamish Rose, Bryn Currie, Nicola Fowler, Sarah Parkin, Clare Worley, Mita Gopal and Robyn Woolands for their help and support, especially my office friends during the final month before submission of this thesis. To my friends Merle Walker, Owen Huta, Raina, Gavin, and Anna Forrstromm he mihi mahana, he mihi aroha ki a koutou mo to tautoko mai. To the University of Canterbury, Tūāpapa Pūtaiao, Ngā Pae o Te Māramatanga, and the Māori Education Foundation, thank you for your financial support over the years. To Gill, Rhonda and Rosalie, who are

our wonderful office staff and the glue that binds the department, thank you for your support, endless chats and helping hands when ever I needed something. Finally, a special thank you to my whanau - Mum, Dad, Kirsty, Michael, Steven, Koa, Simon and family, Trish, Glen, Te Here and her whanau, Aunty Bubbles and Uncle Alan - for their unconditional support and understanding through all my endeavours. To my father whom past away many years ago, he mihi aroha ki a koe, even though the memories are few, I know your love for me was vast and true. Most importantly to my beautiful daughter Te Paea, whom I had during my PhD, and raised by myself with the help of my friends and family, I thank you for your complete and unconditional love and I thank you for letting me complete this part of my/our life, so that we can move forward together into the future. He mihi aroha, he mihi aroha, he mihi aroha ki a koe, taku tino taonga.

This research acknowledges the generous financial support from the Marsden Fund, the Cottrell Research Corporation, and the National Science Foundation Office of Polar Programs and the Department of Energy (Grant No. 0338219). We gratefully acknowledge the AMANDA and SPASE Collaborations, and the on site personnel for their generous logistical support. We gratefully thank our RICE collaborators, Shahid Hussain, whom supplied the computer code to generate flux limits. To David Besson and Josh Meyers for the Effective Volume Monte Carlo codes. Many many thanks goes to David McKay, George Frichter, Derek Boyd, Doug McKay, John Ralston, David Seckel, Adrienne Juett, Tim Miller, Dave Schmitaz, Glenn Spiczak, John Paden, Matt Peters, Alxey Provorov, Igor Zheleznykh, Corrine Cooley, Phillip Wahrlich, Tony Baird, DJ Box and all the other people whom had input or were members of the RICE collaboration.

We gratefully acknowledge the Global Circular Notices (GCN) via the GRBlog[1] search engine and Jochen Greiner for the use of his collated data on his webpage[2]. This research has made use of data obtained from the HETE science team via their website[3], the Interplanetary Network (IPN) data[4] and SWIFT, KONUS and Integral GRB data referenced herein.

Any opinions, findings, and conclusions or recommendations expressed in this material are those of the author and do not necessarily reflect the views of the National Science Foundation and the Marsden Fund.

[1] http://grad40.as.utexas.edu/
[2] http://www.mpe.mpg.de/ ∼jcg/
[3] http://space.mit.edu/HETE/Bursts/Data
[4] http://www.ssl.berkeley.edu/ipn3/

Contents

List of Tables

List of Figures

Chapter 1

Neutrino Astrophysics

Neutrino astronomy seeks to open another window with which to view the Universe. Large scale neutrino detectors provide a unique view of catastrophic events in the Universe but the detection of neutrinos is logistically difficult. The neutrino interaction probability is extremely small and combined with the low expected fluxes means that a large detecting volume is needed. The volume required to probe the neutrino flux that is expected to be produced in extragalactic sources is such that only a detector utilising a natural resource is feasible. The Radio Ice Cherenkov Experiment (RICE) employs the Antarctic ice. Located at the South Pole, RICE is designed to detect radio signals from the electromagnetic showers produced by the interaction of high energy neutrinos in the ice. Radio wave detection of electromagnetic showers exploits the long attenuation lengths of up to 1 km in polar ice and the coherence extending up to 1 GHz for radio Cherenkov emission.

Chapter 1 will present an historical overview of neutrino astrophysics. I will present some of the latest results and limits obtained from RICE and introduce some of the various neutrino projects which have taken place. The fundamental Cherenkov

effect will be introduced in Section 1.4.1, whereby I shall discuss the optical (Section 1.4.3) and radio (Section 1.4.4) detection methods.

Chapter 2 will discuss the general observable properties of gamma ray bursts. I shall discuss their spectral characteristics, in particular empirical correlations. Various GRB progenitors will be discussed in Section 2.4. The phenomenological fireball model is presented in Section 2.5. I also discuss the possible mechanisms to explain the observed prompt and afterglow emission, thus setting us in good stead to discuss the relationship between the observed gamma ray component and the neutrino flux in Chapter 3. Here I introduced the neutrino burst and afterglow models of Waxman and Bahcall. These models are based on the premise that the highest energy cosmic rays are accelerated in GRB shocks up to 10^{20}eV. The production of neutrinos occurs via photomeson production or proton-proton interactions. I use these models later in Chapter 7 to set individual GRB upper limits based on the non-observation of the neutrinos coincident with RICE.

RICE is introduced in Chapter 4. The general analysis technique is discussed in Section 4.5. I shall discuss the backgrounds and systematic uncertainties in RICE. The Monte Carlo simulation which models the effective volume of the array will be introduced in Section 4.6.1, and discusses in particular the recent additions to the Monte Carlo, introducing ray tracing effects which causes a reduction in the effective volume from previous published results.

Chapter 5 will address the attenuation effects of the Earth on the neutrino flux. The attenuation effects on the effective volumes shall be presented in Section 5.2. Well defined peaks are observed at around 30 and 150 degrees (nadir). These angles correspond to a Cherenkov cone which intersects the array optimally parallel to

the horizon. We also present the transformation of GRB co-ordinates to the local coordinates of RICE.

Chapter 6 will present the results of a neutrino search for windowed data around 77 GRBs that occurred during 2001 to 2005. These GRBs occurred while RICE was operating and all 77 GRBs could be localised with the RICE sensitivity zone. I shall outline the analysis technique used to remove anthropogenic signals from the data set. I also present an efficiency estimation of the analysis technique, with a higher efficiency than the general analysis.

Chapter 7 will present upper limits on the neutrino prompt and afterglow fluxes based on a model discussed in Chapter 3. The limits are presented for 27 of the GRBs which had some kind of redshift associated with them. The other 50 GRBs are included in the appendices.

1.1 Historical Overview

By the 1920's a model of the atomic nucleus was postulated that contained protons and electrons. For an element, ${}^{A}Z$, the number of protons is A and the number of electrons, A-Z (eg. ${}^{4}He$, contains 4 protons and 2 electrons.). Fundamental problems arose from this model yielding to the violation of spin statistics, conservation of energy and momentum. In 1930 Wolfgang Pauli rescued the theory by postulating a new particle, a third component to the nucleus, which interacted only weakly with matter. This particle he called the neutron which was later renamed a neutrino. The "neutron' was a neutral spin half particle, and was less than 1% of the mass of a proton. This theory not only rescued the spin statistics, but was able to account for the apparent non-conservation of energy and momentum and the observed continuous

energy spectrum of the electrons in the β-decay process[7]:

$$n \rightarrow p + e^{-} + \bar{\nu}_e. \tag{1.1}$$

After Enrico Fermi produced a consistent quantitative theory for the beta decay of nuclei, Bethe and Peierls [8] were able to calculate the cross-section for the interaction of a neutrino and a nucleon. This yielded a cross-section of $\approx 10^{-43}\text{cm}^2$ for MeV energies. This extremely small cross-section meant that there were no methods at the time which could detect such an interaction. For the next ten years the neutrino was considered undetectable, with Pauli stating, "...I have predicted something which shall never be detected experimentally" [9].

The first neutrino detector was built by Reines and associates [10]. This detector used water for the target and was placed near a powerful fission reactor with an expected antineutrino flux of 1.2×10^{13} cm^{-2}s^{-1}. This detector successfully measured the inverse beta decay reaction verifying the existence of the neutrino. Since then neutrinos have been observed from many sources. Some examples of natural sources of neutrinos are: cosmic-ray air showers, producing atmospheric neutrinos in the energy range $0.1 - 1000$ GeV; the Sun, producing $0.1 - 20$ MeV solar neutrinos from fusion reactions; and core collapse supernovae which produce neutrinos with energies ≤ 50 MeV.

The standard model prescribes a neutrino which is a massless, neutral, spin-half lepton with helicity of -1 and $+1$ for the neutrino and its antiparticle respectively. In the standard model there are three generations of neutrinos, ν_e, ν_μ, and ν_τ. The existence of the sterile neutrino which does not interact via any force except gravity

has also been proposed [11]. However, recent results obtained by Miniboone [12] disfavour its existence.

It is now accepted that neutrinos do have mass although the mass is too small to have been measured at the time of writing of this thesis. The evidence for neutrino mass comes from experiments which show that reactor, atmospheric and solar neutrinos change flavours. Starting in the late 1960s, several experiments found that the flux of electron neutrinos arriving from the Sun was between one third and one half the flux predicted by the Standard Solar Model. This discrepancy became known as the solar neutrino problem. In 1998 the Super-Kamiokande experiment detected oscillations in the atmospheric neutrino flux [13]. Since then oscillation has been observed by several experiments in atmospheric neutrinos [14, 15], solar neutrinos [16, 17], reactor anti-neutrinos [18] and accelerator neutrinos [19]. In particular the solar neutrino observations from the Sudbury Neutrino Observatory [16] have provided compelling evidence that the missing electron neutrinos from the Sun had changed into neutrinos of other flavours resolving the solar neutrino problem.

The oscillations occur because the neutrino flavour eigenstates $\mid \nu_\alpha >,\ \alpha = e, \mu, \tau$ are related to the neutrino mass eigenstates $\mid \nu_i >,\ \alpha = 1, 2, 3$ through a mixing matrix $U_{\alpha,i}$. This means that a neutrino which at $t = 0$ is a flavour eigenstate α, will at a later times be a time-dependent combination of mass eigenstates:

$$\mid \nu_\alpha(t=0)\rangle \rightarrow \sum_{i=3}^{3} U_{\alpha i} \exp(-iE_i t) \mid \nu_i > \ . \tag{1.2}$$

E_i is the eigenvalue of the Hamiltonian operator in the vacuum and so is the energy of the mass eigenstate. The mixing matrix $U_{\alpha i}$ can be expressed in terms of

three angles: θ_{12}, θ_{13}, and θ_{23}, and a phase δ:

$$U = \begin{pmatrix} c_{12}c_{13} & s_{12}c_{13} & s_{13}e^{-i\delta} \\ -s_{12}c_{23} - c_{12}s_{23}s_{13}e^{i\delta} & c_{12}c_{23} - s_{12}s_{23}s_{13}e^{i\delta} & s_{23}c_{13} \\ s_{12}s_{23} - c_{12}c_{23}s_{13}e^{i\delta} & -c_{12}s_{23} - s_{12}c_{23}s_{13}e^{i\delta} & c_{23}c_{13} \end{pmatrix} .$$

In this expression $c_{jk} := \cos(\theta_{jk})$ and $s_{jk} := \sin(\theta_{jk})$. The probability for a neutrino to oscillate from a flavour state α to a flavour state β in a time t starting from the emission of the neutrino at $t = 0$ is given by:

$$P_{\nu_\alpha \to \nu_\beta} = \delta_{\alpha\beta} - 4 \sum_{j>i} U_{\alpha i} U_{\beta i} U_{\alpha j} U_{\beta j} \sin^2 \left(\frac{\delta m_{ij}^2 L}{4E_\nu} \right) , \tag{1.3}$$

with units using $c = \hbar = 1$ and where δm_{ij}^2 is the difference of the squared masses of the i and j eigenstates.

For neutrino sources that emit polychromatically, the probability is averaged over the entire energy spectrum. Also the emission regions are spread over a large range, of the order of a parsec. These effects lead to smearing and the sin term averages to 0.5 in Equation 1.3.

The favoured interpretation of the various neutrino measurements is that solar neutrino detection basically provides information on θ_{12} while the atmospheric neutrino measurements provide θ_{23} and the reactor experiments θ_{13}. The mixing angles

are given approximately as:

$$\theta_{12} \approx \pi/6 \tag{1.4}$$

$$\theta_{23} \approx \pi/4 \tag{1.5}$$

$$\theta_{13} \approx 0\,. \tag{1.6}$$

This leads to a mixing matrix of the form:

$$U = \begin{pmatrix} 0.87 & 0.5 & 0 \\ -0.35 & 0.61 & 0.71 \\ 0.35 & -0.61 & 0.71 \end{pmatrix}\,.$$

If the number of electron-type neutrinos is denoted by n, one can obtain that 60% of electron neutrinos, ν_e, will survive, 20% will transition to muon neutrinos, ν_μ and 20% to tau neutrinos, ν_τ. Similarly for ν_μ, 40% of ν_μ will survive and 20% will transition to ν_e and 40% will transition to ν_τ. For an initial flux flavour ratio at the source of $F_e : F_\mu : F_\tau = 1 : 2 : 0$ we then get a ratio of $((0.6 \times 1n + 0.2 \times 2n = n):(0.2 \times 1n + 0.4 \times 2n = n):(0.2 \times 1n + 0.4 \times 2n = n)$, which gives a flux ratio at the detector of $F_e : F_\mu : F_\tau = 1 : 1 : 1$.

1.2 Probing the Universe with Neutrinos

Our knowledge of the Universe has been derived from the observation of particles of various energies. We are able to observe photons over a large spectral range from radio to gamma rays and detect cosmic-ray protons and light nuclei over a large energy range. Neutrinos complement this multi-messenger set, offering a unique view

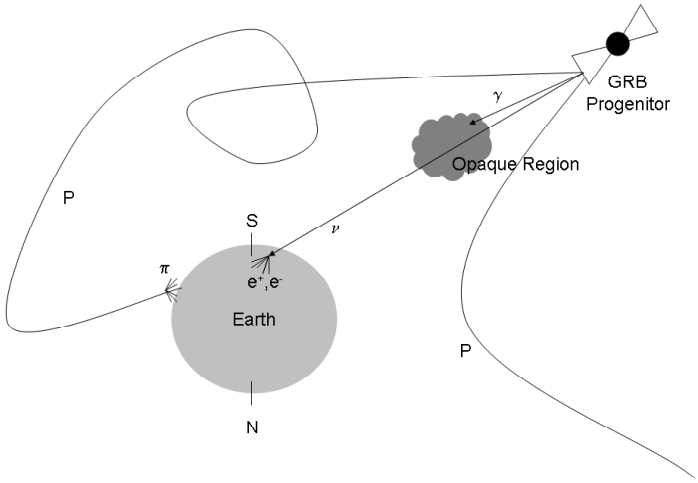

Figure 1.1: Proton deflection in magnetic fields: The neutrino's neutral characteristic and small cross-section means they are unaffected by magnetic fields and large, normally, opaque regions. However, charged protons are deflected in the galactic magnetic fields and do not directly point back to their source, whilst both photons and protons can be blocked by dense regions.

into regions from which other particles cannot be detected. As mentioned previously, neutrinos have an extremely low interaction probability which means that neutrinos may be able to escape or pass through regions opaque to photons and other particles. Also, because the neutrino is neutral it will not suffer any deflection in magnetic fields unlike the charged cosmic-rays. Thus neutrinos will be able to point back to their origin (see Figure 1.1). Although the neutrino's small cross-section makes the neutrino ideal for observing regions of the Universe opaque to photons and cosmic-rays, it also makes them extremely difficult to detect. In order to observe them either a large neutrino flux is required or an extremely large detector/interaction volume. The volume required and the type of detectors being used and constructed are discussed in Section 1.4 of this Chapter.

1.3 High-energy Neutrino Sources

Cosmic-ray protons up to 10^{20} eV have been observed [20, 21, 22], but it is still a mystery as to where these particles are produced. Models for cosmic-ray production can be divided into two classes: top-down models and bottom-up models. In top-down models cosmic-rays are the decay products of early Universe remnant particles or from topological defects [23], whereas in bottom-up scenarios cosmic-rays originate in cosmic accelerators. It is expected that any acceleration site producing high energy cosmic ray protons would also produce neutrinos as explained below. Thus any bottom-up model for cosmic-ray production predicts that there are high-energy neutrino sources in the Universe.

Cosmic accelerators are associated with dense collapsing regions such as exploding stars, Active Galactic Nuclei (AGNs) and Gamma Ray Burst (GRB) progenitors. When objects collapse an accretion disk forms to conserve angular momentum. As in many other astrophysical collapse phenomena, jets are thought to be produced emanating outward from the poles. Within these jets expanding shells of material are expected to have different speeds. Faster expanding shells will therefore catch up to slower shells and produce shocked material. It is within these shocks that particle acceleration can occur via the Fermi mechanism. The Fermi mechanism accelerates particles through collisions with magnetic inhomogeneities on repeated passage back and forward through shock fronts in the jets.

The argument that neutrinos will be produced at cosmic-ray acceleration sites is as follows. A fraction of the protons accelerated in the jets will undergo interactions with other protons and photons which are present both in the jets and in the surrounding matter. Charged pions produced in these interactions will decay into neutrinos and other decay products:

$$\begin{array}{rcccl} p+\gamma \rightarrow & \Delta^+ & & & \\ & \downarrow & & & \\ & n & + & \pi^+ & \\ & & & \downarrow & \\ & & & \nu_\mu + \mu^+ & \\ & & & & \downarrow \\ & & & & e^+ + \nu_e + \bar{\nu}_\mu, \end{array} \tag{1.7}$$

and

$$\begin{array}{lcccc} p+p \rightarrow p+p & +\pi^+ & +\pi^- & +\pi^0 \\ & \downarrow & \downarrow & \downarrow \\ & e^+\nu_e\bar{\nu}_\mu\nu_\mu & e^-\bar{\nu}_e\nu_\mu\bar{\nu}_\mu & \gamma+\gamma. \end{array} \tag{1.8}$$

Whilst photons can be produced via:

$$\begin{aligned} p + \gamma \rightarrow \quad & \Delta^{+} \\ & \downarrow \\ & p \quad + \quad \pi^{0} \\ & \qquad\quad \downarrow \\ & \qquad\quad \gamma + \gamma. \end{aligned} \tag{1.9}$$

Kaon production can also occur, aswell as π^{-} production and subsequent decay products from neutron interaction. The $n\pi^{+}$ channel dominates neutrino production via the delta resonance, $\Delta(1234)$. It is also assumed that negatively and positively charged pions are produced equally.

The decay of positively charged pions will lead to a flavour ratio of neutrinos at the source of:

$$F_e : F_\mu : F_\tau \ = 1 : 2 : 0 \ . \tag{1.10}$$

Using Equations 1.3 to 1.6 it can be shown that in the long distance limit the flavour ratio approaches:

$$F_e : F_\mu : F_\tau \ = 1 : 1 : 1 \ . \tag{1.11}$$

GRBs are one of the proposed sites for the production of high energy cosmic rays [24, 25]. Waxman [24] pointed out that the rate of energy that must be produced to support the observed flux of high energy cosmic-ray protons ($10^{19} - 10^{21}$ eV) is comparable to that produced in gamma-rays by GRBs. This spawned an industry

of building models which yielded the required particle production and explained the observed photon emission from GRBs. The proposed photon emission models are split into two categories: leptonic and hadronic. The leptonic emission models suggest that high energy photons are produced by the electrons undergoing synchrotron and inverse Compton scattering. In the hadronic emission models the high-energy photons result from collisions of accelerated protons (cosmic-rays) with photons which produce pions. The neutral pions decay to give the desired GRB photons:

$$p + \gamma \rightarrow p + \pi^0 \rightarrow p + 2\gamma \, . \tag{1.12}$$

Charged pions would also be formed and decay to neutrinos and other products as described in Equations 1.7 to 1.8.

Theoretical models have predicted the detection of high energy neutrinos from GRBs with next generation neutrino telescopes. If observed, this will then confirm GRBs as (at least one of) the production sites for the highest energy cosmic-rays and lend validity to hadronically produced photon emission. The search for neutrinos from GRBs forms the main theme of this thesis. Other projects have attempted to verify this but as yet have yielded a null result [26, 27, 28, 2].

Figure 1.2 shows the neutrino flux model predictions for various sources (dashed lines). These are shown with the corresponding RICE calculated upper limits (95% confidence level: solid lines) as RICE is the neutrino detector used in this thesis. Neutrino flux limits from other detectors are reviewed in [47]. The illustrative AGN models of Protheroe (PR) [29] and Mannheim [30], Stecker [31] and Berezinsky and Zatsepin [32] (M(B)) are ruled out at 95% C.L.. However the Waxman-Bahcall model (WB) [41] is below the RICE limits. The Greisin-Zastsepin-Kuzmin (GZK) [33, 34,

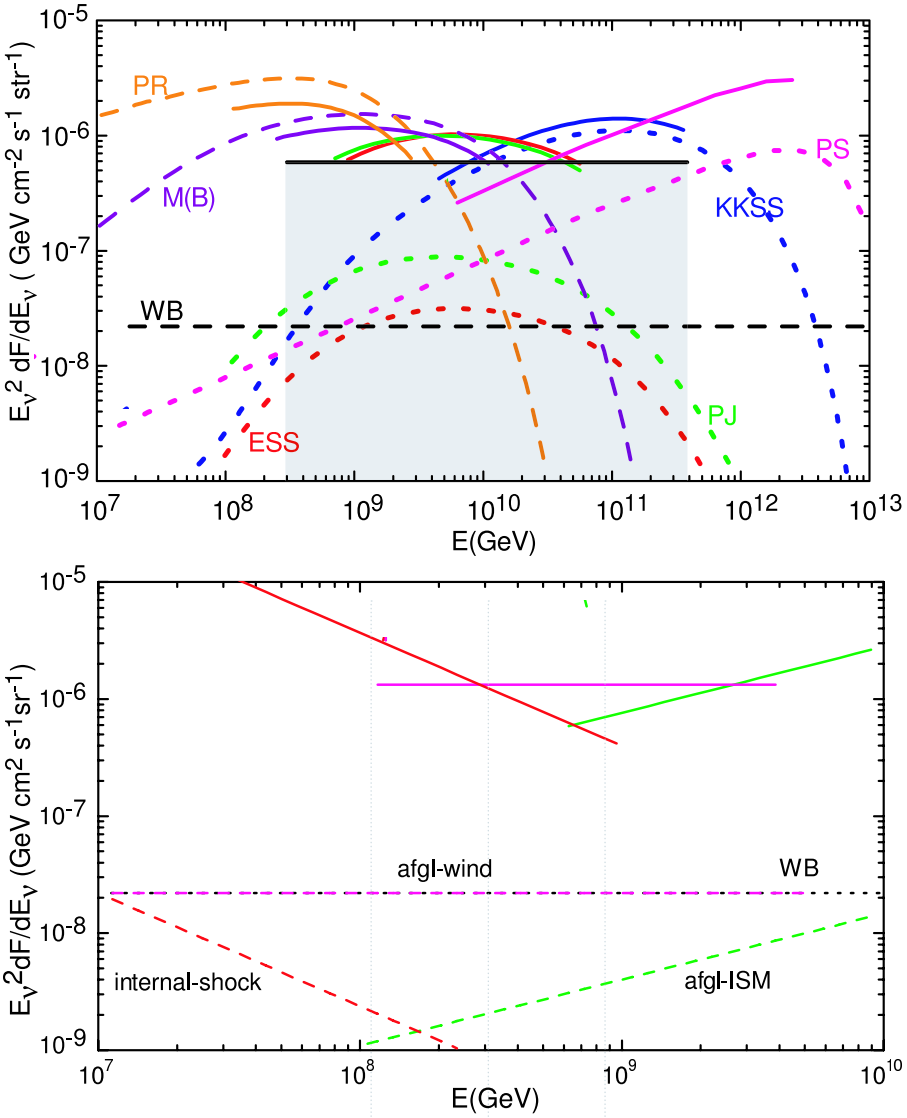

Figure 1.2: (Top) Upper bounds on total (all flavour) neutrino fluxes for Active Galactic Nuclei (AGN) models PR [29] and M(B) [30, 31, 32], Greisin-Zastsepin-Kuzmin (GZK) [33, 34, 35] neutrino models of ESS [36], PJ [37], and KKSS [38], the topological defect model PS [39, 40], and the Waxman-Bahcall bound (WB) [41] due to all flavour NC+CC interactions, based on 1999-2005 RICE livetime of about 20500 hrs. Dashed curves are for model fluxes and the thick curves are the corresponding bounds. The energy range covered by a bound represents the central 80% of the event rate. (Bottom) Bounds on diffuse neutrino fluxes from GRBs derived from RICE data. The bounds are for the internal shock [42], afterglow-ISM [43], and afterglow-wind [44] neutrino flux models using updated results [45, 46] for the fluxes. Systematic errors have not been folded into calculation of upper limits.

35][1] neutrino flux models due to Engel et al., [36] (ESS), Protheroe and Johnson (PJ) [37] and Kalashev et al., [38] (KKSS) differ substantially. ESS and PJ, keyed to models of the stellar formation rate, are below the RICE sensitivity. The KKSS flux, constructed to saturate bounds derived from EGRET observations, is just barely consistent with the RICE 95% C.L. limit, i.e. RICE should have detected 2 events for this model but observed none. The topological defect model of Protheroe and Stanev [39, 40] (PS) falls below the RICE sensitivity. The lower panel shows the diffuse neutrino fluxes predicted by representative GRB models and the RICE limits. The models are the internal shock [42], afterglow-ISM [43], and afterglow-wind [44] neutrino flux models using updated results [45, 46] for the fluxes.

1.4 Neutrino Telescopes

The solar, atmospheric, reactor and accelerator neutrino detectors mentioned above have a typical volume of order 1×10^{-5} km^3. These detectors probe fluxes of order 10^{10} cm^{-2}s^{-1} (solar neutrinos) to 0.1 cm^{-2}s^{-1} (atmospheric neutrinos). [2] The goal of neutrino telescopes is to observe the cosmic high-energy neutrinos with energies in the TeV to EeV range. The flux models for cosmic neutrino fluxes predict fluxes of order 10^{-5} to 10^{-8} cm^{-2}s^{-1}, which are many orders of magnitude smaller. Although the cross-section for neutrino interaction does increase with neutrino energy this is only a linear effect and cubic kilometre detector volumes are required to observe the high-energy neutrinos.

[1] The Greisin-Zastsepin-Kuzmin (GZK) limit predicts that ultra high energy cosmic rays above 5×10^{19}eV will interact with cosmic microwave background photons. The interaction will produce charged pions via the delta resonance which will subsequently produce neutrinos.

[2] The atmospheric neutrino flux is a steeply falling function of energy. The flux indication given is 1 GeV atmospheric neutrinos.

The two main detector techniques used for the solar and atmospheric neutrino detectors are radiochemical and Cherenkov based. Radiochemical involves measuring the transformation of atoms into a radioactive element from the inverse beta decay process induced by an electron neutrino. The number of neutrinos is estimated by observing the radioactive decay after purging the material from the main vessel to the observation area. However, this method is lengthy, taking around a month to complete the observation cycle, and yields no directional information. It is not feasible to scale this technique to kilometre cubed size detectors.

Cherenkov detectors exploit the production of Cherenkov radiation from the products of the interaction of a neutrino with the target material. Cherenkov radiation is produced when charged particles that produce electromagnetic radiation travel through a medium faster than the speed of light in that medium. Neutrino detection through Cherenkov radiation is well-suited to scaling to cubic kilometre detectors.

1.4.1 Cherenkov radiation

In 1934 Pavel Cherenkov discovered blue light being emitted from radioactive sources in water [48]. Later described by Ilja Frank and Igor Tamm [49], Cherenkov radiation is analogous to a sonic boom with the charged particle generating a photonic shock wave as it travels. This arises from the disruption of the local electromagnetic field in the medium as the charged particle passes through it. Electrons in the atoms of the medium are displaced and polarized by the electromagnetic field of the charged particle. Photons are emitted as the electrons restore themselves to equilibrium after the disruption has passed. When the disruption travels faster than the speed at which

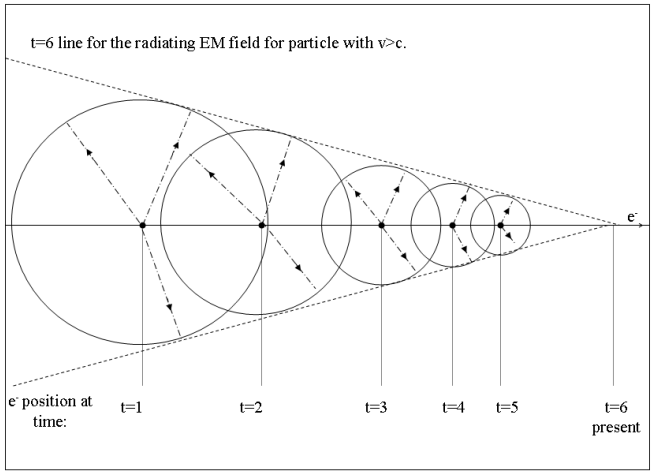

Figure 1.3: Cherenkov emission for a charged particle above threshold $v > c/n$. The circles show the isotropic emission along the track. After a time t the particle has moved a distance vt while the light sphere has grown by c/nt in that time.

light propagates in the medium, the emitted photons constructively interfere and intensify the observed radiation at a characteristic angle to the path of the charged particle. This angle is known as the Cherenkov angle and is given by the Mach relation:

$$cos\theta = \frac{1}{\beta n}, \tag{1.13}$$

where $\beta = v/c$, with v being the speed of the particle, c is the speed of light and n is the refractive index of the medium. The Cherenkov effect is shown in Figure 1.3. In order for the effect to occur the following condition must be met:

$$\beta > \frac{1}{n}\,. \tag{1.14}$$

1.4.2 Neutrino Interactions

Neutrinos interact through the neutral (via Z-boson exchange) and charged (via W-boson exchange) current interactions. In the charged current interaction the neutrino, if energetic enough, will created its lepton partner (e, μ, τ). These particles, or their products if they decay or interact, radiate Cherenkov radiation which can be detected. Flavour information can be obtained through the differences in interaction and decay rates of the three charged leptons. In the neutral current interaction the neutrino transfers energy and momentum to a nucleon and leaves the detector. The energy imparted to the nucleon leads to it initiating a cascade of particles which produce Cherenkov radiation. The cascade is referred to as a hadronic cascade. All neutrino flavours can interact through the neutral current but no flavour information can be obtained.

1.4.3 Optical Cherenkov Neutrino Telescopes

Optical Cherenkov neutrino telescopes using photomultiplier-tubes dispersed throughout the detector medium have been, and are in the process of being, constructed using natural abundant transparent material such as lake and sea water, and the Antarctic ice as the target medium. These detectors are optimised to detect the optical Cherenkov radiation emitted from muons produced in ν_μ charged current interactions. Unlike electrons or tauons, muons can travel great distances before stopping and with close to the same direction as the incoming neutrino. The muon radiates Cherenkov radiation as it travels through the detector and the track can be reconstructed using the time the light is detected by an array of photomultiplier-tubes.

High energy neutrino detectors generally must be placed deep underground or in deep water to avoid background interference by cosmic-rays. The first large scale optical telescope was the NT200 Baikal Neutrino Telescope in Lake Baikal in Siberia. The original configuration was an umbrella-like frame carrying 8 strings with 24 optical modules. In April of 2005 the 10 Mton scale detector, NT200+, was put into operation.

There are currently three neutrino detection projects under construction in the Mediterranean sea, ANTARES [3] [50], NEMO [4] [51] and NESTOR [5] [52]. ANTARES currently has 10 out of its planned 12 strings deployed up to a depth of approximately 2500 m and has identified muon tracks. The final configuration will have an instrumented volume of 0.03 km^3. NEMO is being constructed near the coast of Italy at a depth of around 3500 m. The first tower was deployed in 2006 and one or more additional towers are planned. NESTOR is being deployed near the coast of Greece at a depth of 3800 m. The first phase was deployed in 2003 and results identifying horizontal atmospheric muons have been presented [53]. Through these three efforts an optimal design and location will be chosen in the Mediterranean to build KM3NeT [54], a 1 km^3 detector.

The Antarctic Muon and Neutrino Detector II (AMANDA II) [55] experiment was the first neutrino telescope constructed in transparent ice. Located at the South Pole, it is designed to detect optical Cherenkov radiation using photomultipliers deployed on 19 strings at 1500 m to 2000 m below the ice. It is sensitive to 10^{12} to

[3] **Astronomy with a Neutrino Telescope and Abyss environmental RESearch**
[4] **NEutrino Mediterranean Observatory**
[5] **Neutrino Extended Submarine Telescope with Oceanographic Research**

10^{14} eV upcoming neutrinos which traverse through the Earth and interact producing muons. The next generation optical telescope is IceCube [56] which is currently under construction. IceCube is based on the successful AMANDA II detector and will be an array of 4800 PMTs on 80 strings distributed over an area of 1 km^2 at depths of 1400 m to 2400 m [56]. IceCube has been optimised to detect muon neutrinos and anti-neutrinos in the TeV to PeV energy range. As in AMANDA II, it aims to detect the Cherenkov light from the secondary muon produced from the interaction of the neutrino in or near the instrumented volume [56]. Currently IceCube has deployed 29 strings (31st December 07).

1.4.4 Radio Cherenkov Neutrino Telescopes

Radio Cherenkov neutrino telescopes exploit the Askaryan effect, which describes the coherence at radio wavelengths of the sum of the Cherenkov emission from a cascade of particles. In the MHz to GHz range the Cherenkov power scales quadratically with neutrino energy. This combined with favourable attenuation conditions means the effective volume of radio-based neutrino detectors is believed to surpass their optical counterparts above PeV energies [57].

The Askayran effect was described by Askaryan [58] in 1961. Askaryan noted that in high-energy cascades in normal matter photons and electrons will pull electrons from the host material and positrons will annihilate. This results in the cascade having a net negative charge. As the cascade develops, atomic electrons in the target medium are swept into the forward moving shower via Compton scattering. Positrons annihilate and a net charge accumulates, $Q_{tot} \approx E_s e/4$, where E_s is the shower

energy in GeV [59, 60, 61, 62, 63, 64, 65, 66, 67, 68, 69]. Such cascades produce broadband Cherenkov radiation for wavelengths much larger than the dimensions of the shower ($\lambda_{E-field}^{Cherenkov} \gg r_{Moliére}$), whereby the emitting region acts like a point charge and will emit radio wavelengths coherently.

The Askaryan effect was verified by Saltsburg et. al [70] more than 40 years after Askaryan's original paper, using a beam of high-energy photons fired into a block of silicon at the Stanford Linear Accelerator Center (SLAC). Their results showed that the observed radio frequency radiation was consistent with Askaryan's predicted coherent radio frequency emission from an induced charged particle cascade and strongly supports experiments designed to detect radio Cherenkov emission from high energy neutrino and cosmic-ray interactions. Although these observations formed a basis for observation of this effect in water it took until 2006 for the verification of the effect in ice. This was done by the Antarctic Impulsive Transient Antenna (ANITA) experiment performed at the Stanford Linear Accelerator Center (SLAC). They used a 7.5 metric ton ice target and obtained the first observation of the Askaryan effect in ice of coherent impulsive radio Cherenkov radiation which was found to be consistent with theory [71].

In the context of neutrino detection, the Askaryan effect plays a role in the case of the charged current electron-neutrino interaction and for the neutral current interaction for all flavours. The electron produced in the charged current electron-neutrino interaction travels only a short distance before initiating a shower of particles. This shower is termed electromagnetic as the shower particles will be electrons, positrons and photons. As mentioned above, the energy and momentum imparted to a nucleon

in the neutral current interaction of any flavour neutrino also leads to a shower of particles. This shower will initially have some hadronic constituents and is referred to as a hadronic shower. Through the Askaryan effect the hadronic and electromagnetic showers from ultra-high energy neutrino interactions will produce radio Cherenkov radiation which can be detected by radio receivers.

For further details of the Askaryan effect, upon which the radiowave detection technique is based on, the reader is referred to [58]. Its experimental verification in a testbeam environment is discussed in [70, 72]. The expected radio-frequency signal from a purely electromagnetic shower are discussed in [73, 74, 75, 76], whilst hadronic showers can be found in [77]. The effects due to the LPM effect are discussed in [73].

Projects such as ANITA [6] [78], FORTE [7] satellite [79], GLUE [8][80], SALSA [9][81], ARIANNA [10] [82] and RAMAND [83] all aim to use this radiowave neutrino detection technique. ANITA, which is sensitive in the energy range of $10^{18.5}$ to $10^{23.5}$ eV, is a balloon-borne experiment which aims to detect from above the radio emission arising from neutrino interactions in the Antarctic ice sheet. The first full ANITA flight successfully flew in December 2006 with three and a half loops of Antarctica. ARIANNA is a new project which proposes to use radio receivers on top of the Ross Ice Shelf and look for the radio emission from interacting neutrinos reflected from the water ice boundary. The FORTE satellite records bursts of electromagnetic waves arising from near the Earth's surface in the radio frequency range. A search of the

[6] **ANtarctic Impulsive Transient Antenna Experiment**
[7] **Fast On-orbit Recording of Transient Events**
[8] **Goldstone Lunar Ultra-high energy neutrino Experiment**
[9] **Salt dome Shower Array**
[10] **Antarctic Ross Iceshelf ANtenna Neutrino Array**

FORTE database for events consistent with neutrino interactions in the Greenland ice sheet has been performed and limits obtained [84]. The SalSA experiment plans to use salt as the target material by instrumenting part of a salt dome. A number of projects seek to detect the radio emission from neutrinos interacting in the Moon by looking for an enhanced radio signal in the direction of the Moon. RAMAND uses the Kalyazin radio telescope, GLUE, the Goldstone telescope and LUNASKA the Square Kilometre Array.

Radio detection techniques have also been considered as probes to detect monopoles [85], TeV-scale gravity [86, 87, 77, 88], and tau-neutrinos [89].

In this thesis we examine the data from the Radio Ice Cherenkov Experiment (RICE), a radio Cherenkov telescope which searches for neutrino interactions occurring in the cold polar ice at the South Pole. The ice has favourable transmission properties for radio detection with typical attenuation lengths of a kilometre in the MHz range. The RICE detector is described further in Chapter 4. The successor to RICE is the AURA [90] experiment. Combining RICE, ANITA and IceCube technology and knowledge, a 10-100 kilometre array of radio detectors is planned. Trial deployment of AURA detectors took place in the 2006-07 austral summer and further deployment is planned this year [90].

Chapter 2

Gamma Ray Burst Phenomenology

2.1 Overview

Gamma Ray Bursts (GRBs) are intense flashes of radiation outputting approximately 10^{51} to 10^{54} ergs of energy [91, 92, 93]. The flux has been observed over an energy range of 10 keV to 300 MeV, with the bulk of the energy emitted in the gamma ray band between approximately 0.1-1 MeV [94]. The phenomenon starts with an initial burst which can last from a few milliseconds to several hundreds of seconds. The burst is then followed by what is termed the "afterglow", which can last up to several days following the primary flash.

GRBs were first observed by four Vela spacecrafts placed in geocentric orbit above the Earth. The project jointly run by the Advanced Research Projects of the United States Department of Defense and the United States Atomic Energy Commission was originally designed to detect nuclear weapons detonation. The Vela craft however detected flashes of localized gamma rays which would outshine all other sources put together. Distributed randomly, 16 in total of these gamma ray "bursts" were observed from 1969 to 1972 lasting from 0.1 s to 30 s long. The discovery of this phenomenon

was first published in 1973 [95], with the decades to follow seeing great interest in the observation and theoretical development of GRBs. The four Vela satellites continued to observe GRB phenomena up until termination in April 1979, ending a ten year period and measuring a total of 73 GRB phenomena. The next generation of GRB detectors have now observed $\approx$ 4000 GRB events. The latest observations were due to collaborative efforts with spacecraft and ground-based observatories from all over the world such as the Interplanetary Network [96], Swift [97], and Integral [98].

Originally thought to be produced within our own galaxy, the isotropy of the bursts suggested that they originated at cosmic distances. The BeppoSAX satellite was the first to obtain a redshift for a GRB host galaxy by observing the GRB proper and the afterglow in the X-ray, optical and radio spectral range. This was for GRB970228 with the host galaxy being confirmed at z=0.95 using the Keck II 10 m telescope. Now over 100 GRB redshifts have been obtained and the distribution of redshifts is discussed in the next section which describes GRB observations.

Also a clear distinctive subclass of GRBs has emerged called X-ray rich (XRR), X-ray flashes (XRF) and Gamma Ray Repeaters (GRR). XRFs are defined by a larger fraction of X-ray (2-30 keV) emission than GRBs. This group of X-ray rich GRBs is also thought to be correlated to X-ray flashes. GRB repeaters characteristically emit an intense burst of gamma rays at irregular intervals. It is uncertain if GRBs, XRFs or XRRs are related.

2.2 Observations

After the discovery of GRBs, observations were limited to observing only the initial burst. Theory predicted that a counterpart emission should be observable in the X-ray and optical wavelengths. The main difficulty was that it was very difficult to obtain accurate locations in order to do follow up observations. At such high energies gamma rays cannot be focused thus making localizations difficult to obtain. It became the key aim to achieve accurate locations such that collaborating telescopes could make observations. GRB detectors were placed on various interplanetary and solar system probes back in the early 70's, creating an interplanetary network (IPN) [1]. Using the arrival times of the burst at the various space detectors, error boxed localisation with arc-minute precision was possible to attain. The most accurate localisations are obtained when widely spaced detectors are used in the triangulation. The key point here is that many of the locations relied, and sometimes still do, on more than three detectors registering the burst so that an accurate triangulation can be made. The further apart the detectors are the smaller the error of the triangulation.

Today the IPN has nine operating satellite members with three widely spaced satellites. Mars Odyssey is placed in orbit around Mars, the satellite MESSENGER is enroute to Mercury and Ulysses which was placed in heliocentric orbit around the sun [99]. The capabilities of detectors is largely dependant on payload weight restrictions. This limits the number of onboard components, and hence limits the number of detectors and the sensitivity range. Satellite lifespan has also limited both the capabilities and the long term regularity of high precision localisations. As technologies

[1] Since gamma-rays are readily absorbed by the Earth's atmosphere, observations of gamma-rays on Earth are restricted to Cherenkov techniques and large scale arrays.

improved individual experiments were able to independently obtain accurate localisations. The Burst and Transient Source Experiment (BATSE)[94] could obtain GRB positions to 3-5 degrees in real time (1-2 s). However, this level of accuracy was still not good enough for follow up observations by optical and radio telescopes, although BATSE was one of the most successful detectors, observing over 2074 GRBs. It was fundamental in determining the isotropy of GRBs, while other detectors, such as KONUS [100], can only determine the ecliptic latitude of the burst. Decades after the first GRB detection, the Bepposax (Italian/Dutch Satellite)[101] detector could detect locations to within about 5 arcminutes. Using its X-ray instrument Bepposax was instrumental in detecting the first counterpart afterglow of GRB 970228 [102]. Bepposax was able to slew its camera in about 3 hours and could contact optical and radio collaborators to initiate follow up observations.

The SWIFT [97] satellite has opened up an exciting new era for GRB observations. SWIFT is a multi-wavelength detector capable of observing GRBs and their afterglows in the gamma-ray, X-ray, ultraviolet, and optical wavelengths. It is able to slew its detectors around and observe the afterglow within an impressive 20 to 75 seconds of the burst occurring. This has enabled, for the first time, the observation of the afterglow immediately after the burst proper. It is also able to localise bursts to within a few arcminutes in 15 seconds. Today SWIFT has observed over 300 bursts since its launch in 2004.

2.2.1 Temporal Properties

The observed GRB temporal profiles are observed in a variety of shapes and durations. The profiles, although different, can be roughly categorized. The Fast Rise Exponential Decay (FRED) describes a single pulse whose rise time is much shorter than the decay time. Then there are single, double and multiple peak bursts. There is no pattern of brightness of pulses. Figure 2.1 shows examples of GRB temporal profiles showing these variations [94]. A repetitive pattern has been observed in bursts which modulates the structure. This characteristic fluctuation is called time variability and has an average value of 0.01-0.1 s.

The duration is generally defined by the t_{90} and sometimes the t_{50} times. The t_{90} is defined as the time during which the total counts increase from 5% to 95% above the background, representing the time that 90% of the photons are above the background. Similarly the t_{50} is the time 50% of the photons are above the background. Observations by BATSE showed evidence of a bimodal distribution in the duration which separates GRBs into two distinct classes: short bursts (< 2 s) and long (> 2 s) [103]. These were correlated to their spectral hardness ratios, with short GRBs being predominantly hard (higher energy) and long GRBs being predominantly soft (lower energy). Prior to the BATSE catalogue [104], bimodalilty could not be confirmed due to detector insensitivities and temporal resolutions [103]. However, others have suggested that a tri-modal distribution exists [105, 106].

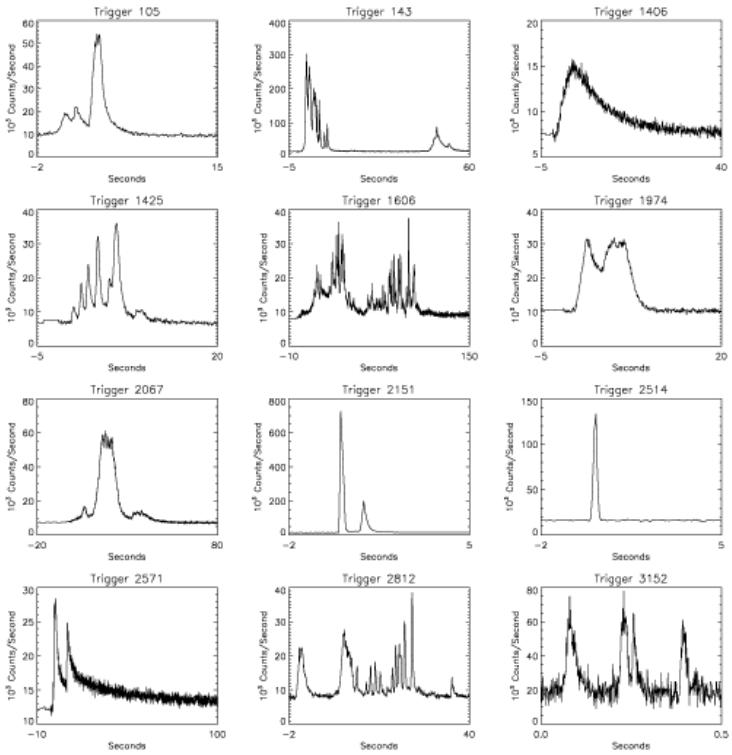

Figure 2.1: GRB temporal patterns, for FRED, single, double pulse and multiple peaks [94].

2.2.2 Spectral Properties

The variation in spectra is far less than the temporal behavior. GRBs typically emit most of the energy in the 50-1000 keV range. However, photons have been observed to a few keV and up to 18 GeV [107]. There are no lines and the spectrum is continuous.

Several photon models consisting of two to five free parameters have been used elsewhere [94] to describe these non-thermal spectra. Typically GRB spectra can be described by the Band function [94], a double power law which is smoothly joined:

$$F_\gamma = \epsilon_\gamma \frac{dn_\gamma}{d\epsilon_\gamma} = \begin{cases} A(\epsilon_\gamma/100)^{-\alpha}\exp(-\epsilon_\gamma(2-\alpha)/\epsilon_{\gamma,peak}) & \text{if } \epsilon_\gamma \leq \epsilon_{\gamma,Break} \\ A\{(-\alpha+\beta)\epsilon_{\gamma,peak}/[100(2-\alpha)]\}^{\beta-\alpha}\exp(\alpha-\beta)(\epsilon_\gamma/100)^{-\beta} & \text{if } \epsilon_\gamma > \epsilon_{\gamma,Break}\,, \end{cases} \tag{2.1}$$

where $\epsilon_{\gamma,Break} = (\beta-\alpha)\epsilon_{\gamma,peak}/(2-\alpha)$, A is the amplitude in photon $s^{-1}cm^{-}2$ keV^{-1}, α is the low spectral index, β the high spectral index, and the "peak" energy is the maximum energy in the $\epsilon_\gamma dn_\gamma/d\epsilon_\gamma$. For typical values of α and β the $\epsilon_{\gamma,Peak}$ and $\epsilon_{\gamma,Break}$ (known hereafter as $\epsilon_{\gamma,b}$) are equal. It is customary to approximate the Band function as a broken power law:

$$F_\gamma = \epsilon_\gamma dn_\gamma/d\epsilon_\gamma \propto \begin{cases} \epsilon_\gamma^{-\alpha} & \text{if } \epsilon_\gamma \leq \epsilon_{\gamma,b}, \\ \epsilon_\gamma^{-\beta} & \text{if } \epsilon_\gamma > \epsilon_{\gamma,b}. \end{cases} \tag{2.2}$$

The break energy is typically $\epsilon_{\gamma,b} \sim 250$ keV and α and β have typical values of 0 to 1.5 and 2 respectively. Evidence also suggests that bursts soften (higher to lower energy emission) with time. The fluence (time integrated flux) typically ranges from

10^{-7} to 10^{-4} erg cm^{-1}. Figure 2.2 shows some examples of prompt GRB spectra, showing the typical values of α and β, for two types of fit, a single power law and BAND fit [97].

2.2.3 Redshift distribution

With the introduction of new gamma ray detectors such as SWIFT and INTEGRAL the number of redshifts obtained has dramatically increased in the last year or so with over 100 GRB redshifts now obtained. Figure 2.3 is a histogram of the number of GRBs binned in redshift bins of 0.5 redshift. Redshifts obtained by SWIFT have shown a scarcity of redshifts between $z = 1$ and $z = 2$. Whether or not these are just an abberation due to detector selection effects, statistical fluctuation or something more physical is unclear[108].

GRBs are thought to be possibly produced by the collapse of massive stars. If this is indeed the case then one expects that the GRB formation rate should follow that of the star formation rate (SFR). Figure 2.3 shows the current GRB redshift distribution, and shows that GRBs peak at $z \approx 1$. However the SFR peaks at $z \approx 2$. Observational selection effects such as detector thresholds and energy ranges are suspected to skew the GRB redshift distribution, due to individual capabilities of detectors. Earlier investigations by Weinberg et al., found that the actual GRB rate was approximately proportional to the SFR [109]. Most recently Guetta and Piran [108] have investigated whether long duration GRBs follow the SFR, comparing observed GRB redshifts from various detectors. They found that SWIFT GRBs do not follow the SFR for several models. They did however find a reasonable fit when considering a GRB rate with a

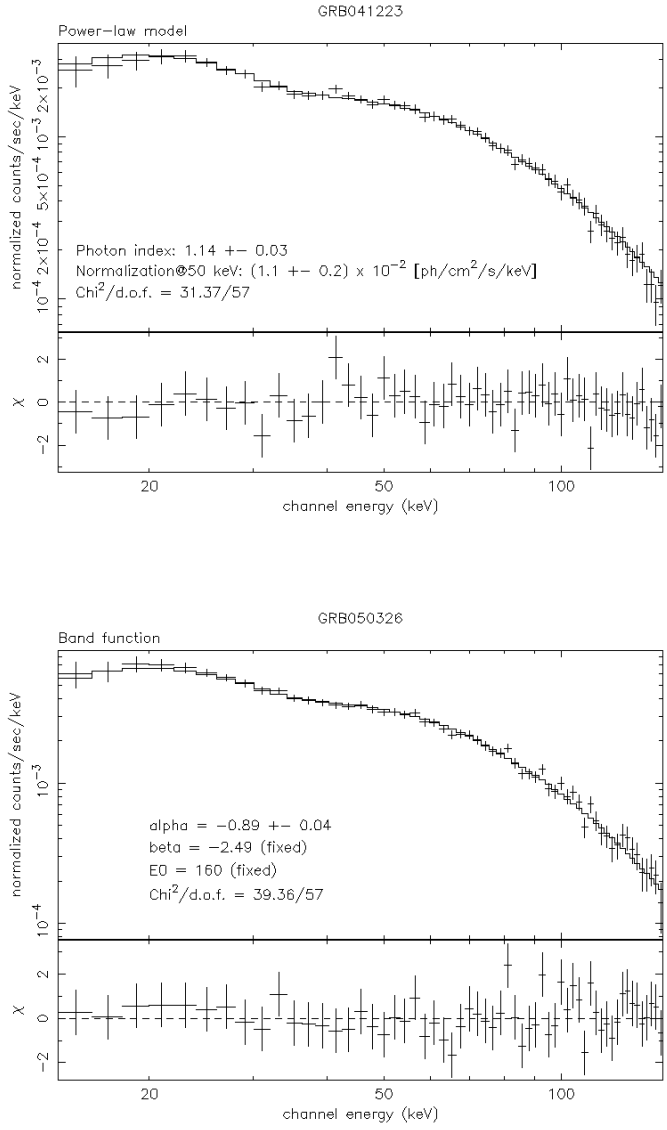

Figure 2.2: GRB spectra, showing the typical values of α and β, for two types of fit, a single power law and BAND fit[94].

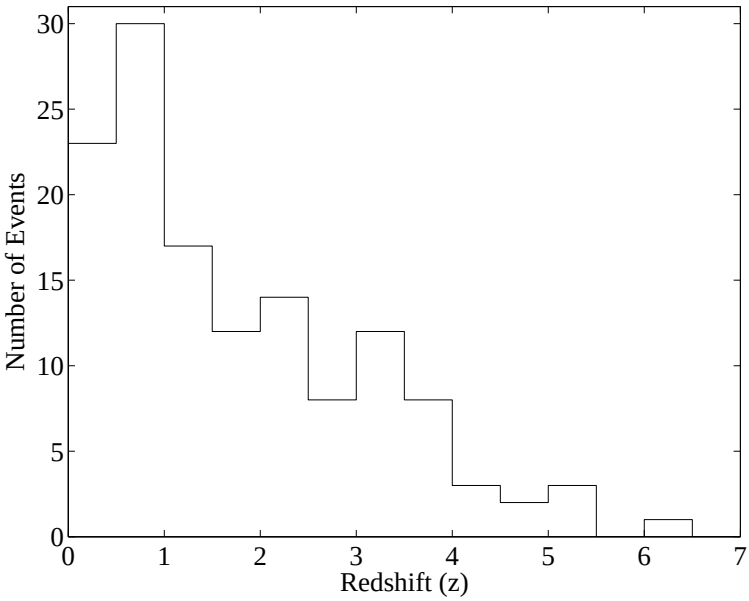

Figure 2.3: Distribution of 133 GRB redshifts obtained as of September, 2007.

high redshift enhancement, which could possibly be due to a preferential formation of long GRBs in low metallicity regions.

2.3 Empirical Correlation and Distance Estimators

There is increasing evidence for the proposed correlation between the spectral properties and energetics of GRBs. It has been suggested that there is a correlation between the apparent isotropic energy[2] of the prompt emission and the intrinsic peak energy of the emission, $E_{\gamma,iso} \propto E^{0.5}_{\gamma,Peak}$ (in $\epsilon_\gamma F_\gamma$) [110, 111, 112, 113, 114]. Similarly a correlation has been found between the $E_{\gamma,Peak}$ and the peak luminosity [115]. Ghirlanda [116] found that peak energy and the apparent isotropic photon energy were correlated by, $E_{\gamma,iso} \propto E^{0.7}_{\gamma,Peak}$, and more recently Ghirlanda [117] found the correlation relationship:

$$\epsilon_{\gamma,b} = \frac{300}{1+z}\left(\frac{E_{\gamma,iso}}{10^{53}\text{ergs}}\right)^{0.56}\text{keV}, \tag{2.3}$$

which is known hereafter as the Ghirlanda relationship [117]. Equation 2.3 is used later in Chapter 6 to estimate values for the peak/break energy of the GRB photon power spectrum.

[2]The apparent isotropic energy refers to the energy which would be isotropically emitted from the source if the energy was not beamed. The actual energy beamed/jetted is $(4\pi/\Omega)E_{\gamma,iso}$.

2.3.1 Pseudo Redshifts

The determination of such correlations have proven particularly useful in estimating redshift values. Fenimore and Ruiz [118] showed a possible correlation between the absolute luminosity of the burst and time variability, implementing it to determine redshifts for 220 BATSE [94] GRBs. Guidorzi et al., [119] also found a correlation between the GRB variability and the peak luminosity.

Atteia [120] based on the earlier works of [121] and [122] suggested that the E_{Peak}, $E_{\gamma,iso}$ and duration(t_{90}) were correlated and was worth further investigation as a possible redshift estimator. P*é*langeon et al., [123, 124] proposed an improved redshift estimator relating more specifically the peak energy and the bolometric luminosity in a 15 second most energetic part of the emission (period of highest fluence), to the redshifts. This correlation has been tested against "measured" redshifts and has been shown to better than a factor of 2. An interactive redshift calculator is available online, however GRB spectral data is required for its use. Other methods also required high quality spectral data, which during 2001 to 2005 was not readily available. Therefore in this research pseudo redshift values were taken from the online catalog and publications where available [124, 123].

2.4 Gamma-Ray Burst Progenitors

By 1992 there were over 100 GRB progenitor models. Observational evidence is used to constrain models. Prior to the discovery of the first GRB redshift, which yielded conclusive evidence that GRBs occurred at cosmological distances, many exotic progenitors had been postulated ranging from direct stellar flares from nearby stars[125]

to asteroid impacts onto neutron stars[126]. One of the first scenarios postulated was that by Colgate earlier in 1968 suggesting that supernova shocks in stellar surfaces in distant galaxies could be responsible for the production of GRBs[127]. Currently favoured theories have moved toward this type of scenario, supported by observations of host galaxies of GRBs being associated with star forming regions [128]. This provided evidence towards GRBs being from the death of massive stars.

The most widely accepted model for GRBs is the Collapsar[3] model, whereby the GRB is produced by the collapse of a compact object to form a central black hole with an accretion disk(BHAD). The rapid accretion of stellar matter into the hole releases large amounts of energy $\approx 10^{51}$ ergs. Some of the energy is deposited at the rotation axis of the star. The heated gas at the poles then expands in a jet like fireball which penetrates the surface of the star. [129]. This process is thought to occur via the collapse of a single massive star or via the merger of a compact binary system. Whatever the engine is, it needs to be able to generate around 10^{51} to 10^{54} erg of energy. The energetics require the accretion disk to have a mass of around 0.1 $M_{\odot}$. The energy is thought to be possibly produced via the Blandford-Znajek process involving energy extraction from the large magnetic fields present in the progenitor or tapped from gravitational energy either from the gravitational potential energy from the torus accreting onto the black hole, or from the rotational energy of the black hole itself [130, 131]. This large amount of energy can be alleviated by the beaming of a collimated relativistic flow with an opening angle of $1^{\circ} < \theta < 20^{\circ}$.

The number of progenitor models today are still vast. Three overarching categories

[3]The Collapsar was originally coined to describe a collapsed star, this term is still used.

of models are: mergers of neutron stars or blackholes; core collapse of massive stars (hypernova); and the collapse of a neutron star into a black hole (supranova) [132]. Some clues such as the observed bimodal or trimodality of bursts suggest that more than one progenitor scenario are responsible for producing different duration bursts. Long duration GRBs are associated with massive star progenitors, such as Wolf-Rayet (WR) stars [133]. Whilst the leading candidate for short GRBs is the merger of binary systems, whereby both of the candidates are compact objects [133]. Possible systems are double neutron star mergers (DNS), neutron star-black hole (NS-BH) mergers and white dwarf-black hole mergers (WDBH).

Progenitor models must also must be comparable to the observed GRB rate. GRBs are rare and are observed around once a day on average. They have a per galaxy rate of around 10^{-4} yr^{-1} galaxy^{-1}, for which 2/3 are long duration GRBs [134]. GRB beaming means that only a small fraction of GRBs are observed increasing the actual GRB rate by a factor of $10 - 1000$ or higher[134]. The GRB rate is around $1/1000^{th}$ the rate of supernovae.

GRBs have been associated with core-collapse supernovae(SNe), with strong evidence to suggest that most long-duration soft-spectrum GRBs are accompanied by massive stellar explosions(Type Ib/c)[135]. Not all SNe are thought to produce GRBs. The total energy output for a standard SNe is around 10^{51}erg, which is roughly equivalent to the energy requirements of a beamed GRB. It is expected that a supernova bump be observed in the afterglow light curve. A very powerful class of explosion termed a hypernova, refers to particularly energetic explosions with kinetic energies $\geq 10^{52}$ erg. This is an order of magnitude larger that SNe, which are supposed to

be produced by $13 - 20$ solar mass stars, whilst hypernova are expected to be from massive stars of the order $M \geq 25 M_{\odot}$ and are likely to form black holes rather than neutron stars[136]. It has also been investigated that these GRB hypernova could possibly be created by the merger of two compact objects, such as two neutron stars, instead of by one single star.

A Supranova refers to a supermassive neutron star (exceeding several solar masses) that collapses to a black hole [137]. The collapse could be due to loss of angular momentum via a pulsar wind destabilizing the centrifugal force support, or if the NS cools and has insufficient spin to stop collapse. The neutron star could also possibly collapse due to the accretion of the surrounding accretion disk. In this model there is firstly a supernova, which could be more energetic than normal supernova, which forms a supermassive neutron star. Then a few weeks or months later the neutron star collapses and produces a GRB. A supernova bump is not expected to be observed in this model unless the delay is only a few days.

Many of the models incorporate some sort of pulsar or pulsar like object. Energetics requires a magnetic field of the order 10^{15} G within this source type. It has been suggested that highly magnetized neutron stars could form by the gravitational collapse of an accreting white dwarfs with anomalously high magnetic fields in binaries. The rapidly rotating and strongly magnetized neutron stars would lose their rotational kinetic energy on a time scale of seconds or less in a pulsar like mechanism. The energy available in this case would come from the rotational and magnetic energies of the neutron star. These energies are of the order of a few 10^{51} ergs for

a neutron star rotating near breakup. The rotation of the magnetic field would create a strong electric field and an electron-positron plasma that is initially optically thick and in thermodynamic quasi-equilibrium. A very strong magnetic field would form and the pulsar would produce a relativistic Poynting-flux-dominated flow. It has been suggested [138, 139] that energy is dissipated from the magnetic field to the plasma and then via plasma instability to the observed γ rays outside the γ-ray photosphere which is at around 10^{13}cm . At this distance the pulsar wind breaks down and the intense electromagnetic wave are generated. The particles are accelerated by the electromagnetic waves to Lorentz factors of 10^6 and produce the non-thermal spectrum.

The Merger Models; NS binary merger or NS-BH binary mergers, also produce BHAD systems. These models are associated with short GRBs. These mergers occur due to degrading obits. The merger rate is approximately 10^{-6} events per year per galaxy [140]. A merger releases approximately 5×10^{53} ergs, with most of the energy released in the form of low-energy neutrinos and gravitational waves. It is proposed that there is sufficient energy to produce a GRB, in which the mechanism to produce the burst has been proposed that a thousandth of the neutrinos annihilate and pair produce which in turn produces photons, $\nu + \bar{\nu} \rightarrow e^+ + e^- \rightarrow \gamma + \gamma$. This is however highly debated based on energetic arguments. Alternatively another source of energy is the formation once again of a BHAD system.

Within both the Supranova and Collapsar models, both are associated with supernova or supernova like events. In the supranova model the GRB jet does not have to punch a hole through the stellar envelope. Instead the ejecta propagates nearly

through free space, possibly polluted by pulsar wind.

2.5 Fireball Model

The fireball model is a generic description of a relativistic outflow from a compact object and is independent of any type of GRB progenitor model. The observed photon spectrum gives clues as to how the fireball must behave. The requirement that there is a relativistic outflow comes from the necessity to resolve the compactness problem. The compactness problem is that non-thermal emission is observed from GRBs while a naive calculation implies that the sources are optically thick. The naive calculation goes as follows. The observed time variability, discussed in Section 2.2.1, of $t_v \leq 0.01$ s, constrains the initial dimension of the region by the light crossing time, $ct_v = 10^5$ m. The observed fluence and distance estimations yield GRB luminosities in the range between $10^{51} - 10^{54}$ ergs of energy. Such a large luminosity in a compact region gives a large optical depth to pair production ($\gamma\gamma \rightarrow e^{\pm}$). Photons are, however, observed at energies greater than 1 MeV, therefore some mechanism must prevent these high energy photons undergoing pair production.

A natural way to overcome the compactness problem is for the source to expand ultra-relativistically otherwise known as a fireball. If the source expands at some Lorentz factor, Γ, then the energy of the photons in the source frame are smaller by a factor of Γ, compared to that in the observer frame. This makes most of the photons below the threshold for pair production in the source frame. A lower limit to Γ has been derived to prevent photons of energy, ϵ_γ, annihilating with photons of energy, $\epsilon_t \sim 1$ MeV [141, 142, 143]:

$$\Gamma \geq 10^2 \left[(\epsilon_\gamma/10\mathrm{GeV})(\epsilon_t/\mathrm{MeV})\right]^{1/2}. \tag{2.4}$$

The observed gamma-ray emission is thought to be produced by accelerated particles in the ejected flow (fireball) via synchrotron emission. Some mechanism is needed to convert the kinetic energy of the flow into the internal energy of the particles [144]. Shock collisions provide such a mechanism and would naturally be expected in an irregular outflow with faster parts of the flow catching up to slower parts. External shocks would also be expected as the ejecta collides into the interstellar medium (ISM) or some pre-ejected stellar wind from some previous event [144]. Internal shocks are thought to produce the prompt or main burst, whilst the external shocks the observed afterglow, see Figure 2.4.

2.5.1 Burst photon emission

The photon spectra predicted by the synchrotron radiation of shock-accelerated electrons, internal to the burst, is broadly consistent with observed GRB spectra. We outline the steps used to derive the photon spectra assuming it is due to the synchrotron radiation of shock-accelerated electrons. In particular, we include the relationships which will be needed to calculate the expected neutrino flux.

The characteristic frequency of the synchrotron radiation (averaged over the pitch angle) from an electron moving with Lorentz factor γ across a randomly orientated magnetic field of strength B is:

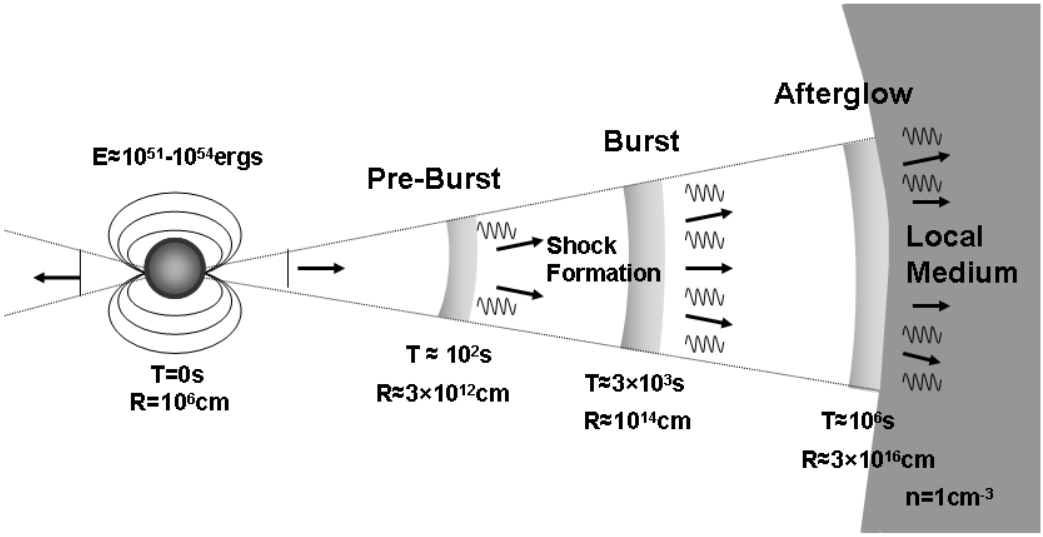

Figure 2.4: Schematic of a GRB produced from internal shocks and afterglow from external shocks in a relativistic jet emanating from a progenitor (possibly from core collapse). Internal shocks produce γ-rays and neutrinos, whilst external shocks produce UV, Optical, Radio, X-rays and higher energy neutrinos.

$$\omega_{syn} = \frac{3eB}{2m_e c}\gamma^2 \,, \tag{2.5}$$

corresponding to an energy:

$$E_{syn} = \frac{3\hbar eB}{2m_e c}\gamma^2 \,. \tag{2.6}$$

The Lorentz factor, γ, can be expressed in terms of the energy of the electron in the fireball frame:

$$E_e = \gamma m_e c^2 \,. \tag{2.7}$$

The magnetic field strength is unknown but it is assumed that a fraction, ϵ_B, of the internal energy, U_{int}, of the gamma ray burst is carried by the magnetic field. Then the energy density of the magnetic field is:

$$\frac{B^2}{8\pi} = \epsilon_B U_{int} \,, \tag{2.8}$$

and U_{int} is related to the observed luminosity of the GRB L_γ through:

$$U_{int} = U_\gamma/\epsilon = 1/\epsilon \frac{L_\gamma}{4\pi r^2 \Gamma^2 c} \,, \tag{2.9}$$

where U_γ is the photon energy density in the source rest frame and ϵ is the conversion efficiency of the total internal energy to gamma rays. The second equality relates the photon energy density to the luminosity with the Γ factor transforming between the source and observer frames and r is the source size. The source size is

related to the variability time of the GRB through $r \approx 2\Gamma^2 c t_v$. [4]

The synchrotron power can be written as a function of the ratio of the frequency to the characteristic frequency and the total synchrotron power is obtained by integrating the product of this function and the distribution of electron energies. The internal shocks are expected to be mildly relativistic in the fireball rest frame and results related to particle acceleration in sub-relativistic shocks are expected to be valid. In particular, the electrons present in the fireball are expected to be accelerated to a power law energy distribution:

$$\frac{dN_e}{dE_e} dE_e \propto E_e^{-p} dE_e \,, \tag{2.10}$$

where $p \approx 2$. Using this in the integral for the total synchrotron power one deduces that the differential photon spectrum for slow electron cooling (short dynamical time scales compared to radiative cooling) is:

$$\frac{dN_\gamma}{dE_\gamma} \propto E_\gamma^{-p/2-1/2} \,, \tag{2.11}$$

and for fast electron cooling (long dynamical time scales compared to radiative cooling):

$$\frac{dN_\gamma}{dE_\gamma} \propto E_\gamma^{-p/2-1} \,. \tag{2.12}$$

[4] In the observer frame all photons propagate at a direction making an angle $< 1/\Gamma$. Photons which are emitted on the edge of the cone are delayed compared to those emitted on the line of sight by $r/2\Gamma^2 c$. Thus a limit on the observed variability time constrains the size of the source through this relationship [145].

The break in the Band function (Equation 2.2) is commonly explained to be due to a transition from the slow electron cooling regime to the fast cooling regime at high energies [146]. An alternative explanation is through assuming an Inverse Compton scattering scenario.

2.5.2 Afterglow photon emission

The GRB afterglow is produced by the fireball colliding with the ISM or some pre-ejected stellar material via external forward and reverse shocks. Afterglow photons are observed in the optical, radio and x-ray energy range. Electrons and protons are accelerated in shocks propagating backward into the ejecta "reverse shocks" [43, 147]. These electrons radiate optical-UV photons via synchrotron emission. Again we outline the major features of the calculation of the afterglow photon spectrum and refer the reader to [43, 147] for more details.

The afterglow interactions occur at a distance much larger than the initial radius, r_i, at around:

$$r_e = (3E_{\text{kin, iso}}/[4\pi n_{\text{ex}} m_p c^2 \, , \Gamma_i^2])^{1/3} \tag{2.13}$$

where $n_{\text{ex}} = 1$ atom cm^{-3}, which is the average density of the ISM consisting predominantly of neutral hydrogen. At this radius, r_e, the total isotropic energy of the burst will equal the energy in the accumulated interstellar medium[5] ($(4/3)\pi r_e^3 n_{ex} m_p c^2 \Gamma_i^2$).

[5]Two factors of Γ_i arise, one from the density which has a component in the boost direction, whilst the other arises from the rest mass energy of the ISM.

At r_e the fireball lorentz factor will begin to decrease. For radii less that r_e the density of the accumulated ISM is not great enough to slow the fireball down. The total kinetic energy of the jet is assumed throughout the calculations to be:

$$E_{\text{kin, iso}} = E_{\gamma,\text{iso}}/\epsilon_e \simeq 10 E_{\gamma,\text{iso}} \, . \tag{2.14}$$

ϵ_e is the fraction of the isotropic equivalent kinetic energy from shock accelerated electrons from synchrotron or inverse compton scattering[6]. At around $t = t_{90}$ the fireball transitions with the reverse shock crossing the shell and most of the fireball energy is transferred to the ISM. The flow approaches the self-similar blast wave solution of Blandford and McKee [148] with bulk Lorentz factor of the reverse-shocked plasma shell given by:

$$\Gamma_e = \frac{1}{4}\left[\frac{17 E_{\text{kin,iso}}}{\pi n_{\text{ex}} m_{\text{p}} c^5 t_{90}^3}\right]^{1/8} \tag{2.15}$$

$$\approx 195 \left(\frac{E_{\text{kin,iso}}}{10^{54}\ \text{ergs}}\right)^{1/8} \left(\frac{t_{90}}{10\ \text{s}}\right)^{-3/8} \left(\frac{n_{\text{ex}}}{1\ \text{cm}^{-3}}\right)^{-1/8} \, . \tag{2.16}$$

The reasoning behind calculating the afterglow photon synchrotron spectrum is similar to that described in the previous section, where we discussed the synchrotron radiation from the electrons accelerated in the burst itself. The difference is that now we use the characteristic energies and Lorentz factors appropriate for the interaction of the burst with the interstellar medium. The photon number spectrum is as in Equations 2.11 and 2.12 with $p = 2$, yielding:

[6]Here we have not included the radiative efficiency, ϵ_r. If included then Equation 2.14 would be $E_{\text{kin, iso}} = E_{\gamma,\text{iso}}/\epsilon_e/\epsilon_r$.

$$\epsilon'_\gamma \frac{dN'_\gamma}{d\epsilon'_\gamma} \simeq n'_{\gamma,c} \times \begin{cases} (\epsilon'_\gamma/\epsilon'_{\gamma,c})^{-1/2} \; ; \; \epsilon'_{\gamma,m} < \epsilon'_\gamma < \epsilon'_{\gamma,c} \\ (\epsilon'_\gamma/\epsilon'_{\gamma,c})^{-1} \; ; \; \epsilon'_\gamma > \epsilon'_{\gamma,c} \, , \end{cases} \tag{2.17}$$

where $n'_{\gamma,c}$ is the characteristic number density of photons in the reverse shock, and $\epsilon'_{\gamma,m}$ and $\epsilon'_{\gamma,c}$ are, respectively, the synchrotron photon energies for the minimum Lorentz factor of the electrons and for the Lorentz factor obtained by equating the synchrotron cooling time to the dynamic time. Expressions for these quantities are now given.

In the un-shocked plasma frame the minimum Lorentz factor of the reverse shock accelerated electrons is:

$$\gamma'_{e,\min} \simeq \epsilon_e (m_p/m_e)(\Gamma_i/\Gamma_e) \, , \tag{2.18}$$

where ϵ_e is the fraction of the thermal energy density (in the plasma rest frame) that is carried by electrons. This relationship is derived [43] by noting that the thermal energy per proton in the shocked ejecta is $\simeq (\Gamma_R - 1) m_p c^2$ where Γ_R is the Lorentz factor of the reverse shock in the frames of the unshocked plasma. Γ_R is mildly relativistic with $\Gamma_R - 1 \sim \Gamma_i/\Gamma_e$.

The magnetic field of the reverse shock in the comoving plasma frame is:

$$B'_e = (8\pi \epsilon_B n_{\rm ex} m_p c^2 \Gamma_e^2)^{1/2} \, , \tag{2.19}$$

where the fraction of the internal energy carried by the magnetic field in the shocked fluid, ϵ_B is again set as in the burst models to 0.1. The peak photon energy produced via synchrotron emission from the minimum Lorentz factor for electrons is as in Equation 2.6:

$$\epsilon'_{\gamma,m} = \hbar c(3\gamma'^2_{e,\rm min} eB'_e)/(2m_e c^2)\ . \tag{2.20}$$

The characteristic shock-accelerated electron Lorentz factor obtained by equating the synchrotron cooling time to the dynamic time, $t_{\rm dyn} = r_e/4\Gamma_e^2 c$, is:

$$\gamma'_{e,c} = 6\pi m_e c/(\sigma_{\rm Th} B'^2_e \Gamma_e t_{\rm dyn})\ . \tag{2.21}$$

This corresponds to a peak synchrotron energy radiated by these accelerated characteristic electrons in the magnetic field, B'_e, of:

$$\begin{aligned} \epsilon'_{\gamma,c} &= \hbar c \frac{3\gamma'^2_{e,c} eB'_e}{2m_e c^2} \\ &\approx 0.2 \left(\frac{E_{\rm kin,\ iso}}{10^{54}\ {\rm ergs}}\right)^{-19/24} \left(\frac{\Gamma_i}{300}\right)^{4/3} \left(\frac{t_{90}}{10\ {\rm s}}\right)^{3/8} \left(\frac{n_{\rm ex}}{1\ {\rm cm}^{-3}}\right)^{-17/24}\ {\rm eV}\ . \end{aligned} \tag{2.22}$$

The number density of photons in the reverse shock is approximately given by the total synchrotron radiation power by all electrons at $\epsilon'_{\gamma,c}$ divided by $\epsilon'_{\gamma,c}$. The specific luminosity at the peak synchrotron photon energy is: [43, 147]

$$L_{\epsilon_{\gamma,m}} = \frac{\Gamma_e}{2\pi\hbar} \frac{e^3 B'_e}{2m_e c^2} N_e\ , \tag{2.23}$$

where N_e is the total number of electrons in the reverse shock ($N_e \approx E_{\rm kin,iso}\Gamma_i m_p c^2$). The characteristic photon number density in cm^{-3} in the comoving frame is then:

$$
\begin{aligned}
n'_{\gamma,c} &= \frac{L_{\epsilon_{\gamma,m}}}{4\pi c r_e^2 \Gamma_e} \left(\frac{\epsilon'_{\gamma,m}}{\epsilon'_{\gamma,c}}\right)^{1/2} \\
&\simeq \frac{E_{\text{kin, iso}}}{8\pi^2 \hbar c r_e^2} \frac{e^3 B'_e}{m_e c^2 m_p c^2 \Gamma_i} \left(\frac{\epsilon'_{\gamma,m}}{\epsilon'_{\gamma,c}}\right)^{1/2} \\
&\approx 4.3 \times 10^{12} \left(\frac{E_{\text{kin, iso}}}{10^{54}\ \text{ergs}}\right)^{19/24} \left(\frac{\Gamma_i}{300}\right)^{2/3} \\
&\quad \times \left(\frac{t_{90}}{10\ \text{s}}\right)^{-3/8} \left(\frac{n_{\text{ex}}}{1\ \text{cm}^{-3}}\right)^{41/24}\ \text{cm}^{-3}\,. \qquad (2.24)
\end{aligned}
$$

In the next chapter neutrino production in GRBs is considered. The neutrinos are produced from interactions of high energy protons accelerated along with the electrons. The protons and electrons follow the same distribution so that the spectral indices for the electron spectra inferred from the observed gamma ray spectra apply to the proton spectra as well.

Chapter 3

Neutrino Production in Gamma Ray Bursts

Within the GRB fireball context several models have been developed which describe the production of neutrinos via fireball particle interactions. These models have predicted neutrino production in the precursor, prompt and afterglow phases for various progenitor scenarios [42, 43, 45, 149]. The neutrino are produced in all these models via photomeson ($p\gamma$) or via proton-proton (pp) interactions by protons accelerated in the GRB shocks [45], where $p\gamma$ are the dominant interactions. Here I give particular attention to Waxman and Bahcall's prompt burst model [42, 147] in Section 3.1 and afterglow model [43, 147] in Section 3.2, which are used as the basis for calculations in Chapter 7.

3.1 Neutrino Burst Proper Model

The Waxman and Bahcall [42, 147] neutrino burst model is set within the framework of the generic fireball model discussed in the previous chapter. The neutrinos are produced by the decay of pions which are produced through the interaction of protons that are assumed to be co-accelerated with the electrons. The GRB photons are

produced in the fireball via synchrotron radiation. The neutrino energy spectrum can be related to the GRB photon spectrum and a full derivation is given in [150]. Here we outline the major features of this calculation.

Pions are produced via the Delta resonance, Δ^+:

$$\begin{aligned} p + \gamma \rightarrow \quad & \Delta^+ \\ & \downarrow \\ & n \quad + \quad \pi^+ \\ & \qquad\quad \downarrow \\ & \qquad\quad \nu_\mu + \mu^+ \\ & \qquad\qquad\quad \downarrow \\ & \qquad\qquad\quad e^+ + \nu_e + \bar{\nu}_\mu, \end{aligned} \tag{3.1}$$

and

$$\begin{aligned} p + \gamma \rightarrow \quad & \Delta^+ \\ & \downarrow \\ & p \quad + \quad \pi^0 \\ & \qquad\quad \downarrow \\ & \qquad\quad \gamma + \gamma. \end{aligned} \tag{3.2}$$

At the Δ resonance the interaction cross-sections are very large, $\sigma = 5 \times 10^{-28}\text{cm}^2$. In order for this interaction to occur the proton energy must satisfy the following condition:

$$\epsilon'_p \geq \frac{m_\Delta^2 - m_p^2}{4\epsilon'_\gamma} \,, \tag{3.3}$$

where ϵ'_p is the proton energy and ϵ'_γ is the photon energy. Primed quantities represent quantities in the rest frame of the fireball plasma and unprimed quantities are in the observer's frame. Equation 3.3 corresponds to:

$$\epsilon'_p \epsilon'_\gamma \simeq 0.3 \text{ GeV}^2 \quad \text{or} \quad \epsilon_p \epsilon_\gamma \simeq 0.3 \Gamma_i^2 \text{ GeV}^2 \,. \tag{3.4}$$

Here Γ_i is the Lorentz factor of the burst, which was referred to as Γ in the previous chapter. Here we use the i subscript to distinguish Γ_i from the Lorentz factor Γ_e appropriate at later times when the fireball transfers most of its energy into the inter-stellar medium. Γ_e is important in determining the after-glow emission of the GRB. The Δ^+ decays to charged and neutral pions with the charged pions decaying to neutrinos and leptons, and the neutral pion decaying to two photons. Equipartition is assumed for the π^+ decay, that is the energy is evenly distributed to the four final state leptons. In the interaction the proton is expected to lose a fraction of its energy, $\langle \chi_{p \to \Delta^+} \rangle = 0.2$, resulting in a neutrino energy:

$$\epsilon_\nu = \frac{1}{4} \langle \chi_{p \to \Delta^+} \rangle \epsilon_p \,. \tag{3.5}$$

The energy of the produced neutrinos is directly proportional to the energy of the protons, while the product of the photon and proton energies remains constant due

to the energy constraint of Equation 3.3. Hence the photon and neutrino energies are inversely proportional and the neutrino spectrum traces the inverse of the spectrum of the GRB photons.

Figure 3.1 shows schematically the relationship between the neutrino energy spectrum expected from a GRB photon energy spectrum.(a) Shock accelerated proton spectrum and the photon energy spectrum with break energy, $\epsilon_{\gamma,b}$, separating the two power laws. (b) The opacity for the $p + \gamma \rightarrow \Delta^+$ interaction which is required to satisfy the energy condition $\epsilon_p \epsilon_\gamma = 0.3\Gamma^2 \mathrm{GeV}^2$. The optical depth changes its shape when expressed as a function proton energy. Note the inverse relationship consistent with $\epsilon_\gamma \epsilon_p = const.$ (c) The resultant neutrino energy spectrum for energies below the synchrotron break (described later). The neutrino spectrum follows the shape of the optical depth[147].

As mentioned in the previous chapter, the GRB photon spectrum can be described by the broken power law approximation to the Band function given in Equation 2.2 and repeated here:

$$F_\gamma = \epsilon_\gamma dn_\gamma / d\epsilon_\gamma \propto \begin{cases} \epsilon_\gamma^{-\alpha} & \text{if } \epsilon_\gamma \leq \epsilon_{\gamma,b}, \\ \epsilon_\gamma^{-\beta} & \text{if } \epsilon_\gamma > \epsilon_{\gamma,b}. \end{cases} \tag{3.6}$$

Then, assuming that the protons have a power law spectrum $\frac{dn_p}{d\epsilon_p} \sim \epsilon_p^{-2}$ where the maximum energy is $\leq 10^{20}$ eV which is consistent with the observed cosmic-ray energy spectrum [24], the neutrino spectrum is given as:

$$\epsilon_\nu^2 \Phi_\nu^s = \mathcal{A} \times \begin{cases} (\epsilon_\nu/\epsilon_{\nu,b1})^{\beta-1} \ ; \ \epsilon_\nu < \epsilon_{\nu,b1} \\ (\epsilon_\nu/\epsilon_{\nu,b1})^{\alpha-1} \ ; \ \epsilon_{\nu,sb} \geq \epsilon_\nu \geq \epsilon_{\nu,b1} \\ (\epsilon_{\nu,sb}/\epsilon_{\nu,b1})^{\alpha-1}(\epsilon_\nu/\epsilon_{\nu,sb})^{-2} \ ; \ \epsilon_\nu > \epsilon_{\nu,sb} \ , \end{cases} \tag{3.7}$$

for each neutrino flavour, ν_μ, $\overline{\nu}_\mu$ and ν_e, at the source. $\epsilon_{\nu,b1}$ and $\epsilon_{\nu,sb}$ are break energies and $\mathcal{A}$ is the normalisation constant. We discuss each of these constants further below. We note that Taboada and D'Agostino [151] have shown that using the broken power approximation to the Band function can lead to increased uncertainties in the neutrino flux. A complete Band function cannot be extracted, however, for many bursts and we expect that the uncertainty introduced will be less in the energy range probed by RICE.

The break in the neutrino spectrum, $\epsilon_{\nu,b1}$, is related to the break in the photon spectrum, $\epsilon_{\gamma,b}$, through Equations 3.4 and 3.5. In the observer's frame:

$$\epsilon_{\nu,b1} = \frac{0.015\Gamma_i^2}{(1+z)^2} \left(\frac{\epsilon_{\gamma,b}}{\mathrm{GeV}}\right)^{-1} \mathrm{GeV}, \tag{3.8}$$

where the source redshift dependence has also been introduced. The spectrum is steeper above $\epsilon_{\nu,sb}$ as at higher energies the pions will lose energy due to synchrotron emission before decaying. This will be significant when the synchrotron loss time:

$$t'_{synchrotron} = \frac{3m_\pi^4 c^3}{4\sigma_T m_2^2 \epsilon_\pi U'_B}, \tag{3.9}$$

becomes comparable with the pion lifetime:

$$\tau'_\pi \approx \frac{2.6 \times 10^{-8} \epsilon'_\pi}{m_\pi c^2}. \tag{3.10}$$

Thus the radiative losses become important when $\epsilon_\pi > \epsilon_{\pi,sb} \approx 4\epsilon_{\nu,sb}$ where:

$$\epsilon_{\nu,sb} = \frac{10^{11}\Gamma_i}{4(1+z)} \left(\frac{B'_i}{\mathrm{G}}\right)^{-1} \text{ GeV}. \tag{3.11}$$

For neutrinos produced from muon decay the lifetimes are expected to be 100 times longer than that of pions. This results in the energy cutoff being 10 times smaller than that of Equation 3.11 [150]. An expression for the magnetic field, B'_i, in the fireball can be obtained using Equations 2.8 and 2.9.

$$B'_i = \sqrt{\frac{2\epsilon_B L_{\gamma,\mathrm{iso}}}{\epsilon r_i^2 \Gamma_i^2 c}} = 5 \times 10^4 \left(\frac{L_{\gamma,\mathrm{iso}}}{10^{52}\ \mathrm{ergs/s}}\right)^{1/2} \left(\frac{\Gamma_i}{300}\right)^{-3} \left(\frac{t_v}{0.01\ \mathrm{s}}\right)^{-1} \text{ G}, \tag{3.12}$$

where $\epsilon_B \approx \epsilon \approx 0.1$ [150]. Both the Lorentz factor, Γ_i, and the variability, t_v, (0.001 to 1 s) can vary over a large range. Therefore the radius of the fireball, which is given by $r_i \simeq 2\Gamma_i^2 c t_v$, can also vary greatly. In our analysis in Chapter 7 we take $\Gamma_i = 300$ and $t_v = 0.01$.

In order to calculate the normalisation constant, $\mathcal{A}$, we assume that the shock accelerated proton isotropic luminosity in the fireball and the isotropic gamma ray luminosity are equal, $L_{p,\mathrm{iso}} \simeq L_{\gamma,\mathrm{iso}}$. The total proton energy is $\sim 10 E_{\gamma,\mathrm{iso}}$ which is consistent with the assumed equipartition fraction, $\epsilon \sim 0.1$, of the total isotropic kinetic energy of the fireball, $E_{\mathrm{kin,\ iso}}$. The average fraction of the energy converted from the shock accelerated proton (at the Δ^+ resonance) to the energy of the pion

is assumed to be $f_\pi \leq 0.2$, which is suitable for optically thin sources ($\tau_{optical} \approx 1$)[1]. The pre-factor in Equation 3.7 can then be written as:

$$\mathcal{A} \equiv \frac{1}{2}\frac{f_\pi}{4}\frac{S_\gamma}{t_{90}} = 1.56 \times 10^{-6} \left(\frac{f_\pi}{0.2}\right) \left(\frac{S_\gamma}{10^{-6}\text{ergs/cm}^2}\right) \left(\frac{t_{90}}{10\text{s}}\right)^{-1} \text{GeV cm}^{-2}\ \text{s}^{-1} \quad (3.13)$$

where the $t_{\text{burst}} = t_{90}$ is the duration of the burst. The factors of $\frac{1}{2}$ and $\frac{1}{4}$ arise due to the assumption of equal decay probabilities, $\Delta^+ \rightarrow \pi^+/\pi^0$, and energy equipartition among the π^+ decay products, respectively. After oscillations in the vacuum there is a $1:1:1$ ratio of neutrino flavours at the detector with $\Phi_{\nu_e+\overline{\nu}_e} = \Phi_{\nu_\mu+\overline{\nu}_\mu} = \Phi_{\nu_\tau+\overline{\nu}_\tau} = \Phi^s_\nu$.

3.2 Afterglow Neutrinos

The GRB afterglow is produced by the fireball colliding with the ISM or some pre-ejected stellar material via external forward and reverse shocks. As in the case of the prompt burst, the key relationship for obtaining the neutrino spectrum is between the energy of the observed photons, ϵ_γ and the shocked protons, ϵ_p, undergoing photomeson interaction at the Δ^+ resonance given in Equation 3.3. Afterglow photons are observed in the optical, radio and X-ray energy range. For 10 eV to 1 keV photons, protons with energies of $\approx 10^{19}$ to 10^{21} eV are required to satisfy the Δ^+ resonance condition. This yields neutrino energies of the order 10^{18} eV [42, 147]. These neutrinos are produced at the initial stage of the fireball interacting with the external medium and occur over a period of time comparable to the duration of the GRB prompt phase [43, 147].

[1] A derivation of f_π can be found in [150]. The fraction is dependant on the ratio of the size of the shock and the proton mean free path. All of which occur over a large range.

Electrons and protons are accelerated in shocks propagating backward into the ejecta with the observed afterglow emission attributed to the synchrotron radiation of the accelerated electrons. The combination of the high energy protons and low energy photons produces the high energy neutrinos via photomeson production. To determine the neutrino spectrum we follow the same procedure as in the prompt phase with the neutrino spectrum tracing the inverse of the spectrum of the GRB photons. The afterglow photon spectrum was given in the previous chapter Equation 2.17. Again, assuming that the protons have a power law spectrum $\frac{dn_p}{d\epsilon_p} \sim \epsilon_p^{-2}$, the afterglow neutrino spectrum is:

$$\epsilon_\nu^2 \Phi_\nu^s = \frac{f_\pi}{8} \frac{S_\gamma}{t_{90}} \times \begin{cases} (\epsilon_\nu / \epsilon_{\nu,b2}) \ ; \ \epsilon_\nu < \epsilon_{\nu,b2} \\ (\epsilon_\nu / \epsilon_{\nu,b2})^{1/2} \ ; \ \epsilon_{\nu,\max} \geq \epsilon_\nu \geq \epsilon_{\nu,b2}, \end{cases} \tag{3.14}$$

for each neutrino flavour, ν_μ, $\bar{\nu}_\mu$ and ν_e, at the source. In this expression $\epsilon_{\nu,b2}$ and $\epsilon_{\nu,\max}$ are the neutrino break energy and maximum neutrino energy respectively and are discussed below. Again, the flavour ratios on Earth, after vacuum oscillation, would be $\Phi_{\nu_e+\bar{\nu}_e} = \Phi_{\nu_\mu+\bar{\nu}_\mu} = \Phi_{\nu_\tau+\bar{\nu}_\tau} = \Phi_\nu^s$, each with a duration of $t_{\rm glow} = t_{90}$.

The neutrino break energy, $\epsilon_{\nu,b2}$, is the neutrino energy corresponding to the characteristic photon energy, $\epsilon'_{\gamma,c}$ given previously by Equation 2.22. The photon break energy for the prompt emission was given in Equation 2.22. Following similar arguments which lead to Equation 3.8, we can obtain:

$$\epsilon_{\nu,b2} = \frac{0.015\Gamma_e}{(1+z)} \left(\frac{\epsilon'_{\gamma,c}}{\rm GeV} \right)^{-1} \ {\rm GeV}. \tag{3.15}$$

The maximum neutrino energy, $\epsilon_{\nu,max}$, is dependant on the maximum energy of the shock accelerated protons. This can be found by equating the shorter of the

synchrotron cooling and the dynamic times with that of the shock acceleration time $\epsilon'_p/(ecB'_e)$. Including the redshift dependence and the usual assumptions relating the neutrino energy to the proton energy ($\epsilon_\nu = \frac{<x_{p\to\Delta^+}>}{4\epsilon_p}$), the maximum neutrino energy is given by:

$$\epsilon_{\nu,\max} = \frac{<x_{p\to\Delta^+}>}{4(1+z)}(eB'_e r_e). \tag{3.16}$$

Unlike the prompt phase, the proton to pion efficiency, f_π, may be lower than 0.2 in the afterglow phase. We calculate f_π for reverse shock accelerated protons to interact with photons of energy $\epsilon'_{\gamma,c}$ (Equation 2.22) at the Δ^+ resonance as:

$$\begin{aligned} f_\pi &= \min(1, \tau'_{p\gamma\to\Delta^+}) <x_{p\to\Delta^+}> \\ &\approx 0.2 \left(\frac{E_{\text{kin},iso}}{10^{54}\text{ ergs}}\right)\left(\frac{n_{\text{ex}}}{1\text{ cm}^{-3}}\right)^{3/2}, \end{aligned} \tag{3.17}$$

where $\tau'_{p\gamma\to\Delta^+} \approx \sigma_{p\gamma\to\Delta^+}(r_e/\Gamma_e)n'_{\gamma,c}$ is the optical depth using Equation 2.24, and $\sigma_{p\gamma\to\Delta^+} = 5\times10^{-28}$ cm^2 is the $p\gamma$ cross-section at the Δ^+ resonance.

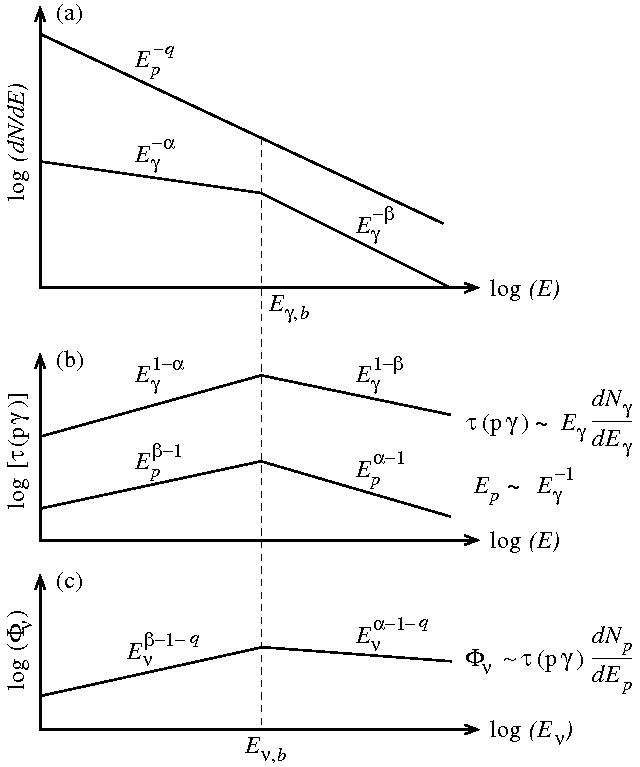

Figure 3.1: The relationship between the neutrino energy spectrum expected from a GRB photon energy spectrum.(a) Shock accelerated proton spectrum and the photon energy spectrum. (b) The opacity for the $p + \gamma \rightarrow \Delta^+$ interaction which is required to satisfy the energy condition $\epsilon_p \epsilon_\gamma = 0.3\Gamma^2 \mathrm{GeV}^2$. The optical depth changes its shape when expressed as a function proton energy. (c) The resultant neutrino energy spectrum which follows the shape of the optical depth[147].

Chapter 4

The Radio Ice Cherenkov Experiment

Neutrino detection is logistically difficult. Low fluxes and interaction probabilities means large natural resources are needed as the detector medium. This is particularly important for the highest energy neutrinos above 10^{14} eV. Although optical neutrino telescopes have paved the way for high energy neutrino detection, radio-based neutrino telescopes exploit the long attenuation lengths (on the order of kilometres) associated with longer wavelengths in dense materials. The coherence extending up to 1GHz of the Cherenkov signal emitted from the resultant electromagnetic shower. In Chapter 1 we discussed the Askaryan effect and some of the main detectors using this technique. RICE aims to use radio receivers to detect signals produced from the interaction of high energy neutrinos with nucleons in the ice via charged or neutral current neutrino interactions. The general RICE concept is shown in Figure 4.1 where in the charged current case the neutrino interacts with a nucleon and produces its leptonic counterpart, the electron. The electron knocks off surrounding atomic electrons which are pushed into the forward moving shower. Broadband Cherenkov radiation is produced as a result of the shower propagating faster than the speed of

light in ice, causing an analogous effect to the sonic boom. The emitted radiation is in the form of Cherenkov radiation which is produced in a cone. If it intercepts the antenna and is energetic enough, the antenna will register a hit. The RICE detector is shown relative to its surrounding in Figure 4.2.

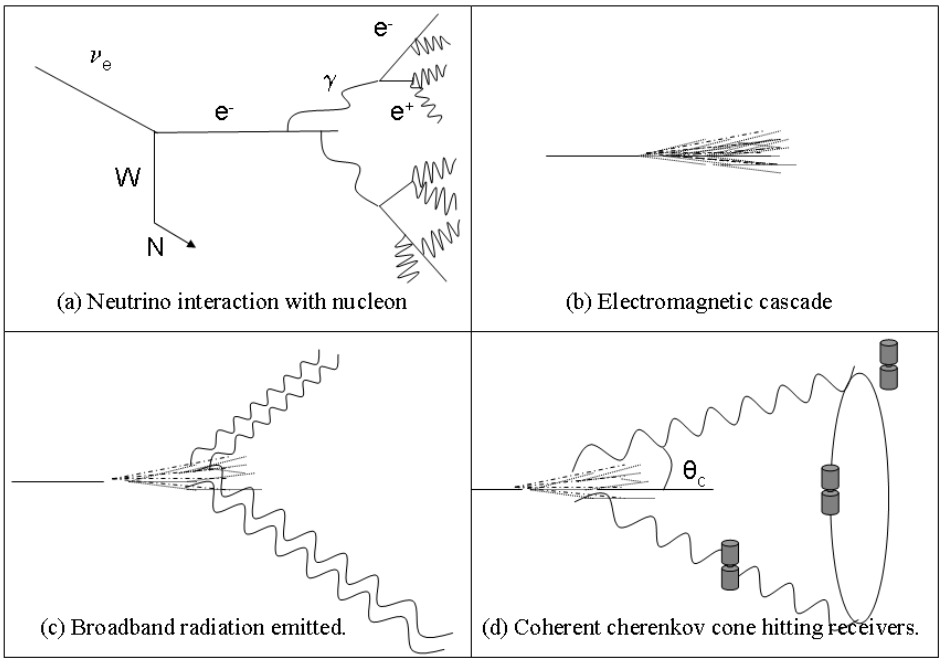

Figure 4.1: The production of in-ice showers via neutrino-nucleon interaction in ice.

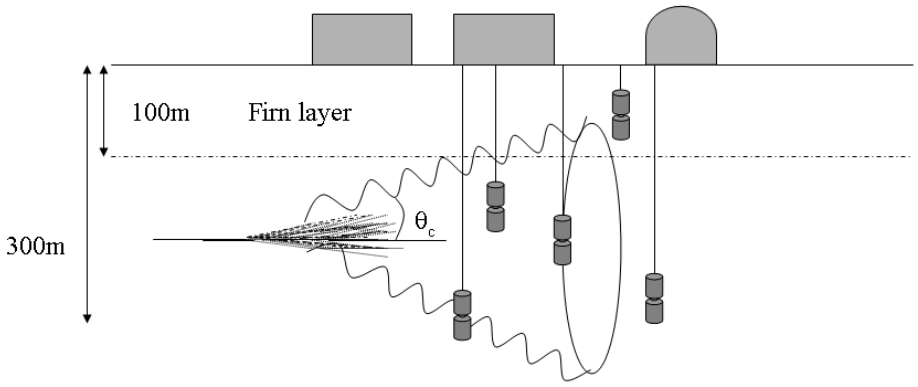

Figure 4.2: An electromagnetic shower in ice producing a Cherenkov signal in the RICE array.

In this chapter I summaries the most recent results of RICE[152]. In Section 4.1 I begin with an historical review of the detector and Section 4.2 describes its current configuration. The data acquisition rate and a summary of the data intake between 1999 and 2005 is shown for later reference [152]. Section 4.4 discusses the different backgrounds for which the neutrino analysis regime must distinguish a unique neutrino signal. The general analysis technique is outlined in Section 4.5. Lastly, a description of the effective volume Monte Carlo is given in Section 4.6.1 including some diffuse effective volume results from the most recent RICE [152] paper. This

chapter summarises the latest results of RICE presented in Kravchenko et al.,[152]. For a detailed discussion of the detector calibration and modelling the reader is referred to Kravchenko et al.,[152, 153].

4.1 A Brief History of RICE

The first RICE receivers were deployed in October 1995. The array originally consisted of 2 radio receivers (Rx) co-deployed with another neutrino experiment called AMANDA-B [154]. An under-ice transmitter (Tx) was introduced to the array to calibrate the system and to ensure that the signals could be detected with the required precision. Cross talk between various components as well as amplifier oscillation problems lead to the need of an improved system. Therefore, in 1996-1997, the first three dedicated RICE receivers and one under-ice transmitter were added to the array. Later signals produced by the AMANDA experiment's photomultiplier tubes at frequencies below 100 MHz indicated the requirement of a high-pass filter on future radio receivers. The years to follow saw the deployment of three receivers and two transmitters between 1997-1998 and 1998-1999; then six receivers and six more with one transmitter between 1999-2000 [155].

4.2 RICE Schematics

The RICE experiment currently consists of an array of 20 radio receivers (Rx) and transmitters (Tx) distributed in an approximate 200m$\times$200m$\times$200m volume, at 100m-300m depths [155]. The receivers are housed in a nylon cylindrical pressure vessel

and are designed to withstand high pressures exceeding 20 atmospheres. The signal from each receiver is boosted in the ice by a 36-DB amplifier and carried via coaxial cable to the surface observatory. The signal is then filtered (suppressing noise contributions below 200 MHz), re-amplified (either 52 or 60-DB gain), and fed into a CAMAC (Computer Automated Measurement And Control) crate. After initial discrimination (using a LeCroy 3412E discriminator) the signal is routed into a NIM (Nuclear Instrumentation Module) crate where the trigger logic resides. A valid trigger signal initiates readout of receiver waveforms, as recorded on HP54542 digital oscilloscopes. Also deployed are three large TEM surface horn antennas which are used to veto surface-generated noise. The detector is intended to have a sensitivity to detect PeV neutrinos and above.

The current RICE configuration is given in Table 4.1. Minor changes have occurred between 2001 and 2005 such as channel 11 shifting to just 2 m below the surface. For a further discussion on deployment and configuration the reader is referred to Kravchenko et al., [155].

Figure 4.3 and Figure 4.4 show graphically the RICE array configuration against the Amunsden South Pole base. The neutrino detectors RICE, AMANDA [154], and IceCube [56] are shown. The MAPO (Martin A. Pomerantz Observatory) building houses the Data Acquisition (DAQ) system of AMANDA, RICE and other experiments. MAPO is centered at x=40 m, y=30 m, z=0 m on the surface and is connected to the array via approximately 600 to 1000 feet of coaxial cable. Dispersion effects in the cables have been investigated and found to be negligible. The AMANDA array is located in the same region as RICE. Residing at 600 m below is the AMANDA-A

Table 4.1: RICE Antenna Positions

Channel hole	x (m)	y (m)	z (m)
0 (A11)	4.8	102.8	-166
1 (A6)	-56.3	34.2	-213
2 (A13)	-32.1	77.4	-176
3 (A12)	-61.4	85.3	-103
4 (A6)	-56.3	34.2	-152
5 (A7)	47.7	33.8	-166
6 (B2)	78.0	13.8	-170
7 (B3)	64.1	-18.3	-171
8 (B1)	43.9	7.3	-171
9 (B3)	64.1	-18.3	-120
10 (B1)	43.9	7.3	-120
11 (B4)	67.5	-39.5	-168
12 (A18)	66.3	74.7	-110
13 (A15)	-95.1	-38.3	-105
14 (A16)	-46.7	-86.6	-105
15 (A19)	95.2	12.7	-347
19 (A15)	-95.1	-38.3	-135

detector and at 2400 m below is the AMANDA-B detector. The IceCube experiment, currently under construction, will encircle the AMANDA experiment and be centered at approximately 200 m northwest of the origin. When completed it will radially extend to 500 m in a hexagonal configuration. The successor of RICE is the planned AURA [90] neutrino radio Cherenkov array which is not shown but will cover over an area of 100 km^2 at the South Pole centered around IceCube. The South Pole Air Shower Experiment (SPASE-2) [156] is also shown located at x $\approx$ -150 m, y ≈ -350 m on the surface. The RICE cartesian co-ordinate system adopts the AMANDA convention and is defined by a +y direction coinciding with grid north defined by the Greenwich meridian.

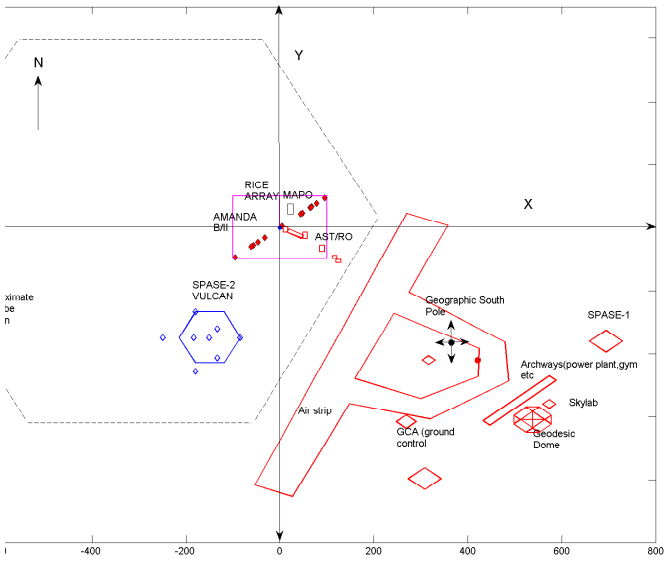

Figure 4.3: An aerial view of the Amunsden South Pole base. The RICE array is located 800 m north west of the geographic South Pole. The IceCube [157, 56], AMANDA[157, 154] and SPASE-2 [156] experiments are shown; AURA [90] is off the scale.

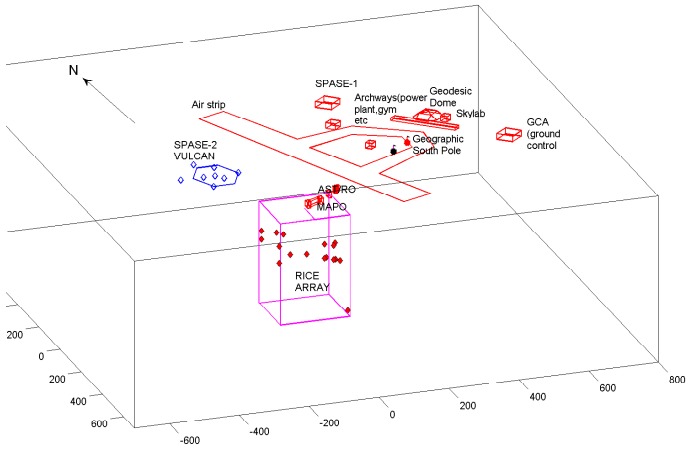

Figure 4.4: The schematic diagram of the current RICE detector configuration relative to the South Pole base. MAPO and ASTERO buildings which house electronics for various projects are shown above. The landing air strip and sections of the base are shown located near the geographic South Pole.

4.3 Current Data

4.3.1 Trigger Summary

Certain criteria, referred to as trigger conditions, determine whether a signal will be recorded and is worthwhile of further analysis. The main trigger is called general and is a self-trigger which requires four antenna receivers to fire over threshold within a 1.25 μs gate. The 1.25 μs time window corresponds to the propagation of an electromagnetic signal through the array. The random noise trigger, called unbiased, is the trigger which is forced periodically by the DAQ system, currently at a period of 600

seconds. The external triggers 1 and 2 refer to if ≥ 1 under-ice RICE antenna registers a signal above threshold in coincidence with a high-amplitude SPASE[1] event or ≥ 1 under-ice antenna registers a signal above threshold in coincidence with a 30-fold PMT AMANDA-B event. Two primary vetoes are also used to eliminate background noise. The first veto rejects signals if one of the surface horn antennae registers a signal in co-incidence with the first of the three trigger criteria above. The second veto eliminates data if the under-ice antenna register signals which have timings consistent with that from a surface generated source. Trigger 4 is the hardware surface veto trigger which are events that have been rejected by some veto criteria. Trigger 5 is if either of the External 1 or 2 is the trigger, leaving the external veto trigger which records a certain amount of vetoed events for checking if the veto trigger is working correctly [153].

If any of the above triggers are satisfied and no veto signalled then the time of the hit is recorded with an 8.192 μs buffer of data stored in an HP54542 digital oscilloscope at 1Gsa/s (for each Channel) is written to disk along with the time of the recording. The raw trigger rate before the veto is implemented is every 0.033 seconds. After the vetoes are implemented the trigger rate is reduced to every 10 to 100 seconds. However, there are other limitations to the rate at which data is taken. These are the speed at which the information can be recorded, which takes about 10 s per event, as well as the time to perform the veto which is about 10 ms/event. The signal measurement is limited also by the presence of the satellite uplink, which sends information from the pole approximately once a day. The satellite signal transmits

[1]South Pole Air Shower Experiment-an array of scintillation detectors situated 200m from the geographic south pole used to detect cosmic-ray air showers.

at 303 MHz and floods the receivers, thus restricting data-taking to times outside the satellites transmission periods [153].

4.3.2 Data Summary

Table 4.2 shows the entire data summary for the period covering 1999 to August, 15th, 2005. Typically, in a 24 hour period 1000 data triggers pass the fast online hardware veto and the software surface veto. An offline analysis is implemented on this data to remove background events. An efficiency has been determined using simulated hadronic and electromagnetic showers embedded in real data for this process (see Section 4.5.4). In the table the total runtime and livetime is given for each year. The total time the South Pole Station LES communications satellite uplink is on is also given. The total number of triggers are also shown and for each trigger type.

Table 4.2: RICE-II Data Summary through to August, 15th, 2005.

	1999	2000	2001	2002	2003	2004	2005
Total RunTime (10^6s)	0.18	22.3	4.6	19.9	24.5	11.6	15.1
Total LiveTime (10^6s)	0.10	15.7	3.3	13.6	17.1	9.4	14.9
DeadTime (303 ON) (10^6s)	0.03	3.7	1	4.1	5.6	1.1	0
$\geq$4-hit General Trig. (10^4)	0.26	30.6	6	16.9	13.8	9.4	26.5
Unbiased Trig. (10^4)		3.3	1.3	3.5	4.4	2.5	4
AMANDA-coincident Trig. (10^4)	0.06	1.9	2.4	0.016	0.056	0.075	0.002
SPASE-coincident Trig. (10^4)		0.48	0.003	0.47	0.021	0.001	0.067
Veto Trig. (10^4)	1.2	11182.8	317.4	12973.9	3153.9	142.5	471

4.4 Backgrounds

Backgrounds can be generally classified into one of the three classes: continuous wave (CW) backgrounds; true thermal noise backgrounds; and loud transients. CW backgrounds are expected to have long time over threshold and large time residuals from the vertex fit due to uncorrelated multiple sources. A presence in all trigger types (unbiased, forced and general) is expected and the fourier spectrum will be dominated by one frequency and its overtones. The hit multiplicity is roughly constant and signals may be periodic and easily recognisable.

True thermal noise backgrounds tend to reconstruct their vertices toward the center of the array at x = 0, y = 0, z = 120 m [152]. Very small time over thresholds are almost indistinguishable to real neutrino induced signals. These are the most likely to survive through to, and pass, hand inspection. However, large time residuals may result. A fourier spectrum dominated by frequencies characteristic of RICE receiver components should be seen and no double pulses or temporal correlations are expected.

Loud transients are the dominant background. These are in ice sources such as the AMANDA and IceCube photomultiplier electronic and surface generated signals. Filtering is necessary to suppress these backgrounds leaving the dominant transient as anthropogenic surface generated noise. These signals are expected to have a large time over threshold and a non-thermal structure in their time and frequency domains.

There is clear evidence that some anthropogenic backgrounds are periodic [152]. Some sources such as the satellite mentioned above[158] have been identified, other

sources however remain unknown.

Muons produced by cosmic-ray interactions have a vertical flux of $E\Phi(E) \approx 2.5 \times 10^{-3}(100\ \mathrm{PeV}/E_\mu)^3\ \mathrm{km}^{-3}\mathrm{sr}^{-1}\mathrm{yr}^{-1}$ for above PeV energies [152]. The expected atmospheric neutrino flux above 100 PeV is $E\Phi(E) \sim 2{\times}10^{-20}(100\ \mathrm{PeV}/E)^3\mathrm{cm}^{-2}sr^{-1}s^{-1}$[152]. Both have been modelled and found to be below the detectability of RICE. The small fluxes from atmospheric neutrinos and muons above 100 PeV means that unlike their optical counterparts, RICE can avoid these problematic backgrounds. However, this also means that RICE is unable to use them as a calibration beam [152].

Cosmic air showers are able to produce radio signals such as the production of geo-synchrotron radiation in the atmosphere, and transition and Cherenkov radiation from the showers impacting on the ice. In order to be detectable by RICE the signal must be coherent as well as having a favourable shower geometry. RICE has not studied this in detail.

Transition radiation occurs when the shower hits the ice. Coherent emission occurs in a small fraction of the shower impact radius, and the transition radiation is forward peaked making multiple antenna hits unlikely. This effect has not been properly modelled [152].

The Askaryan pulse produced by the core of the shower hitting the ice is of particular interest to RICE. The pulse must originate from a transverse region of the order of tens of centimetres, which is comparable to shower cores where the highest energy particles reside. Remaining interactions occur 1 km above the ice and require a γ factor of around 10^4 to produce tens of GeV energies for e^-, e^+ and bremsstrahlung

γ's. The pure proton composition case has been modelled with a rate of around 0.5 events per km^2 year. One year of RICE data was also searched for coincidences with SPASE, but none were observed [159].

Radio frequency noise associated with solar activity has been investigated. RICE has seen no correlation between data and active solar periods [158].

4.5 The Analysis Programme

The analysis programme begins by determining timing information for each RICE receiver. This information is fed into reconstruction routines which determine the best estimate for the vertex from which the signal originated. In order to distinguish the difference between non-neutrino backgrounds and actual neutrino induced events RICE generally looks at the characteristics of the following criteria:

- Vertex reconstruction of source.
- Waveform characteristic such as the time over threshold.
- Reliability of the vertex fit using time residuals.
- Radio Frequency conditions at time.
- Fourier spectrum of hit channels.
- Clean hits without multiple pulses.
- Hit multiplicity.
- Time since last trigger.

The criteria used in the analysis in this thesis will be described in Chapter 6. Further details of the criteria used in a general RICE analysis can be found in [152].

The number of events found can be used to place limits on particular flux models using the effective volume of the RICE array, which is estimated using Monte Carlo simulations and the livetime of the detector. The timing determination, vertex reconstruction Monte Carlo effective volume, and livetime aspects of the analysis are discussed further below.

4.5.1 Timing Calibration

Determining the times at which the antennae are hit by an arriving signal is one of the most challenging tasks. This is due to the complex nature of the waveforms which are recorded by the DAQ. We show in Figure 4.5 shows two separate examples of anthropogenic signals for the first 10 channels of RICE. The left figure shows a multiply peaked signal, whilst the second is a singular peak. Both these signals successfully vertexed to the surface. Many methods are used to obtain the times, such as the time that the maximum voltage occurs and the time of the first excursion above $6\sigma_{rms}$ in a waveform. A matched filter algorithm which is designed to match an observed waveform to that of a reference signal waveform is also being investigated. This reference signal will be modelled on the antenna response to incoming signals.

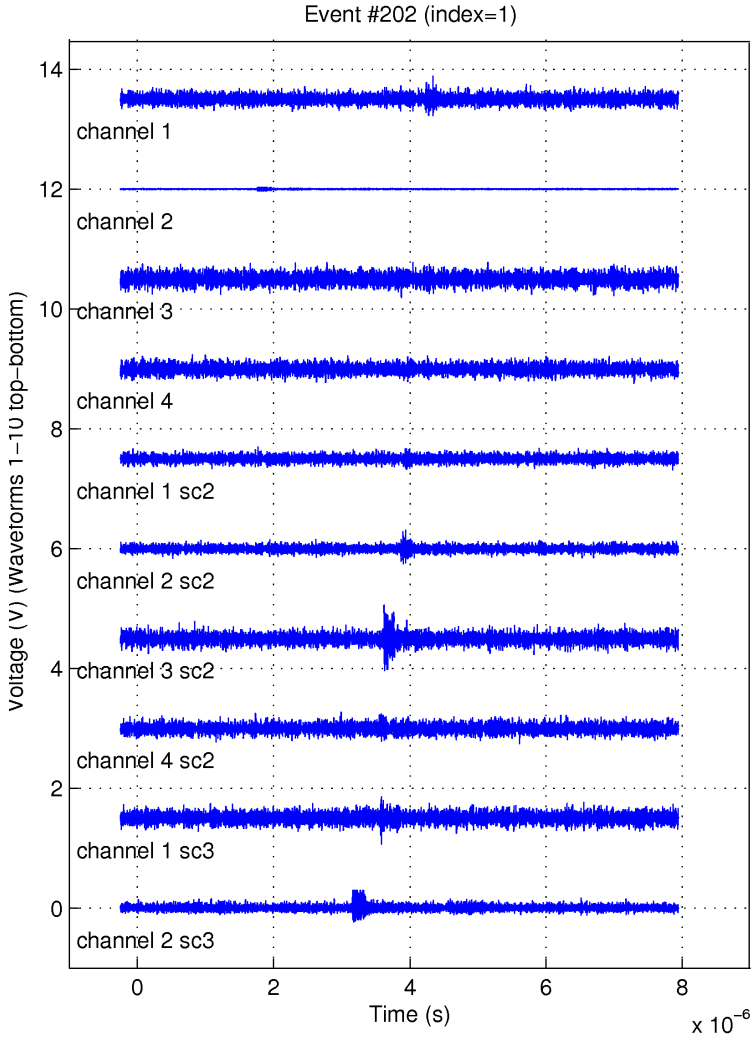

Figure 4.5: A typical singular peaked surface generated signal in channels 1 to 10 of the RICE array.

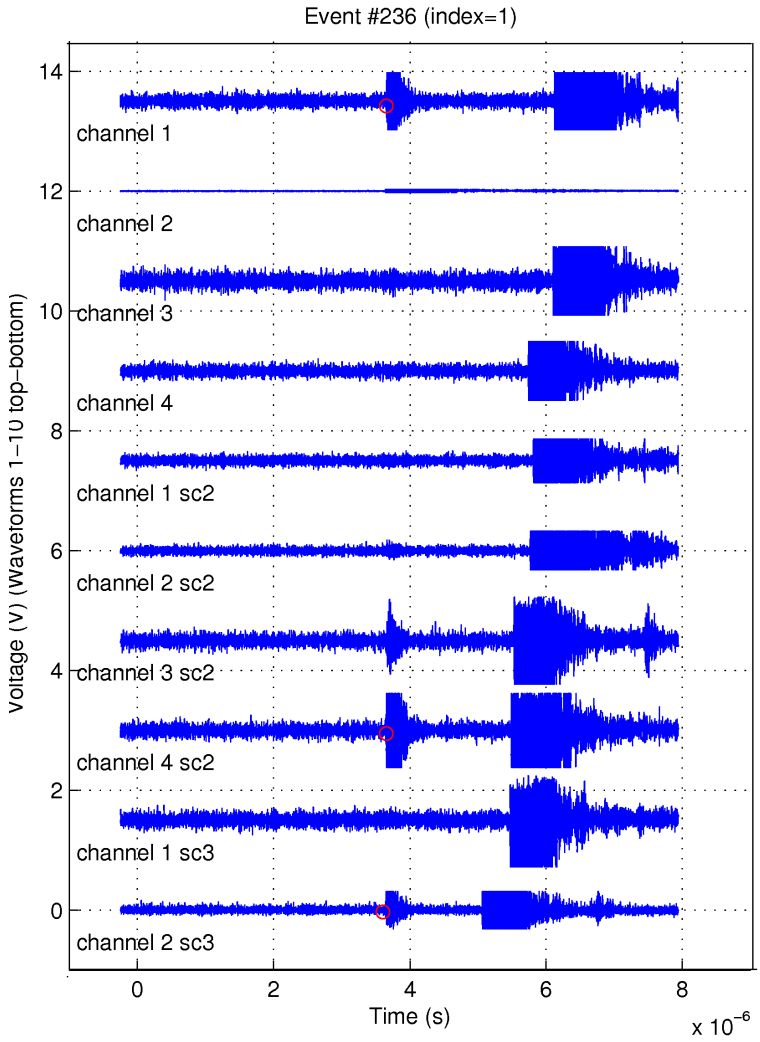

Figure 4.6: A typical multiply peaked surface generated signal in channels 1 to 10 of the RICE array.

In the analysis presented in this thesis we use an inspection method for determining the hit times. This is possible for the GRB coincident data due to the reduction in data size through the selection of events in time windows around GRB detection times. This method is described in Chapter 6.

Using these various timing techniques one hopes to accurately reconstruct the vertex of the signal. This allows separation of surface generated noise from valid neutrino events and would be used in the direction reconstruction of any neutrino events observed. In order to do this the RICE group have developed various vertex reconstruction algorithms.

4.5.2 Event Reconstruction

Reconstruction of an event and its source is based on knowing the antenna array geometry and ice properties. Using the timing which one expects an electromagnetic signal to propagate through the ice and hit each antenna, the events can be reconstructed and the most likely source location and direction can be identified by performing a χ^2 minimisation analysis. The grid based procedure attempts to locate the most optimal location of the vertex by testing each possible co-ordinate position (x, y, z) in a 1 km $\times$ 1 km $\times$ 1 km cube. This is done by calculating times for a signal originating from each possible cube to reach the antenna and comparing them to the measured times off the voltage signal waveforms. The cubes or steps from point to point have a resolution size of 8 m, testing a total of just under 2×10^8 possible co-ordinate points. The optimal vertex is then chosen using a χ^2 analysis comparing calculated times to antennas for the tested vertex to actual times measured. The smallest time difference corresponds to the optimal vertex. This algorithm is advantageous with its easy implementation of a varying refractive index within the ice. However, it is disadvantaged by its slowness and its resolution dependence. Reduction of the resolution to 1 m will increase the number of points to be tested to 1×10^9 slowing the reconstruction algorithm [153]. The analytic method attempts to solve

4 simultaneous equations to obtain the source location. Using equations of the form $|r_{Rx,i} - r_{source}| = (c/n)t_i (i = 1, 2, 3, 4)$, where $r_{Rx,i}$ is the vector from the origin to the ith receiver; t_i the time of the hit at that receiver; c represents the speed of light; and n the refractive index. The solution at most has two roots, with any solutions that are complex or violating causality being eliminated. The disadvantage of this method is that it does not incorporate a varying refractive index and uses a constant value [153]. These two methods have been compared with that of surveyed vertex locations from a transmitter. The results indicate that these two methods are consistent [153, 152].

4.5.3 Dielectric Constant in Ice

In order to calculate the vertex accurately the index of refraction and its dependence must be known. Thus far the most accurate index of refraction has been calculated using the dielectric constant, $\eta(\omega)$, which contains both absorptive and refractive properties of the ice within its complex and real components respectively. Using this the index of refraction dependence on depth in polar ice has been determined by combining temperature and density profiles as a function of depth by the AMANDA group. Experimental trials within the RICE array using transmitter and receiver locations in combination with Fermat's principle has fine tuned a $n(z)$ profile most agreeable with the RICE experimental results. The most recent profile is shown in Figure 4.7 in which the first 150 m down shows a strong dependence on refractive index with depth with an asymptotic trend to $n = 1.8$ below 150 m. Attenuation of the radio signal in the ice has also been investigated as a function of density, frequency and temperature. This was found to be insignificant for the size of the RICE array.

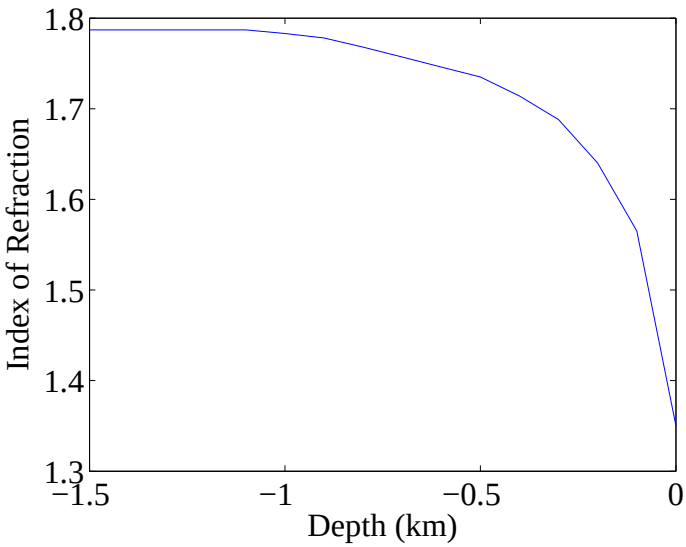

Figure 4.7: The refractive index of polar ice as a function of depth used in Monte Carlo simulations and vertex reconstruction.

4.5.4 Event Reconstruction Efficiency η

The efficiency, η, is determined by embedding simulated neutrino induced collision events into unbiased data. These events are analysed as real data using the same timing determination, event reconstruction and cut procedure. The proportion of events remaining divided by the total number of embedded events gives the efficiency.

4.5.5 Livetime

The livetime is calculated online from measurements of the deadtime incurred per surface veto and also the deadtime incurred per recorded event. Additional deadtime is incurred by the CW South Pole Station activity (303 MHZ satellite uplink), as well as the time between the end of one RICE data-taking run and the beginning

of the next during the winter months when the experiment is often not continuously accessible. We estimate uncertainties in deadtime to be less than 5%.

4.6 Discriminator Threshold

The array automatically sets the discriminator setting to remove the bulk of the noise originating from anthropogenic events. However, the higher the threshold the smaller the effective volume. This is shown later in Figure 4.9.

4.6.1 Monte Carlo Simulation and the Effective Volume

A sophisticated Monte Carlo code is used to model the effectiveness of the RICE array. The code models 60,000 neutrino induced showers in a predefined volume[2]. These showers are generated randomly from all directions (4π steradian), simulating showers induced by the neutrinos, their propagation, and their detection in the ice. Neutrinos passing through the Earth are attenuated more than those which originate from above the horizon. The standard output is available with effective volume at different energies at varying discriminator thresholds for each multiplicity[3]. The latest Monte Carlo code yields a much reduced effective volume [152] than earlier publications [160, 161]. A more accurate description of radio wave transmission using correct ray tracing from the shower to the receiver has been implemented, replacing earlier techniques. Prior to ray tracing direct-line tracing was used. Also included now are more accurate parameterisations of the antenna response (effective height), the ice temperature profiles and the radio frequency dielectric constant. DAQ hardware

[2]A test volume which is much larger than the expected range for signal detection

[3]The multiplicity refers to the number of antenna needing to be hit in order to register as a trigger. A multiplicity of 4 is needed for a vertex reconstruction.

parameterisations have also been improved. The effective volume of the array for shower detection is defined as:

$$V_{eff}(E_s) = \frac{1}{2\pi\tau} \int \eta(E_s, \overrightarrow{r}, \hat{n}, t) d\overrightarrow{r}\, d\Omega dt, \tag{4.1}$$

where $\epsilon(E_s, \overrightarrow{r}, \widehat{n}, t)$ is the efficiency of the array to detect an electromagnetic shower of energy, E_s, at some position, $\overrightarrow{r}$, and direction $\widehat{n}$. In the diffuse case it is normalised either by 4π or 2π to account for the solid angle, and τ, the exposure time of the detector.

The effective volumes used in this thesis were obtained using the earlier version of the Monte Carlo code. The complexity of the more recent Monte Carlo code means long processing times, thus a more up to date calculation using the latest generation code was not possible due to time restrictions. To take into account the reduction in volume obtained from the most recent Monte Carlo code I normalised the generation 1 effective volume code output by the ratio of the diffuse effective volume estimates to the current generation output. This introduced an energy dependant normalisation which was multiplied through all effective volumes presented here.

The diffuse effective volume is shown here for a fixed value of the voltage threshold of the receivers. The Monte Carlo for this effective volume calculation has been set to produce showers from neutrinos which come in from 2π steradian. This is to give the average effective volume to all sources which are homogeneously/isotropically distributed in the sky. Figure 4.8 shows the effective volume as a function of energy

for 3 cases: 1) No ray tracing and no Landau Pomeranchuck Migdal effect (LPM) effect; 2) LPM effects but no ray tracing; and 3) Ray tracing and LPM effects included. As discussed in [152] the effective volume is significantly reduced by the inclusion of LPM and ray tracing.

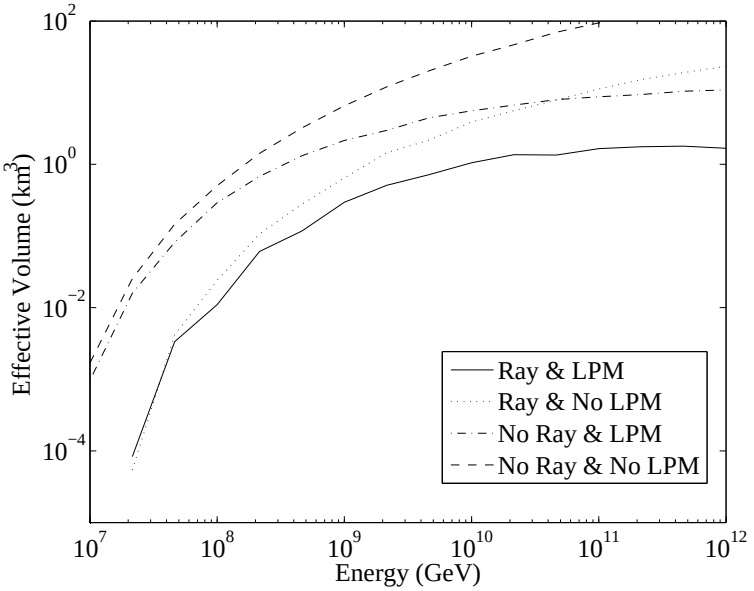

Figure 4.8: The effective volume as a function of energy with and without LPM and ray tracing effects.

Events will not be observed if they are downward events generated below the array as the Cherenkov cone cannot intersect the detectors. At short distances the efficiency is dominated by the width of the cone, whereas at long distances the efficiency is limited by attenuation effects. The efficiency is mostly in the top 1 km of ice [160, 152].

The effective volume depends on the energy of the shower/neutrino, multiplicity settings, threshold setting and the shower energy. Figure 4.9 shows the effective

volume as a function of discriminator setting and energy, showing the reduction of the effective volume as the discriminator threshold increases negatively. Threshold settings are determined by the array automatically to minimise the amount of anthropogenic signals detected. Unfortunately this results in a small detector volume.

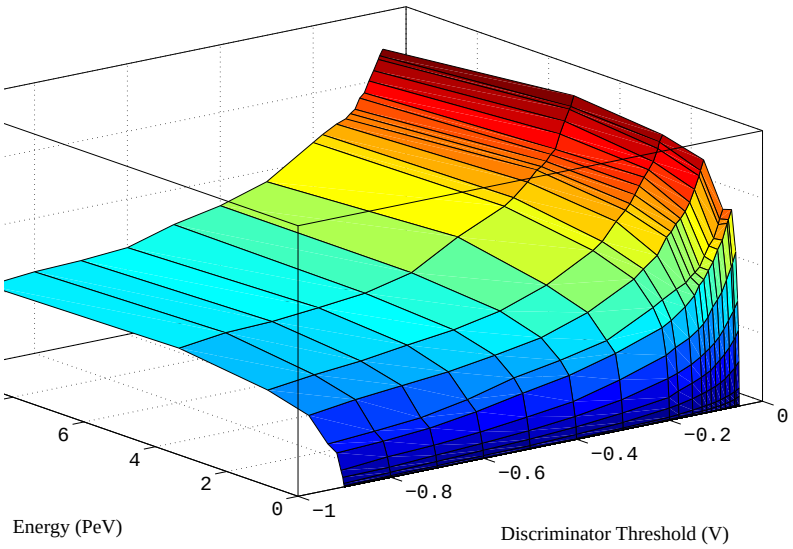

Figure 4.9: The effective volume as a function of detector discriminator threshold.

4.7 Systematic Uncertainties

The event finding efficiency is a combination of the online software veto (ϵ_{online}) and the offline software veto (0.67). Other systematic uncertainties have been investigated, these include:

- Hit recognition.
- Event reconstruction.

- Ray tracing effects.
- Attenuation length.
- Transfer function.
- Total gain.
- Birefringence.
- Monte Carlo associated uncertainties.

The first systematic uncertainty results from inaccurate determination of when an antenna is hit. This can lead to an incorrectly reconstructed vertex causing the events to fail the vertex and time residual requirements. It can be difficult to assess the actual beginning of a signal. Several types of hit definitions are used and have been compared. These are: the maximum voltage in the waveform; the first excursion above 6σ; and the time that gives the best match to one of the four matched filters. The default option is the 6σ but all methods yield similar results. Once the hit times are obtained a vertex can be constructed as described in Section 4.5.2. Vertex reconstruction is found to work well in-ice and close to the array. Later in Chapter 6 we describe a more interactive method for which the hit times are determined visually. An overall reconstruction efficiency uncertainty is estimated to be around 20%.

As seen in Figure 4.7, the refractive index varies significantly in the top 100 m of the ice called the firn. Since many of the RICE receivers are located in this region, radio wavefronts will curve instead of following straight line trajectories. This can cause the Cherenkov radiation, incident at near horizontal and slightly below $\theta \approx \pi/2$,

to bend missing the antennae located in the shadow zone. This causes a reduction in the effective volume. This is shown in Figure 4.10 where ray 1 which is initially on an intersecting course with an antenna is deflected away. Another effect is due to the curvature of the firn, a direct ray which hits the antenna may also have another hit from an indirect signal. This is seen in Figure 4.10, with ray 2 deflecting back into the volume and intersecting with the antenna. The most recent Monte Carlo simulations include ray tracing effects, which yield a much reduced effective volume from that of previous publications [160]. However ray tracing effects were found to have little effect on systematic uncertainties.

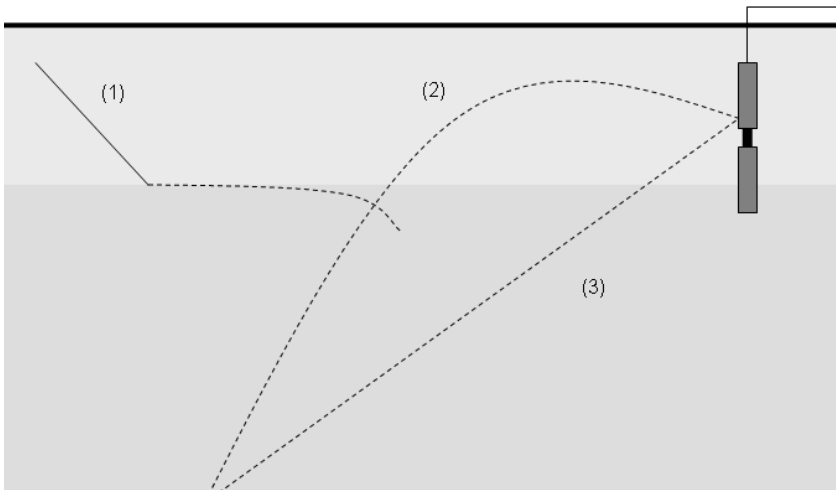

Figure 4.10: Ray tracing effects due to the changing refractive index in the top 100m of the ice(firn). Ray 1 originally going to intersect an antenna is deflected away. A direct signal hits an antenna with Ray 3, but is hit by another signal(Ray2) which deflects back into the volume.

An estimated 5% uncertainty is estimated in the deadtime incurred in events. The effect of the antenna gain on the uncertainties has also been investigated. Monte

Carlo simulations have been run to estimate the effect of changes in the gain. For large neutrino energies the effective volume resulted in variations of the order of 20%. Attenuation lengths also have an uncertainty associated with it. These become more significant with energy. The resultant uncertainty this makes in the effective volume is folded into the overall systematic uncertainty [152].

Other uncertainties arise in the transfer function of different dipoles (around $5-10\%$ variation between dipoles). Variations in the transfer function from air to ice will also incur uncertainties. Birefringence has also been considered, however no evidence suggests this to have any effect.

Systematic errors are not explicitly included in the upper limits calculations. It should be noted that large uncertainties are incurred by the effective volume/sensitivity and that these should be taken into consideration upon interpretation of upper limits results.

March 4, 2009©

Chapter 5

Monte Carlo Simulation

The angular dependence of the effective volume is due primarily to the attenuation effects of the Earth. Recent results [152] have shown that a much reduced effective volume is found when ray tracing effects are included in the calculations compared to previously published results [160]. Results presented here represent an earlier study prior to the implementation of ray tracing but inclusive of attenuation and LPM effects. A normalisation was applied to the effective volumes throughout these calculations as described in section 4.6.1. Future papers will include effective volumes using the latest Monte Carlo simulations.

We begin in Section 5.1 with a discussion on the attenuation effects of the Earth on the neutrino flux. Section 5.2 presents the results of the angular dependence study for the effective volume. In Section 5.3 I discuss the transforms required to convert GRB localisations to RICE co-ordinates for the determination of individual effective volumes.

5.1 Earth Properties

An incoming neutrino flux will be attenuated by the Earth as it traverses through the different layers such that $\Phi_f(E,\phi) = \kappa(\phi)\Phi_i(E)$, where Φ_i and Φ_f are the initial and final neutrino fluxes respectively and $\kappa(\Phi)$ is the attenuation coefficient. The attenuation is dependant on the density and composition of the different layers of the Earth. These are well described by the Earth composition Preliminary Reference Earth Model (PREM) [162], which describes ten density regions of the Earth as a function of radial distance and is shown in Figure 5.1. The rapid drop in density is the transition between the core and the lower mantle. However, other layers are not so definitely resolved [163].

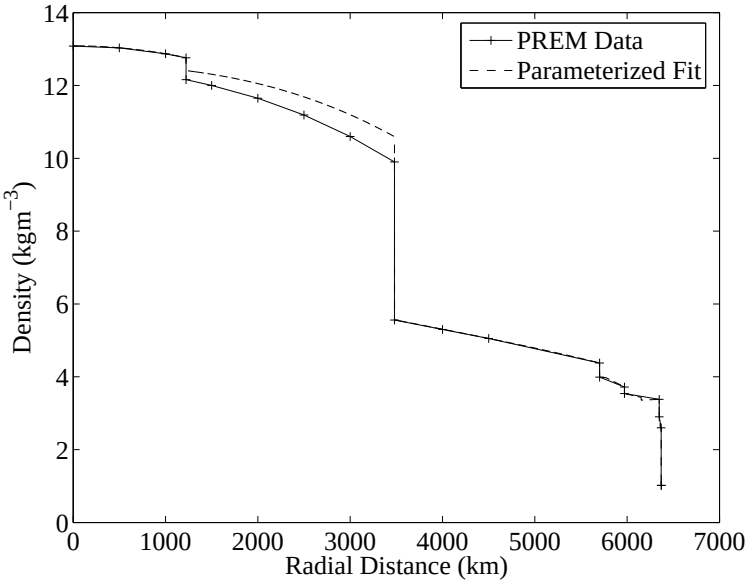

Figure 5.1: The density dependence on the radial distance of the Earth using the Preliminary Earth Model (PREM) [162] compared to the parameterised fit used in the RICE analysis.

The attenuation coefficient is described by:

$$\kappa = \exp(-\sigma_{eff}(E_\nu, \gamma)\frac{t(\phi)}{m_N}) \,, \tag{5.1}$$

where $t(\phi)$ is the column depth; m_N, the nucleon mass; γ, the spectral index of a flux model; and σ_{eff}, the effective cross-section.

The effective cross-section, $\sigma_{eff}^{\nu N}$, is given by the sum of the charged and neutral current contributions evaluated at E_ν minus a correction term given by the relation:

$$-\sigma_{eff}^{\nu N}(E_\nu) = -\sigma_{CC}^{\nu N}(E_\nu) - \sigma_{NC}^{\nu N}(E_\nu) + \sigma_{corr}^{\nu N}(E_\nu), \tag{5.2}$$

where

$$\sigma_{corr}^{\nu N}(E_\nu) = \int_{E_\nu}^{\infty} dE'_\nu \frac{\phi(E'_\nu)}{\phi(E_\nu)} \frac{d\sigma_{NC}^{\nu N}}{dE_\nu}(E'_\nu, E_\nu) \,. \tag{5.3}$$

These describe the dependence of the correction term on the number of neutrinos available at energies larger than E_ν, and the dependence of the effective cross-section on the flux.

The column depth can be calculated by integrating the nucleon density along the path, l. The path is obtained by relating the entrance angle to the radius. Figure 5.2 shows the column depth as a function of nadir angle [164]. For a typical GRB neutrino flux (see Figure 5.3) the attenuated flux at different energies as a function of nadir angle is shown in Figure 5.4. The lowest energies start at the highest curve, with $E_\nu = 10^{14}$ eV, and increase in energy in powers of ten for the lower curves. We see, as expected, little effect at $E_\nu = 10^{14}$ eV and $E_\nu = 10^{15}$ eV. At around $E_\nu = 10^{16}$ eV we see a decrease starting to occur with a factor of 10 reduction in the flux by $\theta_{Nadir} = 60°$

and a more dramatic drop with increasing energy. This is indicative of the increase in neutrino cross-section with increasing energy.

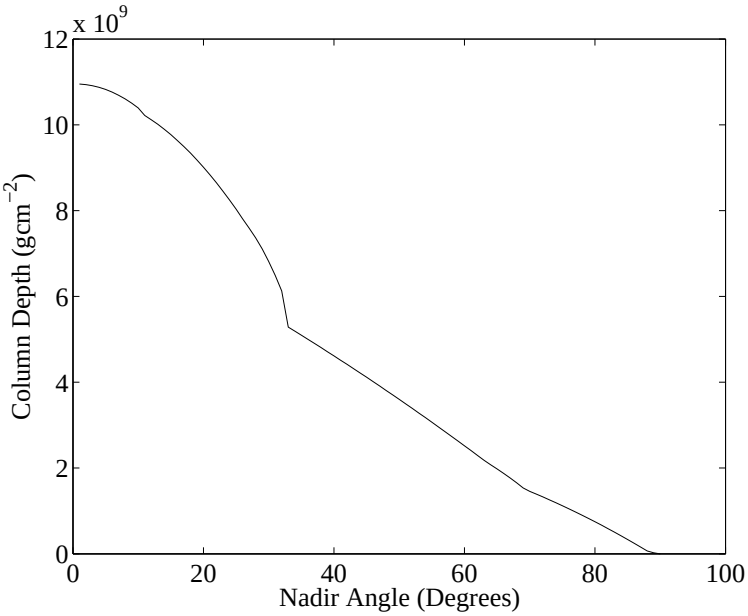

Figure 5.2: The Earth column depth dependance on the nadir angle, θ_{Nadir}, at the South Pole [164].

5.2 Effective Volume Angular Dependence

The angular dependence of the effective volume is particularly important in order to see how the RICE array is sensitive to incoming neutrinos from particular point sources. We saw in the previous section how the neutrino flux is attenuated as a function of nadir angle. In this section we discuss the attenuation effects and the

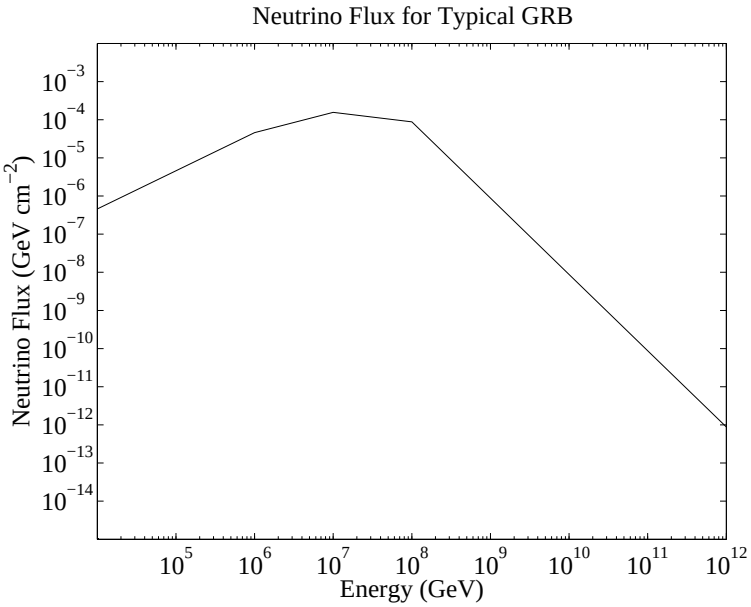

Figure 5.3: A typical GRB neutrino flux.

angular dependence of the effective volume on the nadir angle, θ_{Nadir}, and the azimuthal angle, $\phi_{Azimuth}$, (relative to the RICE co-ordinate system). The angular distribution of shower angle generation was restricted to specific directions. Due to the long processing time of these Monte Carlo simulations the bins were restricted to 30° by 30°, ranging from 0° to 180° in θ_{Nadir} and 0° to 360° in $\phi_{Azimuth}$. The effective volumes were calculated for each bin in the energy range 1 PeV to 10^6 PeV. Figure 5.5 shows the effective volume as a function of nadir angle, θ_{Nadir}, and azimuthal angle, $\phi_{Azimuth}$. The discriminator threshold is set at -0.015 V[1] with an antenna hit multiplicity condition of four [2] and inclusive of the Landau Pomeranchuck Migdal

[1]The discriminator value of -0.015 V corresponds to the settings used as in previous RICE publications, for August, 2000 results [160]

[2]Multiplicity refers to the minimum number of antenna needing to be triggered from the shower.

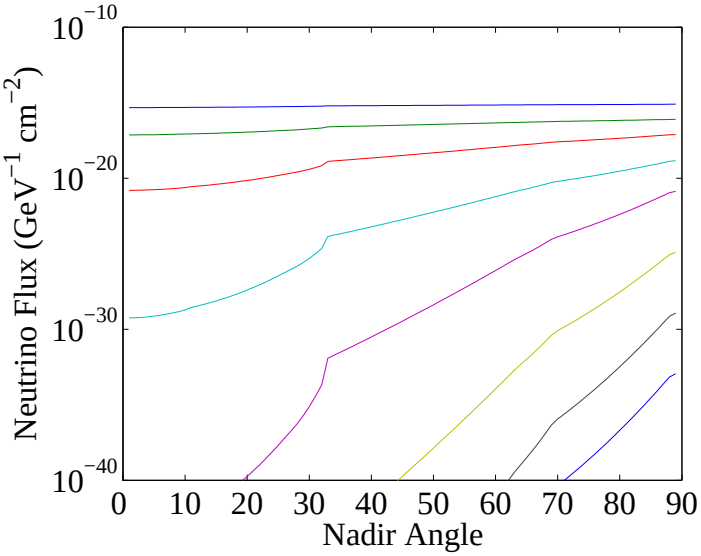

Figure 5.4: The attenuated GRB neutrino flux at different energies as a function of nadir angle, with lowest energies starting at the highest curve ($E_\nu = 10^{14}$ eV) and an increase in energy in powers of ten for the lower curves to $E_\nu = 10^{21}$ eV.

effect (LPM)[165]. This models showers from some angle θ_{Nadir} and $\phi_{Azimuth}$, which corresponds to the incoming angles of the neutrinos. Although we expect the nadir angle to have a significant effect on the effective volume, we also show here the effect of azimuthal angle, which only seems to be significant at lower energies. However, this may be a statistical artifact. The results are consistent with attenuation effects yielding a down turn in the effective volume with higher energies as neutrinos propagate through more planetary layers. RICE is least sensitive to neutrinos originating directly above the array. This is due to the lack on vertical distribution of the receivers. RICE's maximum sensitivity is for signal traversing horizontally through the array as more receivers will be in the direct path. The peaks observed at $\theta_{Nadir} \approx 150°$

and 30° correspond to the shower directions for which the Cherenkov cone, which will be at 57° to the shower direction, will be passing optimally through the array horizontally through the ice. The lower peak positioned at, $\theta_{Nadir} \approx 30°$ is reduced in magnitude due to attenuation effects of the Earth. As the energy increases the attenuation increases until only one peak is prominent at $\theta_{Nadir} = 150°$. However, the overall effective volume increases with energy, as expected. An effective volume of 1 km^3 is reached at 4641 PeV at $\theta_{Nadir} = 150°$ across all values of $\phi_{Azimuth}$.

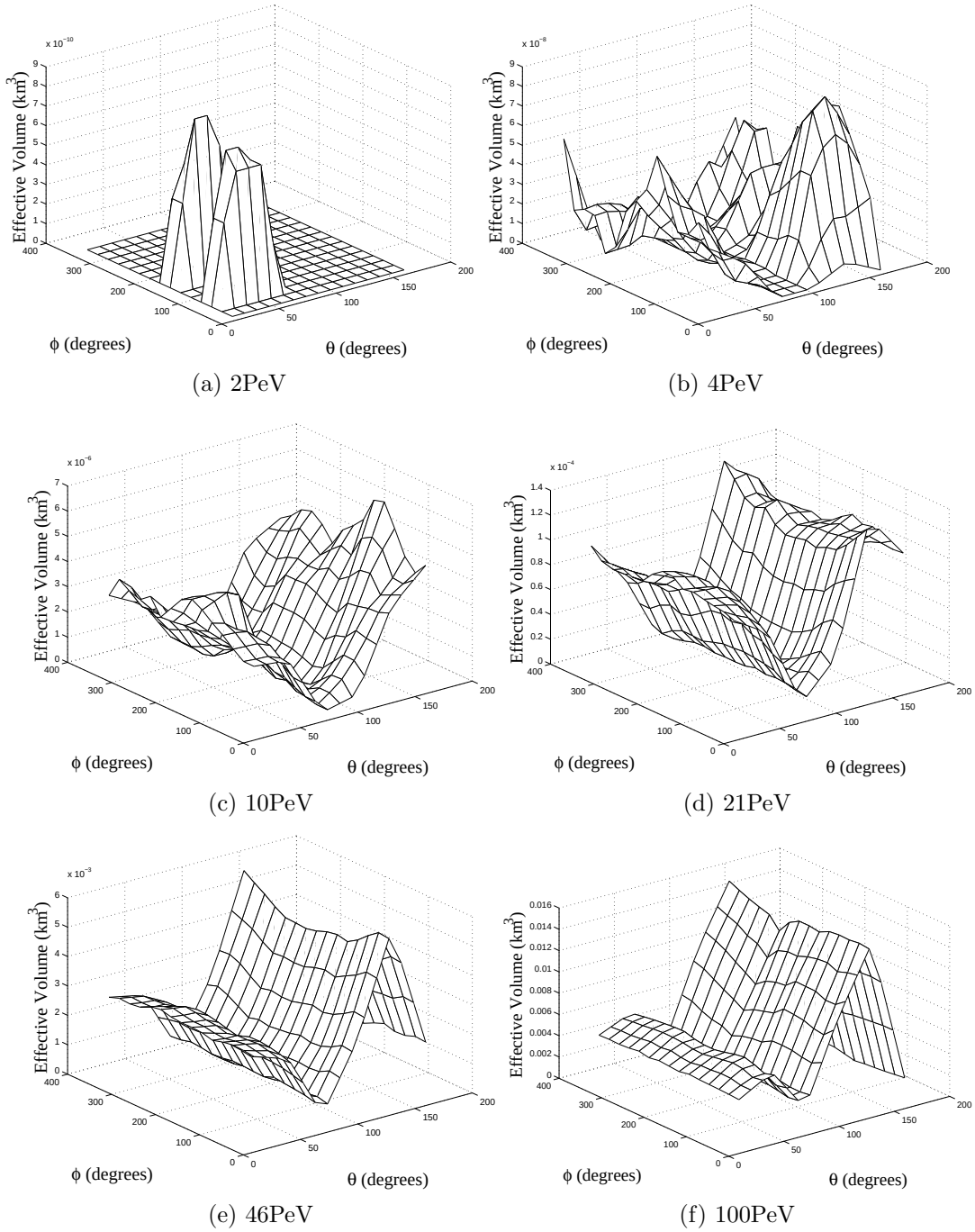

(a) 2PeV (b) 4PeV

(c) 10PeV (d) 21PeV

(e) 46PeV (f) 100PeV

Figure 5.5: The effective volume for RICE (2003 configuration) for specified energies of 2 PeV to 100 PeV as a function of shower direction in θ_{Nadir} and $\phi_{Azimuth}$.

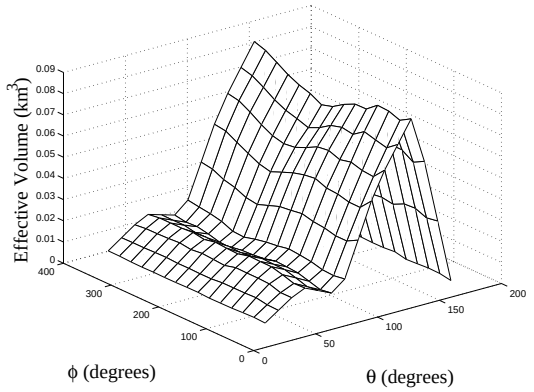

(g) 215PeV

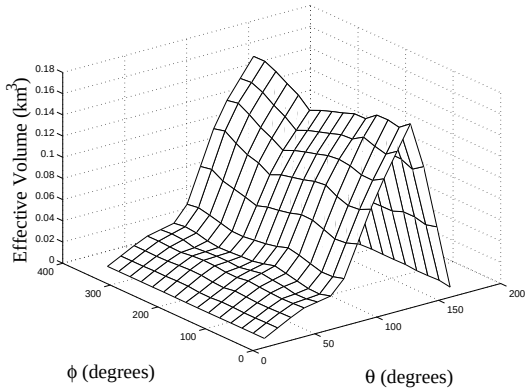

(h) 464PeV

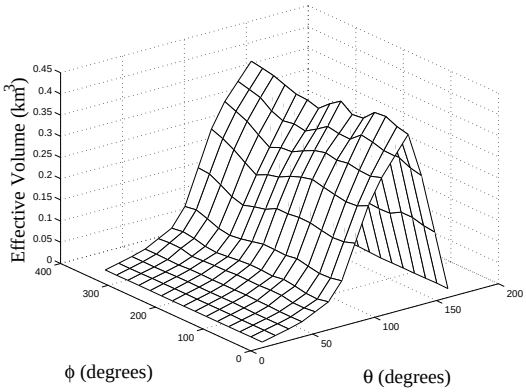

(i) 1000PeV

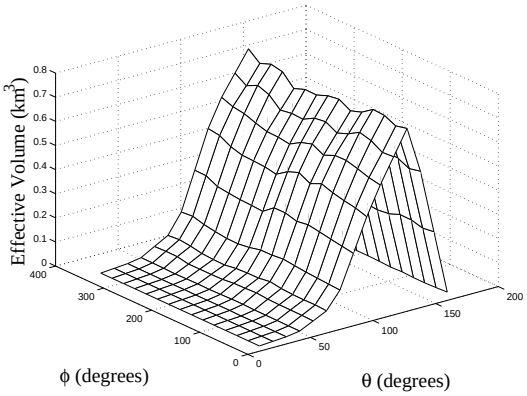

(j) 2154PeV

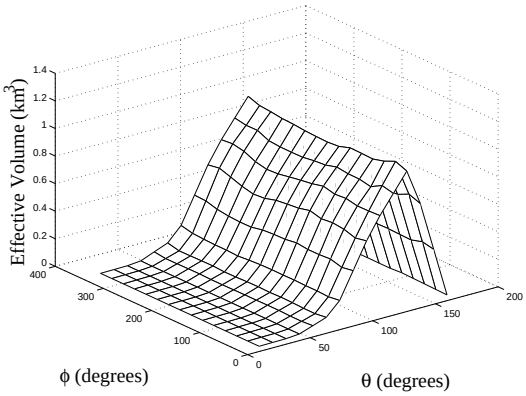

(k) 4641PeV

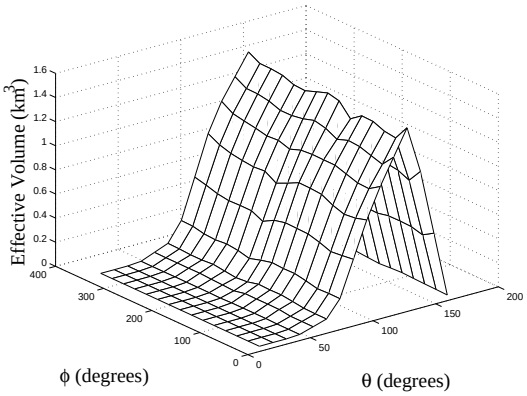

(l) 10000PeV

Figure 5.5: cont... The effective volume for RICE (2003 configuration) for specified energies of 215 PeV to 10^4 PeV as a function of shower direction in θ_{Nadir} and $\phi_{Azimuth}$.

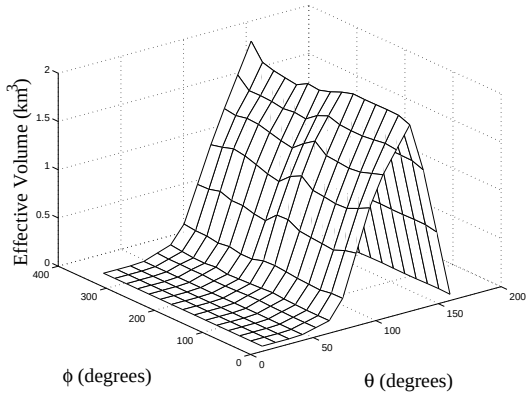

(m) 21544PeV

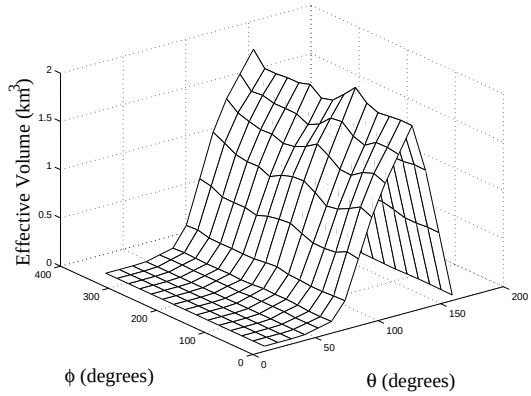

(n) 46415PeV

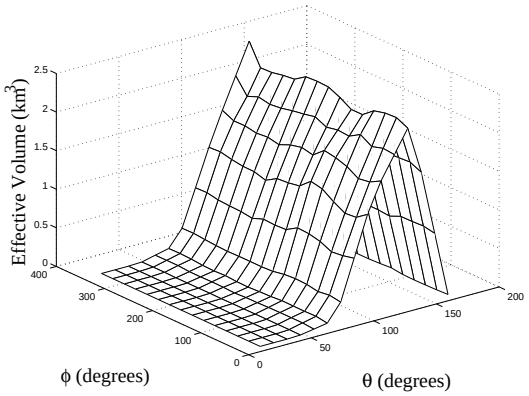

(o) 100000PeV

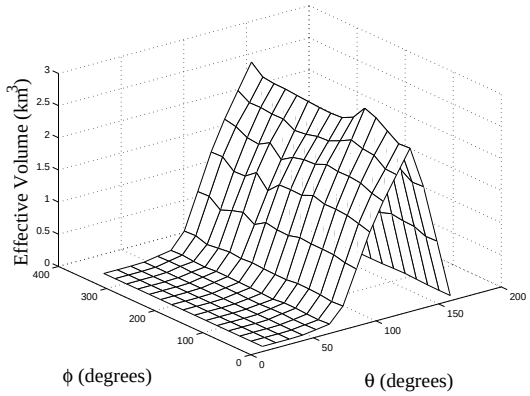

(p) 215443PeV

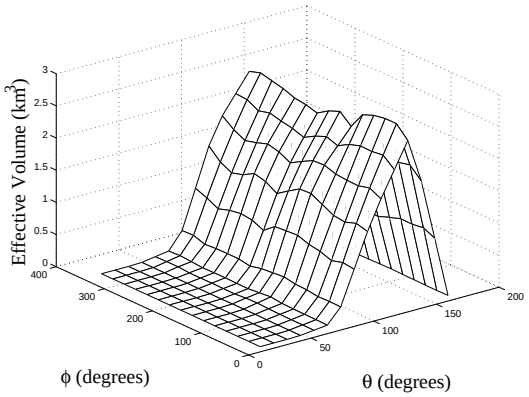

(q) 464159PeV

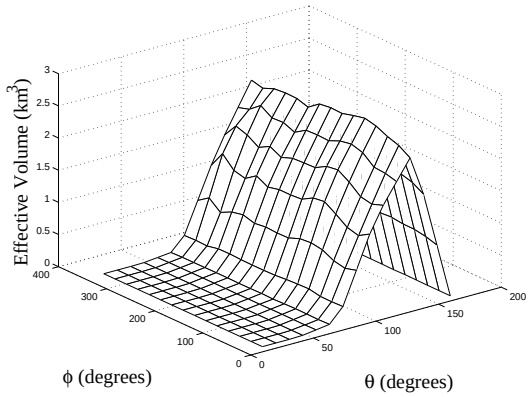

(r) 1000000PeV

Figure 5.5: cont... The effective volume for RICE (2003 configuration) for specified energies of 21544 PeV to 10^6 PeV as a function of shower direction in θ_{Nadir} and $\phi_{Azimuth}$.

Due to the strong dependence of the effective volume on nadir angle it is important to take the appropriate effective volume into account in the calculation of limits of fluxes from particular GRBs. We ran GRB specific Monte Carlo effective volume simulations for all the GRBs in our sample. In each simulation the incident neutrino direction was restricted to be in a 5° by 5° solid angle centered on the GRB coordinates. Thus we estimated the average effective volume appropriate for neutrinos originating from each GRB.

5.3 GRB Localisation Coordinate Transform

The effective volumes for individual GRBs were calculated as in Section 5.2. GRB localisations that were given in equatorial co-ordinates, right ascension (RA) and declination (Dec), were converted to horizon co-ordinates via the transform:

$$A = \arccos \frac{\sin(\delta) - \sin(\phi)\sin(a)}{\cos(\phi)\cos(a)}, \tag{5.4}$$

where:

$$a = \arcsin(\sin(\delta)\sin(\phi) + \cos(\delta)\cos(\phi)\cos(H)), \tag{5.5}$$

A is the azimuth; a is the altitude; δ is the declination; α is the right ascension; and ϕ is the geographical latitude. The hour angle (H) is related to the local sidereal time (LST) and the right ascension by $H = LST - \alpha$.

Geographically RICE is located 800 m along the 315° meridian. Using a Geodetic model the latitude of RICE is given as 89.928°. Therefore the longitude and latitude are:

$$\text{Longitude} = 315^\circ \tag{5.6}$$

$$\text{Latitude} = 89.93^\circ \tag{5.7}$$

Converting from horizon co-ordinates to the local co-ordinates of RICE, whereby the y axis is defined as the grid north position at the co-ordinates (89.93°,315°), the RICE azimuthal angle, $\phi_{Azimuth}$, is simply given as:

$$135^\circ - A = \phi_{Azimuth} \tag{5.8}$$

The conversion from the altitude to θ_{Nadir} only needs a 90° shift giving the relationship:

$$\theta_{Nadir} = 90^\circ + a \tag{5.9}$$

Using these transformations we are able to calculate the GRB angles relative to RICE for each individual point source GRB. The shower angle was restricted to the GRB angle relative to RICE in the effective volume Monte Carlo.

March 4, 2009©

Chapter 6

GRB Neutrino Search with RICE

This thesis aimed to detect neutrinos from GRBs. RICE data was searched for any signal and as a result limits on the number of neutrinos from individual sources could be set. The GRB events which were selected are discussed in Section 6.1 and the RICE data in the period examined is described in Section 6.2. The standard RICE analysis had already examined the RICE data including the times when GRBs were detected. In this chapter I present an independent analysis using a refined method which has a greater efficiency (success) for identifying neutrino induced signals. However, this method relies on a more interactive approach, involving by eye pulse time identification instead of other currently used automated methods. As discussed in Chapter 4, pulse times are essential for reconstructing reliable vertex solutions of signal sources and the vertex position is used as one of the main cuts in the RICE analysis process. In Section 6.3 I describe the method and results of this modified analysis method. The various pulse timing techniques and their effect on vertex reconstruction is compared. I also describe the time over threshold (ToT) and Cherenkov cuts implemented. We finish in Section 6.4 with the results of the efficiency analysis, which was described in the previous chapter.

6.1 GRB Data Set

GRB times were obtained from the master cosmic burst list provided by the Interplanetary Network (IPN)[166]. This list contains confirmed cosmic GRB events with corresponding dates, times and the names of satellites which observed the event. Using this information, RICE logs were searched for corresponding live operating periods. During the years of June 2001 to 2005, a total of 444 cosmic events were triggered during the operational time of RICE. From these, GRB data including localisations were sought in order to confirm if the event was indeed a GRB and if the GRB originated within the effective angular area in the sky sensitive to RICE, as discussed in Chapter 5. However, as discussed previously in Chapter 2, in the era predating SWIFT and post-dating BATSE, good localisations were difficult to obtain. In this era, accurate locations heavily relied on the combined observations of multiple members of the IPN, whereby a triangulation technique was used to determine the localisation. The best localisations using this technique involved widely spaced detectors. However, this was not a regular occurrence, hence accurately localised GRBs were scarce.

Accurate GRB localisations are particularly important for followup observations of GRB afterglows. These afterglow observations enable the determination of GRB redshifts. Although this study indirectly requires localizations for redshift information, we also require localizations for determining the sensitivity of the RICE array to the directions of each individual GRB. For these sensitivity estimations an accuracy requirement to within a few degrees is more than satisfactory. For GRBs with large

localization uncertainties, a sensitivity estimated for a region encompassing the uncertainty can be obtained, similar to a diffuse estimation. These estimations however, can incur large uncertainties in the sensitivity/effective volume estimations which will subsequently impinge on the limits calculation. In other coincidence searches an angular cut was made to determine whether neutrino events were from the same region of the sky as the GRB[3, 1, 2]. As will be described in Section 6.3.3, no neutrino events were left after basic data quality cuts were applied to the RICE data. Thus no directional cut was necessary.

The localisation criteria required that the GRB localization and its error had to be within the RICE sensitivity zone defined in Chapter 5. These results showed that the attenuation effects significantly reduced the neutrino flux, dropping rapidly at energies above 100PeV as the nadir angle goes below the horizon. We set a cut requiring that GRBs be able to be localised within the region of the sky starting at around 30° below the horizon ranging to directly above the detector at the zenith point. Over a 100 GRBs were identified as satisfying this condition. If the error was large, then an average effective volume for the localisation plus the error of the angular region was determined. If the localisation was small, typically less than 1 degree, then a 5 degree by 5 degree region around the localisation was used.

It was found that a handful occurred in a dead zone directly above the detector, whereby the effective volume was zero. This was attributed to the lack of vertical distribution of receivers in the detector. It was also found that some GRBs had no time duration or spectral data. However, 77 GRBs were found to satisfy the localisation criteria, whilst also having some spectral data and occurring during periods

when RICE was operating and live. For these 77 a number of catalogues and sources were used to obtain information as well as formal requests from other researchers. An online data base of the GCN [1] notices called GRBlog was used, Jochen Greiner's GRB webpage [167][2], the SWIFT [97][3], KONUS [168, 100][4], Integral [98] [5], HETE [169][6] and the IPN (Private Communication-K.Hurley) catalogues. GRB localisations were converted to RICE local co-ordinates as described in Chapter 4. Durations, fluences and some spectral data were obtained from these sources which are shown in Chapter 7 and in Appendices A through D.

6.2 RICE Data Set

The total RICE data set for the years 2001 to 2005 is described in Chapter 4, Table 4.2. Over half a million triggers were recorded during this time. Of these triggers data occurring during a ±600s coincidence with the selected 77 GRB times were extracted and analyzed using a modified method to that of the general RICE analysis. This small subset of triggers which occurred during well localized GRB triggers totalled 965. These are summarised in Table 6.1.

Table 6.1 row one summarises the total number of GRBs for each year. The next row gives the total time that was searched for signals in the RICE data. The third row is the total time that was actually live within each year (Total time searched×live-fraction). The remaining rows are the number of triggers occurring by type of trigger as discussed in Chapter 4. As can be seen, 2004, no data triggers occurred during the

[1] Global Circular Network: http://gcn.gsfc.nasa.gov
[2] http://www.mpe.mpg.de/ ∼jcg/grbgen.html
[3] http://swift.gsfc.nasa.gov/docs/swift/archive/grb_table/.
[4] http://www.ioffe.ru/LEA/shortGRBs/Catalog/.
[5] http://mpe.mpg.de/gamma/science/grb/1ACSburst/fullCat_main.html
[6] http://space.mit.edu/HETE/Bursts/Data/

Table 6.1: RICE-II Data summary for GRB windowed data during 2001 through to 2005.

	2001	2002	2003	2004	2005	Total
Total GRBs	2	8	36	0	31	77
Total GRB Window Time (10^2s)	24	96	432	0	372	924
Total Live Time (10^2s)	17.3	73.2	374	0.0	314	778.5
$\geq$4-hit General Trigger	55	140	134	-	399	728
Unbiased Trig.	8	36	90	-	81	215
AMANDA-coincident Trig.	6	-	-	-	-	6
SPASE-coincident Trig.	-	9	1	-	-	10
Veto Trig.	-	5	1	-	-	6
Total Trig.	69	190	226	-	480	965

GRB time windows. This is attributed to a low run time for that year and also the unfortunate loss of some of the RICE data.

6.3 Analysis Method and Results

As outlined in chapter 4, the analysis technique uses various hardware, online and off-line vetoes and cuts to distinguish neutrino events from background signals. The standard analysis technique implemented on theoretically produced data yields an efficiency of $\approx 67\%$. On going improvements have been applied to increase this efficiency. The technique used here is an independent analysis regime which yields a greater efficiency of $\approx 81\%$. The technique utilises some parts of the analysis code used in the general method. The most significant difference is in determining the pulse timing. These pulse timings are used to determine the vertex solution of the signal source and therefore determine whether the signal was anthropogenically produced or produced by an in ice shower. The accurate and consistent identification of pulse times is problematic. Pulse shape variations, saturations and thermal backgrounds

make it difficult to accurately identify pulse times consistently. Earlier studies have found that inaccurate timings can skew the vertex reconstruction significantly. The general analysis technique attempts various different timing methods along with time residual conditions and other requirements to eliminate a signal. The ongoing process to improve the accurate time pulse identification is seen as extremely important as accurate vertex reconstruction are one of the simplest forms of anthropogenic background removal.

6.3.1 The Neutrino Signal

The pioneering Monte Carlo simulation to model the expected radio pulse from a neutrino induced electromagnetic shower was done by Zas, Halzen and Stanev [170]. Later investigations were undertaken using GEANT simulations by Razzaque, Seunarine, McKay and Besson[75]. Both simulations modelled the cascade which developed in a the semi-infinite medium of ice, calculating the number of atomic electron swept into the shower. As previously discussed a shower front develops with a net negative charge. Using this one can predict the expected Cherenkov electric field strength at some point ($\vec{R}$), by summing the Cherenkov electric field vectors, $\vec{E}(\vec{R},\omega)$ for each participating particle in the shower. Both groups yielded similar results with a Cherenkov signal at long distances producing a symmetric pulse at the antenna, approximately 1-2ns wide in the time domain. The resultant power spectrum as a function of frequency rises linearly with frequency. This is to be expected in the long-wavelength limit, where the net charge in the shower front will act as a singular point charge, emitting Cherenkov radiation with an energy per photon: $E = \hbar\omega$ ($E(\omega) \sim \omega$, and $dE/d\omega \sim const.$

In the perfect transmission case where by no cable losses occur, the signal induced on the Cherenkov cone due to a 1 PeV neutrino producing a shower at 1km, will produce a 2μV signal at the antenna. This is comparable to a thermally produced signal at 300K in the bandwidth of the antenna. The finite bandwidth of the antenna will produce a broadening in the time domain of the neutrino induced signal ($\Delta t \sim 1/B$, where B is the experiments bandwidth)[171]. The bandwidth arises from the finite limitations of the antenna response (800 MHz), cable losses as a function of frequency, whereby the high end of the frequency range are attenuated more than the lower. Also hard wired filtering to remove unwanted frequencies $<$ 200 MHz generated by background transmissions. The resultant signal is a pulse which has been stretched in the time domain to around 5ns. More recently the signal is thought to possibly be stretched wider.

The expected neutrino signal is estimated using a detailed Monte Carlo simulation of the RICE experiment. It is divided into four broad parts;

1. Neutrino flux and neutrino-nucleon cross sections modelling.
2. Electromagnetic/Hadronic shower and radio signal generation.
3. Radio signal propagation through ice and its resultant electric field vector $\vec{E}_i(t)$ at the i^{th} antenna
4. Response of the antenna and DAQ hardware of the input voltage, $V_i(t)$.

The Monte Carlo for which the results were presented in Chapter 5 has been improved to now include a fully complex transfer function instead of only the real components. This more accurately determines the signal at the input to the DAQ.

Hadronic showers are now incorporated compared to an estimation using the electromagnetic results. Geometric distortion of the Cherenkov cone due to variations of the index of refraction through the firn, are more accurately determined[160].

When the signal arrives at the DAQ, the Monte Carlo simulation transforms back to the time domain, where it determines its detectability against the discriminator settings of the antenna and checks for a 4-fold coincidence hit within the prescribed 1.2μs time window. Here is an earlier example of the expected voltage at the DAQ of a 10PeV cascade at a typical RICE receiver from different distances [160].

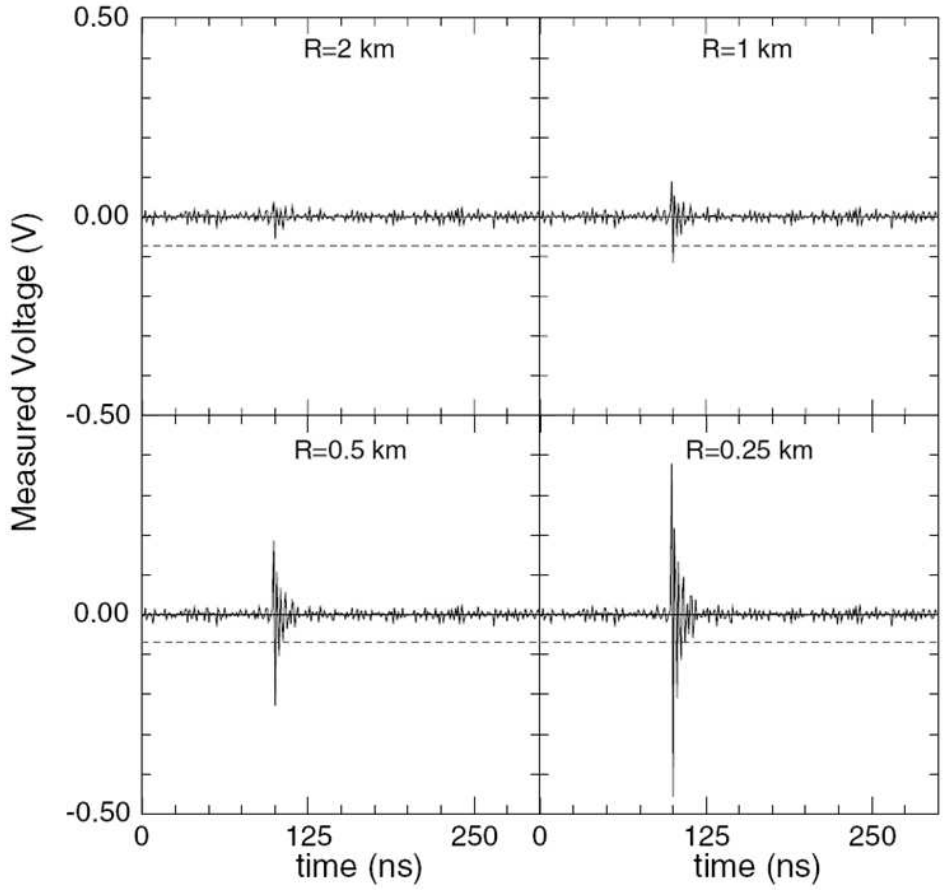

Figure 6.1: An earlier voltage as a function of time expected for a 10PeV cascade at varying distances from a typical RICE receiver. The receiver is oriented along the Cherenkov cone with its dipole axis aligned along the electric field. The dashed line represents the 5σ threshold [160].

6.3.2 Timing Determination Methods

The identification of a neutrino signal amongst the myriad of signals generated above the array is indeed a challenging process. Cuts can be designed to filter out the desired signals from the background events. With a five year period recording some

half a million triggers, the analysis requires automated elimination cuts as discussed in Chapter 4. As described in Section 4.5.2, one of the most definitive ways of determining a neutrino event from an anthropogenic event is via vertex reconstruction. This is where by the vertex is reconstructed using the timings of the signals arriving at each registered antenna. As previously discussed obtaining consistent and accurate timings can be problematic. Multiple peaked signals, thermal noise, and signal shape variation can all contribute to an inconsistent pulse time determination. The close spacing of the detectors in the array however, means that an accurate and consistent timing determination is essential for accurately reconstructing vertices.

Earlier studies in this research and from Baird [172] found that there were variations in determining pulse times, with times varying up to tens of nano seconds. With a data recording time resolution of 1 ns and receiver spatial separation of the order of tens of meters, it was found that small time inconsistencies could have a significant effect on the reconstruction of the source vertex, yielding skewed reconstructed vertices by hundreds of meters.

In the mainstream analysis the Maximum Voltage and Sigma routines have both been used in conjunction with other robust selection requirements to produce a reliable set of cuts. It was found in the previous studies that By-eye timing was far more reliable than these other methods. Although somewhat time consuming and tedious, it offers a more definitive time pulse determination than other techniques. For a small data set visual determination is realistic. In by-eye timing the events are visually inspected and the start of the pulse is estimated based on a consistent criteria.

We show in figures 6.2, 6.3 and 6.4 typical examples of an unbiased, multiple peaked and singular peaked triggers recorded by the RICE DAQ system for the 16 channel configuration of 2001. The mainstream analysis utilyses three methods to determine pulse times, other variations on pulse time determination are discussed elsewhere [172].

Maximum Voltage The time at which the peak voltage occurs in each channel from the start of the 8μs buffer.

Sigma(σ) Criterion First 6 σ excursion above the mean is used where $\sigma = V(t) - \bar{V}_{rms}/V_{s.d}$

TDC Harware Timing The Time-to-Digital-Conversion (TDC) time is the time at which the RICE hardware registers a hit on each detector. This occurs once a signal has exceeded some predetermined threshold which is set to avoid over triggering due to thermal fluctuations or other excessive backgrounds.

Maximum voltage and the Six sigma criterion are compared to By-eye in Figure 6.5. Voltage saturation is also seen here which is typical in many events. Saturation can lead to an incorrectly identified maximum voltage in the signal. The shapes of signals vary from channel to channel and event to event. Typical shapes are triangular shapes with a sharp leading edge and linear drop off toward the mean. Other shapes include eye shaped, hexagonal shape, usually caused by voltage saturation and multiple pulse shapes. Due to the many variations of these signal shapes it is extremely difficult to automate an accurate method to determine the timing of a pulse.

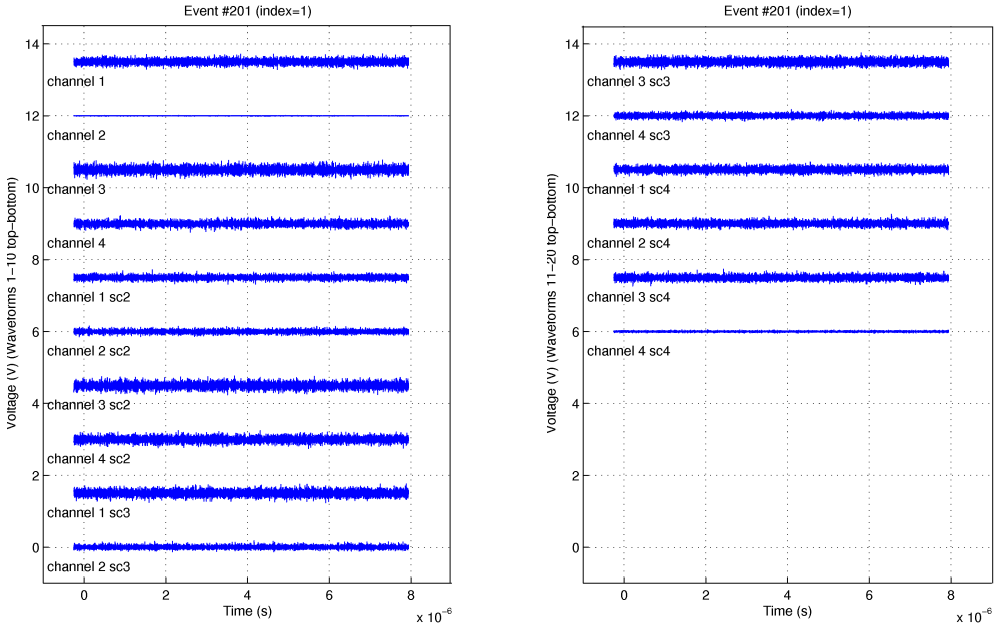

(a) Channel 1-10 (b) Channel 11-16

Figure 6.2: An example of an unbiased trigger for Channels $1-16$

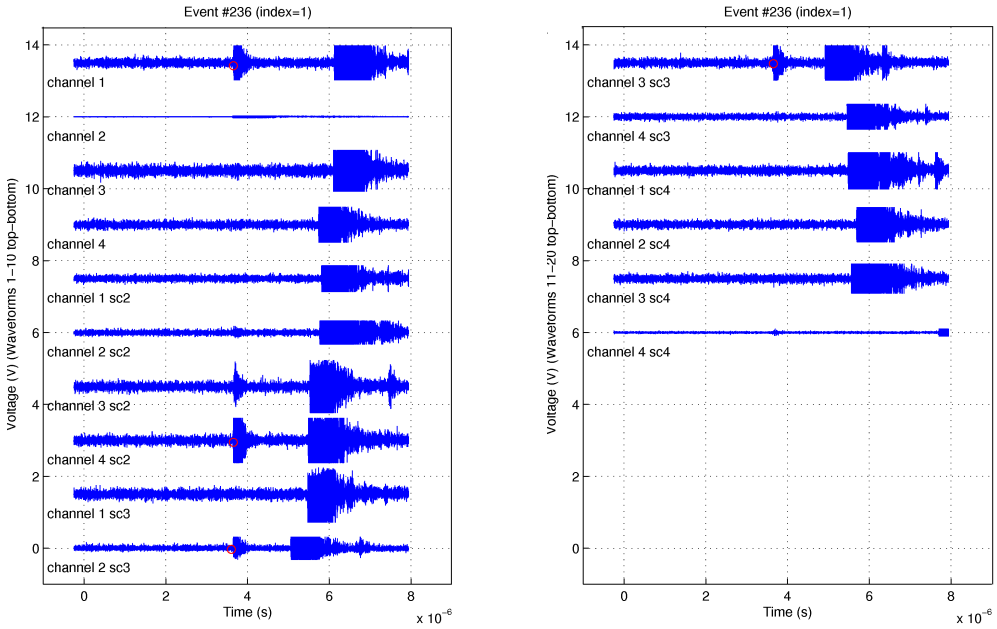

(a) Channel 1-10 (b) Channel 11-16

Figure 6.3: An example of a multiple peaked anthropogenic signal for Channels $1-16$

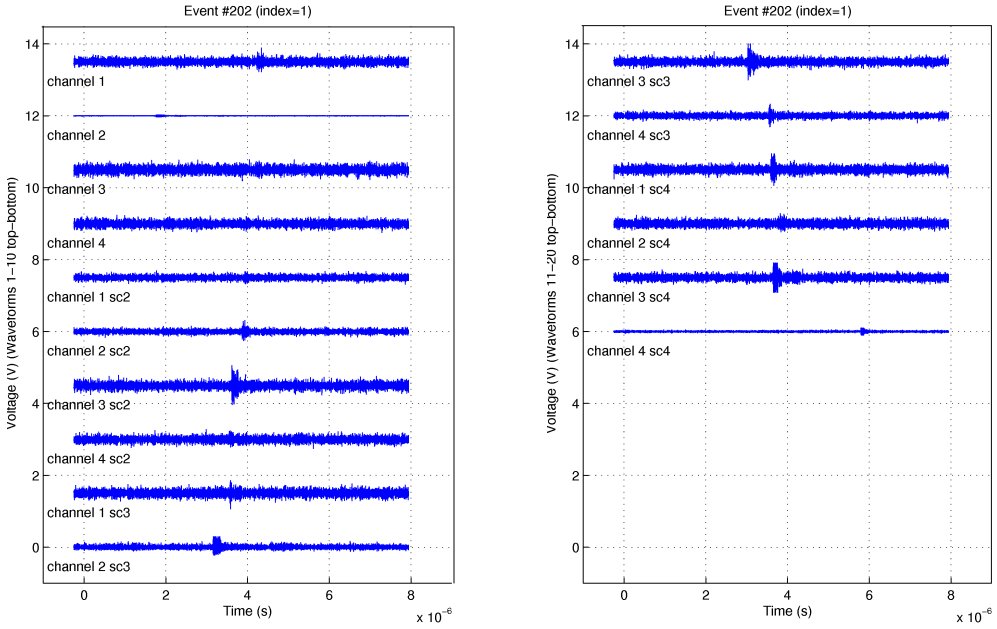

(a) Channel 1-10 (b) Channel 11-16

Figure 6.4: An example of a singular peaked anthropogenic signal for Channels $1-16$

6.3.3 Analysis Cuts

Analysis cuts were applied to the GRB windowed data using a modified analysis method which yielded a greater efficiency than the general RICE analysis. I employ the following cuts to the reduced GRB windowed data set:

Multiple Peak signals. Signals that produce multiple peaks or pulses are characteristic of anthropogenic signals and are removed. Figure 6.3 shows an example of a signal that contains multiple peaks.

Time over threshold ¿100 ns. The expected signal that is indicative of a neutrino event is very short sharp pulse of the order of a few nano-seconds. This was

shown earlier in Figure 6.1. The time-over-threshold (ToT) is the amount of time a signal spends over a predefined voltage[7]. This cut is an effective way to discriminate between long pulses indicative of anthropogenic signals. A more conservative value to that of the main stream analysis of the time over threshold of greater than 100ns is implemented here.

Z Vertex location of reconstructed source > 30m. The reconstructed vertex as discussed in the previous chapter gives the most direct indication of a surface generated (z=0) vs non-surface events. Unlike the generic method we implement here only the grid based vertex search algorithm as this correctly models the refractive index of the ice using a polynomial fit. This method calculates the best fit of the vertex to the triggered times at each antenna. Using the vertex the algorithm then recalculates the times which this vertex would produce at each of the antennas. The vertex which creates a minimal difference between actual and reconstructed times is then deemed the most optimal vertex fit. The time differences or time residuals are obtained for each channel based on the found vertex. If a difference/residual of an antenna exceeds $1.5 \times 10^{-7}\text{ns}^2$ then the antenna is removed from the calculation and the vertex is reconstructed again.

Cherenkov cone fit, χ^2_{cone}/dof< 2. Each event which passes to this cut is tested against the Cherenkov cone hit pattern expected for a neutrino event. The Cherenkov cone is fitted to the reconstructed vertex and the position of the antennas which are hit. The goodness of these fits are required to have a

[7]In this analysis the predefined voltage was defined as six standard deviations above the background.

χ^2/(degrees of freedom) less than 2.

Visual Inspection. Lastly a visual inspection was done to assess whether the signal was a recognisable hit pattern to that of a recognised anthropogenic signal, previously observed. Many of the patterns were recognisable as repeated signals from the same source and were subsequently removed from the analysis.

6.3.4 Analysis Results

A total of 77 time windows for 2001 to 2005 were analysed. The table below summarises the analysis outcomes. The table contains the number of events recorded and the number remaining after each of the cuts. Note that some data blocks were missing and therefore the data set is smaller than expected.

Table 6.2: Cuts applied to windowed RICE data.

Total triggers	965
Events passing 4 X 6σ	736
Events passing signal width test cut TOT$>$ 100 ns and Multiple Pulses	259
Events passing Z$<$ 30m	14
Satisfactorily Cherenkov geometry	0

Table 6.3: The number of triggers left after each cut was implemented to search for high energy ν-induced cascades with the RICE array.

6.4 Analysis Efficiency

The efficiency is obtained by multiplying the online efficiency of 90% [152] at the pole with the offline efficiency of the analysis method. In the case of the standard RICE

analysis this was 67% yielding an overall efficiency of 60%. The efficiency of the analysis method was measured using theoretically simulated neutrino events embedded into real data[8]. The simulated data were constructed using the expected signal from simulated hadronic showers superimposed on real unbiased data [9].A typical example of the efficiency data, was one where the signal had a sharp rise and fall which is characteristic of neutrino induced signal. The same analysis technique was used on the simulated data. Table 6.4 shows the result of applying the cuts to the simulated data consisting of a set of 1,159 neutrino events. A total of 1149 triggers were used to test the analysis technique. Of these 833 were neutrino events and 317 were surface generated signals. Cut one eliminated a significant number of the surface generated events and affected only a small fraction of the neutrino events.

All events passed the time over threshold as, all events had sharp spikes that would last less than a few milliseconds. All had at least 4 hit channels. None had any double pulse characteristics. Most events reconstructed well and below the 30m mark. Most of the neutrino events passed the Cherenkov Geometry cut to the visual inspection stage, with a only a handful of neutrino events failing to pass this cut.Events which had valid neutrino events would sometimes fail due to thermal noise signals skewing the vertex reconstruction. Also some of the unbiased triggers that were used to superimpose neutrino signals onto them, coincided with real anthropogenic signals. The anthropogenic signal throws the vertex which is reconstructed and the neutrino event is masked.

[8]Simulated data was generated by the RICE group

[9]Hadronic simulated data was all that was available and used in this analysis. However it was found by Kravchenko et al.[152], that electromagnetic showers have been shown to produce around the same efficiency [152]. Therefore we assume the efficiency is the same for both shower types.

Table 6.4: The determination of the analysis efficiency for by eye method.

Selection Requirement	MC(%)
Initial Sample	100(%)
Acceptable Time Over threshold	100(%)
> 4 hits	100(%)
Double/Multiple Pulse Rejection	100(%)
High quality Vertex- ie good time residuals	96(%)
Cherenkov Geometry	81(%)

An 81% offline efficiency was obtained. This combined with the 90% online efficiency yields a total efficiency of 73%. This value and the resultant null observation are used in the upper limit calculations in the following chapter.

March 4, 2009©

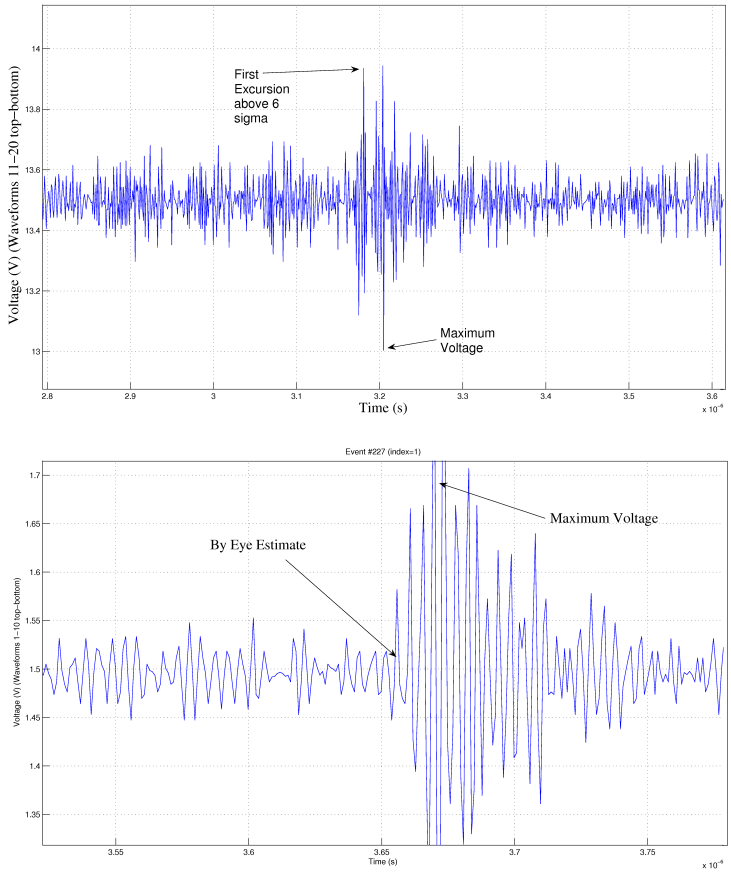

Figure 6.5: The comparison between the maximum voltage, 6σ and by-eye timing determination methods.

Chapter 7

Upper Limits

The non-observation of an event in the RICE data can be used to place bounds on the neutrino flux from each GRB. The expected number of events observed for each GRB is given by $N = \text{livetime } \times t_{90} \times \int \phi \mathcal{A} dE$, where ϕ is the flux and $\mathcal{A}$ is the exposure region given in units of area. The effective volumes $\mathcal{V}(E_{shower})$, estimated by the Montecarlo simulations, is converted to an effective area $\mathcal{A}(E_\nu)$ as follows:

$$\mathcal{A}(E_\nu) = \epsilon C_{EMC} N_{A_\rho} \left[\begin{array}{l} \int_{y_0}^{1} dy \frac{d\sigma^{NC}}{dy} \mathcal{V}_{hd}(yE_\nu) + \frac{2}{3} \int_{y_0}^{1} dy \frac{d\sigma^{CC}}{dy} \mathcal{V}_{hd}(yE_\nu) \\ + \frac{1}{3} \int_{0}^{1} dy \frac{d\sigma^{CC}}{dy} \left(\mathcal{V}_{hd}(yE_\nu) + \mathcal{V}_{em}((1-y)E_\nu) \right) \end{array} \right], \qquad (7.1)$$

where ϵ is the analysis efficiency; C_{EMC} (=0.8) is a constant factor used to account for the reduction in neutrino-nucleon cross sections in oxygen target as opposed to a nucleon target; $N_A\rho$ is Avogadro's number multiplied by the density of ice (0.92 g/cm^3) which gives the total number of target nucleons per unit volume; y is the inelasticity of the interaction, and $\frac{d\sigma^{NC}}{dy}$ and $\frac{d\sigma^{CC}}{dy}$ are the neutrino-nucleon neutral current (NC) and charged current (CC) differential cross sections, respectively, in the Standard Model. There are three integral terms. The first term accounts for the contribution from the NC interactions and is the same for all neutrino flavours; y_0 is

the lower limit on the integral and is due to the finite threshold of the detector. The second term is due to CC interactions of ν_μ and/or ν_τ. The third term is due to the CC interactions of ν_e. We treat ν_e CC interactions separately since both the hadronic and the leptonic parts of the final products contribute to shower development in ice; this is not the case for the other two flavours where the lepton does not contribute to the shower. The factors $\frac{2}{3}$ and $\frac{1}{3}$ are due to the isoflavour assumption of the model flux, namely, $\nu_e : (\nu_\mu + \nu_\tau) :: 1 : 2$. With no events observed, the 95% upper limit constraint $N < 3$ places limits on possible flux models.

In this chapter I present the upper limits on the neutrino flux following the prompt and afterglow Waxman and Bahcall spectral models discussed in chapter 3 for GRBs observed while RICE was live in the period. The results presented here primarily pertain to the subset of 27 GRBs which had estimated redshift information, with the remaining 50 GRBs presented in Appendices A through F. However, where appropriate, some figures will show the total distribution for both known and unknown redshift data sets. The main inputs into the expression for the limit are the neutrino flux and the effective volume for each individual GRB. I firstly present the general GRB information such as trigger time, duration and fluence. The GRB spectral properties are presented and discussed in Section 7.1. Section 7.2 presents the GRB localisations and their transformed local RICE co-ordinates. Detector information pertaining to RICE, the livetime and the detector threshold, as well as a list of satellite detectors triggered during GRBs, are presented in Section 7.3. Section 7.4 and Section 7.5 present the GRB neutrino flux parameters for prompt and afterglow emissions respectively. Lastly, in Sections 7.6, 7.7, and 7.8 I present the limits for the known GRB redshifts for individual and stacked cases leaving the last section to

present some of the event rates. Limits are presented in the energy region where 80% of the neutrino flux occurs.

7.1 GRB Properties

Using the IPN GRB cosmic burst list discussed in Section 2.2, 444 GRBs were found to have occurred during the operational time of RICE from 2001 to 2005. Of these, 77 GRBs were positively identified as localisable in the RICE effective volume zone defined in Section 5.2. Limits were obtained for these 77 GRBs and were divided into two groups: those with redshifts and those without. Table 7.1 summarises some key observational data for the 27 known redshift GRBs. The GRB name is given whereby the first two numbers represent the year followed by the month and day of the GRB trigger. The subsequent columns represent the date, Universal time (UT), duration, and the energy range for which the fluence and duration was measured. The remaining 50 GRBs without redshift estimations are located in Appendix A. Figures 7.1 and 7.2 show the distribution of durations and fluences for all 77 GRBs in the entire data set. As can be seen there is only one GRB which is classified in the short class and the rest are of the long classification.

In the known redshift group GRB020801 and GRB050820A have the longest durations in this subset of 350.8 and 270 s respectively. Whilst in the unknown redshift subset the two longest duration GRBs are GRB030425A and GRB031024A, with durations of 500 and 350 s respectively. The largest fluences for the known redshift group are from GRB051022A and GRB030329A, with fluences of 2.61×10^{-4} and 1.4×10^{-4} ergs cm^{-2} respectively. For the unknown redshift group GRB030422B and GRB030519B have the largest fluences, 8.8×10^{-5} and 6.6×10^{-5} ergs cm^{-2}

respectively. These large fluences have the best potential to give a large neutrino flux.

Obtaining consistent spectral information is difficult. Varying detector energy sensitivities can yield different fluence, duration, peak energy values and spectral fitting results. In order to maintain some sort of consistency, when available the majority of fluence and duration values were taken for the same detector and energy range. To illustrate the variations from detector to detector, we use GRB051022A for which was observed by HETE and KONUS. Different fluence values were measured for which we chose the largest energy range between 20 keV and 2 MeV from KONUS for which obtained a peak energy of 510 keV [173] and a fluence value of 2.6×10^{-4} erg cm^{-}2. This peak energy differs significantly to that reported by HETE, 306 keV[174], which had an energy range of $2 - 300$keV and a fluence value of 1.6×10^{-4} erg cm^{-}2. While the α values were in agreement. This discrepancy could be due the limited energy range of the FREGATE detector[173]. Due to this variation of energy levels and of course the large uncertainties in our other parameters, we can only offer here estimates of possible neutrino fluxes.

Figure 7.1 shows the duration of all 77 GRBs. The majority of the GRBs are long duration GRBs according to the standard bimodal distribution definition discussed in Section 2.2. The fluence distribution is also shown in Figure 7.2 for all 77 GRBs. The majority of the GRBs have a fluence (integrated energy per unit area) between 10^{-6} to 10^{-7} ergs cm^{-2}. The fluence measurements are given for various energy ranges, depending on the range of the detectors. As mentioned above, this can lead

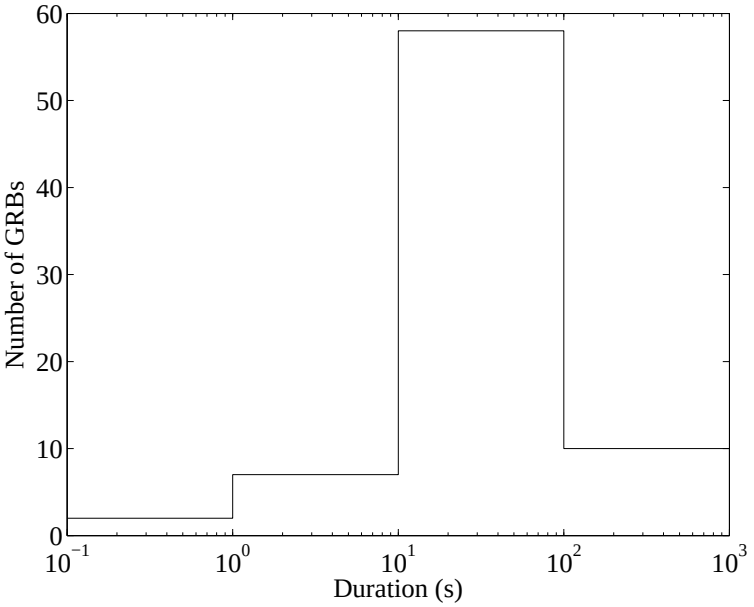

Figure 7.1: GRB durations from Tables 7.1 and A.1 for 77 GRBs with known and unknown redshifts. The majority of the durations are long duration GRBs (> 2s).

of course to a biased distribution of fluences, which could produce an over or under-estimated fluence magnitude. Both Figures 7.1 and 7.2 show the duration and fluence magnitudes for all GRBs (with and without redshift information) from Tables 7.1 and A.1.

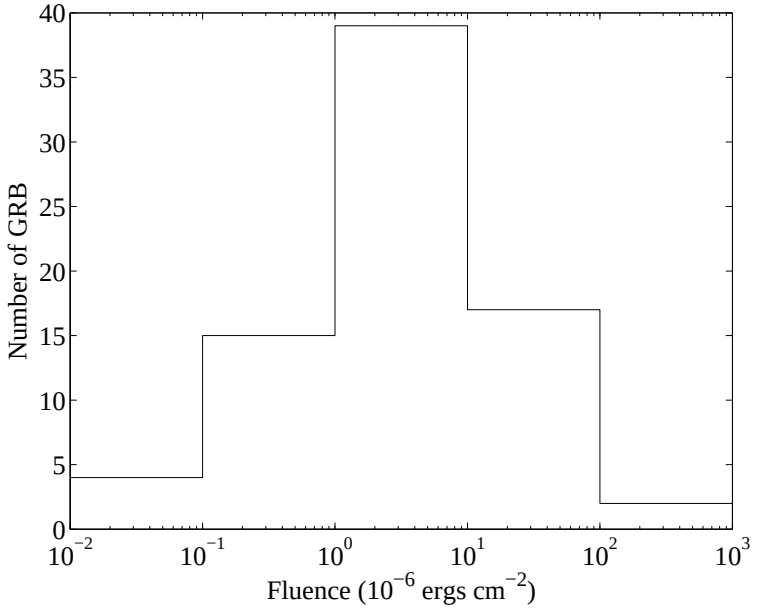

Figure 7.2: GRB fluences from Tables 7.1 and A.1 for 77 GRBs with known and unknown redshifts. The mean fluence of all GRBs is of the order 10^{-6}ergs cm^{-2}.

Table 7.1: GRB properties for 27 GRBs with known redshifts.

GRB Name	GRB Date	Time (UT)	Duration (s)	Fluence (10^{-6}) (ergs cm^{-2})	Energy Range (keV)	Reference
GRB010612	12/06/2001	02:33:14	26.6	5.00	30-400	[169]
GRB020124	24/01/2002	10:41:15	45.9	6.10	30-400	[169]
GRB020418A	18/04/2002	08:38:35	15.0	10.0	25-100	[175]
GRB020801	01/08/2002	12:58:42	350.8	9.50	30-400	[169]
GRB030323	23/03/2003	21:56:58	25.1	0.89	30-400	[169]
GRB030328	28/03/2003	11:20:58	92.6	29.0	30-400	[169]
GRB030329A	29/03/2003	11:37:15	22.8	110	30-400	[169]
GRB030429	29/04/2003	10:42:23	9.20	0.38	30-400	[169]
GRB030528	28/05/2003	13:03:03	53.9	5.60	30-400	[169]
GRB030723A	23/07/2003	06:28:17	34.3	0.04	30-400	[169]
GRB030725A	25/07/2003	11:46:27	38.8	17.0	30-400	[169]
GRB030823A	23/08/2003	08:52:41	67.5	1.30	30-400	[169]
GRB031026B	26/10/2003	05:35:43	32.0	2.80	30-400	[169]
GRB031111A	11/11/2003	16:45:13	5.3	18.0	30-400	[169]
GRB050603A	03/06/2005	06:29:05	12.4	6.36	15-150	[97]
GRB050724A	24/07/2005	12:34:09	96.0	1.00	15-150	[97]
GRB050801A	01/08/2005	18:28:02	19.4	0.31	15-150	[97]
GRB050802A	02/08/2005	10:08:02	19.0	2.00	15-150	[97]
GRB050807A	07/08/2005	10:58:44	28.0	3.99	30-400	[176]
GRB050820A	20/08/2005	06:34:53	270	1.90	15-350	[177]
GRB050824A	24/08/2005	23:12:16	22.6	0.27	15-150	[97]
GRB050826A	26/08/2005	06:18:10	35.5	0.41	15-150	[97]
GRB050908A	08/09/2005	05:42:31	20.0	0.51	15-150	[178]
GRB050922C	22/09/2005	19:55:50	4.50	1.62	15-150	[97]
GRB051021B	21/10/2005	23:31:54	46.5	0.84	15-150	[97]
GRB051022A	22/10/2005	13:07:58	200	261	20-2000	[173]
GRB051111A	11/11/2005	05:59:41	46.1	4.08	15-150	[97]

Table 7.2 presents the spectral properties for the known redshift GRB subset. The remaining spectral properties for the 50 GRBs without redshift estimations are given in Appendix B. The majority of the spectral indices are for α only. Many

detectors did not have the energy range in which to estimate β or to obtain the photon peak energy, ϵ_{peak}. Values of β were obtained only for GRB030328 (β = -2.1) and GRB030329 (β = -2.28). For unknown values of α and β average values are used as -1 and -2 respectively. If the peak energy of the burst was not available then the phenomenological Ghirlanda relationship described by Equation 2.3 was used. Those where the Ghirlanda relationship was used are indicated by the double asterisks. For the energy range of RICE the determination of an accurate value for the break energy is not necessary.

Some GRB redshifts were estimated using the pseudo redshift method [120, 123]. These estimated redshifts are indicated by the single asterisk [120, 123] and are described in Section 2.3. Using spectroscopic and pseudo redshifts the luminosity distance, d_l, was calculated using:

$$H_o \frac{dl}{1+z} = \frac{1}{|\Omega_k|^{1/2}} \text{sinn} \left\{ |\Omega_k|^{1/2} \int_0^{z_1} [(1+z)^2(1+\Omega_m z) - z(2+z)\Omega_\Lambda]^{-1/2} dz \right\} \quad (7.2)$$

where sinn represents sinh if $\Omega_k > 0$ for an open universe and sin for $\Omega_k < 0$. However, for a flat universe ($\Omega_k = 0$ and $\Omega_{total} = 1$), sinn and Ω_k are not present and only the integral remains [179]. We assume a standard Λ dominated cold dark matter (ΛCDM) model with parameters: $H_0 = 70 \text{kms}^{-1}\text{Mpc}^{-1}$, $\Omega_M = 0.3$, and $\Omega_\Lambda = 0.7$.

The isotropic-equivalent γ-ray bolometric luminosity and energy at redshift, z, is given by:

$$E_{\gamma,iso} = 4\pi d_L^2 S_\gamma / (1+z) \,, \quad (7.3)$$

and

$$L_{\gamma,iso} = 4\pi d_L^2 S_\gamma / t_{90} \,, \tag{7.4}$$

where d_L is the luminosity distance; S_γ, the observed fluence in some energy range; and t_{90}, the duration time (as defined in Section 2.2.1).

The luminosity distance depends on the cosmological model used. Different cosmological models will alter the luminosity distance and hence the isotropic luminosity and energy will be affected. This will subsequently affect the upper limit calculations.

Figure 7.3 shows the distribution of peak energies using both actual and inferred values. The inferred values are derived from the Ghirlanda relationship for the known redshift subset. Peak energies tend to cluster below 100 keV. The redshift distribution is shown in Figure 7.4 for the known redshift subset and is compared to the total observed redshift distribution [1]. For interest I also compare the pre-SWIFT and post-SWIFT redshifts which are discussed in Section 2.2.3. Figures 7.5 and 7.1 show the distribution of the isotropic energy and the isotropic luminosity for the known redshift subset. Isotropic energy distribution is more prominent around 10^{52} to 10^{53} ergs and the isotropic luminosity around 10^{51} to 10^{52} ergs s^{-1}.

[1] Here we take the observed redshifts to be those obtained directly and not inferred using redshift correlation relationships.

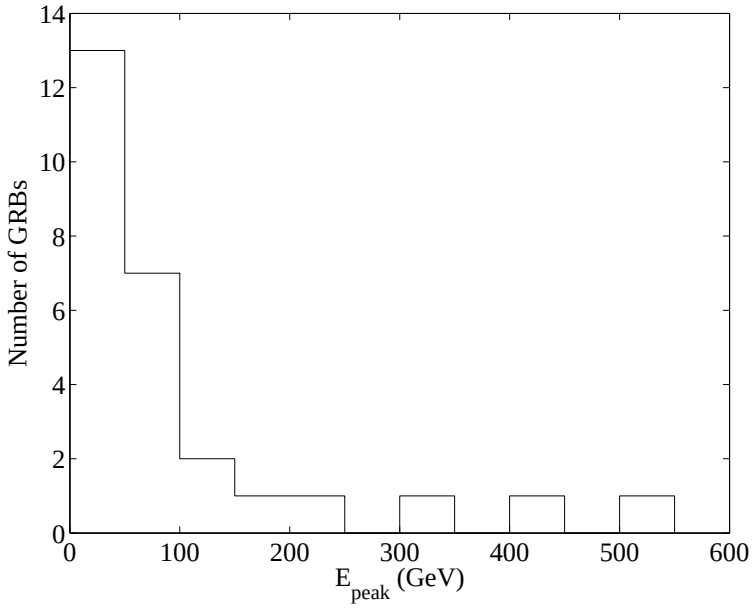

Figure 7.3: Peak energies of all GRBs using actual and those inferred using the Ghirlanda relationship.

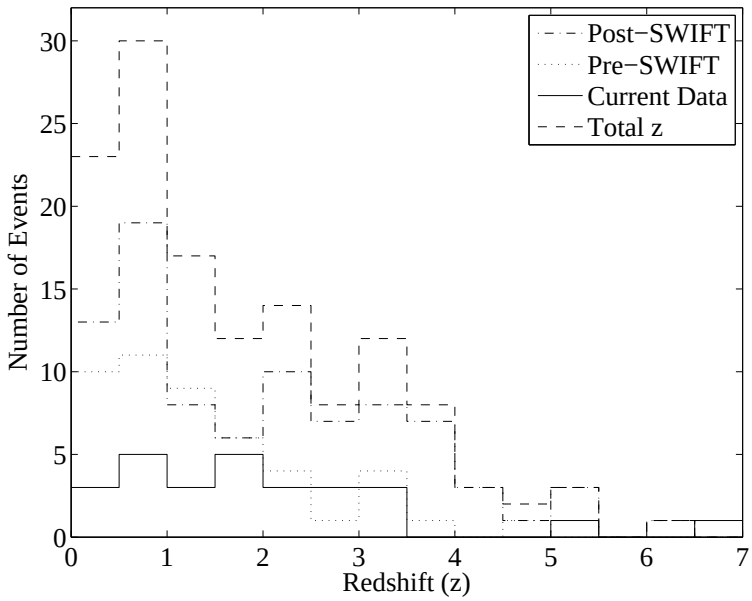

Figure 7.4: GRB redshifts for all GRBs in our data set with known redshifts (-solid line), compared to all redshifts of GRBs as of November 2007 (–), post (-.) and pre (...) SWIFT era redshifts.

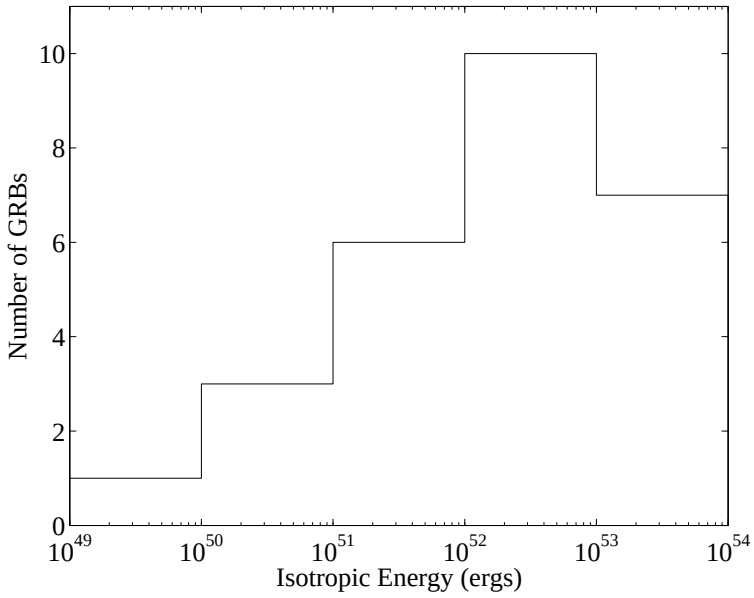

Figure 7.5: The isotropic energies of GRBs with known redshifts, obtained from Table 7.2.

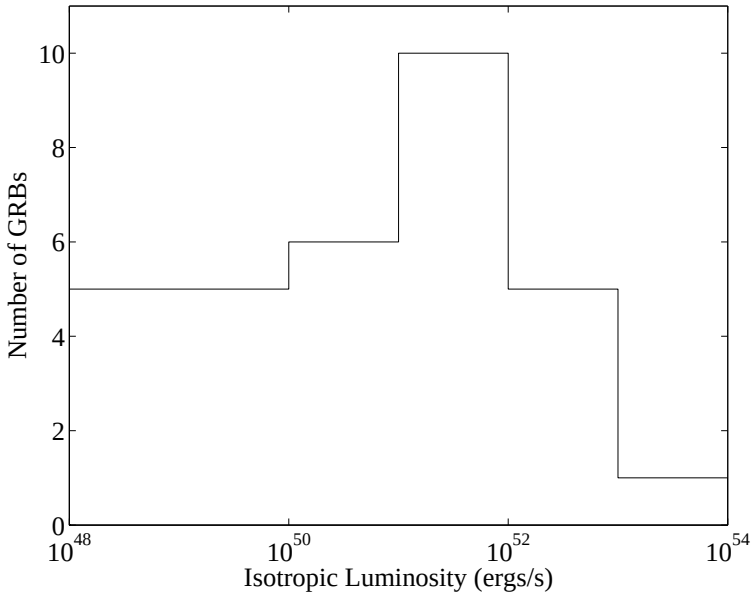

Figure 7.6: The isotropic luminosities of GRBs with known redshifts, obtained from Table 7.2.

Table 7.2: Spectral properties for 27 GRBs with known redshifts. β values are sparse, only two values were obtained for this subset: GRB030328, β -2.1 and GRB030329 -2.28.

GRB Name	α	E_{peak} (keV)	z	dl (Mpc)	$E_{\gamma,iso}$ (ergs)	$L_{\gamma,iso}$ (ergs/s)	Ref.
GRB010612	-1.1	244.5	5.25*	4.9×10^4	2.3×10^{53}	5.5×10^{52}	[180, 169, 124]
GRB020124	-0.8	86.93	3.2	2.7×10^4	1.3×10^{53}	1.2×10^{52}	[180, 169, 167]
GRB020418A	-	84.9**	1.4*	1.0×10^4	5.0×10^{52}	8.0×10^{51}	[124]
GRB020801	-	53.35	1.21*	8.4×10^3	3.6×10^{52}	2.3×10^{50}	[169, 124]
GRB030323	-1.6	29**	3.37	2.9×10^4	2.1×10^{52}	3.6×10^{51}	[180, 167]
GRB030328	-1.14	126.3	1.52	1.1×10^4	1.7×10^{53}	4.6×10^{51}	[180, 169, 167]
GRB030329A	-1.26	67.86	0.168	8.1×10^2	7.4×10^{51}	3.8×10^{50}	[180, 169, 167]
GRB030429	-1.1	35.04	2.66	2.2×10^4	6.0×10^{51}	2.4×10^{51}	[180, 169, 167]
GRB030528	-	31.84	0.782	4.9×10^3	9.0×10^{51}	3.0×10^{50}	[169, 167]
GRB030723A	-	9.66	<2.3	1.8×10^4	4.7×10^{50}	4.5×10^{49}	[169, 167]
GRB030725A	-	102.8	0.89*	5.7×10^3	3.5×10^{52}	1.7×10^{51}	[169, 124]
GRB030823A	-	26.57	0.84*	5.3×10^3	2.4×10^{51}	6.6×10^{49}	[169, 124]
GRB031026B	-	55**	6.67*	6.5×10^4	1.9×10^{53}	4.5×10^{52}	[124]
GRB031111A	-	404.4	2.14*	1.7×10^4	2.0×10^{53}	1.2×10^{53}	[169, 124]
GRB050603A	-1.16	349	2.821	2.4×10^4	1.1×10^{53}	3.4×10^{52}	[97, 169, 167]
GRB050724A	-1.89	7**	0.258	1.3×10^3	1.6×10^{50}	2.1×10^{48}	[97, 167]
GRB050801A	-1.99	13**	1.56	1.1×10^4	1.9×10^{51}	2.5×10^{50}	[97, 167]
GRB050802A	-1.54	38**	1.71	1.3×10^4	1.5×10^{52}	2.1×10^{51}	[97, 167]
GRB050807A	-	171.41	1.73*	1.3×10^4	3.0×10^{52}	2.9×10^{51}	[169, 124]
GRB050820A	-1.25	42**	2.6147	2.2×10^4	2.9×10^{52}	3.9×10^{50}	[97, 167]
GRB050824A	-2.76	8**	0.83	5.3×10^3	4.8×10^{50}	3.9×10^{49}	[97, 167]
GRB050826A	-1.16	5**	0.297	1.5×10^3	9.0×10^{49}	3.3×10^{48}	[97, 167]
GRB050908A	-	21**	3.344	2.9×10^4	1.2×10^{52}	2.6×10^{51}	[178]
GRB050922C	-1.37	36**	2.199	1.7×10^4	1.8×10^{52}	1.3×10^{52}	[97]
GRB051021B	-1.55	72	1.37*	9.8×10^3	4.0×10^{51}	2.0×10^{50}	[97, 97, 124]
GRB051022A	-1.176	510	0.8	5.0×10^3	4.4×10^{53}	3.9×10^{51}	[173, 167]
GRB051111A	-1.32	54**	1.55	1.1×10^4	2.5×10^{52}	1.4×10^{51}	[97][167]

The five GRBs with the largest fluences are GRB051022A, GRB030329A, GRB030328, GRB031111A, and GRB030725A. Which have fluence values of 261, 110, 29, 18 and 17 erg cm^{-2} respectively. From these GRBs we expect the largest neutrino flux. In

the next section we show the localisations and discuss the implications on these five GRBs.

7.2 GRB Localisations

GRBs have an isotropic distribution in the sky. In the pre-SWIFT and post BATSE era accurate localisation information was sparse. There was a large reliance on multiple satellite detection with triangulation techniques used to constrain the localisations (see Section 2.2). This time largely overlaps the 2001 to 2005 period of interest. As previously discussed this has meant that 77 GRBs were able to have positively identified localisations within the defined sensitivity zone of RICE. The right ascension (RA-column two) and declination (Dec-column three) of the GRBs with known redshift are shown in Table 7.3, in degrees, along with the approximate error circle [2] (Column four). For most, the errors are much smaller than 1 degree as the majority of this subset have redshifts derived from spectroscopic data from afterglow observations. In order to observe these afterglow phenomena the GRBs must be extremely well localised.

For this analysis an accurate localisation is not needed. The 1 degree error circles are more than satisfactory for this analysis. The accuracy of the angular cut would come under more scrutiny if an angular cut in the RICE data analysis was required. This would be in order to attempt to validate the GRB as the source of the neutrino signal. However since signals were removed before such a cut was necessary, the localization accuracy is satisfactory for the purposes of estimating the effective volume

[2]The error circle associated with the localization is an approximate uncertainty which contains the constrained localization, sometimes an error box or some other geometry.

for each GRB case. The appropriate angular region determined by the localisation and the error circle was applied when calculating the effective volume, as described in Section 5.2. The RA and Dec for each GRB were converted from equatorial to horizon co-ordinates using Equation 5.5 and Equation 5.4 to obtain the Azimuth (Azi) and Altitude (Alt) respectively and are shown in Table 7.3 columns five and six. These were subsequently converted to local co-ordinates relative to the RICE array using Equations 5.8 (column seven) and 5.9 (column eight) to obtain the approximate shower angles Azimuth_{shower} (Azi_s) and Nadir (θ_s). These were then used in the Monte Carlo code to ascertain the effective volume for neutrinos from each point source GRB as discussed in Section 5.2. The RICE co-ordinates carried over the uncertainties from the localisation. For the larger uncertainty regions seen later in the unknown redshift group (Appendix B), the neutrino showers were induced from random directions within the restricted defined error boundary.

One of the main contributing factors of the detector sensitivity is the attenuation of the neutrino flux through the Earth. For GRBs below the horizon the effective volume is significantly reduced by attenuation effects. Also RICE's shallow position in the ice means that GRBs which occur directly above the detector will have essentially a zero effective volume. Figure 7.7 shows the distribution of the RA and Dec for known redshifts (crosses) and unknown redshifts (No circles). GRBs were chosen based on their localisation which limited the selection to GRBs that were localisable within the RICE sensitivity zone. I also required that the error circle be contained in the zone as well. The acceptable angular region is loosely defined Dec = 60° to 170° in nadir and 360° in azimuth. Some higher declinations were initially included that were greater than 170° but all of these resulted in a null effective volume and were thus removed.

Table 7.3: The localisations and transformed local RICE co-ordinates for the 27 GRBs with known redshift.

GRB Name	RA (°)	Dec (°)	Err Circ (°)	Azi (°)	Alt (°)	Azi$_s$ ϕ_s (°)	Nadir θ_s (°)	Ref:
GRB010612	271	-32	<1	17	32	118	122	[169, 167]
GRB020124	143	-11	<1	264	11	231	101	[169]
GRB020418A	120	-49	<1	189	49	306	139	[175]
GRB020801	316	-54	<1	216	54	279	144	[169]
GRB030323	167	-22	<1	61	22	74	112	[169]
GRB030328	183	-9	<1	232	9	263	99	[169]
GRB030329A	161	22	<1	205	-22	290	68	[169]
GRB030429	183	-21	<1	211	21	284	111	[169]
GRB030528	256	-23	<1	220	23	275	113	[169]
GRB030723A	327	-28	<1	335	28	160	118	[169]
GRB030725A	308	-51	<1	234	51	261	141	[169]
GRB030823A	323	22	<1	263	-22	232	68	[169]
GRB031026B	50	28	<1	337	-28	158	62	[169]
GRB031111A	72	17	<1	176	-18	319	72	[169]
GRB050603A	40	-25	<1	96	25	39	115	[181]
GRB050724A	246	-28	<1	160	27	335	117	[182]
GRB050801A	204	-22	<1	22	22	113	112	[183]
GRB050802A	219	28	<1	161	-28	334	62	[184]
GRB050807A	303	-37	<1	228	37	267	127	[176]
GRB050820A	337	20	<1	315	-20	180	70	[185]
GRB050824A	12	23	<1	96	-23	39	67	[186]
GRB050826A	88	-3	<1	64	3	71	93	[187]
GRB050908A	20	-13	<1	352	13	143	103	[188]
GRB050922C	317	-9	<1	62	9	73	99	[189]
GRB051021B	126	-46	<1	148	45	347	135	[190]
GRB051022A	359	20	<1	176	-20	319	70	[191]
GRB051111A	348	18	<1	253	-18	242	72	[192]

In Table 7.3 we see that three of the five highest fluence GRBs discussed in the previous section, are localised below the horizon. Thus these GRB neutrino fluxes will suffer significant attenuation as they traverse through the earth thus yielding a

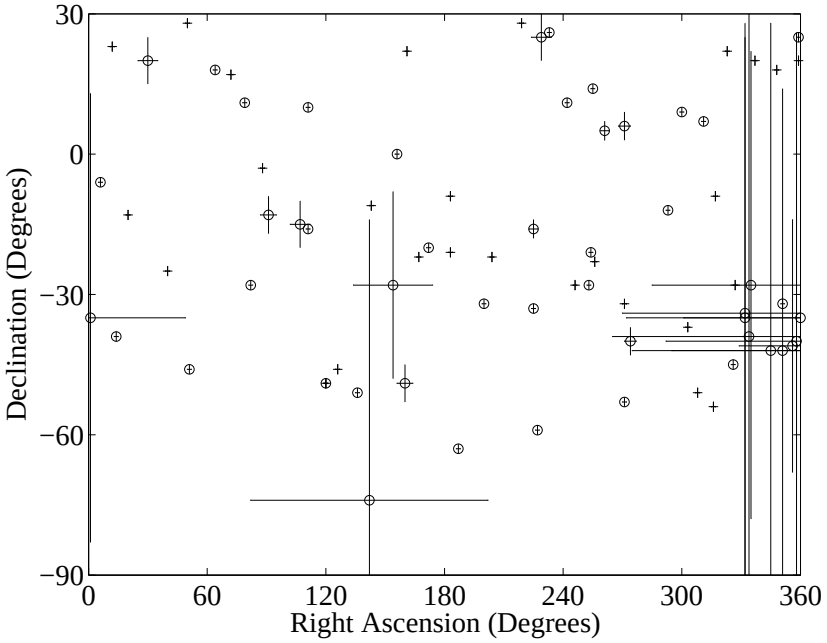

Figure 7.7: Localisations of GRBs with known (no-circles) and unknown (circles) redshift in RA and Dec. Uncertainty regions corresponding to the error circle or error box regions are shown. Uncertainties extending beyond −90 in declination are meaningless and should be ignored.

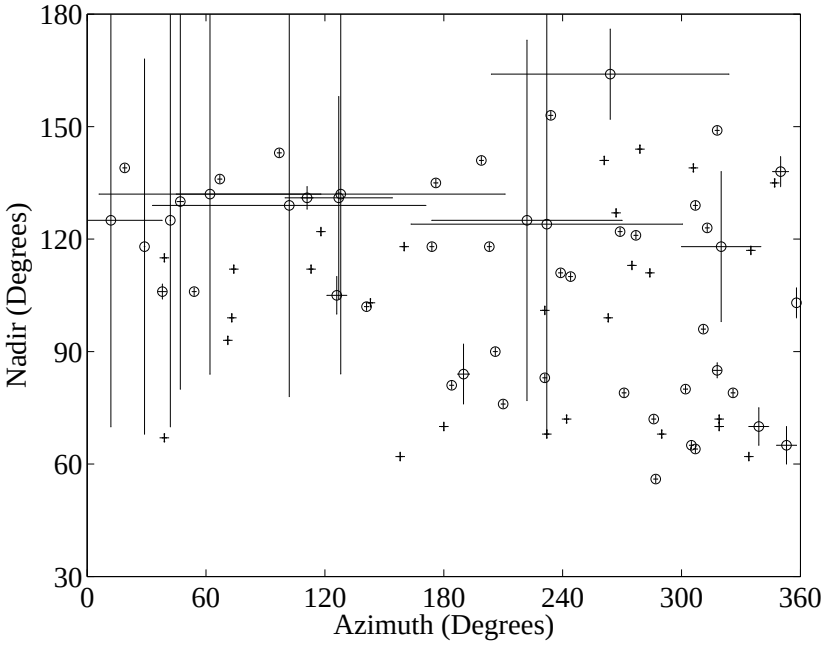

Figure 7.8: Local RICE co-ordinates of GRB localisations with known (no-circles) and unknown (circles) redshift. Uncertainties are calculated robustly.

greatly reduced effective volume. GRB030328 and GRB030725 however would have produced a relatively high flux at the detector as these are positioned in a more optimal direction.

7.3 RICE livetimes and discriminator settings

The RICE livetimes were discussed in Chapter 4. Table 7.4 shows the average livetimes of the RICE array at the time of the GRBs. Livetimes are measured over a 5 minute interval and then averaged over the entire 10 minute window. Livetimes are shown in Figure 7.9 showing that most of the livetimes fall into the 90-100% region. The discriminator values, as discussed in Section 4.6, range from -0.23 to -0.99 V, which are somewhat larger than the earlier RICE publications which have -0.015V settings. The absolute values are represented in Figure 7.10, where the majority of the discriminator values are sitting around actual values of -0.3 and -0.4 V. We saw previously that the effective volume is highly sensitive to the discriminator setting. At times the array will automatically set a higher threshold to combat a high trigger rate due to anthropogenic noise, this however also reduces the energy sensitivity to neutrino signal detection.

Table 7.4: RICE averaged livetimes over a ten minute window, discriminator threshold and satellites triggered for the 27 GRBs with known redshifts.

GRB Name	Average Livetime	Discriminator Threshold (V)	Satellites Triggered
GRB010612	0.59	-0.40	Uly,KON,SAX,HET
GRB020124	0.001	-0.28	Uly,KON,HET
GRB020418A	0.96	-0.35	Uly,Mo,KON,SAX

Table cont...

GRB Name	Average Livetime	Discriminator Threshold (V)	Satellites Triggered
GRB020801	0.94	-0.23	Uly,HET
GRB030323	0.61	-0.62	HET
GRB030328	0.87	-0.36	Uly,KON,HET,INT
GRB030329A	0.49	-0.99	Uly,Mo,KON,HET,HES,INT
GRB030429	0.96	-0.35	HET
GRB030528	0.95	-0.29	Uly,Mo,HET,HES
GRB030723A	0.96	-0.28	HET
GRB030725A	0.98	-0.35	Ulys,Mo,KON,HET,HES,INT
GRB030823A	0.94	-0.86	HET
GRB031026B	0.97	-0.27	Uly,KON,HET,HES
GRB031111A	0.94	-0.33	Uly,KON,HET,HES,INT
GRB050603A	0.92	-0.39	KON,SWI
GRB050724A	0.91	-0.40	KON,XTE,INT,SWI
GRB050801A	0.92	-0.42	SWI
GRB050802A	0.94	-0.42	KON,HES,SWI
GRB050807A	0.89	-0.28	HET,SUZ
GRB050820A	0.60	-0.39	KON,INT,SWI
GRB050824A	0.89	-0.45	HET,SWI
GRB050826A	0.85	-0.41	SWI
GRB050908A	0.86	-0.39	SWI
GRB050922C	0.93	-0.52	Mo,KON,HET,SWI
GRB051021B	0.89	-0.35	SWI
GRB051022A	0.75	-0.27	Mo,KON,HET
GRB051111A	0.68	-0.53	KON,HET,HES,SWI

GRB020124 has a low average livetime of 0.001 which will yield a large limit. This would have otherwise been removed from the analysis, but we leave this here for indicative purposes. GRB030329A has a very high discriminator setting of -0.99. It was shown in Chapter 5 that the larger the discriminator setting the smaller the effective volume.

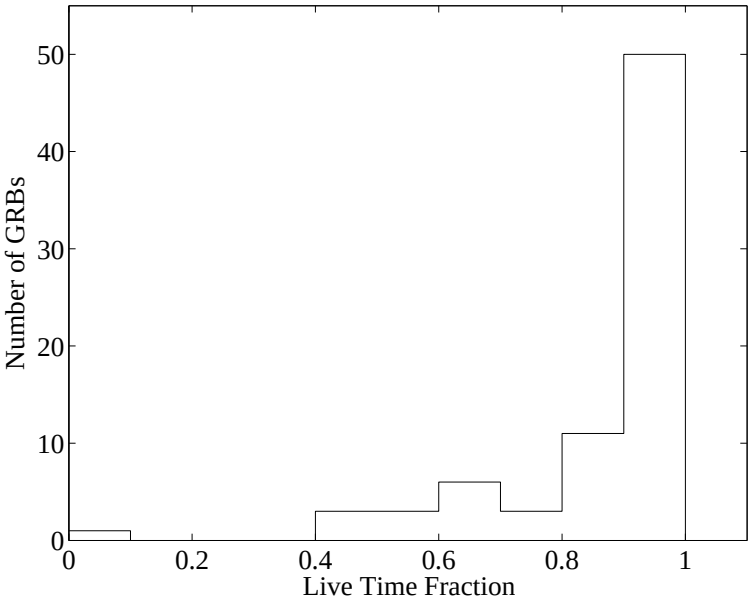

Figure 7.9: RICE livetimes during all GRB triggers with known and unknown redshifts.

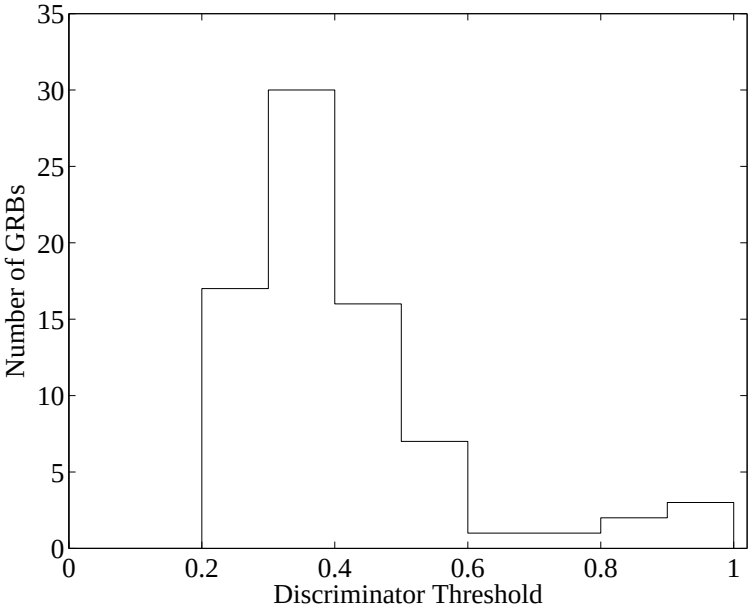

Figure 7.10: RICE discriminator settings during all GRB triggers for known and unknown redshifts.

7.4 GRB Prompt Parameters

The neutrino flux coinciding with the prompt gamma ray component was described in Chapter 3. Here we present the main neutrino prompt flux parameters in Table 7.5. The second column is the prefactor, $\mathcal{A}$, given by Equation 3.13 and used in the expression of the neutrino flux defined in Equation 3.7. The third and fourth columns give the break energies, $\epsilon_{\nu,b1}$ and $\epsilon_{\nu,sb}$. The expression for these were given in Equation 3.8 and Equation 3.11 respectively. For completeness the burst duration, $t_{\rm burst}$, is given again here. Figure 7.11 shows the distribution of neutrino break energies, $\epsilon_{\nu,b1}$ and $\epsilon_{\nu,sb}$. We see that the majority of the bursts have $\epsilon_{\nu,b1}$ at around the energy where the RICE detector starts having a sensitivity. GRB031026B has a very low $\epsilon_{\nu,sb}$, which will lead to a more significantly suppressed higher end of the neutrino energy spectrum.

Table 7.5: Prompt GRB parameters for the 27 GRBs with known redshifts.

GRB Name	$\mathcal{A}$ (GeV cm^{-2}s^{-1})	$\epsilon_{\nu,b1}$ (GeV)	$\epsilon_{\nu,sb}$ (GeV)	$t_{\rm burst}$ (s)
GRB010612A	2.93×10^{-6}	1.41×10^{5}	1.01×10^{7}	26.6
GRB020124A	2.07×10^{-6}	8.80×10^{5}	3.23×10^{7}	45.9
GRB020418A	1.04×10^{-5}	2.76×10^{6}	6.92×10^{7}	15
GRB020801A	4.23×10^{-7}	5.18×10^{6}	4.46×10^{8}	350.8
GRB030323A	5.53×10^{-7}	2.48×10^{6}	5.65×10^{7}	25.1
GRB030328A	4.89×10^{-6}	1.68×10^{6}	8.68×10^{7}	92.6
GRB030329A	7.53×10^{-5}	1.46×10^{7}	6.55×10^{8}	22.8
GRB030429A	6.45×10^{-7}	2.88×10^{6}	8.30×10^{7}	9.2
GRB030528A	1.62×10^{-6}	1.34×10^{7}	4.85×10^{8}	53.9
GRB030723A	1.73×10^{-8}	1.28×10^{7}	6.71×10^{8}	34.3
GRB030725A	6.84×10^{-6}	3.68×10^{6}	1.90×10^{8}	38.8
GRB030823A	3.01×10^{-7}	1.50×10^{7}	9.98×10^{8}	67.5

Table cont...

GRB Name	$\mathcal{A}$ (GeV cm^{-2}s^{-1})	$\epsilon_{\nu,b1}$ (GeV)	$\epsilon_{\nu,sb}$ (GeV)	$t_{\rm burst}$ (s)
GRB031026B	1.37×10^{-6}	4.14×10^{5}	9.17×10^{6}	32
GRB031111A	5.30×10^{-5}	3.39×10^{5}	1.39×10^{7}	5.3
GRB050603A	8.00×10^{-6}	2.65×10^{5}	2.10×10^{7}	12.4
GRB050724A	1.62×10^{-7}	1.31×10^{8}	8.11×10^{9}	96
GRB050801A	2.49×10^{-7}	1.62×10^{7}	3.67×10^{8}	19.4
GRB050802A	1.64×10^{-6}	4.89×10^{6}	1.20×10^{8}	19
GRB050807A	2.22×10^{-6}	1.06×10^{6}	1.01×10^{8}	28
GRB050820A	1.10×10^{-7}	2.48×10^{6}	2.08×10^{8}	270
GRB050824A	1.84×10^{-7}	4.89×10^{7}	1.30×10^{9}	22.6
GRB050826A	1.82×10^{-7}	1.76×10^{8}	6.33×10^{9}	35.5
GRB050908A	3.98×10^{-7}	3.43×10^{6}	6.76×10^{7}	20
GRB050922C	5.62×10^{-6}	3.62×10^{6}	4.05×10^{7}	4.5
GRB051021B	2.80×10^{-7}	3.34×10^{6}	4.38×10^{8}	46.5
GRB051022A	2.04×10^{-5}	8.17×10^{5}	1.32×10^{8}	200
GRB051111A	1.38×10^{-6}	3.86×10^{6}	1.58×10^{8}	46.1

7.5 GRB Afterglow Parameters

In Chapter 3 we described the neutrino flux that would arise during the afterglow phase directly following the burst. Here we present some of the main parameters for this flux model in Table 7.6. Unlike the prompt neutrino emission the pion efficiency needs to be explicitly calculated. Values for these are given in the second column using Equation 3.17. The third column is the prefactor, $\mathcal{B}$, in the expression of the neutrino flux and defined by Equation 3.13. The fourth columns pertain to the afterglow break energy, $\epsilon_{\nu,b2}$ from Equation 3.15 and the fifth is the maximum energy, $\epsilon_{\nu,max}$ from Equation 3.16. For completeness the burst duration, $t_{\rm burst}$, is given again here. Figure 7.12 shows the distribution of the afterglow break energies, $\epsilon_{\nu,b2}$ and $\epsilon_{\nu,max}$. We should again consider that the sensitivity of RICE starts at around 10^7 GeV. For

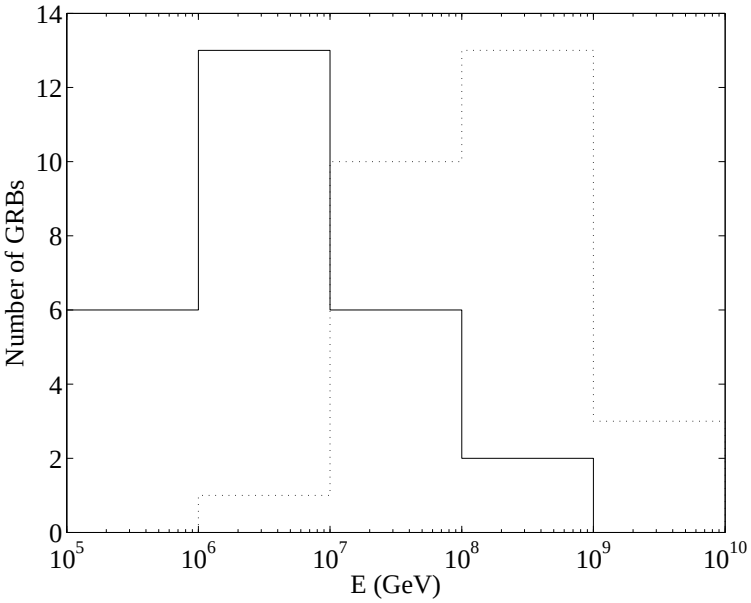

Figure 7.11: The distribution of break energies ($\epsilon_{\nu,b1}$ = solid line, $\epsilon_{\nu,sb}$ = dotted line) for the prompt neutrino emission for GRBs with known redshift.

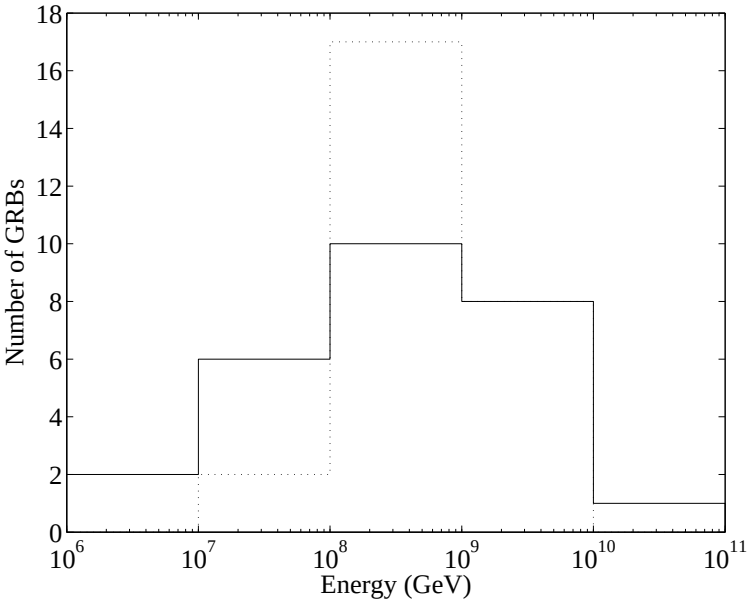

Figure 7.12: The distribution of break energies ($\epsilon_{\nu,b2}$ = solid line, $\epsilon_{\nu,max}$ = dotted line) for the afterglow neutrino emission for GRBs with known redshift.

the 27 GRB known redshift subset the maximum energies are above the sensitivity of the detector, thus limits can be obtained for these. We shall however see later in Appendix F that this is not the case for some of the GRBs in the minimum redshift scenario, for the remaining 50 GRBs.

Table 7.6: Afterglow parameters for the 27 GRBs known redshifts.

GRB Name	f_π	$\mathcal{B}$ (GeV cm^{-2}s^{-1})	$\epsilon_{\nu,b2}$ (GeV)	$\epsilon_{\nu,max}$ (GeV)	$t_{\rm glow}$ (s)
GRB010612A	0.20	2.93×10^{-6}	2.16×10^{9}	8.90×10^{8}	26.6
GRB020124A	0.20	2.07×10^{-6}	1.26×10^{9}	8.28×10^{8}	45.9
GRB020418A	0.20	1.04×10^{-5}	2.11×10^{9}	1.42×10^{9}	15
GRB020801A	0.20	4.23×10^{-7}	1.59×10^{8}	4.06×10^{8}	350.8
GRB030323A	0.20	5.53×10^{-7}	3.52×10^{8}	4.29×10^{8}	25.1
GRB030328A	0.20	4.89×10^{-6}	1.57×10^{9}	1.19×10^{9}	92.6
GRB030329A	0.12	4.59×10^{-5}	5.45×10^{8}	1.03×10^{9}	22.8
GRB030429A	0.10	3.21×10^{-7}	2.85×10^{8}	4.22×10^{8}	9.2
GRB030528A	0.15	1.20×10^{-6}	2.24×10^{8}	5.37×10^{8}	53.9
GRB030723A	0.01	6.72×10^{-10}	1.14×10^{7}	8.88×10^{7}	34.3
GRB030725A	0.20	6.84×10^{-6}	9.51×10^{8}	1.07×10^{9}	38.8
GRB030823A	0.04	5.99×10^{-8}	5.49×10^{7}	2.61×10^{8}	67.5
GRB031026B	0.20	1.37×10^{-6}	1.24×10^{9}	6.09×10^{8}	32
GRB031111A	0.20	5.30×10^{-5}	1.22×10^{10}	2.99×10^{9}	5.3
GRB050603A	0.20	8.00×10^{-6}	3.17×10^{9}	1.38×10^{9}	12.4
GRB050724A	0.003	2.18×10^{-9}	5.21×10^{06}	9.74×10^{7}	96
GRB050801A	0.03	3.93×10^{-8}	8.12×10^{7}	2.69×10^{8}	19.4
GRB050802A	0.20	1.64×10^{-6}	5.02×10^{8}	6.51×10^{8}	19
GRB050807A	0.20	2.22×10^{-6}	7.16×10^{8}	7.75×10^{8}	28
GRB050820A	0.20	1.10×10^{-7}	9.76×10^{7}	2.49×10^{8}	270
GRB050824A	0.01	7.31×10^{-9}	2.87×10^{7}	1.89×10^{8}	22.6
GRB050826A	0.00	1.35×10^{-9}	6.20×10^{06}	1.05×10^{8}	35.5
GRB050908A	0.20	3.89×10^{-7}	2.49×10^{8}	3.62×10^{8}	20
GRB050922C	0.20	5.62×10^{-6}	1.56×10^{9}	1.06×10^{9}	4.5
GRB051021B	0.07	9.33×10^{-8}	9.03×10^{7}	2.95×10^{8}	46.5
GRB051022A	0.20	2.04×10^{-5}	2.93×10^{9}	1.93×10^{9}	200
GRB051111A	0.20	1.38×10^{-6}	4.47×10^{8}	6.34×10^{8}	46.1

7.6 Upper Limits and Ratios

As discussed previously, in the event of a null observation one can set limits on the neutrino flux. Presented here in Table 7.7 are the derived upper limit and the ratios of the limits to the predicted burst and afterglow fluxes at a given neutrino energy for the 27 GRBs with estimated values for the redshift. The remaining 50 GRBs without redshift estimations are located in Appendix G.

Table 7.7: RICE limits and ratios to the predicted burst and afterglow fluxes for 27 GRBs known redshifts.

GRB	Burst			Afterglow		
	ϵ_ν (GeV)	Limit (GeV/cm^2)	Ratio	ϵ_ν (GeV)	Limit (GeV/cm^2)	Ratio
GRB010612	1.0×10^{8}	2.06×10^{4}	5.80×10^{9}	3.07×10^{8}	3.44×10^{3}	1.03×10^{8}
GRB020124	1.0×10^{8}	8.13×10^{6}	2.84×10^{11}	3.07×10^{8}	2.01×10^{6}	2.88×10^{10}
GRB020418A	1.0×10^{8}	1.17×10^{4}	5.42×10^{7}	4.11×10^{8}	1.02×10^{3}	1.12×10^{7}
GRB020801	2.0×10^{8}	2.97×10^{3}	6.68×10^{6}	2.05×10^{8}	5.82×10^{3}	1.15×10^{7}
GRB030323	1.0×10^{8}	4.36×10^{4}	5.23×10^{8}	2.05×10^{8}	1.49×10^{4}	6.16×10^{8}
GRB030328	1.0×10^{8}	2.62×10^{4}	1.53×10^{7}	4.11×10^{8}	2.61×10^{3}	7.34×10^{6}
GRB030329A	3.1×10^{8}	1.95×10^{5}	1.72×10^{7}	3.07×10^{8}	1.56×10^{5}	8.81×10^{7}
GRB030429	1.0×10^{8}	1.33×10^{4}	8.07×10^{8}	2.05×10^{8}	4.95×10^{3}	7.79×10^{8}
GRB030528	2.0×10^{8}	2.12×10^{3}	8.09×10^{6}	2.05×10^{8}	2.80×10^{3}	1.58×10^{7}
GRB030723A	2.0×10^{8}	1.44×10^{3}	8.08×10^{8}	8.08×10^{7}	4.09×10^{4}	2.22×10^{11}
GRB030725A	1.0×10^{8}	7.84×10^{3}	9.85×10^{6}	3.07×10^{8}	1.46×10^{3}	5.69×10^{6}
GRB030823A	3.1×10^{8}	5.91×10^{4}	9.71×10^{8}	1.02×10^{8}	3.86×10^{5}	2.33×10^{10}
GRB031026B	1.0×10^{8}	3.27×10^{4}	3.08×10^{10}	2.05×10^{8}	1.12×10^{4}	5.21×10^{8}
GRB031111A	1.0×10^{8}	7.74×10^{4}	4.94×10^{9}	7.34×10^{8}	5.71×10^{3}	1.13×10^{8}
GRB050603A	1.0×10^{8}	9.46×10^{3}	3.71×10^{8}	4.11×10^{8}	1.26×10^{3}	3.27×10^{7}
GRB050724A	2.1×10^{9}	5.33×10^{2}	9.69×10^{5}	8.08×10^{7}	6.21×10^{4}	2.51×10^{10}
GRB050801A	2.0×10^{8}	3.25×10^{3}	1.82×10^{7}	1.02×10^{8}	1.04×10^{4}	4.07×10^{9}
GRB050802A	1.0×10^{8}	1.08×10^{5}	2.24×10^{8}	2.05×10^{8}	2.09×10^{4}	5.47×10^{8}

Table cont...

GRB	Burst			Afterglow		
	ϵ_ν (GeV)	Limit (GeV/cm^2)	Ratio	ϵ_ν (GeV)	Limit (GeV/cm^2)	Ratio
GRB050807A	1.0×10^{8}	9.10×10^{3}	4.93×10^{7}	3.07×10^{8}	1.54×10^{3}	1.92×10^{7}
GRB050820A	2.0×10^{8}	1.09×10^{5}	4.07×10^{8}	1.02×10^{8}	1.48×10^{5}	1.63×10^{9}
GRB050824A	7.3×10^{8}	1.31×10^{4}	8.95×10^{6}	1.02×10^{8}	1.99×10^{5}	2.12×10^{11}
GRB050826A	5.2×10^{8}	1.49×10^{3}	6.50×10^{7}	1.02×10^{8}	1.61×10^{5}	2.76×10^{11}
GRB050908A	1.0×10^{8}	2.11×10^{4}	2.01×10^{9}	2.05×10^{8}	1.20×10^{4}	6.24×10^{8}
GRB050922C	1.0×10^{8}	2.87×10^{4}	9.78×10^{8}	4.11×10^{8}	4.29×10^{3}	2.15×10^{8}
GRB051021B	3.1×10^{8}	2.92×10^{3}	6.21×10^{6}	2.05×10^{8}	1.08×10^{4}	5.52×10^{8}
GRB051022A	1.0×10^{8}	1.97×10^{5}	1.61×10^{7}	4.11×10^{8}	2.40×10^{4}	1.40×10^{7}
GRB051111A	1.0×10^{8}	4.51×10^{5}	8.27×10^{8}	2.05×10^{8}	1.25×10^{5}	1.44×10^{9}

Many factors can contribute to a good limit, which are indicated by the smallest limit to flux ratio. A large flux will not necessarily yield a good limit result. This must be combined with an optimal localisation, a small detector threshold and high livetime to produce the best result. In the case of the prompt emission a large neutrino flux is primarily dependant on the photon fluence which determines the prefactor, $\mathcal{A}$. The break energy, of course, determines where the slope changes in the neutrino flux. A small neutrino break energy corresponding to a large photon break energy will suppress the higher energy neutrinos more. Thus large neutrino break energies contribute to a larger neutrino flux at higher energies. The effective volume was also shown earlier to be largely dependant on nadir angle, with GRBs localised directly above the array or below the horizon having a significantly reduced effective volume. In Section 4.6.1 we showed the dependance of the effective volume on the detector threshold, showing a greatly reduced effective volume with increasing

detector threshold voltage. Lastly a small livetime will result in a larger limit.

In Figure 7.13 we plot the prompt neutrino fluxes and limits for the GRBs with the five largest prefactors ($\mathcal{A}$). These were GRB030329A, GRB031111A, GRB051022A, GRB020418A, and GRB050603A, in order of decreasing prefactor value. From these the largest fluences are from GRBs GRB051022A and GRB030329A, having a fluence of 261 ergs cm^{-2} and 110 ergs cm $^{-2}$ and their durations were 22.8 and 200 seconds respectively. Although these two GRBs would produce a large neutrino flux, both of these GRBs, as well as GRB031111A were located 20 or so degrees below the horizon resulting in a significantly attenuated neutrino flux. This combined with the fact that GRB030329A had the largest threshold of -0.99 and a relatively small livetime consequently increases the limit and hence limit to flux ratio. Thus these two GRBs do not appear in the top 5 best limits to flux ratios. The neutrino flux, limits and also the effective volumes are shown in Figure 7.17 for these GRBs. We see the down turn in the effective volumes at higher energies for GRB051022A, GRB030329A and GRB031111A due to attenuation effects.

In Figure 7.14 we plot the prompt neutrino fluxes and limits for the GRBs with the smallest neutrino flux to limit ratios. These are for GRB050724A, GRB051021B, GRB020801, GRB030528, and GRB050824A. We see in the figure that none of the GRBs from the top five largest prefactors give the best limits. As mentioned above attenuation effects come into play with a reduction in the effective volume. Also we see from Figure 7.14 that these neutrino fluxes have relatively greater break energies, which as mentioned above contributes more higher energy neutrinos to the flux for which correspond to a greater effective volume at the higher energy end.

We see in Figure 7.18 that the effective volumes are large and unattenuated for all except GRB050824A. We attribute its good ratio to the large high energy neutrino component.

In the afterglow case, the neutrino flux and limits for the five GRBs with the largest prefactor, ($\mathcal{B}$), are shown in Figure 7.15. These are for GRB031111A, GRB030329A, GRB051022A, GRB020418A, and GRB050603A, in increasing value. As in the prompt case, GRB030329A and GRB051022A as well as GRB031111A are located below the horizon. Figure 7.19 shows the largest afterglow prefactor fluxes, limits and effective volumes. The effective volume for the below horizon GRBs show the expected down turn in volume due to attenuation effects. GRB051022A the largest fluence GRB, however survives to be one of the top five best limits. GRB030725A, GRB030328, GRB020418A, GRB020801, and GRB051022A are the five GRBs with the best flux to limit ratios in decreasing order. These are shown in Figure 7.16. This is due to their large effective volumes. Their prefactor values are average, as are their livetimes and discriminator settings. These fluxes, limits and effective volumes are shown in Figure 7.20.

7.7 Source Stacking

Other GRB point source searches have been undertaken [4, 5, 193, 1, 2, 3, 6] and have observed no significant excess neutrino signal above background. Individually these point sources offer a very weak signal, and with current detector sizes a low individual event rate. Although individually weak an accumulative signal which is stronger has not been ruled out. In the case of a non-observation of a neutrino signal, source stacking can be used to obtain a better limit on the GRB neutrino flux. This

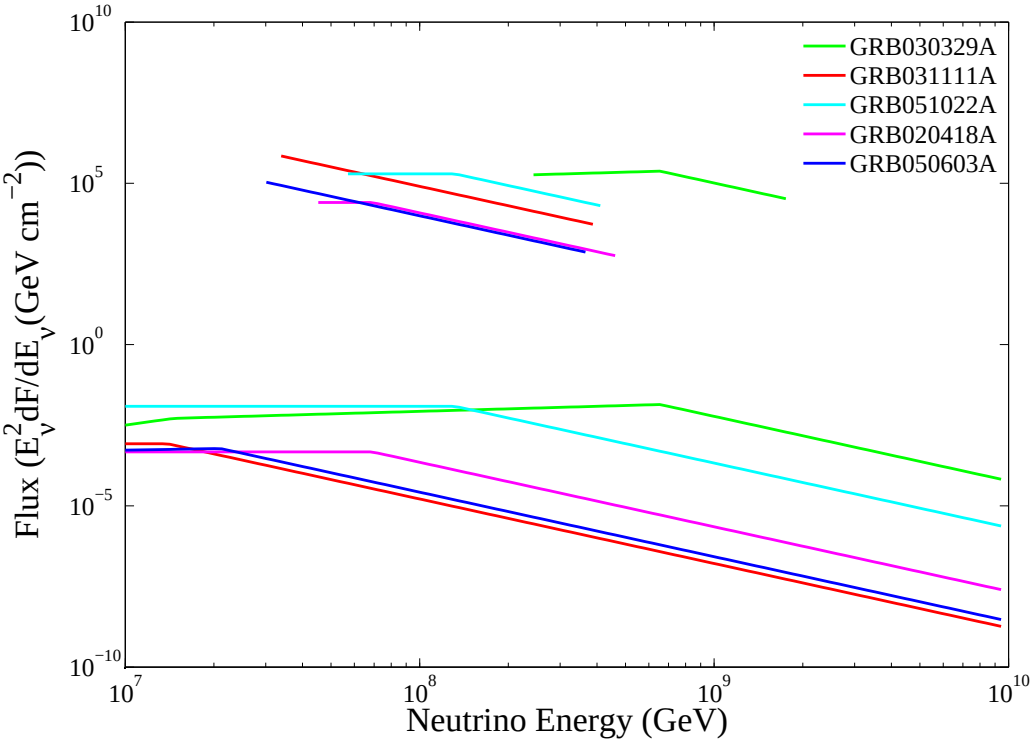

Figure 7.13: Prompt neutrino flux and flux limits for the five GRBs with the largest prefactor, $\mathcal{A}$.

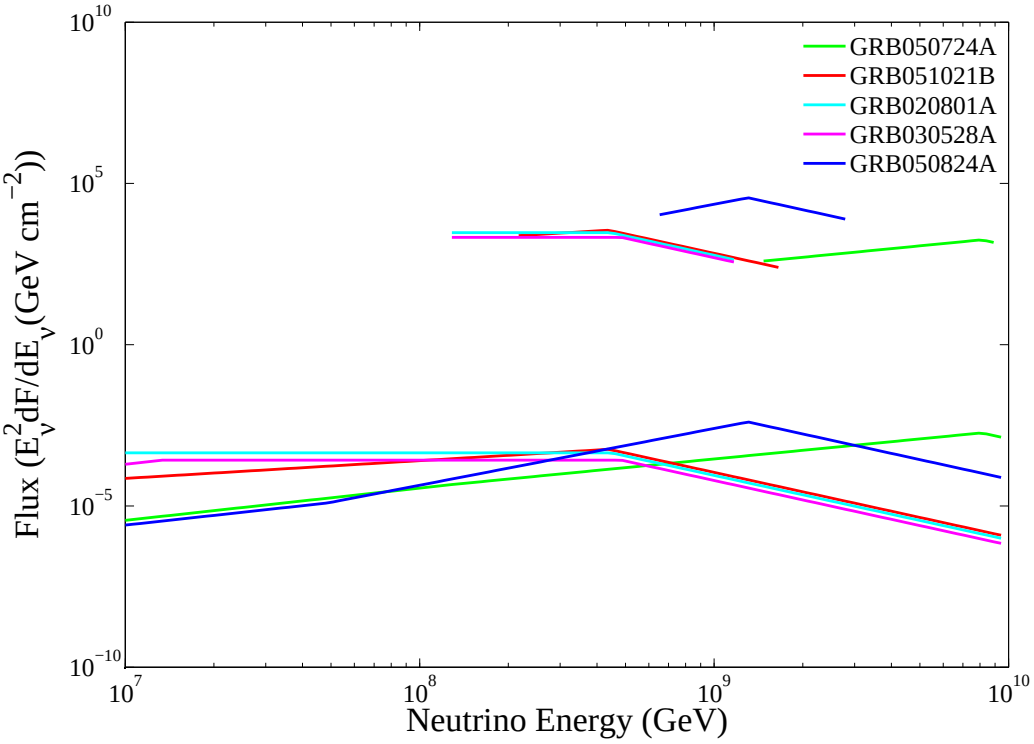

Figure 7.14: Prompt neutrino flux and flux limits for the five GRBs with the smallest limit to flux ratios.

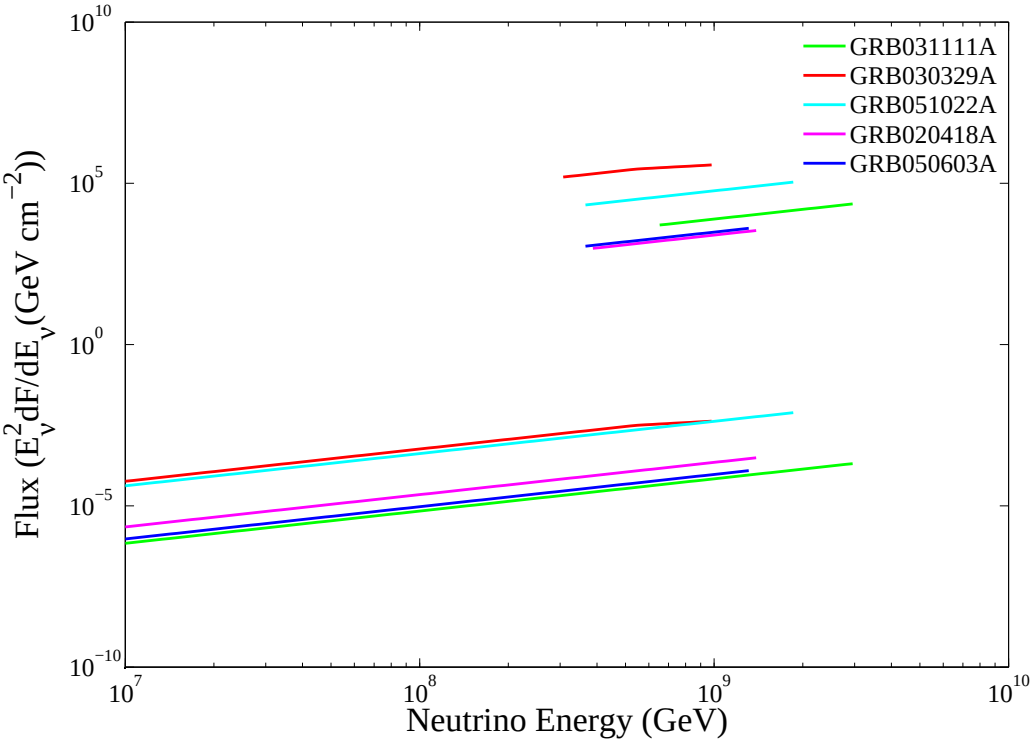

Figure 7.15: Afterglow neutrino flux and flux limits for the five GRBs with the largest prefactor, $\mathcal{B}$.

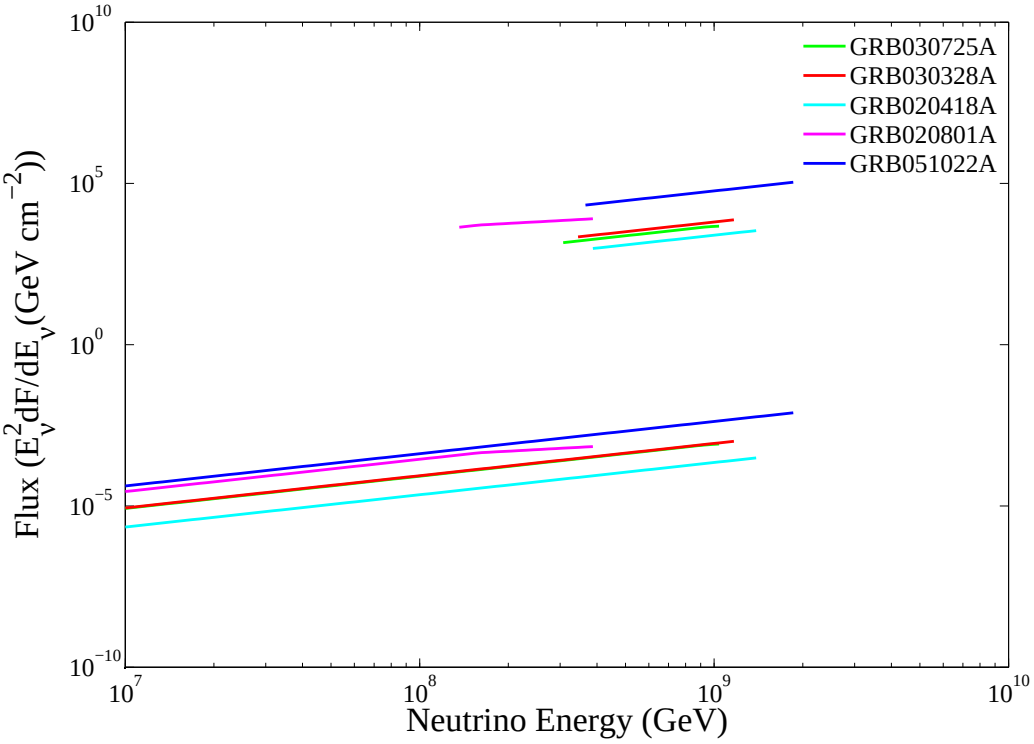

Figure 7.16: Afterglow neutrino flux and flux limits for the five GRBs with the smallest limit to flux ratios.

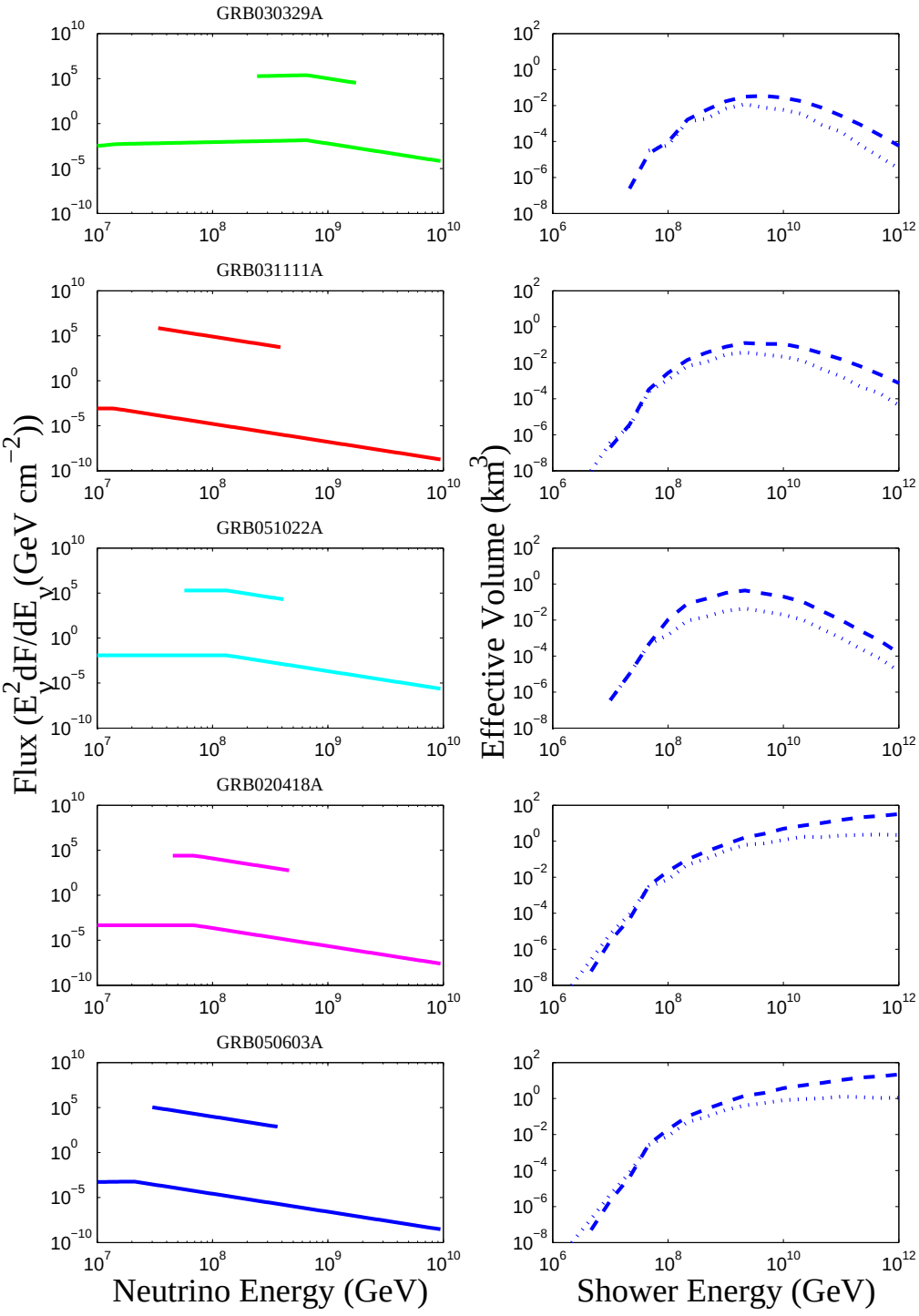

Figure 7.17: Prompt neutrino fluxes, limits and their effective volumes for GRBs with the largest prefactors, ($\mathcal{A}$), in descending order of largest to smallest value.

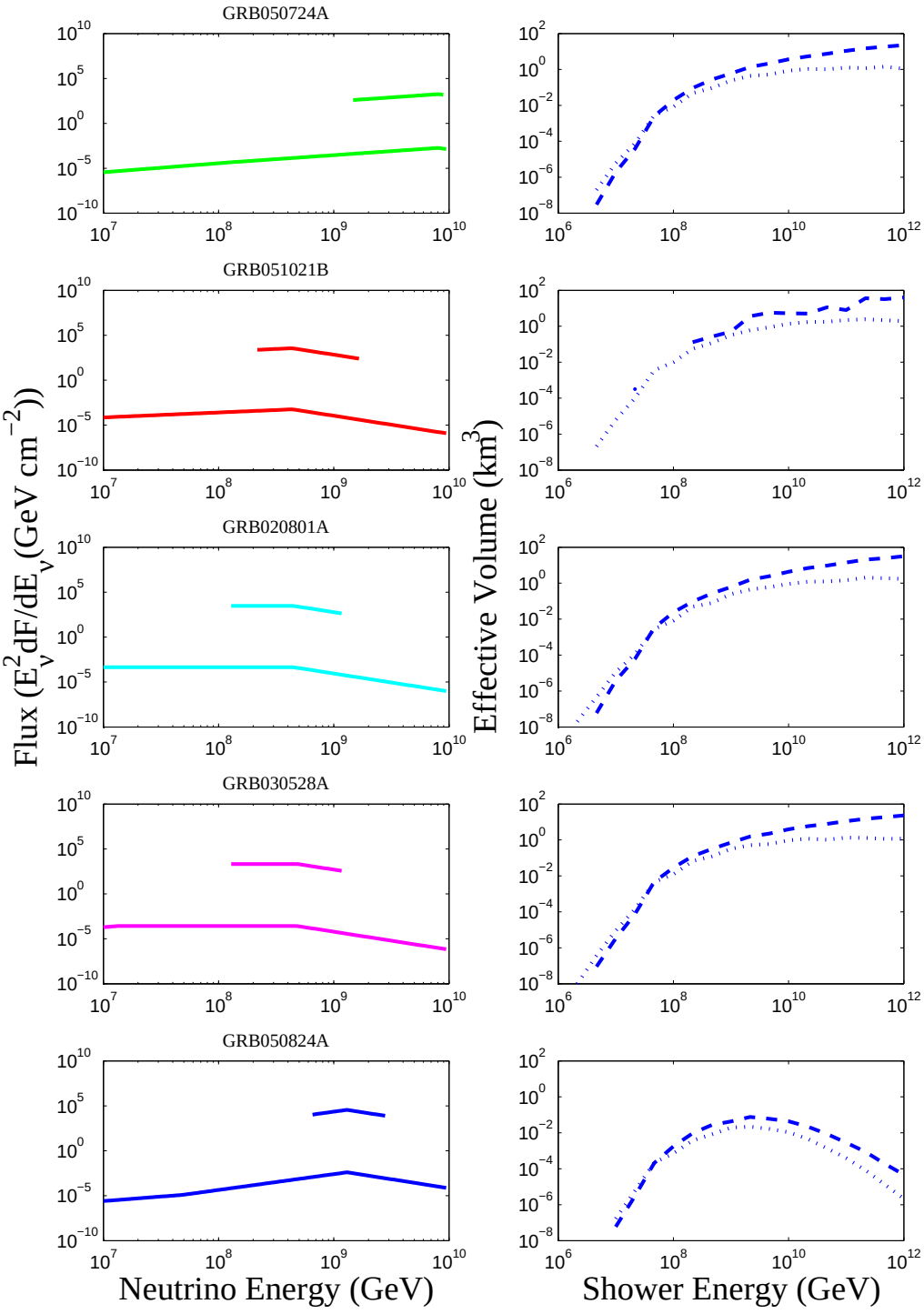

Figure 7.18: Prompt neutrino fluxes, limits and effective volumes for GRBs with the smallest limit to flux ratios, descending in order of smallest to largest.

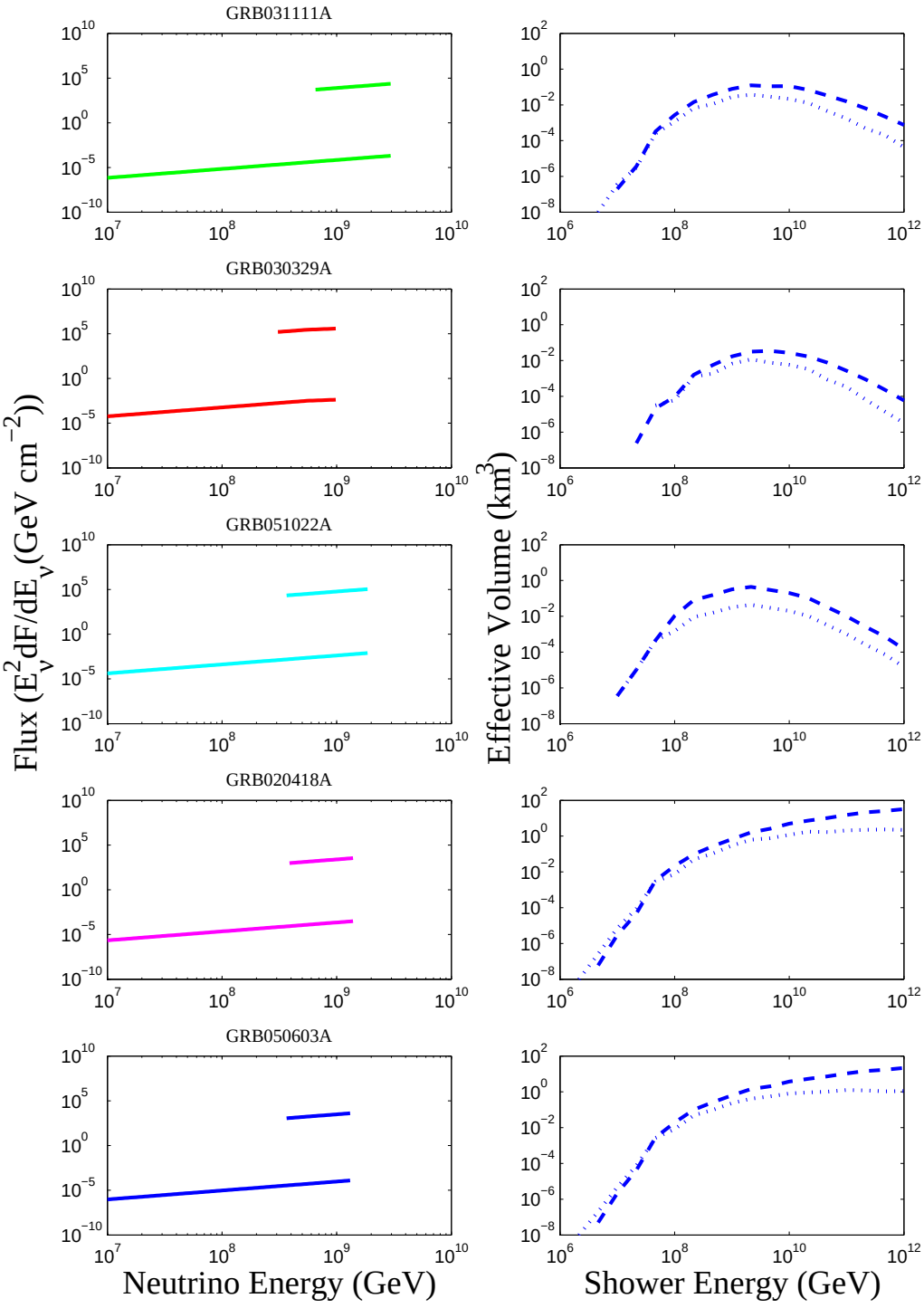

Figure 7.19: Afterglow neutrino fluxes, limits and their effective volumes for GRBs with the largest prefactors, ($\mathcal{B}$), in descending order of largest to smallest value.

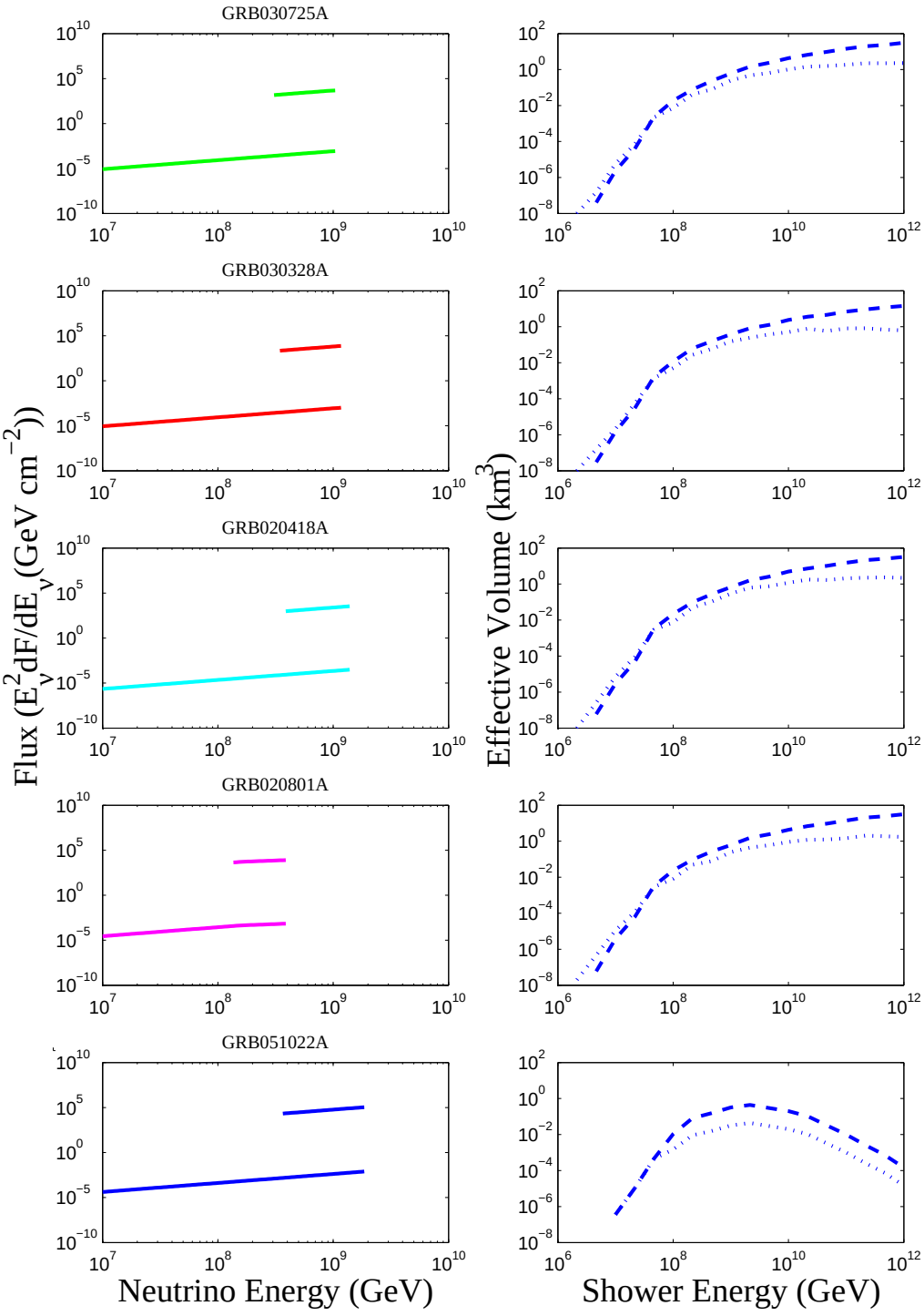

Figure 7.20: Afterglow neutrino fluxes, limits and effective volumes for GRBs with the smallest limit to flux ratios, descending in order of smallest to largest.

has been applied elsewhere for an AGN neutrino analysis [194] and more commonly in gamma-ray astronomy [195, 196].

Here we stack the neutrino fluxes for the 27 GRBs with known redshifts. The individual fluxes are stacked or summed to give an accumulative flux. Using these with the total durations, the average effective volume and livetimes, limits can be set. Figure 7.21 shows the stacked fluxes and limits of the 27 known redshift GRBs for afterglow and prompt emission phases. The total neutrino flux is shown by the set of lower lines in Figure 7.21 for 27 GRBs with known redshifts for both burst (dashed) and afterglow (solid) phases. The higher set of lines are the upper limits inferred using the stacked neutrino flux and the RICE array effective volumes for individual bursts.

7.8 Event Rates

In this last section we present the predictions for the event rates for the most powerful of the known redshift subset, along with predictions using the projected effective volume for the next generation AURA 8 cluster deployment configuration. The effective volume is shown in Figure 7.22. We do not take into account their position in the sky and just use the diffuse result for AURA integrated over the upper $2\pi sr$ above the detector. This is done for indicative purposes only, to look at the capability of AURA to detect individual bursts.

Tables 7.8 and 7.9 show the prompt and afterglow event rates for RICE and the next generation AURA detector, per burst and for 200 GRBs. Although there is usually only a handful of the most powerful bursts per year, we show these results to

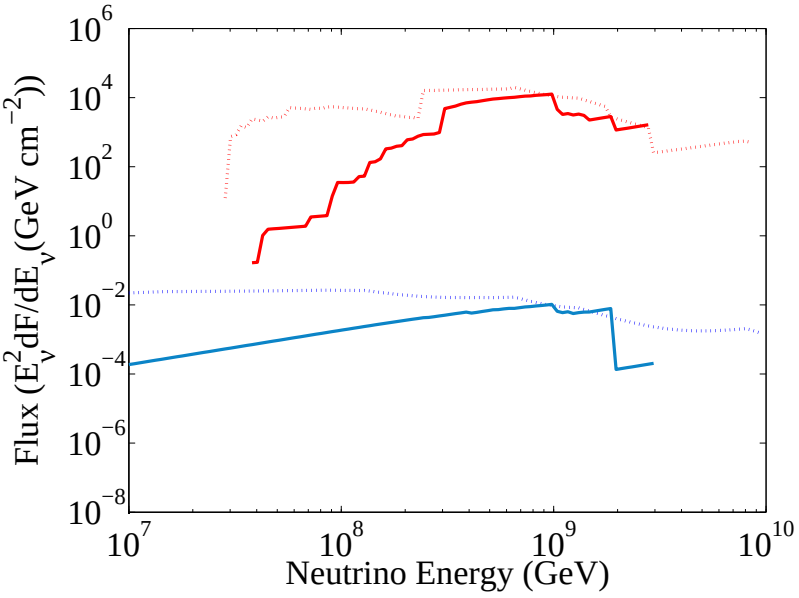

Figure 7.21: Upper limits on the total stacked flux from the 27 GRBs with known redshift, with an assumed isoflavour mix at the detector.The lower pair of lines are the stacked predicted prompt (dashed) and afterglow (solid) neutrino flux using the WB models discussed in Chapter 3. The higher set are the upper limits inferred using the stacked neutrino flux and the RICE array effective volumes for individual bursts.

get an idea of the number of event predicted for 200 similar types of bursts. In order to get an event rate for the AURA-8-cluster configuration, of the order of 1, requires the observation of 200 GRBs similar to GRB030329A, for which was particularly powerful with a fluences of 110 erg cm^{-2}. This strength of burst is uncommon. The event rates of the RICE configuration yields low event predictions. With AURA-8 however we would expect to see an improved event rate of 3 to 4 orders of magnitude.

Table 7.8: The predicted event rates for RICE and AURA's 8 cluster configuration for prompt and afterglow phases for the five largest fluence GRBs.

Event Rates per GRB	RICE		AURA		
GRB Name	Prompt	Afterglow	Prompt	Afterglow	Duration
GRB030329A	4.42×10^{-7}	8.62×10^{-8}	6.72×10^{-3}	1.13×10^{-3}	22.8
GRB03111A	7.95×10^{-10}	3.47×10^{-8}	1.51×10^{-5}	4.57×10^{-5}	5.3
GRB051022A	3.05×10^{-7}	3.50×10^{-7}	3.10×10^{-3}	1.77×10^{-3}	200
GRB020418A	7.13×10^{-8}	3.46×10^{-7}	6.89×10^{-5}	6.98×10^{-5}	15
GRB050603A	1.09×10^{-8}	1.24×10^{-7}	2.08×10^{-5}	5.77×10^{-5}	12.4

Table 7.9: The predicted event rates for 200 GRBs for RICE and AURA's 8 cluster configuration for prompt and afterglow phases for the five largest fluence GRBs.

Event Rates for 200 GRBs	RICE		AURA		
GRB Name	Prompt	Afterglow	Prompt	Afterglow	Duration
GRB030329A	8.84×10^{-5}	1.72×10^{-5}	1.34	2.26×10^{-1}	22.8
GRB03111A	1.59×10^{-7}	6.95×10^{-6}	3.01×10^{-3}	9.14×10^{-3}	5.3
GRB051022A	6.10×10^{-5}	7.00×10^{-5}	6.20×10^{-1}	3.54×10^{-1}	200

GRB020418A	1.43×10^{-5}	6.92×10^{-5}	1.38×10^{-2}	1.40×10^{-2}	15
GRB050603A	2.17×10^{-6}	2.47×10^{-5}	4.16×10^{-3}	1.15×10^{-2}	12.4

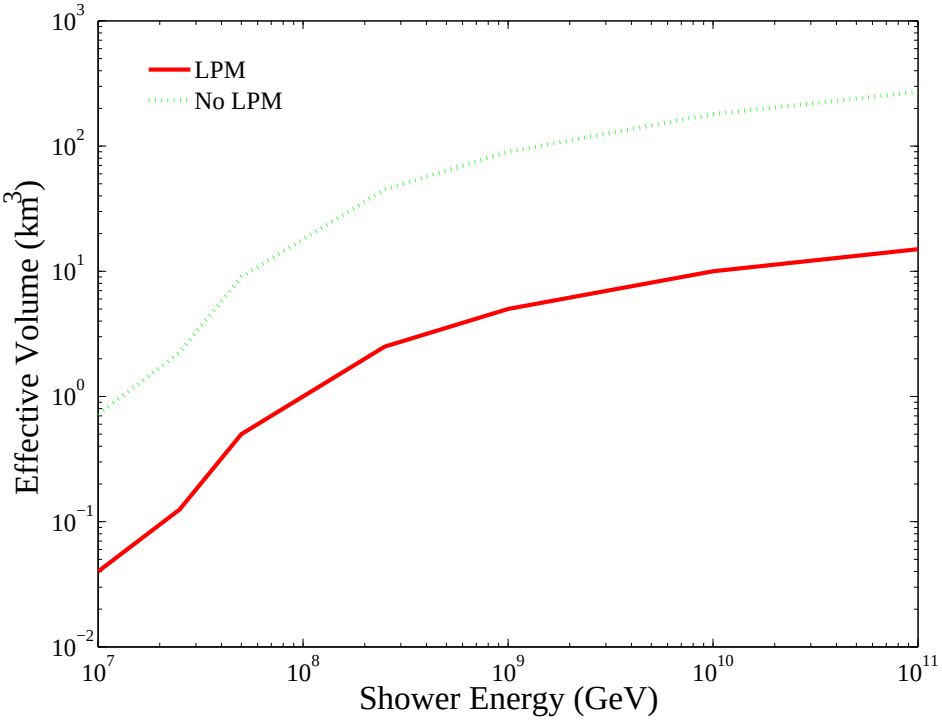

Figure 7.22: The effective volumes with (dashed) and without LPM (solid) effects for the next generation AURA detector for the 8-cluster configuration.

Chapter 8

Discussion and Conclusion

In this thesis we searched for high energy neutrino events in coincidence with GRBs between the years 2001 and 2005 using the Radio Ice Cherenkov Experiment. We searched RICE data within a $\pm$ 600 second time window of 77 GRB events triggered by the IPN. We also required that these GRBs were localisable within the RICE effective zone in the sky which was loosely defined from 30 degrees below the horizon at the South pole and going near the zenith point. The search method was independent of the main analysis technique, involving a more interactive approach for which yielded a greater overall analysis efficiency of 72% compared to 60% of the regular regime. No evidence of a temporal correlation was found. Using the null result, model dependant neutrino flux upper limits for coincident emission with prompt and afterglow photons have been derived at the 95 confidence level for $E_\nu \geq$ 1PeV. Similar neutrino GRB correlation studies have been undertaken by IMB-3 (Irvine-Michigan Brookhaven) [4], AMANDA (Antarctic Muon and Neutrino Array) [5, 193], Super Kamiokande (SK)[1, 2], MACRO (Monopole Astrophysics and Cosmic Ray Observatory)[3] and the LSD (Liquid Scintillator Detector) [6] projects. Unlike the background free RICE all of these projects had some detectable neutrino events from

identifiable and unidentifiable sources. Thus their searches were aimed to determine whether their particular neutrino events were attributable to GRB neutrinos. This was done using time correlation and sometimes directional correlation analysis. All yielded no evidence of a neutrino signal in coincidence with GRBs above their backgrounds.

8.1 GRB-Neutrino Searches

The neutrino GRB correlation searches have been primarily undertaken in the 1990's making use of the complete BATSE GRB catalog [197]. All were in a variety of energy ranges yielding limits from 10^{10} to 10^{-5} GeV cm^{-2}. The IMB-3 (Irvine-Michigan Brookhaven) analysis searched for a correlated neutrino signal with photon emission from GRBs, using BATSE triggers. This group yielded earlier limits of 2×10^4ergs cm^{-2} [198] in an analysis of 183 gamma ray bursts and in a later analysis a limit of 1.2×10^2 cm^{-2} was obtained [4].

The AMANDA [5] analysis searched for neutrinos in coincidence with 73 GRBs reported by BATSE in 2000. Later Hughey [193] extended the study to include more data. The first study yielded no correlation and set limits of a Waxman and Bahcall like spectrum for all flavours at the 90 percent confidence level of 9.5×10^{-7}GeV cm^{-2} s^{-1} sr^{-1}.

MACRO [3] searched for correlations between 1085 upward going muon events and 2328 GRBs in the BATSE 3B and 4B[197] catalogs between 1991 and 1999. They found no statistically significant correlation between MACRO and GRB events in

time or direction. The muon neutrino flux limit for the 2527 GRBs from BATSE was 3.17×10^{-8} cm^{2}s^{-1} and for 32 bursts observed by BeepoSAX was 1.27×10^{-7} cm^{2}s^{-1}.

Super Kamiokande data was searched for neutrinos produced in coincidence with GRBs observed by the BATSE catalog [197] between 1996 and 2000. With no statistically significant excess found above background, limits were set in the energy range of 7 MeV to 100 TeV [1, 2]. Limits in the 2 GeV to 100 TeV energy range were 3.83×10^{-2}cm^{-2} for muon neutrinos.

The LSD(Liquid-Scintillator Detector) neutrino telescope conducted a search for low energy neutrinos, $\nu_{\mu,e,\tau}$ in correlation with 200 GRBs from the BATSE catalog [197]. No candidates were detected and limits to the 90% confidence for 197 of the GRBs were estimated at 1.5×10^{11} cm^{-2} between the energies 9 MeV to 50 MeV [6].

These limits and the stacked RICE limits span over a large energy range from 9 MeV to 10 EeV. We compare these in Figure 8.1. Where limits were obtained per second, an average GRB time of 2s was used and multiplied by the number of GRBs to obtain the correct units. We see that the best bounds yielded thus far have been by the AMANDA group, for which by far had the largest effective volume of all experiments, although RICE's limits are several orders of magnitude weaker, they occur in a higher energy range than other experiments.

8.2 Predicted Event Rates

The predicted event rates were presented in Chapter 7 for five bursts which had the largest flux values. We also calculated the predicted event rate using the projected

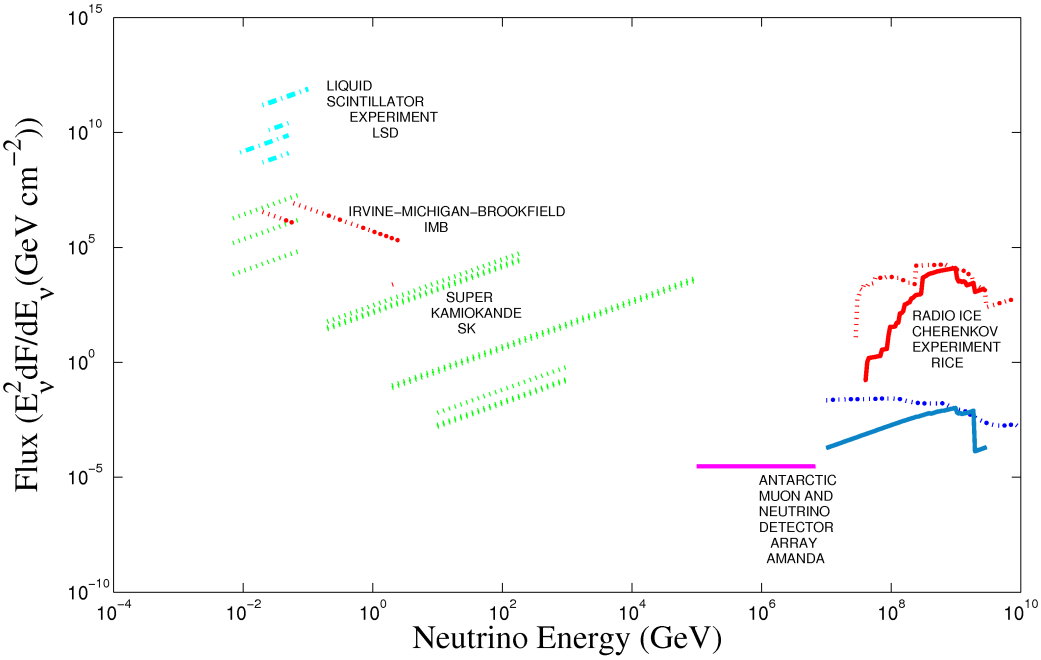

Figure 8.1: GRB upper limits, for Super KamiokandeSK[1, 2], MACRO[3], IMB[4], AMANDA[5], LSD[6] and RICE.

effective volume of AURA for the 8 cluster configuration. We do not account for attenuation effects in the AURA event prediction and use the effective volume which is averaged over the upper 2π ster radian. We see that in Tables 7.8 and 7.9 the event numbers for individual bursts and then the later table the event rates multiplied by 200. In order to have an event rate of around 1 in AURA (8 cluster configuration) requires 200 bursts the same or greater than GRB030329A which had a large fluence of 110 ergs cm^{-2}. However, this burst was particularly powerful and uncommon. Both RICE and the AURA-8 configuration however are not large enough to be sensitive to detecting the neutrino flux of individual GRBs.

However for feasible event rates of 1-5 years we would have to have a larger volume by 200 times. A larger configuration GZK energy neutrino detector has been mooted called IceRay. The design incorporate detectors buried 20m to 200m in the ice. A hybrid detector which contains acoustic antenna has also been proposed and incorporates Ice-Cube, Iceray, and ice top technology. Larger configurations have been mooted with the proposed IceRay project, which is a radio array much larger than RICE or the proposed AURA-8.

8.3 Conclusions

Neutrino astronomy seeks to open another window with which to view the Universe. Large scale neutrino detectors provide a unique view of catastrophic events in the Universe but the detection of neutrinos is logistically difficult. The neutrino interaction probability is extremely small and combined with the low expected fluxes this means that a large detecting volume is needed. The volume required to probe the neutrino

flux that is expected to be produced in extragalactic sources is such that only a detector utilising a natural resource is feasible. The Radio Ice Cherenkov Experiment (RICE) employs the Antarctic ice. Located at the South Pole, RICE is designed to detect radio signals from the electromagnetic showers produced by the interaction of high energy neutrinos in the ice. Radio wave detection of electromagnetic showers exploits the long attenuation lengths of up to 1 km in polar ice and the coherence extending up to 1 GHz for radio Cherenkov emission. In this thesis I presented the results of a neutrino search of the RICE data collected between 2001 to 2005. 444 GRBs were detected during this period. However the analysis was limited to GRBs that localised within the sensitivity zone of RICE. These were 77 GRBs, 27 of which had redshift information and 50 without. Monte Carlo simulations were run with neutrino incident direction corresponding to each GRB localisation. We analysed the RICE data in small time windows of $\pm$600s around each GRB time using an efficient By-Eye method for determining the receiver hit times. This yielded a null result. Using the effective volume of RICE appropriate for each GRB we calculated neutrino flux limits for the GRBs using the models of Waxman and Bahcall [42, 43].

Although the flux limits are several orders of magnitude weaker than the expected flux, the RICE GRB neutrino limits are the only limits in the PeV to EeV energy range. Future improvements in sensitivity will be realised by enlarging the scale of the radio detector array as well as improved individual GRB parameter measurements. The former will be realised with the planned construction of AURA [90] and progress on the latter is already occurring with the launch of SWIFT in 2004.

March 4, 2009©

Bibliography

[1] S. Fukuda et al. Search for neutrinos from gamma-ray bursts using super-kamiokande. *APJ*, 578:317–324, 2002.

[2] D. Turcan and Super-KAMIOKANDE Collaboration. Search for Neutrinos from Gamma-Ray Bursts Using Super-Kamiokande. In *International Cosmic Ray Conference*, volume 5, page 2713, July 2003.

[3] T. Montaruli. MACRO as a Telescope for Neutrino Astronomy. *Proceedings of the 26th International Cosmic Ray Conference. August 17-25, 1999. Salt Lake City, Utah, USA. Under the auspices of the International Union of Pure and Applied Physics (IUPAP).*, 1999.

[4] R. Becker-Szendy et al. A serach for moderate- and high-energy neturino emission correlated with gamma-ray bursts. *ApJ*, 444:415–418, May 1995.

[5] R. Hardtke and The AMANDA Collaboration. The AMANDA Search for High Energy Neutrinos from Gamma-Ray Bursts. In *International Cosmic Ray Conference*, volume 3 of *International Cosmic Ray Conference*, page 1121, 2001.

[6] M. Aglietta et al. Search for low-energy ν_e, ν_μ, ν_τ in coincidence with batse gamma-ray bursts. *Il Nuovo Cimento C*, 5:457–462, 1995.

[7] A. De Gouvea. Tasi lectures on neutrino physics. *hep-ph/0411274v1*, 2004.

[8] H. Bethe and R. Peierls. The neutrino. *Nature*, 532, 1934.

[9] S. M. Bilenky. Bruno Pontecorvo: mister neutrino. *physics/0603039*, March 2006.

[10] C. L. Jr. Cowan et al. Detection of the free neturino: A confirmation. *Science See Saiensu; Vol: 124*, page 103, 1956.

[11] A. Aguilar et al. Evidence for neutrino oscillations from the observation of electron anti-neutrinos in a muon anti-neutrino beam. *Phys.Rev.D*, 64:112007, 2001.

[12] A. Aguilar et al. Search for electron neutrino appearance at the $\delta_m^2 \approx 1ev^2$ scale. *Phys.Rev.Lett*, 98(23):231801, 2007.

[13] The Super-Kamiokande Collaboration and Y. Fukuda et al. Evidence for oscillation of atmospheric neutrinos. *Phys.Rev.Lett*, 81:1562, 1998.

[14] MACRO Collaboration et al. Atmospheric neutrino oscillations from upward throughgoing muon multiple scattering in MACRO. *Phys.Lett.B*, 566:35–44, July 2003.

[15] The Soudan 2 Collaboration. Observation of Atmospheric Neutrino Oscillations in Soudan 2. *ArXiv High Energy Physics - Experiment e-prints*, July 2003.

[16] SNO Collaboration. Direct evidence for neutrino flavour transformation from neutral-current interactions in the sudbury neutrino observatory. *Phys.Rev.Lett*, 89:011301, 2002.

[17] M. Ishitsuka and for the Super-Kamiokande Collaboration. Super Kamiokande results: atmospheric and solar neutrinos. *hep-ex/0406076*, June 2004.

[18] KamLAND Collaboration. First results from kamland: Evidence for reactor anti-neutrino disappearance. *Phys.Rev.Lett*, 90:021802, 2003.

[19] E. Aliu et al. Evidence for Muon Neutrino Oscillation in an Accelerator-Based Experiment. *Phys.Rev.Lett*, 94(8):081802, March 2005.

[20] N. N. Efimov et al. The Energy Spectrum and Anisotropy of Primary Cosmic Rays at Energy $E_0 > 10^{17}$ eV Observed in Yakutsk. In M. Nagano and F. Takahara, editors, *Astrophysical Aspects of the Most Energetic Cosmic Rays*, page 20, 1991.

[21] N. Hayashida et al. Observation of a Very Energetic Cosmic Ray Well Beyond the Predicted 2.7 K Cutoff in the Primary Energy Spectrum. *Phys. Rev. Lett.*, 73(26):3491–3494, December 1994.

[22] D. J. Bird et al. Evidence for correlated changes in the spectrum and composition of cosmic rays at extremely high energies. *Phys.Rev.Lett.*, 71(21):3401–3404, November 1993.

[23] F. Halzen. Lectures on High-Energy Neutrino Astronomy. *Advanced Summer School in Physics 2005: Frontiers in Contemporary Physics; EAV'05, held 11-22 July, 2005 in Cinvestav, Mexico City, Mexico. AIP Conference Proceedings,*, 2006.

[24] E. Waxman. Cosmological origin for cosmic rays above. *ApJ*, 452:L1, 1995.

[25] E. Waxman. High energy neutrinos from gamma-ray bursts. *NuPhB Proceedings Supplements*, 91(1-3):494–500, 2001.

[26] G. Hill and AMANDA Collaboration. Searching for High Energy Muon Neutrinos from Gamma-Ray Bursts with AMANDA. 5:2717, July 2003.

[27] M. Aglietta et al. Search for low-energy $\nu_{e,\mu,\tau}$ and $\bar{\nu}_{e,\mu,\tau}$ in coincidence with BATSE gamma-ray bursts. *Nuovo Cimento C Geophysics Space Physics C*, 18:457–462, October 1995.

[28] M. Aglietta et al. The LVD experiment at Gran Sasso. *Nuovo Cimento C Geophysics Space Physics C*, 18:629–645, December 1995.

[29] R. J. Protheroe. High Energy Neutrinos from Blazars. In D. T. Wickramasinghe, G. V. Bicknell, and L. Ferrario, editors, *IAU Colloq. 163: Accretion Phenomena and Related Outflows*, volume 121 of *Astronomical Society of the Pacific Conference Series*, page 585, 1997.

[30] K. Mannheim. High-energy neutrinos from extragalactic jets. *APh*, 3:295–302, 1995.

[31] F.W. Stecker. Diffuse fluxes of cosmic high-energy neutrinos. *ApJ*, 228(Part 1), 1979.

[32] V. S. Berezinskij and G. T. Zatsepin. Cosmic rays at ultrahigh energies (neutrino?). *Phys.Lett.B*, 28:423–424, 1969.

[33] K. Greisen. End to the Cosmic-Ray Spectrum? *Phys. Rev. Lett.*, 16:748, 1966.

[34] G. T. Zatsepin and V. A. Kuz'min. Upper Limit of the Spectrum of Cosmic Rays. *ZhETF Pis ma Redaktsiiu*, 4:114, August 1966.

[35] G. T. Zatsepin and V. A. Kuz'min. Upper Limit of the Spectrum of Cosmic Rays. *Soviet Journal of Experimental and Theoretical Physics Letters*, 4:78, August 1966.

[36] R. Engel, D. Seckel, and T. Stanev. Neutrinos from propagation of ultrahigh energy protons. *Phys.Rev.D*, 64(9):093010, November 2001.

[37] R. J. Protheroe and P. A. Johnson. Propagation of ultra high energy protons and gamma rays over cosmological distances and implications for topological defect models (Astroparticle Physics 4 (1996) 253). *Astroparticle Physics*, 5:215–215, August 1996.

[38] O. E. Kalashev, V. A. Kuzmin, D. V. Semikoz, and G. Sigl. Ultrahigh-energy neutrino fluxes and their constraints. *Phys.Rev.D*, 66(6):063004, September 2002.

[39] R. J. Protheroe and T. Stanev. Limits on Models of the Ultrahigh Energy Cosmic Rays Based on Topological Defects. *Physical Review Letters*, 77:3708–3711, October 1996.

[40] R. J. Protheroe and T. Stanev. Limits on Models of the Ultrahigh Energy Cosmic Rays Based on Topological Defects. *Phys.Rev.Lett*, 78:3420, April 1997.

[41] E. Waxman and J. Bahcall. High energy neutrinos from astrophysical sources: An upper bound. *Phys.Rev.D*, 59:023002, 1999.

[42] E. Waxman and J. Bahcall. High Energy Neutrinos from Cosmological Gamma-Ray Burst Fireballs. *Phys.Rev.Lett*, 78:2292–2295, March 1997.

[43] E. Waxman and J.N. Bahcall. Neutrino Afterglow from Gamma-Ray Bursts: 10^{19} eV. *ApJ*, 541:707–711, 2000.

[44] Z. G. Dai and T. Lu. Neutrino Afterglows and Progenitors of Gamma-Ray Bursts. *ApJ*, 551:249–253, April 2001.

[45] S. Razzaque, P. Mészáros, and E. Waxman. High Energy Neutrinos from Gamma-Ray Bursts with Precursor Supernovae. *Phys.Rev.Lett*, 90(24):241103, June 2003.

[46] S. Razzaque, P. Meszaros, and E. Waxman. Neutrino signatures of the supernova - gamma ray burst relationship. *Phys.Rev.D*, 69:023001, 2004.

[47] J. K. Becker. High-energy neutrinos in the context of multimessenger physics. *arXiv:0710.1557B*, 710, October 2007.

[48] P. Cherenkov. Visible glow under exposure of gamma-radiation. *Dokl. Acad. Nauk. USSR*, 2:451, 1934.

[49] P. Cherenkov. *Dokl. Acad. Nauk. USSR*, 14:107, 1937.

[50] The ANTARES Collaboration. ANTARES Collaboration Proceedings of ICRC 2007. *arXiv:0711.2683T*, 711, November 2007.

[51] V. Vasiliev, f. t. NEMO 3, and SuperNEMO Collaborations. Search for bb decay with NEMO 3 and SuperNEMO experiments. *ArXiv e-prints*, 710, October 2007.

[52] The NESTOR Collaboration. A measurement of the cosmic-ray muon flux with a module of the NESTOR neutrino telescope. *Astroparticle Physics*, 23:377–392, May 2005.

[53] S. E. Tzamarias. Operation and performance of the NESTOR test detector: A measurement of the atmospheric muon flux. *NuPhB Proceedings Supplements*, 143:355–358, June 2005.

[54] A. Kappes and KM3NeT Consortium. KM3NeT: A Next Generation Neutrino Telescope in the Mediterranean Sea. *ArXiv e-prints*, 711, November 2007.

[55] A. Achterberg et al. Multiyear search for a diffuse flux of muon neutrinos with AMANDA-II. *Phys.Rev.D*, 76(4):042008, August 2007.

[56] A. Karle et al. IceCube - the next generation neutrino telescope at the South Pole. *NuPhB Proceedings Supplements*, 118:388–395, April 2003.

[57] B. Price. *APP*, 5:43, 1996.

[58] G. A. Askaryan. LETTERS TO THE EDITORS: Self-acceleration of a flux of charged particles by induction. *Journal of Nuclear Energy*, 3:42–44, January 1961.

[59] F. Halzen, E. Zas, and T. Stanev. Radiodetection of High Energy Neutrinos: Monte Carlo simulation of pulses in ice. In *International Cosmic Ray Conference*, volume 4 of *International Cosmic Ray Conference*, page 686, August 1991.

[60] E. Zas, F. Halzen, and T. Stanev. Electromagnetic pulses from high-energy showers: Implications for neutrino detection. *Phys.Rev.D*, 45:362–376, January 1992.

[61] J. Alvarez-Muñiz, E. Marqués, R. A. Vázquez, and E. Zas. Comparative study of electromagnetic shower track lengths in water and implications for Čerenkov radio emission. *Phys.Rev.D*, 68(4):043001, August 2003.

[62] J. Alvarez-Muñiz, R. A. Vázquez, and E. Zas. Calculation methods for radio pulses from high energy showers. *Phys.Rev.D*, 62(6):063001, September 2000.

[63] J. Alvarez-Muñiz, E. Marqués, R. A. Vázquez, and E. Zas. Coherent radio pulses from showers in different media: A unified parametrization. *Phys.Rev.D*, 74(2):023007, July 2006.

[64] S. Razzaque et al. Coherent radio pulses from GEANT generated electromagnetic showers in ice. *Phys.Rev.D*, 65(10):103002, May 2002.

[65] S. Razzaque, P. Mészáros, and E. Waxman. Neutrino signatures of the supernova: Gamma ray burst relationship. *Phys.Rev.D*, 69(2):023001, January 2004.

[66] R. V. Buniy and J. P. Ralston. Radio detection of high energy particles: Coherence versus multiple scales. *Phys.Rev.D*, 65(1):016003, January 2002.

[67] S. K. Mandal, S. R. Klein, and J. D. Jackson. Cherenkov radiation from e^+e^- pairs and its effect on ν_e induced showers. *Phys.Rev.D*, 72(9):093003, November 2005.

[68] J. Alvarez-Muñiz, R. A. Vázquez, and E. Zas. Characterization of neutrino signals with radiopulses in dense media through the Landau-Pomeranchuk-Migdal effect. *Phys.Rev.D*, 61(2):023001, January 2000.

[69] S. Hussain and D. W. McKay. Comparative study of radio pulses from simulated hadron-, electron-, and neutrino-initiated showers in ice in the GeV-PeV range. *Phys.Rev.D*, 70(10):103003, November 2004.

[70] D. Saltzberg et al. Observation of the askaryan effect: Coherent microwave cherenkov emission from charge asymmetry in high-energy particle cascades. *Phys. Rev. Lett.*, 86(13):2802–2805, March 2001.

[71] P. W. Gorham, ANITA Collaboration, et al. Observations of the askaryan effect in ice. *Phys.Rev.Lett*, 99(17):171101, 2007.

[72] P. W. Gorham et al. Accelerator measurements of the Askaryan effect in rock salt: A roadmap toward teraton underground neutrino detectors. *Phys.Rev.D*, 72(2):023002, July 2005.

[73] J. Alvarez-Muñiz, R. A. Vázquez, and E. Zas. Calculation methods for radio pulses from high energy showers. *Phys.Rev.D*, 62(6):063001, September 2000.

[74] J. Alvarez-Muñiz, E. Marqués, R. A. Vázquez, and E. Zas. Comparative study of electromagnetic shower track lengths in water and implications for Čerenkov radio emission. *Phys.Rev.D*, 68(4):043001, August 2003.

[75] S. Razzaque et al. Coherent radio pulses from GEANT generated electromagnetic showers in ice. *Phys.Rev.D*, 65(10):103002, May 2002.

[76] R. V. Buniy and J. P. Ralston. Radio detection of high energy particles: Coherence versus multiple scales. *Phys.Rev.D*, 65(1):016003, January 2002.

[77] S. Hussain and D. W. McKay. Comparative study of radio pulses from simulated hadron-, electron-, and neutrino-initiated showers in ice in the GeV-PeV range. *Phys.Rev.D*, 70(10):103003, November 2004.

[78] S. Hoover and the ANITA collaboration. Status of the ANITA experiment. *Journal of Physics Conference Series*, 81:2009, September 2007.

[79] N. G. Lehtinen et al. FORTE satellite constraints on ultrahigh energy cosmic particle fluxes. *Phys.Rev.D*, 69(1):013008, January 2004.

[80] P. W. Gorham et al. Experimental Limit on the Cosmic Diffuse Ultrahigh Energy Neutrino Flux. *Phys.Rev.Lett*, 93(4):041101, July 2004.

[81] D. Saltzberg et al. Introduction to the SALSA, a Saltdome Shower Array as a GZK Neutrino Observatory. *International Journal of Modern Physics A*, 21:252–253, 2006.

[82] S. W. Barwick. ARIANNA: A New Concept for UHE Neutrino Detection. *Journal of Physics Conference Series*, 60:276–283, March 2007.

[83] A. V. Butkevich et al. Prospects for radio-wave and acoustic detection of ultra- and superhigh-energy cosmic neutrinos (cross sections, signals, thresholds). *Physics of Particles and Nuclei*, 29:266–272, June 1998.

[84] N. G. Lehtinen et al. FORTE satellite constraints on ultrahigh energy cosmic particle fluxes. *Phys.Rev.D*, 69(1):013008, January 2004.

[85] M. A. Markov and I. M. Zheleznykh. Large-scale Cherenkov detectors in ocean, atmosphere and ice. *Nuclear Instruments and Methods in Physics Research A*, 248:242–251, 1986.

[86] L. A. Anchordoqui et al. Neutrino bounds on astrophysical sources and new physics. *Phys.Rev.D*, 66(10):103002, November 2002.

[87] L. A. Anchordoqui et al. Inelastic black hole production and large extra dimensions. *Phys.Lett.B*, 594:363–367, August 2004.

[88] J. Jones et al. Tracing Very High Energy Tau Neutrinos from Cosmological Sources in Ice. *International Journal of Modern Physics A*, 20:1204–1211, 2005.

[89] J. Jones et al. Ultrahigh Energy Tau Neutrinos. *International Journal of Modern Physics A*, 20:4656–4663, 2005.

[90] H. Landsman and The AURA Collaboration. AURA next generation neutrino detector in the South Pole. *NuPhB Proceedings Supplements*, 168:268–270, June 2007.

[91] M. Vietri. The acceleration of ultra high energy cosmic rays in gamma ray bursts. *ApJ*, 453:883, 1995.

[92] B. Paczynski. Gamma-ray bursters at cosmological distances. *ApJL*, 308:L43–L46, September 1986.

[93] P.Mészáros. Theories of gamma-ray bursts. *astro-ph-0111170v2*, November 2001.

[94] D. Band et al. BATSE Observations of Gamma-Ray Burst Spectra. I. Spectral Diversity. *ApJ*, 413:281–292, 1993.

[95] R. W. Klebesadel, I. B. Strong, and R. A. Olson. Observations of Gamma-Ray Bursts of Cosmic Origin. *ApJL*, 182:L85, June 1973.

[96] K. Hurley et al. 3rd Interplanetary Network Localization, Time History, Fluence, Peak Flux, and Distance Lower Limit of the February 28, 1997 Gamma-Ray Burst. *astro-ph/9705128*, 1997.

[97] T. Sakamoto et al. The First Swift BAT Gamma-Ray Burst Catalog. *astro-ph/0707.4626*, 707, July 2007.

[98] A. Rau et al. The 1st INTEGRAL SPI-ACS Gamma-Ray Burst Catalogue. *A&A*, 438:1175, 2005.

[99] Interplanetary status report. $http://www.ssl.berkeley.edu/ipn3/$, September 2007.

[100] E. P. Mazets et al. Konus catalog of short GRBs. *astro-ph/0209219*, September 2002.

[101] G. Boella et al. BeppoSAX, the wide band mission for X-ray astronomy. *A&AS*, 122:299–307, April 1997.

[102] P. J. Groot et al. GRB 970228. *IAU Circ.*, 6584:1, March 1997.

[103] C. Kouveliotou et al. Identification of two classes of gamma-ray bursts. *ApJL*, 413:L101–L104, August 1993.

[104] R. D. Preece et al. The BATSE Gamma-Ray Burst Spectral Catalog. I. High Time Resolution Spectroscopy of Bright Bursts Using High Energy Resolution Data. *ApJS*, 126:19–36, January 2000.

[105] R. Mukherjee. High energy gamma-ray emission from blazars: Egret observations. *astro-ph/9901222*, 1999.

[106] I. Horváth. A Third Class of Gamma-Ray Bursts? *ApJ*, 508:757–759, December 1998.

[107] B. L. Dingus and J. R. Catelli. EGRET Detections of the Highest Energy Emission from Gamma-Ray Bursts. December 1998.

[108] D. Guetta and T. Piran. Do long duration gamma ray bursts follow star formation. *Journal of Cosmology and Astro-Particle Physics*, 7:3–+, 2007.

[109] N. Weinberg et al. Determining the gamma-ray burst rate as a function of redshift. *astro-ph/0107549*, 2001.

[110] N. M. Lloyd, V. Petrosian, and R. S. Mallozzi. Cosmological versus Intrinsic: The Correlation between Intensity and the Peak of the νF_ν Spectrum of Gamma-Ray Bursts. *ApJ*, 534:227–238, May 2000.

[111] L. Amati et al. Intrinsic spectra and energetics of BeppoSAX Gamma-Ray Bursts with known redshifts. *A&A*, 390:81–89, July 2002.

[112] T. Sakamoto et al. High Energy Transient Explorer 2 Observations of the Extremely Soft X-Ray Flash XRF 020903. *ApJ*, 602:875–885, February 2004.

[113] D. Q. Lamb, T. Q. Donaghy, and C. Graziani. A unified jet model of X-ray flashes and γ-ray bursts. *New Astronomy Review*, 48:459–464, April 2004.

[114] J. L. Atteia et al. Observation and implications of the E_{peak} - E_{iso} correlation in Gamma-Ray Bursts. In E. Fenimore and M. Galassi, editors, *Gamma-Ray Bursts: 30 Years of Discovery*, volume 727 of *American Institute of Physics Conference Series*, pages 37–41, September 2004.

[115] D. Yonetoku et al. Gamma-Ray Burst Formation Rate Inferred from the Spectral Peak Energy-Peak Luminosity Relation. *ApJ*, 609:935–951, July 2004.

[116] G. Ghirlanda, G. Ghisellini, and D. Lazzati. The Collimation-corrected Gamma-Ray Burst Energies Correlate with the Peak Energy of Their νF_ν Spectrum. *ApJ*, 616:331–338, November 2004.

[117] G. Ghirlanda et al. The peak luminosity-peak energy correlation in gamma-ray bursts. *MNRAS*, 360(1):L45–L49, 2005.

[118] E. E. Fenimore and E. Ramirez-Ruiz. Redshifts for 220 batse gamma-ray bursts determined by variability and the cosmological consequences. *astro-ph/0004176*, 2000.

[119] C. Guidorzi et al. The gamma-ray burst variability-peak luminosity correlation: new results. *MNRAS*, 363(1):315–325, 2005.

[120] J.-L. Atteia. A simple empirical redshift indicator for gamma-ray bursts. *A&A*, 407:L1–L4, August 2003.

[121] N.M. Lloyd-Ronning and E. Ramirez-Ruiz. On the Spectral Energy Dependence of Gamma-Ray Burst Variability. *ApJ*, 576(1):101–106, 2002.

[122] L. Amati et al. Intrinsic spectra and energetics of BeppoSAX Gamma-Ray Bursts with known redshifts. *A&A*, 390:81–89, July 2002.

[123] A. P*é*langeon et al. An improved redshift indicator for gamma-ray bursts, based on the prompt emission. *AIP Conference Proceedings*, 836:149, 2006.

[124] A. P*é*langeon and J.L Atteia. A pseudo-redshift calculator for gamma-ray bursts. *http://cosmos.ast.obs-mip.fr/project/*, 2007.

[125] K. Brecher and P. Morrison. Cosmic Gamma-Ray Bursts from Directed Stellar Flares. *ApJL*, 187:L97+, February 1974.

[126] S. A. Colgate and A. G. Petschek. Gamma ray bursts and neutron star accretion of a solid body. *ApJ*, 248:771–782, September 1981.

[127] S. A. Colgate. Prompt gamma rays and X-rays from supernovae. *Canadian Journal of Physics*, 46:476–+, 1968.

[128] B. Paczynski. Are $Gamma_{R}ayBurstsinStar - FormingRegions. ApJL, 494 : L45 - -L48, February1998.$

[129] S. E. Woosley, W. Zhang, and A. Heger. The Central Engines of Gamma-Ray Bursts. 662:185–192, April 2003.

[130] R. D. Blandford and R. L. Znajek. Electromagnetic extraction of energy from Kerr black holes. *MNRAS*, 179:433–456, May 1977.

[131] C. L. Fryer, S. E. Woosley, and D. H. Hartmann. Formation rates of black hole accretion disk gamma-ray bursts. *ApJ*, 526:152, 1999.

[132] T. Weekes. *Very high energy gamma-ray astronomy.* Bristol: Institute of Physics, 2003.

[133] D. Lazzati. GRB Progenitors and environment. *Nuovo Cimento C Geophysics Space Physics C*, 28:575, July 2005.

[134] C. L. Fryer et al. Constraints on Type Ib/c and GRB Progenitors. *astro-ph/0702338*, 2007.

[135] S. E. Woosley and J. S. Bloom. The Supernova Gamma-Ray Burst Connection. *Annual Review of Atronomy and Astrophysics*, 44:507–556, September 2006.

[136] K. Nomoto, M. Tanaka, N. Tominaga, K. Maeda, and P. A. Mazzali. Hypernovae and their Gamma-Ray Bursts Connection. *ArXiv e-prints*, July 2007.

[137] M. Vietri and L. Stella. A gamma ray burst with small contamination. *ApJ*, 507:L45, 1998.

[138] V. V. Usov. On the Nature of Nonthermal Radiation from Cosmological Gamma-Ray Bursters. *MNRAS*, 267:1035, April 1994.

[139] C. Thompson. A Model of Gamma-Ray Bursts. *MNRAS*, 270:480, October 1994.

[140] R. Narayan, T. Piran, and A. Shemi. Neutron star and black hole binaries in the Galaxy. *ApJL*, 379:L17–L20, September 1991.

[141] A. K. Harding and M. G. Baring. Escape of high-energy photons from relativistically expanding gamma-ray burst sources. volume 307, pages 520–524. AIP, 1994.

[142] P. Meszaros. Gamma-ray burst models: General requirements and predictions. *astro-ph/9502090*, 1995.

[143] P. Meszaros. Gamma-ray bursts. *astro-ph/0605208*, 69:2259, 2006.

[144] T. Piran. Gamma-ray bursts - a puzzle being resolved. *PhR*, 333:529–553, 2000.

[145] P. Meszaros. Gamma-ray bursts. *astro-ph/0605208*, 69:2259–2322, 2006.

[146] T. Piran. The physics of gamma-ray bursts. *astro-ph/0503060*, 76(4):1143–1210, 2005.

[147] D. Besson et al. Limits on the transient ultra-high energy neutrino flux from gamma-ray bursts (GRB) derived from RICE data. *APh*, 26:367–377, January 2007.

[148] R. D. Blandford and C. F. McKee. Fluid dynamics of relativistic blast waves. *Physics of Fluids*, 19:1130–1138, August 1976.

[149] D. Guetta and J. Granot. Neutrinos from gamma-ray bursts in pulsar wind bubbles: $\sim 10^{16}$ev. *Phys.Rev.Lett*, 90, 2003.

[150] D. Guetta et al. Neutrinos from individual gamma-ray bursts in the BATSE catalog. *APh*, 20(4):429–455, 2004.

[151] I. Taboada and M. V. D'Agostino. Correlating prompt GRB photons with neutrinos. *arXiv:0711.2277T*, 711, November 2007.

[152] I. Kravchenko et al. RICE limits on the diffuse ultrahigh energy neutrino flux. *Phys.Rev.D*, 73(8):082002, April 2006.

[153] I. Kravchenko et al. Performance of the rice detector. *astro-ph 0112372*, 2001.

[154] G. Hill and The AMANDA Collaboration. Search for a diffuse flux from sources of high energy neutrinos with AMANDA-B10. In *International Cosmic Ray Conference*, volume 3 of *International Cosmic Ray Conference*, page 1113, 2001.

[155] I. Kravchenko et al. Performance and simulation of the RICE detector. *APh*, 19(1):15–36, 2003.

[156] J. Ahrens et al. Calibration and survey of AMANDA with the SPASE detectors. *NIMPA*, 522:347–359, April 2004.

[157] F. Halzen. Astroparticle physics with high energy neutrinos: from AMANDA to IceCube. *European Physical Journal C*, 46:669–687, June 2006.

[158] C. Cooley. Honors thesis. Whitman College, Walla Walla, WA, 2005.

[159] P. Wahrlich. Master's thesis, Dept. Physics and Astronomy, University of Canterbury, Christchurch, New Zealand, 2005.

[160] I. Kravchenko et al. Limits on the ultra-high energy electron neutrino flux from the RICE experiment. *APh*, 20:195–213, November 2003.

[161] J. Adams. Neutrino telescopes in Antarctica. *Publications of the Astronomical Society of Australia*, 17:13–17, April 2000.

[162] A. M. Dziewonski and D. L. Anderson. Preliminary reference Earth model. *Physics of the Earth and Planetary Interiors*, 25:297–356, June 1981.

[163] P. Jain, J.P. Ralston, and G.M. Frichter. Neutrino absorption tomography of the Earth's interior using isotropic ultra-high energy flux. *APh*, 12(3):193–198, 1999.

[164] R. Gandhi et al. Ultrahigh-energy neutrino interactions. *APh*, 5:81–110, August 1996.

[165] L. Landau and I. Pomeranchuk. *Dokl. Akad. Nauk SSSR 92*, page 735, 1953.

[166] Interplanetary network cosmic burst list. *http* : *//www.ssl.berkeley.edu/ipn*3/, September 2007.

[167] J. Greiner. GRB Page. *http* : *//www.mpe.mpg.de/ jcg/grbgen.html*, September.

[168] E. P. Mazets et al. Konus catalog of short GRBs. *http* : *//www.ioffe.ru/LEA/shortGRBs/Catalog/*, September 2002.

[169] HETE Burst Team. Hete burst summary page. *http* : *//space.mit.edu/HETE/Bursts/Data/*, 2007.

[170] F. Halzen, E. Zas, and T. Stanev. Radiodetection of cosmic neutrinos. A numerical, real time analysis. *Physics Letters B*, 257:432–436, March 1991.

[171] D. Besson. *RICE DAQ Manual*.

[172] A. B. Baird. Rice timing analysis. Master's thesis, Department of Physics & Astronomy, University of Canterbury, 2003.

[173] S. Golenetskii et al. Konus-Wind observation of GRB 051022. *GCN*, 4150:1–+, 2005.

[174] J. Doty et al. GRB 051022: Spectral Analysis Indicates That The Spectrum Is Absorbed. *GCN*, 4145:1–+, 2005.

[175] K. Hurley et al. IPN triangulation of GRB 020418. *GCN*, 1376, 2002.

[176] M. Maetou et al. GRB 050807(HETE 3889): An X-Ray Rich GRB Localized by HETE. *GCN*, 3785:1, 2005.

[177] J. Cummings et al. GRB 050820 Swift-BAT refined analysis. *GCN*, 3835:1, 2005.

[178] G. Sato et al. GRB 050908: Swift-BAT refined analysis. *GCN*, 3951:1, 2005.

[179] S. M. Carroll et al. The Cosmological Constant. *ARA&A*, 30(1):499–542, 1992.

[180] T. Sakamoto et al. Global Characteristics of X-ray flashes and x-ray rich gamma ray bursts observed by Hete-2. *ApJ*, 629(1):311–327, 2005.

[181] P. B. Cameron. GRB 050603: Radio Detection. *GCN*, 3513:1, 2005.

[182] A. M. Soderberg. GRB 050724: Refined Radio Position. *GCN*, 3696:1, 2005.

[183] A. J. Blustin et al. GRB 050801: Swift/UVOT Optical and UV detections. *GCN*, 3733:1, 2005.

[184] K. McGowan et al. GRB 050802: Swift/UVOT observations. *GCN*, 3739:1, 2005.

[185] D. B. Fox and S. B. Cenko. GRB 050820: Optical afterglow from P60. *GCN*, 3829:1, 2005.

[186] S. Campana et al. GRB 050824: XRT refined analysis and possible afterglow detection. *GCN*, 3872:1, 2005.

[187] J. P. Halpern and N. Mirabal. GRB 050826: Optical Afterglow and Host Galaxy. *GCN*, 4749:1, 2006.

[188] W. Li. GRB 050908: KAIT observations. *GCN*, 3945:1, 2005.

[189] J. A. Kennea et al. GRB 050922C: Swift XRT refined analysis. *GCN*, 4022:1, 2005.

[190] J. Racusin et al. GRB 051021B: Swift XRT Position. *GCN*, 4128:1, 2005.

[191] A. d. U. Postigo, F. J. Aceituno, and S. Guziy. GRB 051022, refined optical astrometry. *GCN*, 4164:1, 2005.

[192] V. L. Parola et al. GRB 051111: XRT preliminary analysis. *GCN*, 4261:1, 2005.

[193] B. Hughey and I. Taboada. Neutrino-Induced Cascades From GRBs With AMANDA-II. *Proceedings of the 29th International Cosmic Ray Conference. August 3-10, 2005, Pune, India. Edited by B. Sripathi Acharya, Sunil Gupta,*, 2005.

[194] A. Achterberg et al. On the selection of AGN neutrino source candidates for a source stacking analysis with neutrino telescopes. *APh*, 26:282300, 2006.

[195] A. N. Cillis, R. C. Hartman, and D. L. Bertsch. Stacking searches for gamma-ray emission above 100 mev from radio and seyfert galaxies. *ApJ*, 601(1):142–150, 2004.

[196] A. N. Cillis, D. F. Torres, and O. Reimer. Egret upper limits and stacking searches of gamma-ray observations of luminous and ultraluminous infrared galaxies. *ApJ*, 621(1):139–145, 2005.

[197] BATSE Collaboration. GRB Page. *http* : *//www.batse.msfc.nasa.gov/batse/grb/4bcatalog/*, 2007.

[198] J. LoSecco. Search for gamma-ray correlation with neutrinos. *ApJ*, 425:217–221, April 1994.

[199] K. Hurley et al. IPN triangulation of GRB 020525. *GCN*, 1395:1, 2002.

[200] K. Hurley et al. IPN triangulation of GRB 021023 (small error box). *GCN*, 1653:1, 2002.

[201] K. Hurley et al. IPN triangulation of GRB 021102 (annulus). *GCN*, 1667:1, 2002.

[202] K. Hurley et al. IPN triangulation of GRB 021108 (annulus). *GCN*, 1679:1, 2002.

[203] K. Hurley et al. IPN triangulation of GRB 030127 (annulus). *GCN*, 1833:1, 2003.

[204] K. Hurley et al. IPN triangulation of GRB 030202 (annulus). *GCN*, 1853:1, 2003.

[205] K. Hurley et al. IPN triangulation of GRB 030218 (annulus). *GCN*, 1874:1, 2003.

[206] K. Hurley et al. IPN triangulation of GRB 030307 (annulus). *GCN*, 1937:1, 2003.

[207] K. Hurley et al. IPN triangulation of GRB 030326 (single small error box). *GCN*, 1967:1, 2003.

[208] S. Golenetskii et al. GRB 030329b: detection by Konus-Wind and Helicon-CoronasF. *GCN*, 2025:1, 2003.

[209] K. Hurley et al. IPN triangulation of GRB 030414 (small error box). *GCN*, 2138:1, 2003.

[210] K. Hurley et al. IPN triangulation of GRB 030422B (annulus). *GCN*, 2165:1, 2003.

[211] K. Hurley et al. IPN triangulation of GRB 030425 (single error box). *GCN*, 2173:1, 2003.

[212] K. Hurley et al. IPN triangulation of GRB 030509 (single error box). *GCN*, 2221:1, 2003.

[213] K. Hurley et al. IPN triangulation of GRB 030518B (annulus). *GCN*, 2231:1, 2003.

[214] K. Hurley et al. IPN triangulation of GRB 030523 (annulus). *GCN*, 2248:1, 2003.

[215] K. Hurley et al. IPN triangulation of GRB 030710 (annulus). *GCN*, 2295:1, 2003.

[216] K. Hurley et al. IPN triangulation of GRB 030715 (two large error boxes). *GCN*, 2300:1, 2003.

[217] K. Hurley et al. IPN triangulation of GRB 030721 (large error box). *GCN*, 2331:1, 2003.

[218] K. Hurley et al. IPN triangulation of GRB 030722 (large error box). *GCN*, 2332:1, 2003.

[219] K. Hurley et al. IPN triangulation of GRB 030726 (large error box). *GCN*, 2333:1, 2003.

[220] K. Hurley et al. IPN triangulation of GRB 030919 (large error box). *GCN*, 2398:1, 2003.

[221] S. Golenetskii et al. GRB 030921 triangulation (annulus). *GCN*, 2393:1, 2003.

[222] S. Golenetskii et al. GRB 030922 triangulation (annulus). *GCN*, 2397:1, 2003.

[223] K. Hurley et al. IPN triangulation of GRB 030922B (large error box). *GCN*, 2404:1, 2003.

[224] K. Hurley et al. IPN triangulation of GRB 031016 (two large error boxes). *GCN*, 2423:1, 2003.

[225] K. Hurley et al. IPN triangulation of GRB 031024 (annulus). *GCN*, 2426:1, 2003.

[226] K. Hurley et al. IPN triangulation of GRB 031114 (large error box). *GCN*, 2449:1, 2003.

[227] D. Gotz et al. GRB 050626 - a long GRB detected with INTEGRAL. *GCN*, 3552:1, 2005.

[228] G. Sato et al. GRB 051012: Swift-BAT detection of burst yesterday. *GCN*, 4093:1, 2005.

[229] K. Hurley et al. IPN triangulation of GRB 030329b (large error box). *GCN*, 2055:1, 2003.

[230] K. Hurley et al. IPN triangulation of GRB 030922A (large error box). *GCN*, 2400:1, 2003.

[231] K. Hurley et al. IPN triangulation of GRB 031024 (single error box). *GCN*, 2430:1, 2003.

[232] J. Rhoads. Optical Afterglow of GRB 050607. *GCN*, 3527:1, 2005.

[233] J. L. Racusin et al. GRB 050701: Swift XRT afterglow position. *GCN*, 3557:1, 2005.

[234] J. Greiner, S. Barthelmy, H. Krimm, D. Palmer, and A. Parsons. GRB 050715: Swift-BAT detection. *GCN*, 3621:1, 2005.

[235] S. Covino et al. GRB 050721: optical afterglow confirmed. *GCN*, 3657:1, 2005.

[236] A. Moretti et al. GRB 050726: early Swift XRT analysis results. *GCN*, 3683:1, 2005.

[237] D. C. Morris et al. GRB 050813: Swift XRT afterglow localization. *GCN*, 3790:1, 2005.

[238] J. A. Kennea, D. N. Burrows, and K. Page. GRB 050819: Swift XRT position. *GCN*, 3827:1, 2005.

[239] O. Godet et al. GRB 050822: refined XRT analysis. *GCN*, 3873:1, 2005.

[240] M. Capalbi et al. GRB 050827: XRT possible afterglow detection. *GCN*, 3899:1, 2005.

[241] K. Page, J. Kennea, and D. Burrows. GRB 050911: Swift-XRT position. *GCN*, 3967:1, 2005.

[242] J. S. Bloom. GRB 050915a: IR Transient. *GCN*, 3990:1, 2005.

[243] D. Morris and D. N. Burrows. GRB 050916: XRT position. *GCN*, 3995:1, 2005.

[244] O. Godet et al. GRB 050922B: refined XRT analysis. *GCN*, 4031:1, 2005.

[245] C. Markwardt et al. Refined analysis of the Swift-BAT soft short burst. *GCN*, 4037:1, 2005.

[246] A. Moretti et al. GRB 051001: Swift XRT refined analysis. *GCN*, 4056:1, 2005.

[247] V. Rumyantsev et al. GRB 051006: optical observations. *GCN*, 4094:1, 2005.

[248] A. P. Beardmore et al. GRB 051012: Swift-XRT analysis. *GCN*, 4162:1, 2005.

Appendix A

GRB Properties

The following table summarises some key observational data for the 50 unknown redshift GRBs. The GRB Name is given whereby the first two numbers represent the year followed by the month and day of the GRB trigger. The subsequent columns represent the date, Universal time (UT), duration, fluence and the energy range for which the fluence and duration was measured.

GRB Name	GRB Date	Time (UT)	Duration (s)	Fluence (10^{-6}) (ergs cm^{-2})	Energy Range (keV)	Reference
GRB010613	13/06/2001	7:33:55	153.2	23.00	30-400	[169]
GRB020525A	25/05/2002	5:36:04	25.0	10.00	25-100	[199]
GRB020625B	25/06/2002	11:52:39	2.0	0.01	30-400	[169]
GRB021023A	23/10/2002	2:53:46	15.0	4.10	25-100	[200]
GRB021102A	2/11/2002	15:58:32	10.0	4.10	25-100	[201]
GRB021108A	8/11/2002	5:39:55	25.0	5.10	25-100	[202]
GRB030127	27/01/2003	12:32:32	50.0	29.00	25-100	[203]
GRB030202	2/02/2003	17:21:00	15.0	0.79	25-100	[204]
GRB030218	18/02/2003	11:42:38	200.0	36.00	25-100	[205]

Table cont...

GRB Name	GRB Date	Time (UT)	Duration (s)	Fluence (10^{-6}) (ergs cm^{-2})	Energy Range (keV)	Reference
GRB030307	7/03/2003	14:31:58	3.0	4.70	25-100	[206]
GRB030326A	26/03/2003	10:43:41	10.0	3.50	25-100	[207]
GRB030329B	29/03/2003	15:34:19	65.0	20.00	15-2000	[208]
GRB030414A	14/04/2003	13:48:27	40.0	12.00	25-100	[209]
GRB030422B	22/04/2003	9:01:27	15.0	88.00	25-100	[210]
GRB030425A	25/04/2003	15:48:31	500.0	59.00	25-100	[211]
GRB030509A	9/05/2003	5:50:24	9.0	12.00	25-100	[212]
GRB031518B	18/05/2003	3:12:18	10.0	3.70	25-100	[213]
GRB030519B	19/05/2003	14:04:53	9.6	61.00	30-400	[169]
GRB030523A	23/05/2003	15:30:59	40.0	9.40	25-100	[214]
GRB030710A	10/07/2003	23:05:00	12.0	3.60	25-100	[215]
GRB030715A	15/07/2003	4:25:51	15.0	7.50	25-100	[216]
GRB030721A	21/07/2003	23:41:12	40.0	7.80	25-100	[217]
GRB030722A	22/07/2003	13:31:41	30.0	20.00	25-100	[218]
GRB030726	26/07/2003	6:38:25	30.0	17.00	25-100	[219]
GRB030821A	21/08/2003	5:31:35	18.8	2.70	30-400	[169]
GRB030919A	19/09/2003	21:10:38	13.0	2.00	25-100	[220]
GRB030921A	21/09/2003	8:38:23	16.0	3.00	25-100	[221]
GRB030922A	22/09/2003	8:43:24	35.0	5.20	25-100	[222]
GRB030922B	22/09/2003	18:30:48	18.0	12.00	25-100	[223]
GRB031016A	16/10/2003	23:54:02	10.0	6.00	25-100	[224]
GRB031024A	24/10/2003	9:24:15	350.0	5.00	25-100	[225]
GRB031114A	14/11/2003	21:07:50	12.0	2.20	25-100	[226]
GRB050607A	7/06/2005	9:11:23	26.4	0.59	15-150	[97]
GRB050626A	26/06/2005	3:45:16	60.0	0.87	20-200	[227]
GRB050701A	1/07/2005	11:42:59	21.8	1.36	15-150	[97]
GRB050715A	15/07/2005	22:30:26	51.6	1.49	15-150	[97]
GRB050721A	21/07/2005	4:29:14	98.4	3.62	15-150	[97]
GRB050726A	26/07/2005	5:00:17	49.9	1.94	15-150	[97]
GRB050813A	13/08/2005	6:45:09	0.5	0.04	15-150	[97]
GRB050819A	19/08/2005	16:23:55	37.7	0.35	15-150	[97]
GRB050822A	22/08/2005	3:49:29	103.4	2.46	15-150	[97]
GRB050827A	27/08/2005	18:57:15	50.0	2.10	15-150	[97]
GRB050911A	11/09/2005	15:59:34	16.2	0.32	15-150	[97]
GRB050915A	15/09/2005	11:22:42	52.0	0.85	15-150	[97]
GRB050916A	16/09/2005	16:35:52	49.5	0.93	15-150	[97]

Table cont...

GRB Name	GRB Date	Time (UT)	Duration (s)	Fluence (10^{-6}) (ergs cm^{-2})	Energy Range (keV)	Reference
GRB050922B	22/09/2005	15:02:00	150.9	2.23	15-150	[97]
GRB050925A	25/09/2005	9:04:34	0.1	0.08	15-150	[97]
GRB051001A	1/10/2005	11:11:36	189.1	1.74	15-150	[97]
GRB051006A	6/10/2005	20:30:33	34.8	1.34	15-150	[97]
GRB051012A	12/10/2005	17:05:58	13.0	0.29	15-350	[228]

Appendix B

GRB Localisation to Neutrino Direction Transformation

Presented here are the GRB localisations, error circle and transformed co-ordinates from equatorial to horizon co-ordinates and local RICE co-ordinates for the GRBs with unknown redshifts. As done in Section 5.3 the right ascension and declination were converted to altitude and azimuth in horizon co-ordinates using Equations 5.4 and 5.5. Then using Equations 5.8 and 5.9 the local RICE co-ordinates ϕ_s and θ_s were obtained respectively. The errors for the right ascension and declination presented here are only approximate, as discussed previously the large errors are due to the limited capability of the detectors at the time of measurement. Many factors must come into play in order to get an accurate localisation. Either the individual detector must have an accurate localization system onboard or multiple detectors must observe the event and triangulate the position. The large error boxes or circles produced are the result of these triangulations, or are a result of intersecting fields of view which can also constrain a localisation region. Localisations are only

used if they can definitely be placed in the effective volume angular sensitivity zone. Where two values of uncertainties are given, these pertain to cases where the right ascension and declination uncertainties were vastly different. These were taken into consideration when calculating the individual effective volumes. Uncertainties were calculated robustly and carried through to the effective volume calculations.

GRB Name	RA (°)	Dec (°)	Err Circ (°)	Azi (°)	Alt (°)	Azi$_s$ ϕ_s (°)	Nadir θ_s (°)	Ref:
GRB010613	255	14	<1	285	-14	210	76	[169, 167]
GRB020525A	172	-20	<1	251	20	244	110	[199]
GRB020625B	311	7	<1	264	-7	231	83	[169]
GRB021023A	111	-16	<1	81	16	54	106	[200]
GRB021102A	360	-35	<59	123	35	12	125	[201]
GRB021108A	1	-35	<48	273	35	222	125	[202]
GRB030127	358	-40	<66	88	40	47	130	[203]
GRB030202	356	-41	<27	8	41	127	131	[204]
GRB030218	351	-42	<56	73	42	62	132	[205]
GRB030307	345	-42	<70	7	42	128	132	[206]
GRB030326A	293	-12	<1	354	12	141	102	[207]
GRB030329B	160	-49	<4	145	48	350	138	[229]
GRB030414A	120	-49	<1	116	49	19	139	[209]
GRB030422B	334	-39	<69	33	39	102	129	[210]
GRB030425A	233	26	<1	188	-26	307	64	[211]
GRB030509A	79	11	<1	169	-11	326	79	[212]
GRB031518B	332	-35	<60	93	35	42	125	[213]
GRB030519B	225	-33	<1	182	33	313	123	[169]
GRB030523A	332	-34	<62	263	34	232	124	[214]
GRB030710A	335	-28	<50	106	28	29	118	[215]
GRB030715A	91	-13	<4	137	13	358	103	[216]
GRB030721A	274	-40	<3	24	41	111	131	[217]
GRB030722A	107	-15	<5	9	15	126	105	[218]
GRB030726	254	-21	<1	256	21	239	111	[219]
GRB030821A	326	-45	<1	319	45	176	135	[169]
GRB030919A	142	-74	<60;<12	231	74	264	164	[220]
GRB030921A	261	5	<2	177	-5	318	85	[221]

Table cont...

GRB Name	RA (°)	Dec (°)	Error Circle (°)	Azi (°)	Alt (°)	Azi$_s$ ϕ_s (°)	Nadir θ_s (°)	Ref:
GRB030922A	229	25	<5	142	-25	353	65	[230, 222]
GRB030922B	30	20	<5	156	-20	339	70	[223]
GRB031016A	154	-28	<20	175	28	320	118	[224]
GRB031024A	225	-16	<2	97	16	38	106	[231, 225]
GRB031114A	271	6	<3;<8	305	-6	190	84	[226]
GRB050607A	300	9	<1	311	-9	184	81	[232]
GRB050626A	187	-63	<1	261	63	234	153	[227]
GRB050701A	227	-59	<1	177	59	318	149	[233]
GRB050715A	156	0	<1	289	0	206	90	[234]
GRB050721A	253	-28	<1	292	28	203	118	[235]
GRB050726A	200	-32	<1	226	32	269	122	[236]
GRB050813A	242	11	<1	224	-11	271	79	[237]
GRB050819A	359	25	<1	190	-25	305	65	[238]
GRB050822A	51	-46	<1	68	46	67	136	[239]
GRB050827A	64	18	<1	209	-18	286	72	[240]
GRB050911A	14	-39	<1	188	39	307	129	[241]
GRB050915A	82	-28	<1	321	28	174	118	[242]
GRB050916A	136	-51	<1	296	51	199	141	[243]
GRB050922B	6	-6	<1	184	6	311	96	[244]
GRB050925A	303	34	<1	208	-34	287	56	[245]
GRB051001A	351	-32	<1	218	31	277	121	[246]
GRB051006A	111	10	<1	193	-10	302	80	[247]
GRB051012A	271	-53	<1	38	53	97	143	[248]

Appendix C

RICE Livetimes, Discriminator and GRB Satellite Triggers

As in Section 7.3, here we show the RICE livetimes, and discriminator thresholds in columns 2 and 3 respectively for GRBs with unknown redshifts. Column 4 lists the names of the GRB detectors that detected each GRBs. The naming convention follows that of the IPN [166][1].

GRB Name	Average Livetime	Discriminator Threshold (V)	Satellites Triggered
GRB010613	0.91	-0.40	Uly,KON,HET
GRB020525A	0.81	-0.30	Uly,Mo,KON
GRB020625B	0.97	-0.33	KON,HET,HES
GRB021023A	0.91	-0.36	Uly,Mo,KON,HET,HES
GRB021102A	0.95	-0.29	Uly,KON,HES,INT

[1]Uly = Ulysses, KON = Konus, HET = HETE-II, Mo = Mars Odyssey, HES = RHESSI, INT = INTEGRAL, SWI = Swift, SUZ = Suzaku

Table cont...

GRB Name	Average Livetime	Discriminator Threshold (V)	Satellites Triggered
GRB021108A	0.57	-0.24	Uly,KON,HES
GRB030127	0.82	-0.50	Uly,KON,HET,HES,INT
GRB030202	0.82	-0.33	Uly,KON,INT
GRB030218	0.97	-0.91	Uly,INT
GRB030307	0.94	-0.38	Uly,KON,HET,HES,INT
GRB030326A	0.96	-0.76	Uly,Mo,KON,HES,INT
GRB030329B	0.49	-0.99	Uly,KON,HET,HES
GRB030414A	0.97	-0.36	Uly,Mo,KON,HES,INT
GRB030422B	0.96	-0.32	Uly,KON,HES,INT
GRB030425A	0.97	-0.35	Uly,Mo,KON
GRB030509A	0.97	-0.40	Uly,Mo,KON,INT
GRB031518B	0.95	-0.35	Uly,KON,HES,INT
GRB030519B	0.68	-0.28	Uly,Mo,KON,HET,HES
GRB030523A	0.95	-0.35	Uly,KON,INT
GRB030710A	0.64	-0.40	Uly,KON,HES,INT
GRB030715A	0.98	-0.28	Uly,Mo,KON,INT
GRB030721A	0.96	-0.35	Uly,Mo,KON,INT
GRB030722A	0.96	-0.35	Uly,KON,INT
GRB030726	0.95	-0.28	Uly,Mo,KON,HET,HES,INT
GRB030821A	0.97	-0.87	Uly,Mo,KON,HET,INT
GRB030919A	0.98	-0.28	Uly,Mo,KON,HES,INT
GRB030921A	0.97	-0.34	Uly,Mo,KON,HES
GRB030922A	0.97	-0.28	Uly,Mo,KON,HES
GRB030922B	0.98	-0.28	Uly,Mo,KON,HES
GRB031016A	0.98	-0.50	Uly,KON,INT
GRB031024A	0.94	-0.33	Uly,Mo,KON,INT
GRB031114A	0.93	-0.36	Uly,Mo,KON
GRB050607A	0.91	-0.41	SWI
GRB050626A	0.55	-0.37	SWI
GRB050701A	0.89	-0.38	SWI
GRB050715A	0.70	-0.34	SWI
GRB050721A	0.61	-0.29	KON,SWI
GRB050726A	0.94	-0.41	HES,SWI
GRB050813A	0.90	-0.40	SWI
GRB050819A	0.94	-0.38	SWI
GRB050822A	0.85	-0.41	SWI
GRB050827A	0.91	-0.43	Mo,KON,SWI

Table cont...

GRB Name	Average Livetime	Discriminator Threshold (V)	Satellites Triggered
GRB050911A	0.90	-0.39	HET,SWI
GRB050915A	0.96	-0.58	SWI
GRB050916A	0.48	-0.57	SWI
GRB050922B	0.97	-0.52	SWI
GRB050925A	0.95	-0.44	INT,SWI
GRB051001A	0.95	-0.45	SWI
GRB051006A	0.77	-0.35	HES,INT,SWI,SUZ
GRB051012A	0.94	-0.36	SWI

Appendix D

GRB Parameters

The following table presents the spectral properties for the 50 GRBs without redshift estimations. The spectral indices, α and β, follow the form or parts thereof Equation 2.2. The indices are given where information is available, where the majority are for α only. For unknown values of α and β average values are used as -1 and -2 respectively. Where two indices are presented, these correspond to two different power law models used to fit the data, a power law model and a cutoff power law model. These pertain to the SWIFT GRB data[97] for which we use the first value of α given. The redshift used here is set to z=1. The luminosity distance, is calculated using Equation 7.2 which is used to calculate the bolometric equivalent isotropic energy and luminosity given previously by Equations 7.3 and 7.4. These quantities for other relevant redshifts are not shown here but are used to calculate the parameters in the upcoming appendices. If the peak energy of the burst was not available then the phenomenological Ghirlanda relationship described by Equation 2.3 was used and are indicated by the double asterisks.

GRB Name	α	β	E_{peak} (keV)	dl (Mpc)	$E_{\gamma,iso}$ (ergs)	$L_{\gamma,iso}$ (erg/s)	Ref.
GRB010613	-1	-2	46.25	6.6×10^{3}	6.0×10^{52}	7.9×10^{50}	[180, 169]
GRB020525A	-	-	70.8**	6.6×10^{3}	2.6×10^{52}	2.1×10^{51}	
GRB020625B	-1.1	-	8.52	6.6×10^{3}	3.1×10^{49}	3.1×10^{49}	[180, 169]
GRB021023A	-	-	43**	6.6×10^{3}	1.1×10^{52}	1.4×10^{51}	
GRB021102A	-	-	43**	6.6×10^{3}	1.1×10^{52}	2.1×10^{51}	
GRB021108A	-	-	49**	6.6×10^{3}	1.3×10^{52}	1.1×10^{51}	
GRB030127	-	-	129**	6.6×10^{3}	7.6×10^{52}	3.0×10^{51}	
GRB030202	-	-	17**	6.6×10^{3}	2.1×10^{51}	2.8×10^{50}	
GRB030218	-	-	145**	6.6×10^{3}	9.4×10^{52}	9.4×10^{50}	
GRB030307	-	-	46**	6.6×10^{3}	1.2×10^{52}	8.2×10^{51}	
GRB030326A	-	-	39**	6.6×10^{3}	9.2×10^{51}	1.8×10^{51}	
GRB030329B	-	-	104**	6.6×10^{3}	5.2×10^{52}	1.6×10^{51}	
GRB030414A	-	-	78**	6.6×10^{3}	3.1×10^{52}	1.6×10^{51}	
GRB030422B	-	-	239**	6.6×10^{3}	2.3×10^{53}	3.1×10^{52}	
GRB030425A	-	-	191**	6.6×10^{3}	1.5×10^{53}	6.2×10^{50}	
GRB030509A	-	-	78**	6.6×10^{3}	3.1×10^{52}	7.0×10^{51}	
GRB031518B	-	-	41**	6.6×10^{3}	9.7×10^{51}	1.9×10^{51}	
GRB030519B	-0.8	-1.7	137.6	6.6×10^{3}	1.6×10^{53}	3.3×10^{52}	[180, 169, 167]
GRB030523A	-	-	68**	6.6×10^{3}	2.5×10^{52}	1.2×10^{51}	
GRB030710A	-	-	40**	6.6×10^{3}	9.4×10^{51}	1.6×10^{51}	
GRB030715A	-	-	60**	6.6×10^{3}	2.0×10^{52}	2.6×10^{51}	
GRB030721A	-	-	62**	6.6×10^{3}	2.0×10^{52}	1.0×10^{51}	
GRB030722A	-	-	104**	6.6×10^{3}	5.2×10^{52}	3.5×10^{51}	
GRB030726	-	-	95**	6.6×10^{3}	4.4×10^{52}	3.0×10^{51}	
GRB030821A	-	-	84.26	6.6×10^{3}	7.1×10^{51}	7.5×10^{50}	[169]
GRB030919A	-	-	29**	6.6×10^{3}	5.2×10^{51}	8.0×10^{50}	
GRB030921A	-	-	36**	6.6×10^{3}	7.8×10^{51}	9.8×10^{50}	
GRB030922A	-	-	49**	6.6×10^{3}	1.4×10^{52}	7.8×10^{50}	
GRB030922B	-	-	78**	6.6×10^{3}	3.1×10^{52}	3.5×10^{51}	
GRB031016A	-	-	53**	6.6×10^{3}	1.6×10^{52}	3.1×10^{51}	
GRB031024A	-	-	48**	6.6×10^{3}	1.3×10^{52}	7.5×10^{49}	
GRB031114A	-	-	30**	6.6×10^{3}	5.8×10^{51}	9.6×10^{50}	
GRB050607A	-1.92	-	15**	6.6×10^{3}	1.5×10^{51}	1.2×10^{50}	[97]
GRB050626A	-	-	18**	6.6×10^{3}	2.3×10^{51}	7.6×10^{49}	
GRB050701A	-1.7	-	23**	6.6×10^{3}	3.6×10^{51}	3.3×10^{50}	[97]
GRB050715A	-1.6	-	24**	6.6×10^{3}	3.9×10^{51}	1.5×10^{50}	[97]

Table cont...

GRB Name	α	β	E_{peak} (keV)	dl (Mpc)	$E_{\gamma,iso}$ (ergs)	$L_{\gamma,iso}$ (erg/s)	Ref.
GRB050721A	-1.9	-	40**	6.6×10^3	9.5×10^{51}	1.9×10^{50}	[97]
GRB050726A	-0.9	-	28**	6.6×10^3	5.1×10^{51}	2.0×10^{50}	[97]
GRB050813A	-1.28	-	3**	6.6×10^3	1.2×10^{50}	5.1×10^{50}	[97]
GRB050819A	-2.71	-	11**	6.6×10^3	9.2×10^{50}	4.9×10^{49}	[97]
GRB050822A	-2.37	-	32**	6.6×10^3	6.4×10^{51}	1.2×10^{50}	[97]
GRB050827A	-1.38	-	30**	6.6×10^3	5.5×10^{51}	2.2×10^{50}	[97, 167]
GRB050911A	-1.84	-	10**	6.6×10^3	8.3×10^{50}	1.0×10^{50}	[97]
GRB050915A	-1.39	-	18**	6.6×10^3	2.2×10^{51}	8.6×10^{49}	[97]
GRB050916A	-1.76	-	19**	6.6×10^3	2.4×10^{51}	9.8×10^{49}	[97]
GRB050922B	-2.17	-	31**	6.6×10^3	5.8×10^{51}	7.7×10^{49}	[97, 167]
GRB050925A	-1.76;0.4	-	61	6.6×10^3	2.0×10^{50}	5.7×10^{51}	[97, 97]
GRB051001A	-2.05	-	27**	6.6×10^3	4.6×10^{51}	4.8×10^{49}	[97]
GRB051006A	-1.51	-	23**	6.6×10^3	3.5×10^{51}	2.0×10^{50}	[97]
GRB051012A	-2.19	-	10**	6.6×10^3	7.6×10^{50}	1.2×10^{50}	[97]

Appendix E

GRB Prompt Neutrino Flux Parameters for Unknown Redshifts

The prompt neutrino flux parameters for unknown redshift are presented here. Values of z= 0.0085, 1 and 6.29 corresponding to the minimum, average and maximum GRB redshifts observed at the time of writing this thesis. Using Equation 7.2 and assuming a standard Λ dominated cold dark matter (ΛCDM) model with parameters: $H_0 = 70 kms^{-1}Mpc^{-1}$, $\Omega_M = 0.3$, and $\Omega_\Lambda = 0.7$ as discussed in Chapter 7, these redshifts correspond to luminosity distances of approximately 36.6 ,6612 and 60961 Mpc respectively. Columns one and two of the tables give the GRB name and the prefactor, $\mathcal{A}$, in the expression of the neutrino flux given from Equation 3.7. The third and fourth columns give the break energies, $\epsilon_{\nu,b1}$ and $\epsilon_{\nu,sb}$. The expression for these were given in Equation 3.8 and Equation 3.11 respectively. For completeness the burst duration, $t_{\rm burst}$, is given again here.

Table E.1: Prompt GRB neutrino flux parameters for $z_{min} = 0.085$.

GRB Name	$\mathcal{A}$ (GeV cm^{-2}s^{-1})	$\epsilon_{\nu,b1}$ (GeV)	$\epsilon_{\nu,sb}$ (GeV)	t burst (s)
GRB010613A	2.34×10^{-6}	2.87×10^{7}	9.48×10^{10}	153.2
GRB020525A	6.24×10^{-6}	2.17×10^{9}	5.81×10^{10}	25
GRB020625B	9.36×10^{-8}	1.56×10^{8}	4.74×10^{11}	2
GRB021023A	4.27×10^{-6}	3.57×10^{9}	7.03×10^{10}	15
GRB021102A	6.40×10^{-6}	3.57×10^{9}	5.74×10^{10}	10
GRB021108A	3.18×10^{-6}	3.16×10^{9}	8.14×10^{10}	25
GRB030127A	9.05×10^{-6}	1.19×10^{9}	4.83×10^{10}	50
GRB030202A	8.22×10^{-7}	8.98×10^{9}	1.60×10^{11}	15
GRB030218A	2.81×10^{-6}	1.06×10^{9}	8.66×10^{10}	200
GRB030307A	2.44×10^{-5}	3.31×10^{9}	2.94×10^{10}	3
GRB030326A	5.46×10^{-6}	3.90×10^{9}	6.21×10^{10}	10
GRB030329B	4.80×10^{-6}	1.47×10^{9}	6.63×10^{10}	65
GRB030414A	4.68×10^{-6}	1.96×10^{9}	6.71×10^{10}	40
GRB030422B	9.15×10^{-5}	6.41×10^{8}	1.52×10^{10}	15
GRB030425A	1.84×10^{-6}	8.02×10^{8}	1.07×10^{11}	500
GRB030509A	2.08×10^{-5}	1.96×10^{9}	3.18×10^{10}	9
GRB030518B	5.77×10^{-6}	3.78×10^{9}	6.04×10^{10}	10
GRB030519B	9.92×10^{-5}	9.65×10^{6}	1.46×10^{10}	9.6
GRB030523A	3.67×10^{-6}	2.24×10^{9}	7.58×10^{10}	40
GRB030710A	4.68×10^{-6}	3.84×10^{9}	6.71×10^{10}	12
GRB030715A	7.80×10^{-6}	2.55×10^{9}	5.20×10^{10}	15
GRB030721A	3.04×10^{-6}	2.49×10^{9}	8.32×10^{10}	40
GRB030722A	1.04×10^{-5}	1.47×10^{9}	4.50×10^{10}	30
GRB030726A	8.84×10^{-6}	1.61×10^{9}	4.88×10^{10}	30
GRB030821A	2.24×10^{-6}	1.58×10^{7}	9.70×10^{10}	18.8
GRB030919A	2.40×10^{-6}	5.34×10^{9}	9.37×10^{10}	13
GRB030921A	2.93×10^{-6}	4.25×10^{9}	8.49×10^{10}	16
GRB030922A	2.32×10^{-6}	3.13×10^{9}	9.53×10^{10}	35
GRB030922B	1.04×10^{-5}	1.96×10^{9}	4.50×10^{10}	18
GRB031016A	9.36×10^{-6}	2.89×10^{9}	4.74×10^{10}	10
GRB031024A	2.23×10^{-7}	3.20×10^{9}	3.07×10^{11}	350
GRB031114A	2.86×10^{-6}	5.06×10^{9}	8.58×10^{10}	12
GRB050607A	3.50×10^{-7}	1.06×10^{10}	2.45×10^{11}	26.4
GRB050626A	2.26×10^{-7}	8.51×10^{9}	3.05×10^{11}	60

Table cont...

GRB Name	$\mathcal{A}$ (GeV cm^{-2}s^{-1})	$\epsilon_{\nu,b1}$ (GeV)	$\epsilon_{\nu,sb}$ (GeV)	t burst (s)
GRB050701A	9.74×10^{-7}	6.62×10^{9}	1.47×10^{11}	21.8
GRB050715A	4.51×10^{-7}	6.29×10^{9}	2.16×10^{11}	51.6
GRB050721A	5.74×10^{-7}	3.83×10^{9}	1.92×10^{11}	98.4
GRB050726A	6.07×10^{-7}	5.43×10^{9}	1.86×10^{11}	49.9
GRB050813A	1.37×10^{-6}	4.53×10^{10}	1.24×10^{11}	0.5
GRB050819A	1.45×10^{-7}	1.42×10^{10}	3.81×10^{11}	37.7
GRB050822A	3.71×10^{-7}	4.75×10^{9}	2.38×10^{11}	103.4
GRB050827A	6.55×10^{-7}	5.19×10^{9}	1.79×10^{11}	50
GRB050911A	3.05×10^{-7}	1.50×10^{10}	2.63×10^{11}	16.2
GRB050915A	2.55×10^{-7}	8.62×10^{9}	2.87×10^{11}	52
GRB050916A	2.93×10^{-7}	8.20×10^{9}	2.68×10^{11}	49.5
GRB050922B	2.31×10^{-7}	5.02×10^{9}	3.02×10^{11}	150.9
GRB050925A	1.19×10^{-5}	2.18×10^{7}	4.22×10^{10}	0.1
GRB051001A	1.44×10^{-7}	5.77×10^{9}	3.83×10^{11}	189.1
GRB051006A	6.01×10^{-7}	6.68×10^{9}	1.87×10^{11}	34.8
GRB051012A	3.48×10^{-7}	1.57×10^{10}	2.46×10^{11}	13

Table E.2: Prompt GRB neutrino flux parameters for $z_{ave} = 1$.

GRB Name	$\mathcal{A}$ (GeV cm^{-2}s^{-1})	$\epsilon_{\nu,b1}$ (GeV)	$\epsilon_{\nu,sb}$ (GeV)	t burst (s)
GRB010613A	2.34×10^{-6}	7.30×10^{6}	2.66×10^{8}	153.2
GRB020525A	6.24×10^{-6}	4.78×10^{6}	1.63×10^{8}	25
GRB020625B	9.36×10^{-8}	3.96×10^{7}	1.33×10^{9}	2
GRB021023A	4.27×10^{-6}	7.87×10^{6}	1.97×10^{8}	15
GRB021102A	6.40×10^{-6}	7.87×10^{6}	1.61×10^{8}	10
GRB021108A	3.18×10^{-6}	6.97×10^{6}	2.28×10^{8}	25
GRB030127A	9.05×10^{-6}	2.63×10^{6}	1.35×10^{8}	50
GRB030202A	8.22×10^{-7}	1.98×10^{7}	4.49×10^{8}	15
GRB030218A	2.81×10^{-6}	2.33×10^{6}	2.43×10^{8}	200
GRB030307A	2.44×10^{-5}	7.29×10^{6}	8.23×10^{7}	3

Table cont...

GRB Name	$\mathcal{A}$ (GeV cm^{-2}s^{-1})	$\epsilon_{\nu,b1}$ (GeV)	$\epsilon_{\nu,sb}$ (GeV)	t burst (s)
GRB030326A	5.46×10^{-6}	8.60×10^{6}	1.74×10^{8}	10
GRB030329B	4.80×10^{-6}	3.24×10^{6}	1.86×10^{8}	65
GRB030414A	4.68×10^{-6}	4.31×10^{6}	1.88×10^{8}	40
GRB030422B	9.15×10^{-5}	1.41×10^{6}	4.25×10^{7}	15
GRB030425A	1.84×10^{-6}	1.77×10^{6}	3.00×10^{8}	500
GRB030509A	2.08×10^{-5}	4.31×10^{6}	8.92×10^{7}	9
GRB030518B	5.77×10^{-6}	8.34×10^{6}	1.69×10^{8}	10
GRB030519B	9.92×10^{-5}	2.45×10^{6}	4.08×10^{7}	9.6
GRB030523A	3.67×10^{-6}	4.95×10^{6}	2.12×10^{8}	40
GRB030710A	4.68×10^{-6}	8.47×10^{6}	1.88×10^{8}	12
GRB030715A	7.80×10^{-6}	5.61×10^{6}	1.46×10^{8}	15
GRB030721A	3.04×10^{-6}	5.49×10^{6}	2.33×10^{8}	40
GRB030722A	1.04×10^{-5}	3.24×10^{6}	1.26×10^{8}	30
GRB030726A	8.84×10^{-6}	3.55×10^{6}	1.37×10^{8}	30
GRB030821A	2.24×10^{-6}	4.01×10^{6}	2.72×10^{8}	18.8
GRB030919A	2.40×10^{-6}	1.18×10^{7}	2.62×10^{8}	13
GRB030921A	2.93×10^{-6}	9.38×10^{6}	2.38×10^{8}	16
GRB030922A	2.32×10^{-6}	6.89×10^{6}	2.67×10^{8}	35
GRB030922B	1.04×10^{-5}	4.31×10^{6}	1.26×10^{8}	18
GRB031016A	9.36×10^{-6}	6.36×10^{6}	1.33×10^{8}	10
GRB031024A	2.23×10^{-7}	7.04×10^{6}	8.61×10^{8}	350
GRB031114A	2.86×10^{-6}	1.12×10^{7}	2.40×10^{8}	12
GRB050607A	3.50×10^{-7}	2.33×10^{7}	6.88×10^{8}	26.4
GRB050626A	2.26×10^{-7}	1.88×10^{7}	8.55×10^{8}	60
GRB050701A	9.74×10^{-7}	1.46×10^{7}	4.12×10^{8}	21.8
GRB050715A	4.51×10^{-7}	1.39×10^{7}	6.06×10^{8}	51.6
GRB050721A	5.74×10^{-7}	8.44×10^{6}	5.37×10^{8}	98.4
GRB050726A	6.07×10^{-7}	1.20×10^{7}	5.22×10^{8}	49.9
GRB050813A	1.37×10^{-6}	9.97×10^{7}	3.47×10^{8}	0.5
GRB050819A	1.45×10^{-7}	3.12×10^{7}	1.07×10^{9}	37.7
GRB050822A	3.71×10^{-7}	1.05×10^{7}	6.67×10^{8}	103.4
GRB050827A	6.55×10^{-7}	1.14×10^{7}	5.02×10^{8}	50
GRB050911A	3.05×10^{-7}	3.30×10^{7}	7.36×10^{8}	16.2
GRB050915A	2.55×10^{-7}	1.90×10^{7}	8.05×10^{8}	52
GRB050916A	2.93×10^{-7}	1.81×10^{7}	7.52×10^{8}	49.5
GRB050922B	2.31×10^{-7}	1.11×10^{7}	8.47×10^{8}	150.9
GRB050925A	1.19×10^{-5}	5.53×10^{6}	1.18×10^{8}	0.1

Table cont...

GRB Name	$\mathcal{A}$ (GeV cm^{-2}s^{-1})	$\epsilon_{\nu,b1}$ (GeV)	$\epsilon_{\nu,sb}$ (GeV)	t burst (s)
GRB051001A	1.44×10^{-7}	1.27×10^{7}	1.07×10^{9}	189.1
GRB051006A	6.01×10^{-7}	1.47×10^{7}	5.25×10^{8}	34.8
GRB051012A	3.48×10^{-7}	3.47×10^{7}	6.89×10^{8}	13

Table E.3: Prompt GRB neutrino flux parameters for $z_{max} = 6.29$.

GRB Name	$\mathcal{A}$ (GeV cm^{-2}s^{-1})	$\epsilon_{\nu,b1}$ (GeV)	$\epsilon_{\nu,sb}$ (GeV)	t burst (s)
GRB010613A	2.34×10^{-6}	5.49×10^{5}	7.88×10^{6}	153.2
GRB020525A	6.24×10^{-6}	2.24×10^{5}	4.83×10^{6}	25
GRB020625B	9.36×10^{-8}	2.98×10^{6}	3.94×10^{7}	2
GRB021023A	4.27×10^{-6}	3.69×10^{5}	5.84×10^{6}	15
GRB021102A	6.40×10^{-6}	3.69×10^{5}	4.77×10^{6}	10
GRB021108A	3.18×10^{-6}	3.27×10^{5}	6.76×10^{6}	25
GRB030127A	9.05×10^{-6}	1.23×10^{5}	4.01×10^{6}	50
GRB030202A	8.22×10^{-7}	9.28×10^{5}	1.33×10^{7}	15
GRB030218A	2.81×10^{-6}	1.09×10^{5}	7.20×10^{6}	200
GRB030307A	2.44×10^{-5}	3.42×10^{5}	2.44×10^{6}	3
GRB030326A	5.46×10^{-6}	4.03×10^{5}	5.16×10^{6}	10
GRB030329B	4.80×10^{-6}	1.52×10^{5}	5.51×10^{6}	65
GRB030414A	4.68×10^{-6}	2.02×10^{5}	5.58×10^{6}	40
GRB030422B	9.15×10^{-5}	6.63×10^{4}	1.26×10^{6}	15
GRB030425A	1.84×10^{-6}	8.29×10^{4}	8.89×10^{6}	500
GRB030509A	2.08×10^{-5}	2.02×10^{5}	2.65×10^{6}	9
GRB030518B	5.77×10^{-6}	3.91×10^{5}	5.02×10^{6}	10
GRB030519B	9.92×10^{-5}	1.85×10^{5}	1.21×10^{6}	9.6
GRB030523A	3.67×10^{-6}	2.32×10^{5}	6.30×10^{6}	40
GRB030710A	4.68×10^{-6}	3.97×10^{5}	5.58×10^{6}	12
GRB030715A	7.80×10^{-6}	2.63×10^{5}	4.32×10^{6}	15
GRB030721A	3.04×10^{-6}	2.57×10^{5}	6.92×10^{6}	40
GRB030722A	1.04×10^{-5}	1.52×10^{5}	3.74×10^{6}	30

Table cont...

GRB Name	$\mathcal{A}$ (GeV cm^{-2}s^{-1})	$\epsilon_{\nu,b1}$ (GeV)	$\epsilon_{\nu,sb}$ (GeV)	t burst (s)
GRB030726A	8.84×10^{-6}	1.66×10^{5}	4.06×10^{6}	30
GRB030821A	2.24×10^{-6}	3.01×10^{5}	8.06×10^{6}	18.8
GRB030919A	2.40×10^{-6}	5.52×10^{5}	7.79×10^{6}	13
GRB030921A	2.93×10^{-6}	4.40×10^{5}	7.05×10^{6}	16
GRB030922A	2.32×10^{-6}	3.23×10^{5}	7.93×10^{6}	35
GRB030922B	1.04×10^{-5}	2.02×10^{5}	3.74×10^{6}	18
GRB031016A	9.36×10^{-6}	2.98×10^{5}	3.94×10^{6}	10
GRB031024A	2.23×10^{-7}	3.30×10^{5}	2.56×10^{7}	350
GRB031114A	2.86×10^{-6}	5.23×10^{5}	7.13×10^{6}	12
GRB050607A	3.50×10^{-7}	1.09×10^{6}	2.04×10^{7}	26.4
GRB050626A	2.26×10^{-7}	8.79×10^{5}	2.54×10^{7}	60
GRB050701A	9.74×10^{-7}	6.85×10^{5}	1.22×10^{7}	21.8
GRB050715A	4.51×10^{-7}	6.50×10^{5}	1.80×10^{7}	51.6
GRB050721A	5.74×10^{-7}	3.96×10^{5}	1.59×10^{7}	98.4
GRB050726A	6.07×10^{-7}	5.61×10^{5}	1.55×10^{7}	49.9
GRB050813A	1.37×10^{-6}	4.68×10^{6}	1.03×10^{7}	0.5
GRB050819A	1.45×10^{-7}	1.46×10^{6}	3.17×10^{7}	37.7
GRB050822A	3.71×10^{-7}	4.91×10^{5}	1.98×10^{7}	103.4
GRB050827A	6.55×10^{-7}	5.37×10^{5}	1.49×10^{7}	50
GRB050911A	3.05×10^{-7}	1.55×10^{6}	2.18×10^{7}	16.2
GRB050915A	2.55×10^{-7}	8.91×10^{5}	2.39×10^{7}	52
GRB050916A	2.93×10^{-7}	8.47×10^{5}	2.23×10^{7}	49.5
GRB050922B	2.31×10^{-7}	5.19×10^{5}	2.51×10^{7}	150.9
GRB050925A	1.19×10^{-5}	4.16×10^{5}	3.50×10^{6}	0.1
GRB051001A	1.44×10^{-7}	5.96×10^{5}	3.18×10^{7}	189.1
GRB051006A	6.01×10^{-7}	6.90×10^{5}	1.56×10^{7}	34.8
GRB051012A	3.48×10^{-7}	1.63×10^{6}	2.05×10^{7}	13

Appendix F

GRB Afterglow Neutrino Flux Parameters

The afterglow neutrino flux parameters for unknown redshift are presented here. Values of z= 0.0085, 1 and 6.29 corresponding to the minimum, average and maximum GRB redshifts as in Appendix E, corresponding to luminosity distances of approximately 36.6 ,6612 and 60961 Mpc respectively. Columns one and two of the tables give the GRB name and the prefactor, $\mathcal{B}$, in the expression of the neutrino flux given from Equation 3.14. The third and fourth columns give the break energies, $\epsilon_{\nu,b2}$ and $\epsilon_{\nu,\max}$. The expression for these were given in Equation 3.15 and Equation 3.16 respectively. For completeness the burst duration, $t_{\rm burst}$, is given again here. As explained in Section 3.2 unlike the prompt phase, the proton to pion efficiency, f_π, may be lower than 0.2 in the afterglow phase. Thus f_π is explicitly calculated here using Equation 3.17.

Table F.1: Afterglow GRB neutrino flux parameters for $z_{ave} = 0.085$.

GRB Name	f_π	$\mathcal{B}$ (GeV cm^{-2}s^{-1})	$\epsilon_{\nu,b2}$ (GeV)	$\epsilon_{\nu,\max}$ (GeV)	$t_{\rm glow}$ (s)
GRB010613A	6.09×10^{-5}	7.13×10^{-10}	1.42×10^{5}	1.80×10^{7}	153.2
GRB020525A	2.65×10^{-5}	8.26×10^{-10}	2.58×10^{5}	2.42×10^{7}	25
GRB020625B	3.18×10^{-8}	1.49×10^{-14}	3.60×10^{3}	2.86×10^{6}	2
GRB021023A	1.08×10^{-5}	2.31×10^{-10}	1.67×10^{5}	1.95×10^{7}	15
GRB021102A	1.08×10^{-5}	3.47×10^{-10}	2.26×10^{5}	2.27×10^{7}	10
GRB021108A	1.35×10^{-5}	2.15×10^{-10}	1.39×10^{5}	1.78×10^{7}	25
GRB030127A	7.67×10^{-5}	3.47×10^{-9}	4.07×10^{5}	3.04×10^{7}	50
GRB030202A	2.09×10^{-6}	8.59×10^{-12}	3.69×10^{4}	9.15×10^{6}	15
GRB030218A	9.53×10^{-5}	1.34×10^{-9}	1.75×10^{5}	1.99×10^{7}	200
GRB030307A	1.24×10^{-5}	1.52×10^{-9}	6.33×10^{5}	3.79×10^{7}	3
GRB030326A	9.26×10^{-6}	2.53×10^{-10}	1.96×10^{5}	2.11×10^{7}	10
GRB030329B	5.29×10^{-5}	1.27×10^{-9}	2.38×10^{5}	2.32×10^{7}	65
GRB030414A	3.18×10^{-5}	7.43×10^{-10}	2.14×10^{5}	2.20×10^{7}	40
GRB030422B	2.33×10^{-4}	1.07×10^{-7}	2.78×10^{6}	7.94×10^{7}	15
GRB030425A	1.56×10^{-4}	1.44×10^{-9}	1.39×10^{5}	1.77×10^{7}	500
GRB030509A	3.18×10^{-5}	3.30×10^{-9}	6.56×10^{5}	3.86×10^{7}	9
GRB030518B	9.79×10^{-6}	2.83×10^{-10}	2.06×10^{5}	2.16×10^{7}	10
GRB030519B	1.61×10^{-4}	8.00×10^{-8}	2.77×10^{6}	7.93×10^{7}	9.6
GRB030523A	2.49×10^{-5}	4.56×10^{-10}	1.71×10^{5}	1.97×10^{7}	40
GRB030710A	9.53×10^{-6}	2.23×10^{-10}	1.75×10^{5}	1.99×10^{7}	12
GRB030715A	1.98×10^{-5}	7.74×10^{-10}	2.90×10^{5}	2.57×10^{7}	15
GRB030721A	2.06×10^{-5}	3.14×10^{-10}	1.44×10^{5}	1.81×10^{7}	40
GRB030722A	5.29×10^{-5}	2.75×10^{-9}	4.24×10^{5}	3.10×10^{7}	30
GRB030726A	4.50×10^{-5}	1.99×10^{-9}	3.66×10^{5}	2.88×10^{7}	30
GRB030821A	7.14×10^{-6}	8.00×10^{-11}	9.61×10^{4}	1.48×10^{7}	18.8
GRB030919A	5.29×10^{-6}	6.35×10^{-11}	9.63×10^{4}	1.48×10^{7}	13
GRB030921A	7.94×10^{-6}	1.16×10^{-10}	1.19×10^{5}	1.65×10^{7}	16
GRB030922A	1.38×10^{-5}	1.59×10^{-10}	1.10×10^{5}	1.58×10^{7}	35
GRB030922B	3.18×10^{-5}	1.65×10^{-9}	3.90×10^{5}	2.97×10^{7}	18
GRB031016A	1.59×10^{-5}	7.43×10^{-10}	3.21×10^{5}	2.70×10^{7}	10
GRB031024A	1.32×10^{-5}	1.47×10^{-11}	1.89×10^{4}	6.54×10^{6}	350
GRB031114A	5.82×10^{-6}	8.32×10^{-11}	1.12×10^{5}	1.59×10^{7}	12
GRB050607A	1.57×10^{-6}	2.74×10^{-12}	1.85×10^{4}	6.49×10^{6}	26.4
GRB050626A	2.30×10^{-6}	2.60×10^{-12}	1.43×10^{4}	5.69×10^{6}	60

Table cont...

GRB Name	f_π	$\mathcal{B}$ (GeV cm^{-2}s^{-1})	$\epsilon_{\nu,b2}$ (GeV)	$\epsilon_{\nu,\max}$ (GeV)	$t_{\rm glow}$ (s)
GRB050701A	3.60×10^{-6}	1.75×10^{-11}	4.59×10^{4}	1.02×10^{7}	21.8
GRB050715A	3.94×10^{-6}	8.88×10^{-12}	2.61×10^{4}	7.70×10^{6}	51.6
GRB050721A	9.58×10^{-6}	2.75×10^{-11}	3.63×10^{4}	9.08×10^{6}	98.4
GRB050726A	5.13×10^{-6}	1.56×10^{-11}	3.41×10^{4}	8.80×10^{6}	49.9
GRB050813A	1.16×10^{-7}	7.99×10^{-13}	3.35×10^{4}	8.72×10^{6}	0.5
GRB050819A	9.26×10^{-7}	6.71×10^{-13}	8.77×10^{3}	4.46×10^{6}	37.7
GRB050822A	6.51×10^{-6}	1.21×10^{-11}	2.46×10^{4}	7.47×10^{6}	103.4
GRB050827A	5.56×10^{-6}	1.82×10^{-11}	3.67×10^{4}	9.12×10^{6}	50
GRB050911A	8.39×10^{-7}	1.28×10^{-12}	1.51×10^{4}	5.85×10^{6}	16.2
GRB050915A	2.25×10^{-6}	2.87×10^{-12}	1.55×10^{4}	5.94×10^{6}	52
GRB050916A	2.46×10^{-6}	3.60×10^{-12}	1.75×10^{4}	6.30×10^{6}	49.5
GRB050922B	5.90×10^{-6}	6.80×10^{-12}	1.69×10^{4}	6.20×10^{6}	150.9
GRB050925A	2.01×10^{-7}	1.19×10^{-11}	1.85×10^{5}	2.05×10^{7}	0.1
GRB051001A	4.60×10^{-6}	3.30×10^{-12}	1.14×10^{4}	5.08×10^{6}	189.1
GRB051006A	3.55×10^{-6}	1.06×10^{-11}	3.19×10^{4}	8.50×10^{6}	34.8
GRB051012A	7.67×10^{-7}	1.34×10^{-12}	1.64×10^{4}	6.10×10^{6}	13

Table F.2: Afterglow GRB neutrino flux parameters for $z_{ave} = 1$.

GRB Name	f_π	$\mathcal{B}$ (GeV cm^{-2}s^{-1})	$\epsilon_{\nu,b2}$ (GeV)	$\epsilon_{\nu,\max}$ (GeV)	$t_{\rm glow}$ (s)
GRB010613A	2.00×10^{-1}	2.34×10^{-6}	5.21×10^{8}	7.72×10^{8}	153.2
GRB020525A	2.00×10^{-1}	6.24×10^{-6}	9.46×10^{8}	1.04×10^{9}	25
GRB020625B	5.19×10^{-4}	2.43×10^{-10}	1.32×10^{7}	1.23×10^{8}	2
GRB021023A	1.77×10^{-1}	3.78×10^{-6}	6.13×10^{8}	8.38×10^{8}	15
GRB021102A	1.77×10^{-1}	5.67×10^{-6}	8.31×10^{8}	9.75×10^{8}	10
GRB021108A	2.00×10^{-1}	3.18×10^{-6}	5.10×10^{8}	7.64×10^{8}	25
GRB030127A	2.00×10^{-1}	9.05×10^{-6}	1.49×10^{9}	1.31×10^{9}	50
GRB030202A	3.41×10^{-2}	1.40×10^{-7}	1.35×10^{8}	3.94×10^{8}	15
GRB030218A	2.00×10^{-1}	2.81×10^{-6}	6.44×10^{8}	8.58×10^{8}	200
GRB030307A	2.00×10^{-1}	2.44×10^{-5}	2.32×10^{9}	1.63×10^{9}	3

Table cont...

GRB Name	f_π	$\mathcal{B}$ (GeV cm^{-2}s^{-1})	$\epsilon_{\nu,b2}$ (GeV)	$\epsilon_{\nu,\max}$ (GeV)	$t_{\rm glow}$ (s)
GRB030326A	1.51×10^{-1}	4.13×10^{-6}	7.19×10^{8}	9.07×10^{8}	10
GRB030329B	2.00×10^{-1}	4.80×10^{-6}	8.72×10^{8}	9.99×10^{8}	65
GRB030414A	2.00×10^{-1}	4.68×10^{-6}	7.86×10^{8}	9.48×10^{8}	40
GRB030422B	2.00×10^{-1}	9.15×10^{-5}	1.02×10^{10}	3.41×10^{9}	15
GRB030425A	2.00×10^{-1}	1.84×10^{-6}	5.09×10^{8}	7.63×10^{8}	500
GRB030509A	2.00×10^{-1}	2.08×10^{-5}	2.41×10^{9}	1.66×10^{9}	9
GRB030518B	1.60×10^{-1}	4.62×10^{-6}	7.56×10^{8}	9.30×10^{8}	10
GRB030519B	2.00×10^{-1}	9.92×10^{-5}	1.02×10^{10}	3.41×10^{9}	9.6
GRB030523A	2.00×10^{-1}	3.67×10^{-6}	6.28×10^{8}	8.48×10^{8}	40
GRB030710A	1.56×10^{-1}	3.64×10^{-6}	6.43×10^{8}	8.58×10^{8}	12
GRB030715A	2.00×10^{-1}	7.80×10^{-6}	1.07×10^{9}	1.10×10^{9}	15
GRB030721A	2.00×10^{-1}	3.04×10^{-6}	5.30×10^{8}	7.79×10^{8}	40
GRB030722A	2.00×10^{-1}	1.04×10^{-5}	1.56×10^{9}	1.34×10^{9}	30
GRB030726A	2.00×10^{-1}	8.84×10^{-6}	1.34×10^{9}	1.24×10^{9}	30
GRB030821A	1.17×10^{-1}	1.31×10^{-6}	3.53×10^{8}	6.35×10^{8}	18.8
GRB030919A	8.64×10^{-2}	1.04×10^{-6}	3.53×10^{8}	6.36×10^{8}	13
GRB030921A	1.30×10^{-1}	1.90×10^{-6}	4.39×10^{8}	7.08×10^{8}	16
GRB030922A	2.00×10^{-1}	2.32×10^{-6}	4.04×10^{8}	6.80×10^{8}	35
GRB030922B	2.00×10^{-1}	1.04×10^{-5}	1.43×10^{9}	1.28×10^{9}	18
GRB031016A	2.00×10^{-1}	9.36×10^{-6}	1.18×10^{9}	1.16×10^{9}	10
GRB031024A	2.00×10^{-1}	2.23×10^{-7}	6.92×10^{7}	2.82×10^{8}	350
GRB031114A	9.51×10^{-2}	1.36×10^{-6}	4.09×10^{8}	6.85×10^{8}	12
GRB050607A	2.56×10^{-2}	4.48×10^{-8}	6.80×10^{7}	2.79×10^{8}	26.4
GRB050626A	3.76×10^{-2}	4.25×10^{-8}	5.23×10^{7}	2.45×10^{8}	60
GRB050701A	5.88×10^{-2}	2.86×10^{-7}	1.68×10^{8}	4.39×10^{8}	21.8
GRB050715A	6.44×10^{-2}	1.45×10^{-7}	9.59×10^{7}	3.31×10^{8}	51.6
GRB050721A	1.56×10^{-1}	4.49×10^{-7}	1.33×10^{8}	3.91×10^{8}	98.4
GRB050726A	8.39×10^{-2}	2.54×10^{-7}	1.25×10^{8}	3.79×10^{8}	49.9
GRB050813A	1.90×10^{-3}	1.31×10^{-8}	1.23×10^{8}	3.75×10^{8}	0.5
GRB050819A	1.51×10^{-2}	1.10×10^{-8}	3.22×10^{7}	1.92×10^{8}	37.7
GRB050822A	1.06×10^{-1}	1.97×10^{-7}	9.02×10^{7}	3.21×10^{8}	103.4
GRB050827A	9.08×10^{-2}	2.97×10^{-7}	1.35×10^{8}	3.92×10^{8}	50
GRB050911A	1.37×10^{-2}	2.09×10^{-8}	5.54×10^{7}	2.52×10^{8}	16.2
GRB050915A	3.67×10^{-2}	4.68×10^{-8}	5.70×10^{7}	2.55×10^{8}	52
GRB050916A	4.02×10^{-2}	5.88×10^{-8}	6.42×10^{7}	2.71×10^{8}	49.5
GRB050922B	9.64×10^{-2}	1.11×10^{-7}	6.21×10^{7}	2.67×10^{8}	150.9
GRB050925A	3.29×10^{-3}	1.95×10^{-7}	6.79×10^{8}	8.81×10^{8}	0.1

Table cont...

GRB Name	f_π	$\mathcal{B}$ (GeV cm^{-2}s^{-1})	$\epsilon_{\nu,b2}$ (GeV)	$\epsilon_{\nu,\max}$ (GeV)	$t_{\rm glow}$ (s)
GRB051001A	7.52×10^{-2}	5.40×10^{-8}	4.18×10^{7}	2.19×10^{8}	189.1
GRB051006A	5.79×10^{-2}	1.74×10^{-7}	1.17×10^{8}	3.66×10^{8}	34.8
GRB051012A	1.25×10^{-2}	2.18×10^{-8}	6.02×10^{7}	2.62×10^{8}	13

Table F.3: Afterglow GRB neutrino flux parameters for $z_{ave} = 6.29$.

GRB Name	f_π	$\mathcal{B}$ (GeV cm^{-2}s^{-1})	$\epsilon_{\nu,b2}$ (GeV)	$\epsilon_{\nu,\max}$ (GeV)	$t_{\rm glow}$ (s)
GRB010613A	2.00×10^{-1}	2.34×10^{-6}	2.58×10^{9}	9.00×10^{8}	153.2
GRB020525A	2.00×10^{-1}	6.24×10^{-6}	4.68×10^{9}	1.21×10^{9}	25
GRB020625B	1.22×10^{-2}	5.69×10^{-9}	6.54×10^{7}	1.43×10^{8}	2
GRB021023A	2.00×10^{-1}	4.27×10^{-6}	3.03×10^{9}	9.76×10^{8}	15
GRB021102A	2.00×10^{-1}	6.40×10^{-6}	4.11×10^{9}	1.14×10^{9}	10
GRB021108A	2.00×10^{-1}	3.18×10^{-6}	2.52×10^{9}	8.90×10^{8}	25
GRB030127A	2.00×10^{-1}	9.05×10^{-6}	7.39×10^{9}	1.52×10^{9}	50
GRB030202A	2.00×10^{-1}	8.22×10^{-7}	6.70×10^{8}	4.59×10^{8}	15
GRB030218A	2.00×10^{-1}	2.81×10^{-6}	3.18×10^{9}	1.00×10^{9}	200
GRB030307A	2.00×10^{-1}	2.44×10^{-5}	1.15×10^{10}	1.90×10^{9}	3
GRB030326A	2.00×10^{-1}	5.46×10^{-6}	3.55×10^{9}	1.06×10^{9}	10
GRB030329B	2.00×10^{-1}	4.80×10^{-6}	4.32×10^{9}	1.16×10^{9}	65
GRB030414A	2.00×10^{-1}	4.68×10^{-6}	3.89×10^{9}	1.10×10^{9}	40
GRB030422B	2.00×10^{-1}	9.15×10^{-5}	5.04×10^{10}	3.98×10^{9}	15
GRB030425A	2.00×10^{-1}	1.84×10^{-6}	2.52×10^{9}	8.89×10^{8}	500
GRB030509A	2.00×10^{-1}	2.08×10^{-5}	1.19×10^{10}	1.93×10^{9}	9
GRB030518B	2.00×10^{-1}	5.77×10^{-6}	3.74×10^{9}	1.08×10^{9}	10
GRB030519B	2.00×10^{-1}	9.92×10^{-5}	5.03×10^{10}	3.98×10^{9}	9.6
GRB030523A	2.00×10^{-1}	3.67×10^{-6}	3.11×10^{9}	9.88×10^{8}	40
GRB030710A	2.00×10^{-1}	4.68×10^{-6}	3.18×10^{9}	1.00×10^{9}	12
GRB030715A	2.00×10^{-1}	7.80×10^{-6}	5.27×10^{9}	1.29×10^{9}	15
GRB030721A	2.00×10^{-1}	3.04×10^{-6}	2.62×10^{9}	9.07×10^{8}	40
GRB030722A	2.00×10^{-1}	1.04×10^{-5}	7.71×10^{9}	1.56×10^{9}	30

Table cont...

GRB Name	f_π	$\mathcal{B}$ (GeV cm^{-2}s^{-1})	$\epsilon_{\nu,b2}$ (GeV)	$\epsilon_{\nu,\max}$ (GeV)	$t_{\rm glow}$ (s)
GRB030726A	2.00×10^{-1}	8.84×10^{-6}	6.64×10^{9}	1.44×10^{9}	30
GRB030821A	2.00×10^{-1}	2.24×10^{-6}	1.75×10^{9}	7.40×10^{8}	18.8
GRB030919A	2.00×10^{-1}	2.40×10^{-6}	1.75×10^{9}	7.41×10^{8}	13
GRB030921A	2.00×10^{-1}	2.93×10^{-6}	2.17×10^{9}	8.25×10^{8}	16
GRB030922A	2.00×10^{-1}	2.32×10^{-6}	2.00×10^{9}	7.92×10^{8}	35
GRB030922B	2.00×10^{-1}	1.04×10^{-5}	7.08×10^{9}	1.49×10^{9}	18
GRB031016A	2.00×10^{-1}	9.36×10^{-6}	5.83×10^{9}	1.35×10^{9}	10
GRB031024A	2.00×10^{-1}	2.23×10^{-7}	3.43×10^{8}	3.28×10^{8}	350
GRB031114A	2.00×10^{-1}	2.86×10^{-6}	2.03×10^{9}	7.98×10^{8}	12
GRB050607A	2.00×10^{-1}	3.50×10^{-7}	3.37×10^{8}	3.25×10^{8}	26.4
GRB050626A	2.00×10^{-1}	2.26×10^{-7}	2.59×10^{8}	2.85×10^{8}	60
GRB050701A	2.00×10^{-1}	9.74×10^{-7}	8.33×10^{8}	5.11×10^{8}	21.8
GRB050715A	2.00×10^{-1}	4.51×10^{-7}	4.75×10^{8}	3.86×10^{8}	51.6
GRB050721A	2.00×10^{-1}	5.74×10^{-7}	6.60×10^{8}	4.55×10^{8}	98.4
GRB050726A	2.00×10^{-1}	6.07×10^{-7}	6.20×10^{8}	4.41×10^{8}	49.9
GRB050813A	4.46×10^{-2}	3.06×10^{-7}	6.09×10^{8}	4.37×10^{8}	0.5
GRB050819A	2.00×10^{-1}	1.45×10^{-7}	1.59×10^{8}	2.24×10^{8}	37.7
GRB050822A	2.00×10^{-1}	3.71×10^{-7}	4.46×10^{8}	3.74×10^{8}	103.4
GRB050827A	2.00×10^{-1}	6.55×10^{-7}	6.66×10^{8}	4.57×10^{8}	50
GRB050911A	2.00×10^{-1}	3.05×10^{-7}	2.74×10^{8}	2.93×10^{8}	16.2
GRB050915A	2.00×10^{-1}	2.55×10^{-7}	2.82×10^{8}	2.98×10^{8}	52
GRB050916A	2.00×10^{-1}	2.93×10^{-7}	3.18×10^{8}	3.16×10^{8}	49.5
GRB050922B	2.00×10^{-1}	2.31×10^{-7}	3.07×10^{8}	3.11×10^{8}	150.9
GRB050925A	7.71×10^{-2}	4.57×10^{-6}	3.36×10^{9}	1.03×10^{9}	0.1
GRB051001A	2.00×10^{-1}	1.44×10^{-7}	2.07×10^{8}	2.55×10^{8}	189.1
GRB051006A	2.00×10^{-1}	6.01×10^{-7}	5.79×10^{8}	4.26×10^{8}	34.8
GRB051012A	2.00×10^{-1}	3.48×10^{-7}	2.98×10^{8}	3.06×10^{8}	13

Appendix G

GRB Prompt and Afterglow Neutrino limits

Here we present the upper limits of the prompt and afterglow neutrino fluxes for various energies based on the non-observation of neutrinos and for substituted values of redshift, z= 0.0085, 1 and 6.29 corresponding to the minimum, average and maximum GRB redshifts. We use the spectral parameters given in Appendices E and F and use these to obtain model dependant upper limits. We choose these redshifts to give an indication of the range of limits that could be obtained. Column one of the table gives the GRB name, columns two through four are the limits results for the prompt neutrino flux. The neutrino energy chosen in column two is chosen for indicative purposes only. The limit and ratio of the limit to flux are given in columns three and four respectively. The ratio is of particular importance as this indicates how good the limit is to constraining the flux model. Columns five through seven are some results from the afterglow upper limits. Column five giving a particular neutrino energy and columns six and seven are the relevant limit and ratio of limit

to flux for that particular energy.

As discussed in Chapter 7 one can see from Equation 3.8 that the break in the neutrino spectrum due to the break in the photon energy spectrum has a $1/z$ dependance. These values were shown in Table 7.5 that in the observer frame the first break energy will decrease for larger values of redshift. It can also be shown by dimensional analysis of Equation 3.11 that the prompt neutrino synchrotron break has a $1/z^3$ relationship, thus yielding a decreased break energies for higher redshift. This means at higher redshifts these values are shifted more to lower energies and the contribution of the higher energy neutrinos are suppressed earlier. Thus the reduction of the high energy neutrinos in the flux means that the limits will be greater. This is evident in the results in Table G.3.

In the case of the afterglow however the maximum neutrino energy has several parameters which are redshift dependant. These are the within the magnetic field term through the luminosity, the external radius via the isotropic energy, which has the luminosity distance and redshift terms. The overall dependence yields an increase in maximum energy with redshift. Thus at low redshifts we find that the maximum energy of the neutrinos at times falls below the sensitivity of RICE. Thus no model dependant limits can be obtained in these cases as can be seen in Table G.1.

Table G.1: GRB neutrino flux upper limits and ratios to the WB GRB flux for $z_{min} = 0.085$, for prompt and afterglow phases.

GRB	Burst			Afterglow		
	ϵ_ν (GeV)	Limit (GeV/cm^2)	Ratio	ϵ_ν (GeV)	Limit (GeV/cm^2)	Ratio
GRB010613A	4.1×10^{8}	8.72×10^{3}	8.10×10^{6}	1.4×10^{7}	3.83×10^{8}	1.17×10^{14}
GRB020525A	1.0×10^{9}	4.94×10^{2}	2.20×10^{6}	1.4×10^{7}	3.07×10^{6}	6.70×10^{12}
GRB020625B	4.1×10^{8}	2.66×10^{3}	4.30×10^{9}	-	-	-
GRB021023A	2.1×10^{9}	8.20×10^{2}	7.32×10^{6}	1.4×10^{7}	1.16×10^{7}	1.21×10^{14}
GRB021102A	2.1×10^{9}	9.39×10^{2}	8.38×10^{6}	1.4×10^{7}	5.40×10^{6}	6.55×10^{13}
GRB021108A	2.1×10^{9}	1.45×10^{3}	9.21×10^{6}	1.4×10^{7}	1.75×10^{7}	1.08×10^{14}
GRB030127A	9.3×10^{8}	1.69×10^{3}	1.60×10^{6}	1.9×10^{7}	6.03×10^{6}	1.70×10^{12}
GRB030202A	2.1×10^{9}	8.53×10^{2}	9.93×10^{7}	-	-	-
GRB030218A	1.0×10^{9}	3.25×10^{3}	1.96×10^{6}	1.4×10^{7}	1.09×10^{8}	1.51×10^{13}
GRB030307A	2.1×10^{9}	1.23×10^{3}	8.84×10^{6}	2.4×10^{7}	1.19×10^{6}	1.42×10^{13}
GRB030326A	2.1×10^{9}	1.58×10^{3}	1.80×10^{7}	1.4×10^{7}	7.52×10^{7}	1.17×10^{15}
GRB030329B	2.1×10^{9}	3.65×10^{3}	3.90×10^{6}	1.4×10^{7}	1.36×10^{8}	7.09×10^{13}
GRB030414A	2.1×10^{9}	7.35×10^{2}	1.31×10^{6}	1.4×10^{7}	5.75×10^{6}	7.93×10^{12}
GRB030422B	6.2×10^{8}	1.10×10^{3}	2.77×10^{5}	3.8×10^{7}	1.01×10^{5}	5.71×10^{9}
GRB030425A	5.2×10^{8}	6.08×10^{3}	3.41×10^{6}	1.4×10^{7}	1.03×10^{8}	4.72×10^{12}
GRB030509A	9.3×10^{8}	3.53×10^{3}	1.33×10^{7}	2.7×10^{7}	3.48×10^{6}	6.11×10^{12}
GRB030518B	2.1×10^{9}	1.06×10^{3}	1.10×10^{7}	1.4×10^{7}	1.04×10^{7}	1.48×10^{14}
GRB030519B	3.1×10^{8}	8.41×10^{2}	5.89×10^{5}	3.6×10^{7}	4.71×10^{4}	5.69×10^{9}
GRB030523A	2.1×10^{9}	1.46×10^{3}	3.58×10^{6}	1.4×10^{7}	1.54×10^{7}	3.10×10^{13}
GRB030710A	2.1×10^{9}	1.74×10^{3}	1.90×10^{7}	1.4×10^{7}	2.90×10^{7}	4.02×10^{14}
GRB030715A	2.1×10^{9}	8.62×10^{2}	3.00×10^{6}	1.5×10^{7}	2.02×10^{6}	8.07×10^{12}
GRB030721A	2.1×10^{9}	5.68×10^{2}	1.86×10^{6}	1.4×10^{7}	8.44×10^{6}	2.26×10^{13}
GRB030722A	9.3×10^{8}	6.17×10^{2}	1.05×10^{6}	2.0×10^{7}	1.22×10^{6}	7.19×10^{11}
GRB030726A	9.3×10^{8}	4.37×10^{2}	9.55×10^{5}	1.8×10^{7}	8.86×10^{5}	7.08×10^{11}
GRB030821A	6.2×10^{8}	1.26×10^{3}	9.98×10^{6}	1.4×10^{7}	2.35×10^{8}	4.29×10^{15}
GRB030919A	2.1×10^{9}	7.24×10^{2}	1.98×10^{7}	1.4×10^{7}	3.41×10^{7}	1.13×10^{15}
GRB030921A	2.1×10^{9}	2.37×10^{3}	3.44×10^{7}	1.4×10^{7}	6.41×10^{7}	1.06×10^{15}
GRB030922A	8.2×10^{8}	3.12×10^{3}	4.86×10^{7}	1.4×10^{7}	1.33×10^{8}	6.97×10^{14}
GRB030922B	8.2×10^{8}	3.40×10^{3}	1.44×10^{7}	1.9×10^{7}	9.27×10^{6}	1.49×10^{13}
GRB031016A	2.1×10^{9}	8.30×10^{2}	4.09×10^{6}	1.7×10^{7}	3.10×10^{6}	1.92×10^{13}
GRB031024A	2.1×10^{9}	7.94×10^{2}	5.20×10^{6}	-	-	-
GRB031114A	2.1×10^{9}	2.71×10^{3}	6.38×10^{7}	1.4×10^{7}	1.21×10^{8}	3.57×10^{15}
GRB050607A	2.1×10^{9}	3.78×10^{3}	6.91×10^{8}	-	-	-

Table cont...

GRB	Burst			Afterglow		
	ϵ_ν (GeV)	Limit (GeV/cm^2)	Ratio	ϵ_ν (GeV)	Limit (GeV/cm^2)	Ratio
GRB050626A	3.1×10^{9}	1.64×10^{4}	1.10×10^{9}	-	-	-
GRB050701A	2.1×10^{9}	1.94×10^{3}	9.70×10^{7}	-	-	-
GRB050715A	2.1×10^{9}	1.60×10^{3}	6.94×10^{7}	-	-	-
GRB050721A	2.1×10^{9}	5.41×10^{2}	5.86×10^{6}	-	-	-
GRB050726A	2.1×10^{9}	4.86×10^{2}	1.39×10^{7}	-	-	-
GRB050813A	2.1×10^{9}	4.76×10^{3}	5.01×10^{10}	-	-	-
GRB050819A	2.1×10^{9}	8.18×10^{3}	3.39×10^{9}	-	-	-
GRB050822A	2.1×10^{9}	3.84×10^{2}	7.61×10^{6}	-	-	-
GRB050827A	2.1×10^{9}	7.51×10^{3}	1.90×10^{8}	-	-	-
GRB050911A	2.1×10^{9}	3.74×10^{2}	1.81×10^{8}	-	-	-
GRB050915A	2.1×10^{9}	5.88×10^{2}	6.11×10^{7}	-	-	-
GRB050916A	2.1×10^{9}	1.32×10^{3}	1.19×10^{8}	-	-	-
GRB050922B	2.1×10^{9}	1.02×10^{3}	2.35×10^{7}	-	-	-
GRB050925A	6.2×10^{8}	5.31×10^{3}	1.17×10^{8}	1.4×10^{7}	5.10×10^{7}	1.63×10^{18}
GRB051001A	2.1×10^{9}	4.49×10^{2}	1.52×10^{7}	-	-	-
GRB051006A	2.1×10^{9}	4.43×10^{3}	2.26×10^{8}	-	-	-
GRB051012A	2.1×10^{9}	3.14×10^{2}	1.74×10^{8}	-	-	-

Table G.2: GRB neutrino flux upper limits and ratios to the WB GRB flux for $z_{max} = 1$, for prompt and afterglow phases.

GRB	Burst			Afterglow		
	ϵ_ν (GeV)	Limit (GeV/cm^2)	Ratio	ϵ_ν (GeV)	Limit (GeV/cm^2)	Ratio
GRB010613A	2.0×10^{8}	5.79×10^{4}	5.38×10^{7}	3.1×10^{8}	2.91×10^{4}	4.58×10^{7}
GRB020525A	1.0×10^{8}	8.00×10^{3}	1.71×10^{7}	3.1×10^{8}	1.39×10^{3}	9.15×10^{6}
GRB020625B	3.1×10^{8}	5.19×10^{3}	7.53×10^{9}	1.0×10^{8}	1.49×10^{5}	3.67×10^{13}
GRB021023A	1.0×10^{8}	8.34×10^{3}	4.35×10^{7}	3.1×10^{8}	2.52×10^{3}	2.96×10^{7}
GRB021102A	1.0×10^{8}	1.12×10^{4}	5.81×10^{7}	3.1×10^{8}	2.27×10^{3}	3.61×10^{7}

Table cont...

GRB	Burst			Afterglow		
	ϵ_ν (GeV)	Limit (GeV/cm^2)	Ratio	ϵ_ν (GeV)	Limit (GeV/cm^2)	Ratio
GRB021108A	1.0×10^{8}	9.82×10^{3}	4.11×10^{7}	3.1×10^{8}	4.70×10^{3}	3.27×10^{7}
GRB030127A	1.0×10^{8}	3.74×10^{4}	2.75×10^{7}	4.1×10^{8}	4.07×10^{3}	1.09×10^{7}
GRB030202A	2.0×10^{8}	5.54×10^{3}	1.50×10^{8}	2.0×10^{8}	1.08×10^{4}	1.39×10^{9}
GRB030218A	2.0×10^{8}	4.36×10^{4}	2.59×10^{7}	3.1×10^{8}	1.39×10^{4}	1.72×10^{7}
GRB030307A	1.0×10^{8}	2.70×10^{4}	1.89×10^{8}	5.2×10^{8}	2.20×10^{3}	4.49×10^{7}
GRB030326A	1.0×10^{8}	3.06×10^{4}	1.87×10^{8}	3.1×10^{8}	5.97×10^{3}	1.13×10^{8}
GRB030329B	1.0×10^{8}	6.16×10^{4}	6.58×10^{7}	4.1×10^{8}	1.38×10^{4}	3.13×10^{7}
GRB030414A	1.0×10^{8}	7.17×10^{3}	1.28×10^{7}	3.1×10^{8}	1.60×10^{3}	7.31×10^{6}
GRB030422B	1.0×10^{8}	1.52×10^{4}	2.12×10^{7}	8.2×10^{8}	9.78×10^{2}	2.94×10^{6}
GRB030425A	2.0×10^{8}	3.28×10^{4}	1.19×10^{7}	3.1×10^{8}	1.96×10^{4}	1.18×10^{7}
GRB030509A	1.0×10^{8}	1.04×10^{5}	2.42×10^{8}	5.2×10^{8}	7.56×10^{3}	6.25×10^{7}
GRB030518B	1.0×10^{8}	1.39×10^{4}	8.03×10^{7}	3.1×10^{8}	2.87×10^{3}	5.10×10^{7}
GRB030519B	1.0×10^{8}	7.58×10^{3}	2.90×10^{7}	7.3×10^{8}	5.15×10^{2}	2.50×10^{6}
GRB030523A	1.0×10^{8}	1.07×10^{4}	2.42×10^{7}	3.1×10^{8}	3.54×10^{3}	1.64×10^{7}
GRB030710A	1.0×10^{8}	2.22×10^{4}	1.32×10^{8}	3.1×10^{8}	6.14×10^{3}	9.81×10^{7}
GRB030715A	1.0×10^{8}	8.73×10^{3}	2.49×10^{7}	3.1×10^{8}	1.23×10^{3}	1.22×10^{7}
GRB030721A	1.0×10^{8}	4.28×10^{3}	1.17×10^{7}	3.1×10^{8}	1.75×10^{3}	8.27×10^{6}
GRB030722A	1.0×10^{8}	1.32×10^{4}	1.41×10^{7}	4.1×10^{8}	1.45×10^{3}	5.87×10^{6}
GRB030726A	1.0×10^{8}	7.57×10^{3}	9.51×10^{6}	4.1×10^{8}	1.11×10^{3}	4.56×10^{6}
GRB030821A	2.0×10^{8}	1.48×10^{4}	1.17×10^{8}	3.1×10^{8}	1.07×10^{4}	1.67×10^{8}
GRB030919A	1.0×10^{8}	6.02×10^{3}	6.43×10^{7}	2.0×10^{8}	3.06×10^{3}	1.31×10^{8}
GRB030921A	1.0×10^{8}	1.75×10^{4}	1.25×10^{8}	3.1×10^{8}	9.49×10^{3}	1.49×10^{8}
GRB030922A	1.0×10^{8}	2.50×10^{4}	1.03×10^{8}	2.0×10^{8}	1.15×10^{4}	9.34×10^{7}
GRB030922B	1.0×10^{8}	6.14×10^{4}	1.09×10^{8}	4.1×10^{8}	8.12×10^{3}	5.04×10^{7}
GRB031016A	1.0×10^{8}	1.53×10^{4}	5.46×10^{7}	4.1×10^{8}	2.05×10^{3}	2.10×10^{7}
GRB031024A	2.0×10^{8}	1.97×10^{3}	8.43×10^{6}	1.0×10^{8}	7.68×10^{3}	2.70×10^{7}
GRB031114A	1.0×10^{8}	2.19×10^{4}	2.13×10^{8}	3.1×10^{8}	1.29×10^{4}	3.52×10^{8}
GRB050607A	3.1×10^{8}	8.90×10^{3}	2.99×10^{7}	2.0×10^{8}	6.25×10^{4}	1.02×10^{10}
GRB050626A	3.1×10^{8}	1.00×10^{5}	2.46×10^{9}	1.0×10^{8}	8.68×10^{5}	8.12×10^{10}
GRB050701A	3.1×10^{8}	2.25×10^{4}	4.19×10^{7}	2.0×10^{8}	4.03×10^{4}	1.95×10^{9}
GRB050715A	3.1×10^{8}	6.16×10^{3}	1.38×10^{7}	2.0×10^{8}	2.38×10^{4}	7.26×10^{8}
GRB050721A	3.1×10^{8}	2.20×10^{3}	5.12×10^{5}	2.0×10^{8}	5.90×10^{3}	3.60×10^{7}
GRB050726A	2.0×10^{8}	2.71×10^{3}	3.96×10^{7}	2.0×10^{8}	6.46×10^{3}	1.33×10^{8}
GRB050813A	2.0×10^{8}	2.59×10^{4}	1.03×10^{10}	2.0×10^{8}	4.45×10^{4}	1.76×10^{12}
GRB050819A	6.2×10^{8}	1.19×10^{4}	4.56×10^{6}	1.0×10^{8}	1.41×10^{5}	6.41×10^{10}
GRB050822A	4.1×10^{8}	1.82×10^{3}	1.04×10^{5}	2.0×10^{8}	1.02×10^{4}	1.11×10^{8}

Table cont...

GRB	Burst			Afterglow		
	ϵ_ν (GeV)	Limit (GeV/cm^2)	Ratio	ϵ_ν (GeV)	Limit (GeV/cm^2)	Ratio
GRB050827A	2.0×10^8	2.45×10^4	8.34×10^7	2.0×10^8	6.57×10^4	1.20×10^9
GRB050911A	3.1×10^8	1.17×10^3	1.22×10^7	1.0×10^8	8.27×10^3	6.00×10^9
GRB050915A	3.1×10^8	2.37×10^3	2.01×10^7	1.0×10^8	1.71×10^4	1.75×10^9
GRB050916A	4.1×10^8	6.59×10^3	1.41×10^7	1.0×10^8	4.21×10^4	3.83×10^9
GRB050922B	4.1×10^8	3.09×10^3	4.32×10^5	1.0×10^8	2.45×10^4	3.81×10^8
GRB050925A	1.0×10^8	8.90×10^4	2.73×10^9	3.1×10^8	1.61×10^4	6.08×10^{11}
GRB051001A	5.2×10^8	1.16×10^3	2.91×10^5	1.0×10^8	1.32×10^4	2.76×10^8
GRB051006A	2.0×10^8	1.36×10^4	5.65×10^7	2.0×10^8	4.48×10^4	1.86×10^9
GRB051012A	4.1×10^8	1.13×10^3	4.41×10^6	2.0×10^8	1.82×10^4	1.16×10^{10}

Table G.3: GRB neutrino flux upper limits and ratios to the WB GRB flux for $z_{ave} = 6.29$, for prompt and afterglow phases.

GRB	Burst			Afterglow		
	ϵ_ν (GeV)	Limit (GeV/cm^2)	Ratio	ϵ_ν (GeV)	Limit (GeV/cm^2)	Ratio
GRB010613A	1.0×10^8	1.35×10^5	2.10×10^{10}	3.1×10^8	2.04×10^4	1.59×10^8
GRB020525A	1.0×10^8	7.85×10^3	7.47×10^9	4.1×10^8	1.54×10^3	3.74×10^7
GRB020625B	1.0×10^8	3.89×10^4	3.58×10^{11}	1.0×10^8	1.16×10^5	2.72×10^{12}
GRB021023A	1.0×10^8	1.12×10^4	1.77×10^{10}	3.1×10^8	2.00×10^3	1.03×10^8
GRB021102A	1.0×10^8	1.11×10^4	2.63×10^{10}	3.1×10^8	1.70×10^3	1.18×10^8
GRB021108A	1.0×10^8	1.36×10^4	1.29×10^{10}	3.1×10^8	3.36×10^3	1.16×10^8
GRB030127A	1.0×10^8	3.63×10^4	1.73×10^{10}	5.2×10^8	3.82×10^3	4.02×10^7
GRB030202A	1.0×10^8	1.65×10^4	2.61×10^{10}	2.0×10^8	7.75×10^3	6.87×10^8
GRB030218A	1.0×10^8	1.05×10^5	1.25×10^{10}	4.1×10^8	1.25×10^4	5.75×10^7
GRB030307A	1.0×10^8	1.82×10^4	1.44×10^{11}	5.2×10^8	1.68×10^3	1.70×10^8
GRB030326A	1.0×10^8	4.42×10^4	1.05×10^{11}	4.1×10^8	5.71×10^3	3.02×10^8
GRB030329B	1.0×10^8	9.93×10^4	3.63×10^{10}	4.1×10^8	1.09×10^4	1.23×10^8
GRB030414A	1.0×10^8	8.82×10^3	5.25×10^9	4.1×10^8	1.56×10^3	2.63×10^7
GRB030422B	1.0×10^8	1.33×10^4	2.11×10^{10}	9.3×10^8	8.77×10^2	1.16×10^7

Table cont...

GRB	Burst			Afterglow		
	ϵ_ν (GeV)	Limit (GeV/cm^2)	Ratio	ϵ_ν (GeV)	Limit (GeV/cm^2)	Ratio
GRB030425A	1.0×10^{8}	6.54×10^{4}	3.11×10^{9}	3.1×10^{8}	1.41×10^{4}	4.20×10^{7}
GRB030509A	1.0×10^{8}	6.77×10^{4}	1.79×10^{11}	5.2×10^{8}	6.41×10^{3}	2.62×10^{8}
GRB030518B	1.0×10^{8}	1.58×10^{4}	3.76×10^{10}	3.1×10^{8}	2.31×10^{3}	1.62×10^{8}
GRB030519B	1.0×10^{8}	6.67×10^{3}	2.41×10^{10}	8.2×10^{8}	4.63×10^{2}	9.91×10^{6}
GRB030523A	1.0×10^{8}	1.57×10^{4}	9.37×10^{9}	3.1×10^{8}	2.54×10^{3}	5.84×10^{7}
GRB030710A	1.0×10^{8}	3.01×10^{4}	5.97×10^{10}	3.1×10^{8}	4.40×10^{3}	2.71×10^{8}
GRB030715A	1.0×10^{8}	7.39×10^{3}	1.17×10^{10}	4.1×10^{8}	1.37×10^{3}	5.01×10^{7}
GRB030721A	1.0×10^{8}	7.02×10^{3}	4.17×10^{9}	3.1×10^{8}	1.35×10^{3}	3.15×10^{7}
GRB030722A	1.0×10^{8}	9.79×10^{3}	7.76×10^{9}	4.1×10^{8}	1.21×10^{3}	2.42×10^{7}
GRB030726A	1.0×10^{8}	5.91×10^{3}	4.69×10^{9}	4.1×10^{8}	9.33×10^{2}	1.89×10^{7}
GRB030821A	1.0×10^{8}	3.87×10^{4}	4.90×10^{10}	3.1×10^{8}	6.67×10^{3}	3.00×10^{8}
GRB030919A	1.0×10^{8}	1.01×10^{4}	1.85×10^{10}	3.1×10^{8}	3.07×10^{3}	1.87×10^{8}
GRB030921A	1.0×10^{8}	2.95×10^{4}	4.39×10^{10}	3.1×10^{8}	6.59×10^{3}	3.31×10^{8}
GRB030922A	1.0×10^{8}	4.30×10^{4}	2.92×10^{10}	3.1×10^{8}	1.22×10^{4}	3.26×10^{8}
GRB030922B	1.0×10^{8}	4.79×10^{4}	6.33×10^{10}	4.1×10^{8}	6.38×10^{3}	1.96×10^{8}
GRB031016A	1.0×10^{8}	1.30×10^{4}	3.09×10^{10}	4.1×10^{8}	1.53×10^{3}	7.75×10^{7}
GRB031024A	1.0×10^{8}	9.18×10^{3}	6.24×10^{8}	2.0×10^{8}	8.01×10^{3}	5.73×10^{7}
GRB031114A	1.0×10^{8}	3.86×10^{4}	7.65×10^{10}	3.1×10^{8}	8.77×10^{3}	5.62×10^{8}
GRB050607A	1.0×10^{8}	6.69×10^{4}	4.08×10^{9}	2.0×10^{8}	5.05×10^{4}	3.00×10^{9}
GRB050626A	1.0×10^{8}	1.05×10^{6}	4.16×10^{11}	2.0×10^{8}	1.00×10^{6}	3.11×10^{10}
GRB050701A	1.0×10^{8}	8.83×10^{4}	1.28×10^{10}	2.0×10^{8}	2.60×10^{4}	1.66×10^{9}
GRB050715A	1.0×10^{8}	2.90×10^{4}	1.83×10^{9}	2.0×10^{8}	1.83×10^{4}	6.08×10^{8}
GRB050721A	1.0×10^{8}	8.23×10^{3}	7.15×10^{7}	2.0×10^{8}	4.27×10^{3}	8.12×10^{7}
GRB050726A	1.0×10^{8}	9.16×10^{3}	6.08×10^{9}	2.0×10^{8}	4.19×10^{3}	1.40×10^{8}
GRB050813A	1.0×10^{8}	7.16×10^{4}	2.73×10^{12}	2.0×10^{8}	2.90×10^{4}	1.88×10^{11}
GRB050819A	1.0×10^{8}	8.68×10^{4}	2.94×10^{8}	1.0×10^{8}	8.50×10^{4}	8.10×10^{9}
GRB050822A	1.0×10^{8}	1.13×10^{4}	1.64×10^{7}	2.0×10^{8}	7.01×10^{3}	1.33×10^{8}
GRB050827A	1.0×10^{8}	1.12×10^{5}	1.51×10^{10}	2.0×10^{8}	4.58×10^{4}	1.52×10^{9}
GRB050911A	1.0×10^{8}	8.68×10^{3}	1.38×10^{9}	2.0×10^{8}	8.75×10^{3}	7.90×10^{8}
GRB050915A	1.0×10^{8}	1.89×10^{4}	2.40×10^{9}	2.0×10^{8}	1.76×10^{4}	6.11×10^{8}
GRB050916A	1.0×10^{8}	4.75×10^{4}	1.90×10^{9}	2.0×10^{8}	4.27×10^{4}	1.52×10^{9}
GRB050922B	1.0×10^{8}	3.07×10^{4}	5.16×10^{7}	2.0×10^{8}	2.50×10^{4}	3.59×10^{8}
GRB050925A	1.0×10^{8}	6.13×10^{4}	2.89×10^{12}	3.1×10^{8}	1.35×10^{4}	1.07×10^{11}
GRB051001A	1.0×10^{8}	1.14×10^{4}	2.19×10^{7}	1.0×10^{8}	8.46×10^{3}	2.10×10^{8}
GRB051006A	1.0×10^{8}	6.75×10^{4}	9.42×10^{9}	2.0×10^{8}	3.25×10^{4}	1.47×10^{9}
GRB051012A	1.0×10^{8}	1.61×10^{4}	1.45×10^{9}	2.0×10^{8}	1.29×10^{4}	1.38×10^{9}